

Crustal deformation source monitoring using
advanced InSAR time series and time
dependent inverse modeling

Dissertation
to obtain the academic degree
"doctor rerum naturalium" (Dr. rer. nat.)
for the scientific discipline "Geophysics"
submitted to
the Faculty of Mathematics and Natural Sciences
at the University of Potsdam

Manoochehr Shirzaei
December 2010

Published online at the
Institutional Repository of the University of Potsdam:
URL <http://opus.kobv.de/ubp/volltexte/2011/5077/>
URN <urn:nbn:de:kobv:517-opus-50774>
<http://nbn-resolving.org/urn:nbn:de:kobv:517-opus-50774>

Author's declaration

I declare that the work presented in this thesis is, to the best of my knowledge and belief, original except as acknowledged in the text. Passages in the text, which have been taken literally or analogously from other sources, are marked as such. This statement also includes any figures.

Manoochehr Shirzaei

Potsdam 5.7.2010

Abstract

Crustal deformation can be the result of volcanic and tectonic activity such as fault dislocation and magma intrusion. The crustal deformation may precede and/or succeed the earthquake occurrence and eruption. Mitigating the associated hazard, continuous monitoring of the crustal deformation accordingly has become an important task for geo-observatories and fast response systems. Due to highly non-linear behavior of the crustal deformation fields in time and space, which are not always measurable using conventional geodetic methods (e.g., Leveling), innovative techniques of monitoring and analysis are required.

In this thesis I describe novel methods to improve the ability for precise and accurate mapping the spatiotemporal surface deformation field using multi acquisitions of satellite radar data. Furthermore, to better understand the source of such spatiotemporal deformation fields, I present novel static and time dependent model inversion approaches. Almost any interferograms include areas where the signal decorrelates and is distorted by atmospheric delay. In this thesis I detail new analysis methods to reduce the limitations of conventional InSAR, by combining the benefits of advanced InSAR methods such as the permanent scatterer InSAR (PSI) and the small baseline subsets (SBAS) with a wavelet based data filtering scheme. This novel InSAR time series methodology is applied, for instance, to monitor the non-linear deformation processes at Hawaii Island. The radar phase change at Hawaii is found to be due to intrusions, eruptions, earthquakes and flank movement processes and superimposed by significant environmental artifacts (e.g., atmospheric). The deformation field, I obtained using the new InSAR analysis method, is in good agreement with continuous GPS data. This provides an accurate spatiotemporal deformation field at Hawaii, which allows time dependent source modeling.

Conventional source modeling methods usually deal with static deformation field, while retrieving the dynamics of the source requires more sophisticated time dependent optimization approaches. This problem I address by combining Monte Carlo based optimization approaches with a Kalman Filter, which provides the model parameters of the deformation source consistent in time. I found there are numerous deformation sources at Hawaii Island which are spatiotemporally interacting, such as volcano inflation is associated to changes in the rifting behavior, and temporally linked to silent earthquakes.

I applied these new methods to other tectonic and volcanic terrains, most of which revealing the importance of associated or coupled deformation sources. The findings are 1) the relation between deep and shallow hydrothermal and magmatic sources underneath the Campi Flegrei volcano, 2) gravity-driven deformation at Damavand volcano, 3) fault interaction associated with the 2010 Haiti earthquake, 4) independent block wise flank motion at the Hilina Fault system, Kilauea, and 5) interaction between salt diapir and the 2005 Qeshm earthquake in southern Iran.

This thesis, written in cumulative form including 9 manuscripts published or under review in peer reviewed journals, improves the techniques for InSAR time series analysis and source modeling and shows the mutual dependence between adjacent deformation sources. These findings allow more realistic estimation of the hazard associated with complex volcanic and tectonic systems.

Zusammenfassung

Oberflächendehformationen können eine Folge von vulkanischen und tektonischen Aktivitäten sein, wie etwa Plattenverschiebungen oder Magmaintrusion. Die Deformation der Erdkruste kann einem Erdbeben oder einem Vulkanausbruch vorausgehen und/oder folgen. Um damit drohende Gefahren für den Menschen zu verringern, ist die kontinuierliche Beobachtung von Krustendehformationen eine wichtige Aufgabe für Erdobservatorien und Fast-Response-Systems geworden. Auf Grund des starken nicht-linearen Verhaltens von Oberflächendehformationsgebiet in Zeit und Raum, die mit konventionellen Methoden nicht immer erfasst werden (z.B., Nivellements), sind innovative Beobachtungs- und Analysetechniken erforderlich.

In dieser Dissertation beschreibe ich Methoden, welche durch Mehrfachbeobachtungen der Erdoberfläche mit satellitengestütztem Radar eine präzise und akkurate Abbildung der raumzeitlichen Oberflächendehformationen ermöglichen. Um die Bildung und Entwicklung von solchen raumzeitlichen Deformationsgebieten besser zu verstehen, zeige ich weiterhin neuartige Ansätze zur statischen und zeitabhängigen Modellinversion.

Radar-Interferogramme weisen häufig Gebiete auf, in denen das Phasensignal dekorreliert und durch atmosphärische Laufzeitverzögerung verzerrt ist. In dieser Arbeit beschreibe ich wie Probleme des konventionellen InSAR überwunden werden können, indem fortgeschrittene InSAR-Methoden, wie das Permanent Scatterer InSAR (PSI) und Small Baseline Subsets (SBAS), mit einer Wavelet-basierten Datenfilterung verknüpft werden. Diese neuartige Analyse von InSAR Zeitreihen wird angewendet, um zum Beispiel nicht-lineare Deformationsprozesse auf Hawaii zu überwachen. Radar-Phasenänderungen, gemessen auf der Pazifikinsel, beruhen auf Magmaintrusion, Vulkaneruption, Erdbeben und Flankenbewegungsprozessen, welche durch signifikante Artefakte (z.B. atmosphärische) überlagert werden. Mit Hilfe der neuen InSAR-Analyse wurde ein Deformationsgebiet ermittelt, welches eine gute Übereinstimmung mit kontinuierlich gemessenen GPS-Daten aufweist. Auf der Grundlage eines solchen, mit hoher Genauigkeit gemessenen, raumzeitlichen Deformationsgebiets wird für Hawaii eine zeitabhängige Modellierung der Deformationsquelle ermöglicht.

Konventionelle Methoden zur Modellierung von Deformationsquellen arbeiten normalerweise mit statischen Daten der Deformationsgebiete. Doch um die Dynamik einer Deformationsquelle zu untersuchen, sind hoch entwickelte zeitabhängige Optimierungsansätze notwendig.

Dieses Problem bin ich durch eine Kombination von Monte-Carlo-basierten Optimierungsansätzen mit Kalman-Filtern angegangen, womit zeitlich konsistente Modellparameter der Deformationquelle gefunden werden. Ich fand auf der Insel Hawaii mehrere, raumzeitlich interagierende Deformationsquellen, etwa Vulkaninflation verknüpft mit Kluftbildungen und Veränderungen in bestehenden Klüften sowie zeitliche Korrelationen mit stillen Erdbeben.

Ich wendete die neuen Methoden auf weitere tektonisch und vulkanisch aktive Gebiete an, wo häufig die eine Interaktion der Deformationsquellen nachgewiesen werden konnte und ihrer bedeutung untersucht wurde. Die untersuchten Gebiete und Deformationsquellen sind 1) tiefe und oberflächliche hydrothermale und magmatische Quellen unterhalb des Campi Flegrei Vulkans, 2) gravitationsbedingte Deformationen am Damawand Vulkan, 3) Störungsdynamik in Verbindung mit dem Haiti Beben im Jahr 2010, 4) unabhängige blockweise Flankenbewegung an der Hilina Störungszone, und 5) der Einfluss eines Salzdiapirs auf das Qeshm Erdbeben im Süd-Iran im Jahr 2005.

Diese Dissertation, geschrieben als kumulative Arbeit von neun Manuskripten, welche entweder veröffentlicht oder derzeit in Begutachtung bei 'peer-review' Zeitschriften sind, technische Verbesserungen zur Analyse von InSAR Zeitreihen vor sowie zur Modellierung von Deformationsquellen. Sie zeigt die gegenseitige Beeinflussung von benachbarten Deformationsquellen, und sie ermöglicht, realistischere Einschätzungen von Naturgefahren, die von komplexen vulkanischen und tektonischen Systemen ausgehen.

Acknowledgments

First and foremost I would like to thank my advisors, Thomas R. Walter, who has provided me with the opportunity for doing this PhD and whose advice and mentorship has been tireless, fair and of the highest standard. His characteristics such as being always ready for intensive discussion and open for new idea were always inspiring me.

Thanks also go to the many colleagues that I have worked with, in particular to section 2.1 and my close friends and office mates Hanes, Christoph, Anne, Eoghan, Silke, Ade, Jelenna, Henriete, Michele, Joel and Andrea.

Finally, I thank my parents for their early guidance and later encouragement. And special thanks go to Susanna who has constantly supported me.

The start up of my PhD period was not so easy; however, I got the chance to learn important lessons that help me to become a better human and afterward maybe a good scientist. Now almost at the end of my study I am happy with the achievement that I have done in my scientific carrier, so far, much more than I expected in the beginning. However, it is still not satisfactory, I have a dream....

This work was financially supported by the R&D program GEOTECHNOLOGIEN funded by the German ministry of Education and Research (BMBF) grant 03G0646B, the German Research Foundation (DFG) grant WA1642-1/4. The SBAS-InSAR data utilized in the algorithm test in chapter 5 and 6 were kindly provided by R. Lanari. Radar data used in this thesis were provided by the European Space Agency. SRTM topographic data were provided by the Jet Propulsion Laboratory (JPL).

Table of contents

ABSTRACT	V
ZUSAMMENFASSUNG.....	VII
ACKNOWLEDGMENTS	IX
CHAPTER 1	1
INTRODUCTION.....	1
1.1 GEODETIC MONITORING.....	1
1.1.1 <i>Interferometric synthetic aperture radar</i>	2
1.2 WAVELET BASED ANALYSIS OF IRREGULARLY SAMPLED TIME SERIES	3
1.3 INVERSE MODELING OF VOLCANIC AND TECTONIC DISLOCATION SOURCE	4
1.4 FORWARD MODELING THE VOLCANIC AND TECTONIC STRESS FIELD.....	5
1.5 CONTRIBUTIONS.....	6
1.6 THESIS ROADMAP	7
CHAPTER 2	9
WAVELET BASED INSAR (WABINSAR): A NEW ADVANCED TIME SERIES APPROACH FOR ACCURATE SPATIOTEMPORAL SURFACE DEFORMATION MONITORING...9	
ABSTRACT	9
2.1 INTRODUCTION.....	9
2.2 WAVELET BASED INSAR TIME SERIES (WABINSAR)	11
2.2.1 <i>Interferogram formation</i>	11
2.2.2 <i>Elite interferogram and elite pixel identification</i>	11
2.2.3 <i>DEM inaccuracy correction</i>	14
2.2.4 <i>Time Series Generation</i>	16
2.2.5 <i>Atmospheric Delay Correction</i>	17
2.2.6 <i>Temporal Noise reduction</i>	18
2.3 WABINSAR APPLICATION AND VALIDATION: THE HAWAII TEST CASE	19
2.3.1 <i>WabInSAR processing</i>	20
2.3.2 <i>Reference point selection</i>	23
2.3.3 <i>Spatiotemporal deformation field and validation over Hawaii Island</i>	24
2.4. DISCUSSION	25
2.4.1 <i>Why are wavelets chosen for WabInSAR?</i>	25
2.4.2 <i>The user problem</i>	26
2.4.3 <i>Data filtering or data loss?</i>	26
2.4.4 <i>Atmosphere: Reduction of the largest error source in volcanic and tectonic terrains</i>	26
2.4.5 <i>WabInSAR applied to Hawaii</i>	27
2.4.6 <i>Future developments</i>	27
2.5 CONCLUSION.....	27
CHAPTER 3	30
SATELLITE ORBITAL ERROR REDUCTION USING WAVELET BASED ROBUST REGRESSION APPLIED TO INSAR DEFORMATION DATA.....	30
ABSTRACT	30
3.1 INTRODUCTION.....	30
3.2 METHOD	31
3.3 SYNTHETIC TEST	34
3.4 CASE STUDY.....	35
3.5 SUMMARY AND DISCUSSION.....	35
CHAPTER 4	37

WAVELET ANALYSES OF INSAR TIME SERIES REVEAL BLOCK-LIKE MOVEMENT AND ACTIVITY OF THE HILINA FAULT, HAWAII37

ABSTRACT 37
 4.1 INTRODUCTION 37
 4.2 INSAR DEFORMATION FIELD 38
 4.3 SIGNAL DECOMPOSITION 38
 4.3.1 *Data interpolation and error estimation* 38
 4.3.2 *Hidden signal detection using wavelet transforms* 40
 4.4 APPLICATION TO HILINA FAULT SYSTEM DEFORMATION TIME SERIES 41
 4.5 DISCUSSION 41
 4.6 CONCLUSIONS 43
 4.7 AUXILIARY MATERIAL 43

CHAPTER 545

RANDOMLY ITERATED SEARCH AND STATISTICAL COMPETENCY (RISC) AS POWERFUL INVERSION TOOLS FOR DEFORMATION SOURCE MODELING: APPLICATION TO VOLCANO INSAR DATA CHAPTER 3.....45

ABSTRACT 45
 5.1 INTRODUCTION 45
 5.2 FROM DATA TO DISLOCATION MODEL 47
 5.2.1 *Dislocation problem and optimization* 47
 5.2.2 *Sensitivity analysis of three different analytical models* 48
 5.3 A COMPARISON OF SOPHISTICATED OPTIMIZATION METHODS 52
 5.3.1 *Simulated Annealing (SA)* 52
 5.3.2 *Genetic Algorithm (GA)* 53
 5.3.3 *Randomly iterated search (RI)* 53
 5.3.4 *Statistical Competency (SC)* 54
 5.4 APPLICATION TO SYNTHETIC INSAR DATA 55
 5.5 APPLICATION TO REAL INSAR DATA FROM THE CAMPI FLEGREI CALDERA VOLCANO 57
 5.5.1 *Data set* 58
 5.5.2 *Model uplift period 2000-2001* 59
 5.5.3 *Model subsidence period 2001-2002* 61
 5.6 DISCUSSION 61
 5.6.1 *Sensitivity analysis* 62
 5.6.2 *Advances of the RISC approach* 63
 5.6.3 *Model implication for Campi Flegrei volcano* 63
 5.7 CONCLUSIONS 65
 5.8 AUXILIARY MATERIAL 65

CHAPTER 671

TIME-DEPENDENT VOLCANO SOURCE MONITORING USING INSAR TIME SERIES: A COMBINED GENETIC ALGORITHM AND KALMAN FILTER APPROACH71

ABSTRACT 71
 6.1 INTRODUCTION 71
 6.2 METHODS 73
 6.2.1 *Randomly Iterated Search and Statistical Competency Genetic Algorithm (RISC-GA)* 73
 6.2.2 *Linear Dynamic Kalman Filter (LKF)* 73
 6.2.3 *Combining RISC-GA and LKF for time-dependent nonlinear inversion* 74
 6.3 SYNTHETIC TEST AND VALIDATION 76
 6.4 APPLICATION TO INSAR TIME SERIES AT THE CAMPI FLEGREI VOLCANO 77
 6.5 DISCUSSION 79
 6.5.1 *Time-dependent modeling as the key for volcano source monitoring* 79
 6.5.2 *Applications for monitoring the source under the Campi Flegrei volcano* 80
 6.6 CONCLUSION 82
 6.7 AUXILIARY MATERIAL 83

CHAPTER 7	85
INTERPLAY OF DEFORMATION SOURCES AT HAWAII ISLAND INVESTIGATED THROUGH INSAR TIME SERIES AND TIME-DEPENDENT MODELING	85
ABSTRACT	85
7.1 INTRODUCTION.....	85
7.2 TECTONIC AND MAGMATIC ACTIVITY AT HAWAII ISLAND	86
7.3 METHODS	87
7.3.1 <i>Wavelet based InSAR time series</i>	87
7.3.2 <i>GPS processing</i>	89
7.3.3 <i>Time dependent inverse modeling</i>	90
7.3.4 <i>Cross correlation</i>	91
7.4 RESULTS	91
7.4.1 <i>Deformation field and data validation</i>	91
7.4.2. <i>Time dependent modeling of the deformation sources</i>	93
7.4.3 <i>Identifying volcanic and tectonic interactions on Hawaii Island</i>	94
7.5 DISCUSSION	96
7.5.1 <i>Improvements and limitations of WabInSAR</i>	96
7.5.2 <i>Time dependent modeling</i>	97
7.5.3 <i>Deformation source correlation</i>	97
7.5.4 <i>Hilo Subsidence</i>	98
7.6 CONCLUSION.....	99
CHAPTER 8	100
GRAVITY-DRIVEN DEFORMATION OF DAMAVAND VOLCANO DETECTED THROUGH INSAR TIME SERIES.....	100
ABSTRACT	100
8.1 INTRODUCTION.....	100
8.2 DAMAVAND TECTONIC SETTING AND VOLCANO GEOLOGY	101
8.3 DEFORMATION FIELD AT DAMAVAND VOLCANO.....	102
8.4 DISCUSSION	104
8.5 SUMMARY AND CONCLUSION.....	106
CHAPTER 9	107
THE 12 JAN 2010, HAITI EARTHQUAKE AFFECTED BY ASEISMIC FAULT CREEP	107
9.1 METHODS	108
9.1.1 <i>Satellite radar data</i>	108
9.1.2 <i>Principal component decomposition</i>	109
9.2 AUXILIARY MATERIAL	100
CHAPTER 10	116
GEODETTIC, SEISMIC AND COULOMB STRESS TRANSFER ANALYSIS OF THE 2005 QESHM EARTHQUAKE: COMPETING MODEL INTERPRETATION.....	116
ABSTRACT	116
10.1 INTRODUCTION.....	116
10.1.1 <i>The area of the November 27th, 2005 earthquake on Qeshm Island</i>	117
10.2 DATA SETS USED FOR THE CONCEPTUAL MODELS	118
10.3 A SINGLE FAULT PLANE SOLUTION.....	120
10.4 A COMPLEX DISLOCATION SOURCE SOLUTION	123
10.4.1 <i>Geometric arrangement of faults</i>	123
10.4.2 <i>Slip distribution</i>	126
10.5 DID THE TECTONIC EARTHQUAKE TRIGGER THE SHALLOWER STRUCTURES?.....	126
10.6 DISCUSSION	128
10.6.1 <i>The dataset</i>	128

10.6.2 <i>Inversion</i>	129
10.6.3 <i>Salt-tectonics systems and Earthquake-salt diapir interaction (two-way)</i>	129
10.7 CONCLUION	131
CHAPTER 11	132
SUMMARY AND OUTLOOK	132
11.1 FUTURE DIRECTIONS	132
REFERENCES	134
CURRICULUM VITAE	149

Chapter 1

Introduction

Monitoring of crustal deformation has contributed to our understanding of tectonics, earthquakes, volcanism and landslides. Natural disasters, in particular such as volcanic unrest, require a fast response system including continuous deformation monitoring and analysis scheme. Surface deformation measurements are routinely used to constrain the subsurface geometry of magmatic sources, active faults and the spatial distribution of coseismic slip. Even more importantly, these data provide our primary means for recording aseismic processes such as afterslips, viscoelastic and poroelastic adjustments and so-called silent earthquakes. Geodetic measurements provide invaluable constraints on the interseismic accumulation of strain that might be released in large and damaging earthquakes. Most volcanic eruptions are preceded by inflationary doming and stretching of the crust as large volumes of magma migrate from the mantle through the crust.

The key to understand earthquakes and the eruptive potential of a volcanic system is aided by the stress transfer concept i.e. our ability to characterize the actual state of stress of a volcanic system and to understand how susceptible the system is to small parameter changes. Therefore the first task involves proper monitoring strategies including novel ground and space based observation methods. Modern advances in both the global positioning system (GPS) and interferometric synthetic aperture radar (InSAR) during the last decade, improved our ability to model these and other crustal processes. Having the time series of a deformation field, another important issue is to exploit the full capacity of this observation for modeling the dynamic of the subsurface deformation source. This requires an inversion approach functioning in semi real time manner as required by fast response systems, providing reliable estimation of the source of a deformation field.

In this dissertation I describe several novel methods applicable to volcanic and tectonic processes, including a method for InSAR time series analysis and confident static and dynamic inverse modeling approach. These methods are applied to different volcanic and tectonic regimes and the comparison against independent data shows their success for understanding the acting physical process. These new methods can be used as components of a fast response system to mitigate the hazard associates to natural disasters.

1.1 Geodetic monitoring

Advances in geodesy during the last couple of decades can be outlined by a number of key developments. First, there is a broadening of the spatial scales over which measurements can be performed. The use of artificial satellites boosted the definition and use of global reference systems and enabled the mapping of large areas on earth. Optical remote sensing from spaceborne platforms triggered fast developments in geodesy, especially using stereographic techniques, whereas point positioning entered a new era using global navigation satellite systems (GNSS) [Hanssen, 2002]. On more local scales there is considerable interest in monitoring surface deformations induced by earthquakes, volcanoes, glacier dynamics, post-glacial rebound, and anthropogenic deformation due to the exploration of mineral resources, geothermal energy, and water. Better understanding of these processes requires regular repeat measurements, high accuracy, and a fine spatial resolution.

The accuracy of geodetic observations marks next development. As a result of the increased number of alternative techniques the quality, in terms of the precision and reliability, needs to be balanced with the specific goals of the measurement campaign [Hanssen, 2002].

Moreover, in a more indirect way space geodetic observations can contribute to atmospheric physics. The influence of atmospheric refraction on the propagation velocity of electromagnetic waves is regarded as one of the most important error sources for distance measurement, one of the most elementary geodetic observables. Although space-geodetic techniques such as very long baseline interferometry (VLBI), radar altimetry, and global navigation systems such as GPS, were not designed for atmospheric studies, they contributed considerably to the global understanding of the atmosphere. Currently, GPS observations are used on a routine basis by meteorologists, e.g., for the observation of water vapor distributions [Hanssen, 2002].

Radar interferometry is embedded in this line of geodetic developments, retrieving surface deformation by measuring the backscattered signals in the line-of-sight (LOS) of sensor. This technique combines the characteristics of large-scale imaging and quantitative observations of distances (using phase change measurement). In terms of spatial scales, spaceborne radar interferometers are able to collect observations distributed over the entire earth. Quantitative ranging observations are currently collected over a swath width in the order of 100-500 km, with a resolution of about 2 m. As opposed to optical sensors, the active radar observations can be collected at nighttime, over areas with limited contrast, and through cloud cover. Whilst, using a single-pass interferometric configuration accuracies for elevation observations (e.g. digital elevation model) are comparable to the optical techniques [Hanssen, 2002].

1.1.1 Interferometric synthetic aperture radar

Synthetic Aperture Radar (SAR) are -usually spaceborne- instruments that emit electromagnetic radiation and then record the strength and time delay of the returning signal to produce images of the ground. The emitted waves can be imagined as a sine wave. Conventional SAR images are made up of the amplitude or ‘strength’ of the sine wave. When the sine wave starts to repeat itself (phase angle > 360 degrees), one cycle of phase has occurred.

If we collect two separate images from exactly the same satellite position but at different times with noting that the target area does not change, one would expect the two sine waves from each image to have identical phase. In practice, the position of the satellite between two image acquisitions is never identical, and the corresponding difference in the path (distance between satellite and ground) means there is a difference in phase between the two signals (i.e. a phase shift). The physical path difference can be expressed as an integer number of wavelengths plus the fraction of one wavelength. It can also be expressed as a difference in phase angle between the two signals [Ferretti *et al.*, 2007].

Interferometric synthetic aperture radar (InSAR) makes use of this phase information by subtracting the phase value in one image from that of the other, for the same point on the ground. This is generating the interference between the two phase signals and is the basis of interferometry.

The phase difference for any point on the ground will take a value ranging from zero to 360 degrees. Neighboring ground points will yield other values of phase difference owing to changes in the path difference [Ferretti *et al.*, 2007]. For a collection of points in a given area of ground, the 360 possible degrees of phase difference can be quantized into 256 grey levels and visualized as a fringe of differing grey level intensities. An interferogram image is made up of many such fringes [Ferretti *et al.*, 2007]. Fringes can be thought of as a collection of contours where each unique grey level within and along the fringe corresponds to a constant phase difference. The constant phase difference within a fringe is directly related to constant path difference. In turn, path difference is a function of ground elevation as this affects the distance to the satellite. Therefore, constant path difference can be related to constant elevation. i.e. the phase difference contours within the fringe are indeed height contours, regardless of the environmental disturbances such as atmospheric delay [Ferretti *et al.*, 2007].

Two distinct types of InSAR processing can be distinguished: *additive* interferometry and *multiplicative* interferometry. The signal resulting from the former is obtained by the incoherent summing of the amplitudes of two input signals. This results in so-called “amplitude” fringes. In multiplicative interferometry one is also able to measure the interferometric phase by coherent cross-multiplication of the two input signals. The phase data imply a better accuracy, as the fraction of the phase cycle is much easier to determine accurately. In 2D applications, a phase-cycle is often referred to as a [Hanssen, 2002].

For the conventional InSAR to work successfully, a degree of similarity or correlation must exist in the surface properties between the two image acquisitions. In most parts of the world, particularly temperate regions, correlation between images will degrade with time due to changing/moving vegetation, differing climatic conditions, termed ‘temporal decorrelation’. Correlation tends to remain good in arid, desert regions where little change occurs. Coherence image represents the correlation that exists between corresponding pixels of the two images [Ferretti et al., 2007].

The SAR frequency and bandwidth are used to determine the radar wavelength, and hence its sensitivity to surface displacement, topographic height, temporal decorrelation, and range resolution. The geodetic applications of spaceborne repeat-pass SAR interferometry can be categorized in roughly four disciplines (i) deformation mapping with mm–cm accuracy, (ii) topographic mapping with a relative accuracy of 10–50 m, (iii) thematic mapping based on change detection, and (iv) atmospheric delay mapping with mm–cm accuracy in terms of the excess path length [Hanssen, 2002].

However, the estimation of topography had been the main focus for the early applications of radar interferometry, yielding elevation accuracies comparable with optical methods, albeit valuable due to the all-weather capability of radar. Nevertheless, the experiments with the repeat-pass configuration clearly demonstrated an even more spectacular application; deformation monitoring. The relative LOS movement of scatterers with respect to a reference location in the image could be measured as a fraction of the wavelength, yielding cm to mm accuracies for L-band, C-band, and X-band radars [Hanssen, 2002].

A problem in this application is that, for an effective baseline larger than zero, the deformation signal is always mixed with topographic signal. A suitable solution to this problem was *differential* interferometry, where the topographic signal obtained from a so-called *topographic interferogram* (or a reference elevation model) was scaled to the baseline conditions of the *deformation interferogram* and subtracted from it, yielding a *differential interferogram* [Hanssen, 2002].

The first demonstration of differential radar interferometry for mapping the displacement field of the Landers earthquake was reported by Massonnet et al. [1993], who used a reference elevation model to remove the topographic phase signal.

While conventional InSAR, measuring static deformation field, is a proven, very effective technique to detect deformation, almost any interferogram includes large areas where the signals decorrelate and no measurement is possible. Where measurement is possible, overprinting of the deformation signal with signal due to variation in atmospheric properties is a further issue. Moreover an effective monitoring system requires continuous observation strategy beyond the static deformation field obtained by conventional InSAR.

Relatively recent analysis techniques, persistent scatterer (PS) InSAR and small base line sub set (SBAS) address both the decorrelation and atmospheric problems of conventional InSAR and provide the dynamic map of the deformation field. However, the implementations of PS in original form have been mostly limited to applications where there are many bright scatterers, which are usually man-made structures. In contrast SBAS even shows merits in area where no bright scatterers exist such as rural and mountainous area. However both of them require in different stage of processing some assumption about the temporal behavior of deformation field.

In this dissertation, we describe a novel InSAR time series approach, so-called WabInSAR (Wavelet based InSAR), that identifies and extracts the 3D map of the deformation field, applicable in areas undergoing non-steady deformation, with no prior knowledge of the variations in deformation rate (see chapter 2). WabInSAR relies on multi-master interferometry. It employs variety of wavelet based, Wiener and Kalman filters to reduce major sources of environmental artifacts. The noise is reduced pixel by pixel for all those areas that exhibit reliable interferometric phase changes. Furthermore, WabInSAR is strengthened by a novel approach for correcting the effects of satellite orbit error (see chapter 3). Further detail, test and validation of WabInSAR are presented in chapters 2, 3, 7, 8 and 9.

1.2 Wavelet based analysis of irregularly sampled time series

InSAR observations are usually sampled irregularly in time. In contrast, most of the mathematical transforms, are applicable to evenly sampled data sets [Pollock, 1999]. One way to construct a time series of regularly sampled observations within a range of a discrete set of points is to use interpolation. Various methods are used for interpolating a discrete set of points, such as linear,

quadratic, piecewise cubic Hermite polynomial (PCHP) and cubic Spline (CS) interpolation [Fritsch and Carlson, 1980]. PCHP and CS are often preferred because the interpolation error is usually small and also avoids an oscillatory behaviour of the interpolator. This may preserve the accuracy of the interpolation for monotone and smooth enough signals. The procedure for calculating PCHP and CS is similar, but the PCHP only guarantees the continuity of the first derivatives while CS provides a continuity condition to the second derivative, too. This means CS is more accurate for smooth data while PCHP leads to less oscillation for non smooth data sets [Fritsch and Carlson, 1980]. PCHP is generally less expensive to compute and applicable to large data sets.

Herein we present a new wavelet based approach for analyzing unevenly sampled time series of deformation field in a statistical manner (see chapter 4). This technique first estimates the interpolation error using a Monte Carlo simulation approach. Later, this error is propagated through wavelet transform to the coefficients using error propagation theory. This helps to build a statistical test for evaluating wavelet coefficients.

This approach is applied to a long time series of deformation field over Hilina fault system in Hawaii Island to detect hidden block-wise motions (see chapter 4).

1.3 Inverse modeling of volcanic and tectonic dislocation source

Modeling approaches can be divided into broad classes of analytic and numeric. Finite element modeling (FEM) is a widely used numerical technique for finding approximate solutions of partial differential equations (PDE) as well as of integral equations. The solution approach is based either on eliminating the differential equation completely (steady state problems), or rendering the PDE into an approximating system of ordinary differential equations, which are then numerically integrated. The development of FEM approach mostly began by advent of large processing units, because usually intensive calculation is required. However FEM usually provides an approximate solution for complex problem.

In contrast, by assuming a predefined parametric solution, analytical modeling approaches try to provide a precise solution for the problem. However, the predefined parametric solution is usually a very simplified version of the real scenario. This means analytical modeling technique provides a precise solution for a simplified problem.

These analytical models are widely used in volcanic and tectonic studies. Since first that the relation between surface deformation and magmatic sources of Japanese volcanoes was investigated via an analytical formulation of an inflating point source in an elastic half space [Mogi, 1958], many other developments in the field of analytical models and their applications have been achieved to constrain magmatic source parameters specifically based on surface deformation data. Okada [1985] presented a closed formulation to explain parameters of a rectangular dislocation source causing surface deformation in an elastic half space. This model is applicable to volcanic deformation as well and earthquake simulation, treating the source as a finite rectangular fault that is either subject to opening or subject to strike and dip slip motions. Shortly afterward, Davis [1986] presented an analytical expression of an ellipsoidal inflating cavity buried in an elastic half space that causes deformation at the surface and enables us to explore the surrounding stress field. This research was ground for other developments, such as an analytical expression of finite sphere in half space [McTigue, 1987] and pressurized dipping ellipsoidal source [Yang *et al.*, 1988]. Despite their simplicity, these models have successfully explained observed deformation fields resulting from volcanic and tectonic activities over the past 60 years [Dzurisin, 2006], which together with independent geophysical and geological evidence demonstrated the validity of this kind of analytical expression to define the geometrical and mechanical parameters of the source of volcanic deformation.

High resolution mapping of spatiotemporal deformation fields can provide important information about earthquake as well as volcanic source geometries and associated physical processes. Retrieving the information about the source of observed deformation field, numerical and analytical inverse modeling techniques are utilized. For instance, modeling approaches can provide the specific characteristics of a magma chamber based on geodetic data. The inferred characteristics of the magma

chamber (or “source”) can include diverse geometric parameters such as location, and volume pressure and change. These physical variables are especially important for hazard assessment, including volcano monitoring or fast response teams.

The procedure to obtain parameters of an analytical model from an observed displacement field is an inverse problem. From a mathematical point of view, there are many different techniques for solving an inverse problem, and to investigate magma chambers processes (see chapter 5). A sophisticated inversion (optimization) technique requires a balance of *robustness* and *efficiency*. Geophysical solutions presented in the literature often provide details about the location and/or strength of a deformation source without knowing the sensitivity of the data and/or the model, which are directly related to the quality of the result. In order to evaluate the robustness of an inversion, the sensitivity of source parameters to the observations has to be evaluated first. Moreover, because space geodetic datasets are spatially and temporally increasingly large, the handling of this quantity of data together with their full variance-covariance matrix reflecting observation quality and relative weight has become a major difficulty in optimization problems.

Moreover, in past years, there has been significant technical development in the detection of spatiotemporal surface deformation fields. Dense, continuous Global Positioning System (GPS) networks [Segall and Davis, 1997] and Interferometric Synthetic Aperture Radar (InSAR) time series [Berardino et al., 2002; Ferretti et al., 2001b] provided valuable information about the temporal evolution of deformation fields. These new developments yield daily and monthly deformation measurements with millimeter precision over regional scales [Dixon et al., 2006; King et al., 1995; Segall and Matthews, 1997; Tizzani et al., 2007]. To investigate the source of the time series of deformation field, an inversion scheme is commonly applied to either short or selected periods, and therefore provides merely a “snapshot” of a particular stage of a system. Modern developments in the field of deformation time series require appropriate progress in the inversion tools to address the full spatiotemporal capacity of the observations.

Inhere, we detail two novel inversion approaches so-called RISC-GA and RISC-SA stands for randomly iterated search and statistical competency Genetic Algorithm (GA) and Simulated Annealing (SA) dealing with static deformation field. The main limitation of the existing algorithms is becoming trapped in a local minimum because, for example, of an inappropriate cooling schedule.

An improvement is shown by combining the standard SA and GA with a randomly iterative (RI) approach. Another important aspect is obtaining a confidence region for the parameters by implementing a statistical competency (SC) test. The statistic used here considers observation quality and model deficiency together. Combining RI and SC, we presented a sophisticated inversion algorithm. These two approaches provide a reliable estimation of the subsurface deformation source in a semi real time manner.

In the following RISC-GA is combined with Kalman Filter (KF) and lead to a new time dependent inversion approach provide time consistent deformation source model. The rationale for this combination includes the fact that the requirements of a KF are good a priori estimation of the initial covariance matrix of the parameters and their initial value. The advantages of our approach are (1) it is applicable to nonlinear systems; (2) the ability for handling irregularly sampled observations; (3) the capacity to incorporate heterogeneous observations; (4) the recursive manner that allows for efficient assessment of new data sets and expanding time series; and (5) the ability to be less sensitive to initial values and the requirement of only a rough estimation of search space.

Further detail, test and validation of these approaches are presented in chapters 5, 6, 7, 9 and 10.

1.4 Forward modeling the volcanic and tectonic stress field

Several triggering mechanisms may govern volcanic and tectonic activities. However, change of the state of stress inside the system might be the most effective one and in this case there might be a potential for an eruption or earthquake. Thus a major requirement of an early warning system is confident characterization of the state of stress of the system on different time scales. Therefore improved monitoring techniques together with time dependent modeling approaches help to identify the state of the stress in the system as a function of time and may lead to successful forecasting a volcanic and tectonic activity.

Further detail and tests of the stress models are presented in chapters 9 and 10.

1.5 Contributions

There are five main focuses of this dissertation. First we describe a new Wavelet based InSAR time series approach (WabInSAR) that improves our knowledge about the 3D surface deformation field. Second, we describe a new wavelet based approach for investigating deformation time series aiming to identify hidden signals. Third, we detail a new confident static inversion algorithm as a combination of Genetic Algorithm and Simulated Annealing in iterated manner (RISC-GA/SA). Fourth, we present a new time dependent inversion algorithm as a combination of RISC-GA and Kalman Filter. Fifth, we apply these tools to investigate the deformation field at volcanic and tectonic area to improve our understanding about underlying physical process. Below we summarize the contributions of this work:

a) InSAR time series approach

1. We design and implement a new algorithm for generating accurate time series of deformation field using InSAR.
2. We design and implement a new algorithm to identify less noisy pixels (i.e. elite pixels) using wavelet transform in series of interferogram integrating interferometric phase and amplitude in a statistical manner without any assumption about deformation behavior.
3. We design and implement a new filter to reduce contribution of the topography error in InSAR time series using 2D Legendre wavelets.
4. We design and implement a new filter to reduce effect of atmospheric delay in InSAR time series 3D wavelet transforms.
5. We design and implement a new algorithm for correcting orbital error in repeat pass interferometry.

b) Time series analysis and pattern recognition

1. We design and implement a new algorithm for hidden component detection in unevenly sampled data sets of InSAR time series using wavelet decomposition.

c) Static and dynamic inversion

1. We design and implement a new algorithm for confident inversion of the surface deformation data using Genetic Algorithm.
2. We design and implement a new algorithm for confident inversion of the surface deformation data using Simulated Annealing.
3. We design and implement a new algorithm for confident time dependent inversion of the time series of surface deformation data using Genetic Algorithm and Kalman Filter.

d) Geophysical application

1. We resolved the discrepancy between depths of shallow dislocation source at Campi Flegrei.
2. We find episodic linear pressure change at Campi Flegrei deformation source associated to linear flux into show reservoir.
3. We obtained first island-wide spatiotemporal deformation field analysis at Hawaii Island.
4. We obtained first island-wide time dependent deformation field model at Hawaii Island.
5. We find complex spatiotemporal interplay of deformation field sources at Hawaii Island.
6. We find that the silent events beneath Kilauea south flank play a significant role in interplay of deformation at Hawaii Island.
7. We find that Damavand volcano is slowly gravitationally spreading.
8. We resolved the discrepancy between deep aftershocks and concentrated surface deformation field of 2005 Qeshm earthquake.
9. We find that the 2010 Haiti earthquake is affected by aseismic slip prior to the event.

1.6 Thesis Roadmap

Chapters 2 to 10 of this thesis are written as independent studies including 9 manuscripts that have been already published or are in press or under review in scientific journals. It is therefore possible to read each chapter independently without the necessity of reading any previous chapters first. For each associated manuscript there are multiple authors, however, the author of this dissertation is the primary researcher and author in each case.

Chapter 2 is primarily concerned with the development of a new InSAR time series (WabInSAR) technique based on multi-master interferometry. WabInSAR extract spatiotemporal map of the deformation field from those pixel carrying less noise. It employs variety of wavelet based filter to reduce the effects of environmental artifacts and retrieve accurate deformation field. For validating WabInSAR we apply it on Hawaii Island undergoing very complex volcanic and tectonic deformation. This chapter is under review in *IEEE Transaction on Geoscience and Remote Sensing*.

Chapter 3 describes a new approach for correcting the orbital error in spaceborne InSAR using a combination of wavelet transform and robust regression. This approach is applicable to noisy interferograms where the orbital error is obscured by other effects such as deformation signal and atmospheric delay. This chapter is under review in *IEEE Transaction on Geoscience and Remote Sensing*.

Chapter 4 describes a new wavelet based approach for detecting hidden signals in unevenly sampled geophysical time series. Inhere we first developed a Monte Carlo approach for estimating interpolation error assuming a monotone signal. The estimated error is propagated to the wavelet transform coefficients and helps to assess them in a statistical manner. This approach is applied to a time series of deformation over the Hilina fault system at the south flank of Kilauea and reveals block-wise motion at this fault zone. This chapter is under review in *Geophysical Research Letters*.

Chapter 5 presents two new robust inversion methods (RISC-GA/SA) as a combination of Genetic Algorithm and Simulated Annealing in an iterated a statistical manner. These two approaches are thoroughly tested on synthetic and real data sets. These approaches are important elements for a fast response system when a timely confident estimation of the source parameters is required. This chapter is published in *Journal of Geophysical Research*.

Chapter 6 describes a novel time dependent inversion methods for modeling volcanic processes that vary in strength, location, and style over time as a combination of Genetic Algorithm and Kalman Filter (RISC-GA-KF). This approach is timely and useful since new advances in the filed of InSAR time series provides us with valuable spatiotemporal information of the deformation field on volcanic area. Exploiting full strength of these data sets requires new time dependent an inverse method which is addressed inhere. This chapter is accepted for publishing in *Journal of Geophysical Research*.

Chapter 7 is concerned with the application of the RISC-GA-KF for dynamic modeling the source of deformation field obtained using WabInSAR at Hawaii Island. This study provides first time dependent island-wide multiple deformation source models at Hawaii Island. We find that complex deforming sources are interplaying over the time and silent earthquakes underneath Kilauea south flank play a significant role in type and degree of this mutual relationship. This chapter is under review in *Journal of Geophysical Research*.

Chapter 8 presents the result of applying WabInSAR to Damavand volcano in northern Iran. In this manuscript we showed that the whole volcano is deforming and the most promising scenario explaining the observed signal is gravitationally-driven spreading. This chapter is under review in *Geology*.

Chapter 9 is about application of WabInSAR and RISC-GA to preseismic monitoring of the Haiti 2010 earthquake. We find that aseismic slip on the adjacent segment of the coseismic rupture on Enriquillo fault zone has affected this earthquake. This chapter is under review in *Nature*.

Chapter 10 is concerned with the application of the RISC-GA to hybrid modeling the aftershock data and the coseismic deformation of 2005 Qeshm earthquake in southern Iran. In this study we present an alternative model for the coseismic deformation source that resolves discrepancy between aftershocks and surface deformation data. This chapter is under review in *Society of America Bulletin*.

Chapter 11 provides a summary of the thesis and suggestions for future work.

Chapter 2

Wavelet based InSAR (WabInSAR): a new advanced time series approach for accurate spatiotemporal surface deformation monitoring¹

M. Shirzaei and T. R. Walter

Section 2.1, Dept. Physics of the Earth, GFZ German Research Centre for Geosciences, Telegrafenberg, 14473 Potsdam, Germany

Abstract

High resolution interferometric synthetic aperture radar (InSAR) allows for the investigation of displacements of the ground associated with various geologic processes such as volcanic activity and earthquakes. Repeated satellite data acquisitions permit displacement monitoring as a function of time, and thus InSAR is increasingly considered as a sophisticated monitoring tool. However, significant error sources may contribute to the phase observation and bias the data interpretation in time and space. Through the generation of InSAR-time series and the study of the phase signal behavior at high-quality pixels, many of these artifacts can be estimated and corrected.

In this study, we present a new wavelet based (Wab) algorithm that intends to generate, evaluate and correct InSAR time series data and, thereby, obtain an accurate spatiotemporal deformation field. WabInSAR first statistically approaches the generation of InSAR time series with an emphasis on the non-stationary signal behavior. Then to reduce the effects of different artifacts, such as topographic error, atmospheric delay and temporal decorrelation noise, we employ a novel suite of wavelet based Wiener and Kalman filters.

We applied the WabInSAR algorithms to a data set of radar images over Hawaii Island known to be difficult for use in InSAR studies. The backscattered SAR signal and displacement map was found to be contaminated by atmospheric delay and a distorted topography that challenged different aspects of the WabInSAR algorithm. We compared the identified artifacts to independent works and validated the retrieved deformation time series against the continuous GPS data. Hence, this work demonstrates the capacity of the WabInSAR approach to precisely retrieve the dynamics of displacing ground under difficult conditions.

2.1 Introduction

Interferometric synthetic aperture radar (InSAR) is a rapidly developing methodology with increasing relevance for the study and monitoring of ground displacements [Ferretti *et al.*, 2007]. InSAR normally uses satellite radar images acquired from approximately the same viewing geometry. Through complex multiplication of the backscattered phase contribution, maps of deformation or digital elevation models are generated. The common difficulties encountered in the conventional

¹ MS developed the approach and processed the data. All authors were involved in discussion and writing the paper.

InSAR techniques include signal decorrelation and environmental contaminants [1]. Because of the temporal behavior of environmental contaminants, such as clouds and vegetation, some of the difficulties are commonly approached by time series analysis [Ferretti *et al.*, 2007]. Currently, there are two main categories of InSAR time series generation; first, the permanent (or persistent) scatterer (PS), which is relevant to those approaches that identify good pixels upon their phase stability in time and/or space [Ferretti *et al.*, 2001b; Hooper *et al.*, 2004; Kampes, 2005], and second, the small base line subsets (SBAS), which are relevant to the approaches that select good pixels based on spatial interferometric coherence maps [Berardino *et al.*, 2002; Schmidt and Bürgmann, 2003]. While the PS approach uses the single master interferometry, the SBAS approach by definition employs the multi-master interferometry and, hence, interferograms with small spatial baselines. Several similarities regarding signal handling, processing and denoising are present in the PS and SBAS approaches. Both favor sparse phase unwrapping to reduce the negative impact of the noisy pixels. Both approaches apply filtering routines to reduce the effect of digital elevation model (DEM) errors and of the atmospheric delay [Berardino *et al.*, 2002; Ferretti *et al.*, 2001a; Hooper *et al.*, 2007]. The common disadvantages of the PS approach are the requirement of a large number of images and its model assumption for assessing the temporal deformation behavior. Most SBAS processing approaches, in contrast, are free from the assumptions of a deformation model. However, in the SBAS approach the associated DEM error filtering relies on models, such as a cubic polynomial model assumption for simulating a deformation temporal behavior (see eq. 25 in [Berardino *et al.*, 2002]). The processing time for the PS approach is often significantly less than for SBAS because it consumes only a small number of interferograms and pixels, while SBAS also considers highly redundant observations that help to estimate the contribution of temporal random noise.

Addressing these limitations and integrating advantages, we herein propose a novel InSAR time series method combining these strengths fully free from the assumptions about the temporal behavior of a deformation field. We combine these approaches with a suite of spatiotemporal filters for topography, atmosphere artifact and temporal decorrelation noise reduction. The core of our approach is based on the wavelet theory, which can classify the components of the data in terms of the frequency content in time and space and, therefore, perform quality estimation and error reduction. The itinerary of our wavelet based InSAR (WabInSAR) time series approach is first to address the issue of the pixel identification in a way that integrates all spatial and temporal information (such as phase and amplitude stability in time and coherence in space) in a statistical manner. This technique helps to identify good pixels and, therefore, may lead to accurate phase unwrapping and data refinement. Second, we present novel filters for reducing most of the artifacts relevant to InSAR time series. We investigate different wavelet families in an attempt to address the main sources of environmental errors, i.e., topographic error and atmospheric delay. The reason for using wavelets is straightforward because wavelets bear the capacity for adaptive signal analysis, hidden texture detection and the potential for extracting transient components [Chou and Wang, 2004; Gendron *et al.*, 2000; Goswami and Chan, 1999; Grossmann *et al.*, 1987; Newland, 1997; Pazos *et al.*, 2003; Rezai and Ventura, 2002; Zha *et al.*, 2008]. In the simple case, the continuous wavelet transform of a function $f(x) \in L^2(R)$ is defined by [Daubechies, 1992]:

$$W_f(a,b) = \int_{-\infty}^{+\infty} f(x)\Psi_{a,b}(x)dx \quad , \quad \Psi_{a,b} = \frac{1}{\sqrt{a}}\Psi\left(\frac{x-b}{a}\right) \quad , \quad a > 0 \quad (2.1)$$

where a is the scale and b is the translation. The form $\Psi \in L^2(R)$ describes the mother wavelet function if it satisfies $\int_{-\infty}^{+\infty} \Psi(x)dx = 0$. The discrete wavelet transform is obtained by setting $a = 2^{-j'}$ and $b = i'2^{-j'}$, where $j', i' \in Z$.

Equation (2.1) can be efficiently calculated in the frequency domain [Torrence and Compo, 1998]. As described by Torrence and Compo [1998], using numerical methods, we are able to estimate a sort of equivalent Fourier frequency, the so-called pseudo frequency, for each scale associated with a different continuous and discrete mother wavelet function (see [Torrence and Compo, 1998] and references therein).

The conceptual advantage of wavelets in comparison to Fourier analysis is that wavelet transforms can be very diverse because there is no significant restriction on the selection of the wavelet mother function, which makes wavelet based filters very flexible for analyzing signal behavior and incorporating different auxiliary information. We apply wavelets in order to combine the strengths and overcome the weakness of earlier InSAR time series approaches.

In the following, after describing the main idea and the steps of InSAR time series generation and filtering in the WabInSAR approach, we test it with data from Hawaii Island. Hawaii Island exhibits a complex non-linear deformation associated with volcanic activity and faulting, contaminated by significant atmospheric artifacts [Foster *et al.*, 2006; Rosen *et al.*, 1996]. To validate WabInSAR for this challenging example case, we compare the results to an independent deformation time series obtained from the observation of continuous GPS (cGPS) networks.

2.2 Wavelet based InSAR time series (WabInSAR)

2.2.1 Interferogram formation

The formation of interferograms is a standard procedure, which we briefly outline herein for completeness. Similar to the SBAS approach, we begin by considering $N + 1$ images acquired over the same area at time steps (t_0, t_1, \dots, t_N) . First, we generate a number of k possible interferograms by considering B^T and B^\perp as the maximum temporal and spatial baselines, respectively. The topographic phase is simulated and subtracted using satellite ephemeris data and an available digital elevation model (DEM). The phase change ($\delta\varphi^k$) at a pixel located at a coordinate (ζ, η) in the k -th interferogram may be formulated as follows [Ferretti *et al.*, 2007]:

$$\delta\varphi^k(\zeta, \eta) = \varphi_{def}^k(\zeta, \eta) + \varphi_{topo}^k(\zeta, \eta) + \varphi_{atm}^k(\zeta, \eta) + \varphi_{noise}^k(\zeta, \eta) \quad (2.2)$$

where φ_{def}^k is the phase contribution due to ground deformation, φ_{topo}^k is the phase error due to the inaccuracy in the topographic model, φ_{atm}^k is the phase error due to atmosphere delay, and φ_{noise}^k is the phase noise due to other types of signal decorrelation. Because we are interested in φ_{def}^k , the other phase contributors ($\varphi_{topo}^k, \varphi_{atm}^k$ and φ_{noise}^k) can be considered contaminants and should be reduced to achieve a high level of φ_{def}^k accuracy.

Because retrieving the useful information from very noisy pixels is critical and contaminated pixels also diminish the accuracy of the unwrapping procedure on other pixels, the algorithm is based on a sparse but less noisy group of pixels as detailed in the following section.

2.2.2 Elite interferogram and elite pixel identification

Elite pixels are distinguished as those that are less distorted by decorrelation [Zebker and Villasenor, 1992]. As further detailed below, an elite interferogram is one that contains a small number of noisy pixels, i.e., the pixels are relatively less corrupted by decorrelation and hold higher quality phase information. For identifying both elite interferograms and elite pixels, we employ a combination of wavelet transforms and a Wiener filter. The Wiener filter was originally designed to reconstruct a noise-free signal. However, if the signal and noise are not independent in the frequency domain or if the signal is blurred, the Wiener filter works inversely and may even amplify the noise. We overcome this limitation by combination with wavelet transforms as follows. We analyze complex phase values, comprising the amplitude and the phase combined [Zha *et al.*, 2008]. We use a family of orthogonal wavelets, the so-called Daubechies wavelet, of order L . The Daubechies wavelets have a given support width of $2L - 1$ and a high capacity for detecting localized effects [Daubechies, 1992]. Examples of Daubechies mother wavelets at different orders are shown in Figure (2.1), where wavelets with lower orders (e.g., db1) have a comparable narrow support, while higher orders (e.g., db9) appear smoother at the expense of the associated support width. In other words, the mother

wavelets of lower orders appear to be more suitable to detect transient signal components. In contrast, higher orders apply to broader components yet may disregard very rapid changes, which means that, depending on the application, we may need to use mother wavelets of different orders or – preferably – a variety of wavelets.

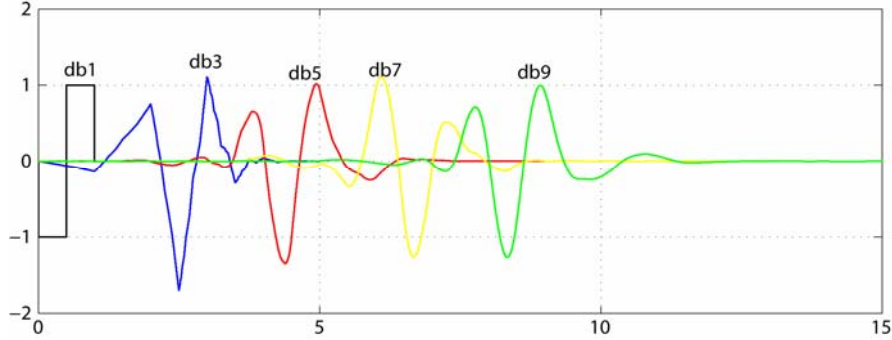


Figure 2.1. Examples of Daubechies mother wavelets of different orders used together with Wiener filter to identify elite pixels.

We therefore first decompose the complex interferometric phase into a real (x^r) and an imaginary (x^i) part. We consider the complex interferometric phase as [Hanssen, 2002]

$$x^r(\zeta, \eta) + jx^i(\zeta, \eta) = (A_m(\zeta, \eta) \cos(\delta\varphi(\zeta, \eta)) + e^r) + j(A_m(\zeta, \eta) \sin(\delta\varphi(\zeta, \eta)) + e^i) \quad (2.3)$$

where A_m is the amplitude and $j = \sqrt{-1}$. Resulting from decorrelation and system noise, e^r and e^i denote the zero mean Gaussian variables added to the real and imaginary parts. Therefore, the real and imaginary parts are as follows:

$$x^r(\zeta, \eta) = A_m(\zeta, \eta) \cos(\delta\varphi(\zeta, \eta)) + e^r \quad (2.4)$$

$$x^i(\zeta, \eta) = A_m(\zeta, \eta) \sin(\delta\varphi(\zeta, \eta)) + e^i$$

With the aim to estimate e^r and e^i , we decompose each part of (2.4) in the wavelet domain using a multiresolution analysis [Mallat, 1989]:

$$x^p(\zeta, \eta) = \sum_{i_x}^{M-1} \sum_{i_y}^{M-1} v_{i_x i_y}^p \Phi_{J i_x i_y}(\zeta, \eta) + \sum_{j'}^{J-1} \sum_{i_x}^{M-1} \sum_{i_y}^{M-1} \sum_{\varepsilon}^3 v_{j' i_x i_y}^p w_{j' i_x i_y}^\varepsilon \Psi_{j' i_x i_y}^\varepsilon(\zeta, \eta) \quad , \quad p = r, j \quad (2.5)$$

$$\Psi_{j' i_x i_y}^\varepsilon(\zeta, \eta) = \begin{cases} \Psi_{j' i_x}^\varepsilon(\zeta) \cdot \Phi_{j' i_y}^\varepsilon(\eta) & , \quad \varepsilon = 1 \\ \Phi_{j' i_x}^\varepsilon(\zeta) \cdot \Psi_{j' i_y}^\varepsilon(\eta) & , \quad \varepsilon = 2 \\ \Psi_{j' i_x}^\varepsilon(\zeta) \cdot \Psi_{j' i_y}^\varepsilon(\eta) & , \quad \varepsilon = 3 \end{cases}$$

$$\Phi_{J i_x i_y}(\zeta, \eta) = \Phi_{J i_x}(\zeta) \cdot \Phi_{J i_y}(\eta)$$

$$v_{j' i_x i_y}^p = \langle x^p(\zeta, \eta), \Psi_{j' i_x i_y}^\varepsilon(\zeta, \eta) \rangle \quad , \quad v_{j' i_x i_y}^p = \langle x^p(\zeta, \eta), \Phi_{j' i_x i_y}^\varepsilon(\zeta, \eta) \rangle \quad (2.6)$$

where Φ and Ψ are the smoothing and the mother wavelet function, respectively, v and w are the smoothing and wavelet coefficients, respectively, J is the number of wavelet scales and $\langle \cdot, \cdot \rangle$ is a functional inner product operator. This multiresolution analysis classifies the enveloping noise and signal in different wavelet scales. The wavelet coefficients mostly carry information about the high frequency components of the real and the imaginary part, i.e., noise. Given the noisy wavelet coefficients, to estimate the noise-free coefficients (S) we thereafter may employ a Wiener filter [Robinson and Treitel, 1967; Zha et al., 2008]:

$${}^p S_{j' i_x i_y}(\zeta, \eta) = {}^p w_{j' i_x i_y} - \frac{{}^p \tau^2}{{}^p \sigma_1^2 + {}^p \mu_1^2} {}^p w_{j' i_x i_y} \quad , \quad p = r, i \quad (2.7)$$

$$\begin{aligned}
{}^p\mu_1 &= \frac{1}{\Theta\Gamma} \sum_{l,l'} {}^p w_{j'}(l,l') \\
{}^p\sigma_1^2 &= \frac{1}{\Theta\Gamma} \sum_{l,l'} ({}^p w_{j'}(l,l'))^2 - ({}^p\mu_1)^2 \\
{}^p\tau^2 &= \frac{1}{T} \sum_T {}^p\sigma_{1T}^2
\end{aligned}$$

where $\Theta \times \Gamma$ is a local neighborhood window of each pixel and T is the number of windows. After obtaining the denoised wavelet coefficients, we reconstruct the noise-free real (\hat{x}^r) and imaginary (\hat{x}^i) parts of the complex interferometric phase using equation (2.5). In the following, the real (e^r) and imaginary (e^i) parts of the noise are obtained by

$$e^r = x^r - \hat{x}^r, \quad e^i = x^i - \hat{x}^i \quad (2.8)$$

For more detail about the use of the window size and tuning parameters in InSAR applications the reader is referred to the recent literature on noise reduction in interferograms using wavelet and Wiener filtering [Zha *et al.*, 2008].

The estimation of e^r and e^i is directly associated with the decorrelation and system noise. We therefore can utilize this information and interpret it as a signal to noise ratio (SNR), applicable for any particular pixel in an interferogram.

The estimated complex interferometric noise for each pixel in k interferograms is $\{e_1^r + je_1^i, e_2^r + je_2^i, \dots, e_k^r + je_k^i\}$, with a mean value of (m^r, m^i) and a standard deviation of (σ^r, σ^i) . Assuming statistical independence between real and imaginary parts of the noise, the following bivariate normal distribution is found at each pixel:

$$f(e^r, e^i) = f(e^r) \cdot f(e^i) = \frac{1}{2\pi\sigma^r\sigma^i} e^{-\frac{1}{2}\left(\left(\frac{e^r-m^r}{\sigma^r}\right)^2 + \left(\frac{e^i-m^i}{\sigma^i}\right)^2\right)} \quad (2.9)$$

We define the mean error for each interferogram by averaging the estimated phase noise of its pixels as $\gamma_k^p = \frac{1}{MM'} \sum_{MM'} e_k^p$, ($p = r, i$), with a standard deviation of β_k^p , where M and M' are the number

of pixels along the range and azimuth. By defining the total average error as $\mu^p = \frac{1}{MM'} \sum_{MM'} m^p$,

($p = r, i$), and assuming the statistical expectation of γ_k^p as μ^p , we follow Vanicek and Krakiwesky [1982] and derive 1D statistics that are applied for both parts, e^r and e^i [Vanicek and Krakiwesky, 1982] as follows:

$$\frac{\gamma_k^p - \mu^p}{\beta_k^p / \sqrt{k}} \sim t_{k-1}, \quad p = r, i \quad (2.10)$$

where t is the student probability density function. By specifying a significance level of α (or confidence level $1 - \alpha$), the confidence interval for γ_k^p can be expressed as

$$\mu^p - t_{\alpha/2, k-1} \beta_k^p / \sqrt{k} \leq \gamma_k^p \leq \mu^p + t_{\alpha/2, k-1} \beta_k^p / \sqrt{k}, \quad p = r, i \quad (2.11)$$

If this test fails for any of the real (e^r) or imaginary (e^i) parts, the interferogram is deleted from the data set. If the test is successful, the interferogram is considered as an elite interferogram and further used in the analysis. The deletion process continues until no temporally isolated subset persists. In other words, all interferograms either are connected and/or their subsets temporally overlapped. Using this procedure we are identifying k' elite interferograms, for which we now need to identify elite pixels. Similar to the previous step, if the associated complex interferometric noise of each pixel in k' elite interferograms is $\{e_1^r + je_1^i, e_2^r + je_2^i, \dots, e_{k'}^r + je_{k'}^i\}$ with an average value of (m''^r, m''^i) and a standard deviation of (σ''^r, σ''^i) , the bivariate normal distribution in equation (2.8) can be modified as follows:

$$f(e^r, e^i) = \frac{1}{2\pi\sigma^r\sigma^i} e^{-\frac{1}{2}\left(\left(\frac{e^r-m^r}{\sigma^r}\right)^2 + \left(\frac{e^i-m^i}{\sigma^i}\right)^2\right)} \quad (2.12)$$

Considering the total average noise $\mu'^p = \frac{1}{MM'} \sum_{MM'} m'^p$ and the statistical expectation of m'^p as μ'^p in a statistic way similar to equation (2.10), one may obtain the following 1D statistic:

$$\frac{m'^p - \mu'^p}{\sigma'^p / \sqrt{k'}} \sim t_{k-1}, \quad p = r, i \quad (2.13)$$

By specifying a significance level of α , the confidence interval for m' can be expressed as

$$\mu'^p - t_{\alpha/2, k-1} \sigma'^p / \sqrt{k'} \leq m'^p \leq \mu'^p + t_{\alpha/2, k-1} \sigma'^p / \sqrt{k'}, \quad p = r, i \quad (2.14)$$

Similar to what was done before, if this test fails for any of the real or imaginary parts, the pixel is deleted; otherwise, it is defined as an elite pixel and considered for the rest of the analysis. Therefore, in this approach all of the pixels are considered to be elite pixels, which contain a noise history that is either close to zero or follow a normal distribution function in both the real and imaginary parts. As a result, in comparison to other InSAR time series approaches where the good pixels are those that contain less noise only, our approach may identify a much larger group of elite pixels. The approach considers the spatial similarity and temporal stability of the complex phase observations in a statistical manner. The other advantage of this approach is that it is applicable to a small data set, i.e., a minimum number of two interferograms.

In the following, to retrieve the displacement field ($\delta\phi$), a standard operator for unwrapping the modulo 2π phase observation is employed [Berardino *et al.*, 2002; Ferretti *et al.*, 2001b]. Phase unwrapping (PU) is done in two dimensions using a minimum cost flow approach similar to what was used by earlier workers [Costantini, 1998; Costantini and Rosen, 1999], which is not further detailed here.

2.2.3 DEM inaccuracy correction

An important step is to reduce the effect of the digital elevation model (DEM) inaccuracy, Δh , which is the difference between the true topography and the DEM used in the InSAR processing routine for topographic phase reduction. Earlier workers consider a temporal information and reduced this error using a low pass filter in time [Berardino *et al.*, 2002; Ferretti *et al.*, 2001b]. This method requires an assumption about the temporal behavior of the deformation field, such as a linear or cubic polynomial function that approximates the inflating volcano or moving fault. Such simplified assumptions, however, are not fulfilled in many real cases because geologic processes may act on many different scales, from instantaneous to periodic to highly non-linear trends. Therefore, in an attempt to reduce the DEM error we are using the spatial information where our signal is properly sampled and the aliasing effect is reduced. Earlier studies suggested that the most significant contribution to the height inaccuracy Δh is a high frequency pixel-to-pixel noise (see section 2.5.4 in [Kampes, 2005]). We address this hypothesis and identify the phase contribution of Δh in the unwrapped phase at a pixel located at the coordinate of (ζ, η) in k th interferogram [Hanssen, 2002] to be

$$\phi_{topo}^k(\zeta, \eta) = \frac{4\pi}{\lambda} \frac{B_{\perp}^k}{R^k(\zeta, \eta) \sin \theta(\zeta, \eta)} \Delta h(\zeta, \eta) \quad (2.15)$$

where λ is the radar wavelength, R^k is slant range from satellite to pixel (ζ, η) , B_{\perp}^k is the perpendicular baseline and θ is the local incidence angle, which varies in the case of the ENVISAT satellite between $\sim 20^\circ$ and $\sim 45^\circ$ for different imaging modes and swaths.

We exploit the spatial information in order to estimate the pseudo spatial frequency properties of the DEM error as a result of SAR geometry. To perceive the meaning of pseudo frequency, we employ mathematics and simply expand equation (2.15) to Legendre polynomials [Heiskanen and Moritz, 1967] as follows:

$$\frac{1}{\sin \theta(\zeta, \eta)} = \frac{1}{\sqrt{1 - \cos^2 \theta(\zeta, \eta)}} = \sqrt{2} \sum_{m=0}^{\infty} P_m(\cos^2 \theta(\zeta, \eta))$$

$$\varphi_{\text{topo}}^k(\zeta, \eta) = \frac{4\pi}{\lambda} \frac{\sqrt{2} B_{\perp}^k \Delta h}{R^k(\zeta, \eta)} \sum_{m=0}^{\infty} P_m(\cos^2 \theta(\zeta, \eta)) = A^k(\zeta, \eta) \sum_{m=0}^{\infty} P_m(\cos^2 \theta(\zeta, \eta)) \quad (2.16)$$

where P_m is the Legendre polynomial (LP) of order m . This equation implies that the contribution of the DEM inaccuracy can be considered as a power series of the LP scaled with the pixel-to-pixel variable amplitude. The argument of the LP is the incidence angle, which is known to vary smoothly in radar images, which may mean that the LP is unable to present a distinguishable undulation on a short intervals. Fortunately, because LPs are independent base functions for the space domain, they can identify variations even on this short interval, even in relatively high orders. Figure (2.2) shows normalized LPs of the order 0 - 50 versus 5° changes in the incidence angle, simulated for ENVISAT image mode acquisitions. Despite the slight change in the incidence angle, the LPs exhibit significant undulations. This mathematical extension corroborates that (a) the DEM error contributes a high frequency component in the magnitude of the observed phase, and (b) the DEM error preserves a sort of pseudo spatial frequency property.

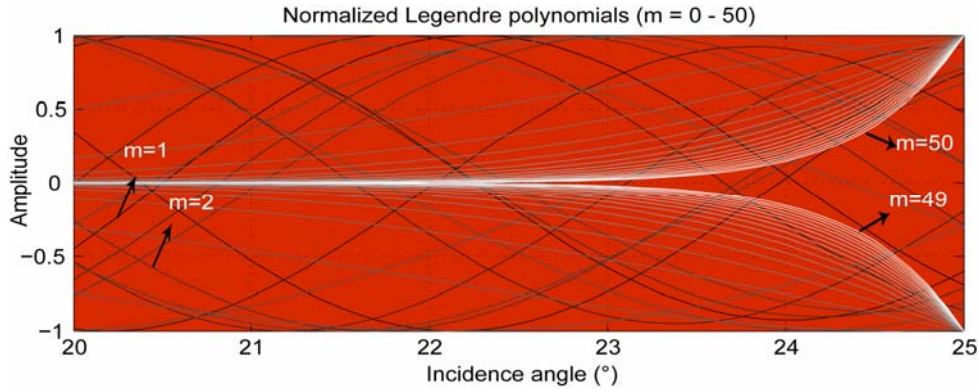


Figure 2.2. Examples of the normalized Legendre polynomials up to an order of 50, showing fluctuations of these function versus 5° relevant to the incidence angle change across the radar image in ENVISAT strip mode imaging.

In first approximation, any efficient 2D low pass filter may be used for reducing the high frequency DEM error. However, we have additional information about the DEM error in the form of the LPs, which now allows more sophisticated filtering methods to be applied. Therefore, we design an adaptive low pass spatial filter based on Legendre polynomial wavelets (LPWs) [Lira *et al.*, 2003] to extract the pixel-to-pixel high frequency components of the DEM error from the unwrapped phase. The reason for choosing LPWs is that the wavelet has shown merits when dealing with transient non-stationary signals. In particular, LPW is sophisticated when the effects are very local, as they are in the case of the expected pixel-to-pixel DEM error. The success of a wavelet based filter is high if both the analyzing signal and chosen wavelet mother function have a similar shape [Daubechies, 1992; Goswami and Chan, 1999]. Further details of the mother wavelets used here for identifying elite pixels are given in Table 2.1. We follow earlier works that applied a wavelet based spatial low pass filter [Qu *et al.*, ; Yuegang *et al.*, 2007] and perform the following working steps necessary for the DEM error correction on the k -th interferogram:

- 1- Threshold: We estimate the upper bound of the equation (2.15) by assuming a maximum DEM error value. The latter can often be obtained from earlier studies (see [Gorokhovich and Voustantiouk, 2006]).
- 2- Multiresolution analysis: We decompose the unwrapped phase by use of LPW.
- 3- Filtering: We apply a hard threshold to the wavelet coefficients based on the upper bound of equation (2.15).
- 4- Noise free signal: We reconstruct the unwrapped phase using filtered coefficients.

5- *Error estimation*: The corrected DEM error is obtained by subtracting the results of the step 4 from the original unwrapped phase.

Table 2.1. The coefficients of smoothing function of LPW filter for orders of 1, 2 and 3

	m=1	m=2	m=3
h₀	$-\sqrt{2}/2$	$-5\sqrt{2}/16$	$-63\sqrt{2}/256$
h₁	$-\sqrt{2}/2$	$-3\sqrt{2}/16$	$-35\sqrt{2}/256$
h₂		$-3\sqrt{2}/16$	$-30\sqrt{2}/256$
h₃		$-5\sqrt{2}/16$	$-30\sqrt{2}/256$
h₄			$-35\sqrt{2}/256$
h₅			$-63\sqrt{2}/256$

Therefore, the main difference between this DEM correction approach and earlier works is that it does not rely on a model assumption for the temporal behavior of the expected deformation. Avoiding such a model is a major advancement for detection of and quantifying non-linear time series of deformation signals that are under-sampled (as they usually are) and where associated aliasing errors exist. Hence, the advantage of this approach is that it is applicable to a single interferogram. It is even applicable for investigation of InSAR data sets in full resolution where a high resolution DEM is not available and also for estimating the time dependent terms of the DEM error, which is significant for urban areas (e.g., fast growing cities).

We further tested the DEM error correction approach based on a synthetic data set (see Appendix A).

2.2.4. Time Series Generation

The mathematical relation between the observations in a time interval of t_a and t_b and the displacements to be identified were as follows:

$$\delta\bar{\phi}_q = \psi_{t_b} - \psi_{t_a} \quad 1 \leq q \leq k' \quad (2.17)$$

where $\psi = [\psi_1, \dots, \psi_N]^T$, that is, the vector of N unknown displacements associated to a pixel at coordinates (ζ, η) and $\delta\bar{\phi} = [\delta\bar{\phi}_1, \dots, \delta\bar{\phi}_{k'}]^T$ and the vector of k' known unwrapped interferograms that have been DEM corrected. Equation (2.16) might be expressed in a matrix form by

$$A\hat{\psi} = \delta\bar{\phi} - \varepsilon_\phi \quad (2.18)$$

where A is the design matrix, ε is observation error and $\hat{\psi}$ is the estimated deformation time series. To solve equation (2.18), we use the best linear unbiased estimate (BLUE) approach [Bjerhammer, 1973]. BLUE can be applied to a rank deficient (e.g., for isolated but temporally overlapping subsets) or to the full rank problem (e.g., for connected network of SAR images without isolated subsets).

Assuming $E\{\varepsilon_\phi\} = 0$, where $E\{\cdot\}$ is the statistical expectation, $E\{\varepsilon_\phi \varepsilon_\phi^T\} = Q$ and $\varepsilon_{\hat{\psi}} = \hat{\psi} - E\{\hat{\psi}\}$ (the estimated time series error) the following BLUE approach equation (2.18) might be inverted according to the following constraints [Bjerhammer, 1973]:

$$\begin{aligned} \varepsilon^T Q^{-1} \varepsilon &\rightarrow \min \\ \varepsilon_{\hat{\psi}}^T \varepsilon_{\hat{\psi}} &\rightarrow \min \end{aligned} \quad (2.19)$$

Therefore the solution is expressed in [Bjerhammer, 1973] as

$$\hat{\psi} = A^T (AA^T)^{-1} (A^T Q^{-1} A)^{-1} A^T Q^{-1} \delta\bar{\phi} \quad (2.20)$$

The variance-covariance matrix of $\hat{\psi}$ can hence be expressed as

$$Q_{\hat{\psi}} = E\{\varepsilon_{\hat{\psi}} \varepsilon_{\hat{\psi}}^T\} \quad (2.21)$$

and it can estimate the precision of the time series. The advantage of BLUE is that it estimates unknowns as an unbiased minimum variance. Therefore, in the absence of systematic errors, this approach preserves both accuracy and precision of the time series (for more detail and the mathematical proof see [Bjerhammer, 1973]). In brief, the above approach directly considers the displacement field time series as an unknown, which is the main difference with the original form of the SBAS approach, where the mean phase velocity between acquisitions is estimated following the singular value decomposition approach. We note, however, that in the case of connected interferograms with no isolated subset, using algebraic calculation these two solutions can be converted to each other.

2.2.5 Atmospheric Delay Correction

Interferograms from various regions of interest, especially with significant topographic relief (such as at volcanoes), are subject to a significant source of error that results from atmospheric delay of the radar waves. Commonly, this process is thought to be the result of a change in the atmospheric conditions between two acquisitions [Hanssen, 2002]. Several earlier approaches proposed to reduce such atmospheric artifacts using the spatiotemporal information [Ferretti *et al.*, 2001a; Hanssen, 2002]. Here we essentially follow a similar concept; however, we achieve it using a novel 3D spatiotemporal wavelet-based filter. The rationale is that this artifact, while having spatial low frequency and temporal high frequency properties, behaves as a non-stationary process [Tatarski, 1961] because the atmosphere properties (pressure, temperature and humidity) are mostly characterized by hourly, daily and seasonal variations. Regarding the radar satellite revisit time (i.e., 35 day for ENVISAT), the majority of these effects are not retrievable due to aliasing effects. The atmosphere, therefore, may introduce a high frequency temporal effect that is found to be comparable to random noise [Tatarski, 1961]. However, the seasonal components and spatial decorrelation lengths are retrievable and also site dependent.

In our approach, the spatiotemporal signal is decomposed using wavelet multiresolution analysis (see section 2.2.2). The wavelet coefficients at the scales that have a wavelength similar to atmosphere spatial decorrelation length and temporal frequency smaller to the assumed temporal frequency of the atmospheric delay are discarded.

The designed filter comprises two distinct parts: a discrete 2D wavelet in space and a continuous 1D wavelet in time. The 3D filter is obtained by the tensor product of these two components. The discrete 2D part is characterized by variable window sizes [Daubechies, 1992]. The window size is twice of the root mean square radius (RMSR) of the wavelet function that may be calculated in 1D by [Goswami and Chan, 1999]

$$\begin{aligned}
 rmsr &= \frac{1}{\|\Psi\|} \left[\int_{-\infty}^{+\infty} (x - x^*)^2 |\Psi(x)|^2 dx \right]^{\frac{1}{2}} \\
 x^* &= \frac{1}{\|\Psi\|^2} \int_{-\infty}^{+\infty} x |\Psi(x)|^2 dx \\
 \|\Psi\| &= \left[\int_{-\infty}^{+\infty} |\Psi(x)|^2 dx \right]^{\frac{1}{2}}
 \end{aligned} \tag{2.22}$$

In equation (2.22), $|\cdot|$ is the absolute value operator. The window size is different than the spatial pattern of the deformation signal but consistent with the spatial decorrelation length of the atmospheric artifact. For the 1D temporal part, we use continuous wavelet transforms with a high ability for extracting hidden components and time-frequency localization [Daubechies, 1992; Torrence and Compo, 1998]. We note that there exists a variety of applicable continuous wavelets such as Morlet and derivatives of Gaussian (DOG) with different characteristics and applications [Torrence and Compo, 1998]. Herein, to build the 1D temporal filter, we use DOG wavelets, which are localized in the time and frequency domains. Moreover, we found that implementing a higher order of the derivation provides a better frequency localization for the mother wavelet.

In summary, the atmospheric contribution to the apparent deformation field is reduced through following steps:

1-Threshold: We assume a maximum spatial decorrelation length and highest temporal frequency of the atmospheric artifacts.

2-Multiresolution analysis: We decompose the deformation signal using the 3D wavelet filter.

3-Filtering: We apply a threshold to the detail coefficients of the temporal and spatial wavelet decomposition based on step (1).

4-Noise free signal: We reconstruct the corrected signal using the filtered coefficients.

Further detail on the 3D spatiotemporal wavelet based filter parameters and adjustment of the decorrelation length are given in the chapter 2.3, where we apply WabInSAR to a data set of radar images over Hawaii Island.

2.2.6. Temporal Noise reduction

To reduce temporal noise and estimate the linear velocity for each pixel, we use a linear dynamic Kalman filter, which does not require any assumption about the deformation behavior. We apply an approach that is very similar to the processing method widely used in GPS time series generation [Hofmann-Wellenhof et al., 2000]. For the InSAR data, we assume each pixel to be a constantly moving vehicle subject to a random acceleration. Moreover, it is assumed that the displacement of the pixel at any time $t > t_0$ is observed (obtained in section 2.5) and that the observation variance is known (the variance matrix is obtained from section 2.2.4). The dynamics of the deformation time series in our case may be described by

$$X_{t+1} = AX_t + w_t$$

$$A = \begin{bmatrix} 1 & \Delta t \\ 0 & 1 \end{bmatrix}, X_t = [\hat{\psi}_t \quad v_t]^T, w \sim N(0, S_w) \quad (2.23)$$

In equation (2.23), $\hat{\psi}$ is the vector of final deformation time series, Δt is the time difference between radar acquisitions, v is a constant velocity of the deformation time series samples, and w is the vector of system noise. The observation model can be expressed as

$$\bar{\psi}_{t+1} = BX_{t+1} + e_{t+1}$$

$$B = [0 \quad 1], e \sim N(0, S_e) \quad (2.24)$$

where $\bar{\psi}$ is the deformation time series obtained after atmospheric correction (see section 2.2.5) and e_t is the noise of the measurements. After matrix calculation we may express the filtered parameters (\hat{X}_{t+1}) as [Grewal and Andrews, 2001];

$$\begin{aligned} \hat{X}_{t+1}^+ &= \hat{X}_{t+1}^- + \bar{K}_{t+1} [\bar{\psi}_{t+1} - B\hat{X}_{t+1}^-] \\ P_{t+1}^+ &= [I - \bar{K}_{t+1}B]P_{t+1}^- \\ \hat{X}_{t+1}^- &= A\hat{X}_t^+ \\ P_{t+1}^- &= AP_t^-A^T + S_w \\ \bar{K}_{t+1}^- &= P_{t+1}^-B^T [BP_{t+1}^-B^T + S_e]^{-1} \end{aligned} \quad (2.25)$$

In equation (2.25), \hat{X}_{t+1}^+ , P_{t+1}^+ , \hat{X}_{t+1}^- , P_{t+1}^- and \bar{K}_{t+1} are the posterior estimate and covariance, a priori estimate, variance and the Kalman gain matrix, respectively.

The relative temporal noise level of the data set is therefore reduced. In addition, one can obtain even smoother time series by applying further backward and forward Kalman filtering runs. However, the user should be aware that by smoothing the time series, some local information may be lost.

The pixel-wise Kalman filtering may nevertheless produce a spatial high frequency noise, which is on the order of time series variance estimated as explained in section (2.2.4). We note that this effect is

similar to the contribution of the DEM inaccuracy and can be further reduced by applying the approach as described in section (2.2.3).

WabInSAR Flowchart

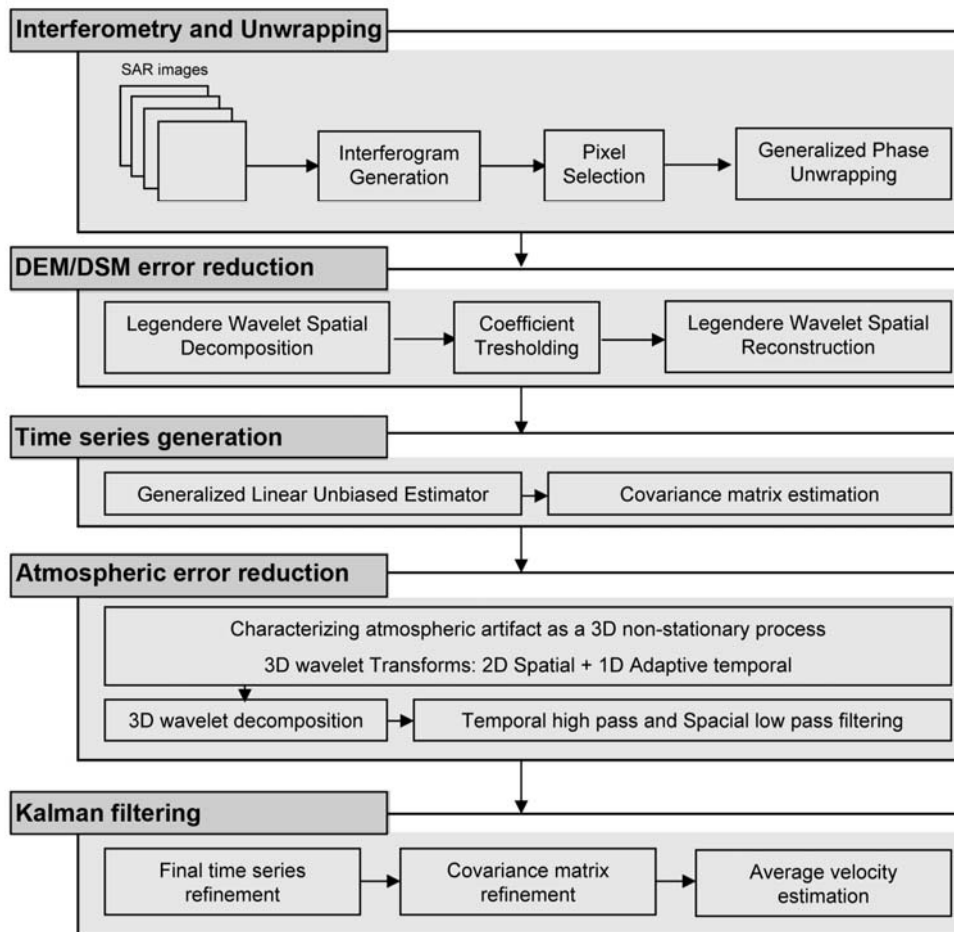


Figure 2.3. WabInSAR Flowchart, for generating InSAR time series of surface deformation and reducing significant environmental artifacts.

Here we should emphasize that the use of “Linear Kalman Filter” does not mean that a linear model for the temporal signal behavior is assumed. It rather means that the system dynamic from each time step to the next one is considered being linear with an uncertainty in the range of observation variance. Therefore the initial statement for proposing a fully model free approach is still valid.

In chapter 2.3, we apply the WabInSAR approach to a SAR data set acquired over Hawaii Island. Figure (2.3) presents the flowchart summarizing the steps of the WabInSAR approach for generating the time series.

2.3 WabInSAR application and validation: The Hawaii test case

As a case study to test WabInSAR we selected Hawaii Island, hosting two of the earth’s most active volcanoes, Mauna Loa and Kilauea (Fig. 2.4). It is known that the volcanic and tectonic deformation field has a complex spatial and temporal pattern over this island [Amelung et al., 2007; Miklius and Cervelli, 2003; Segall et al., 2006]. In addition to the nonlinear and high rate deformation, the large decorrelation noise and atmospheric perturbation [Foster et al., 2006; Zebker et al., 1997] make this target difficult for conventional interferometry but ideal for assessing the strength of the WabInSAR approach.

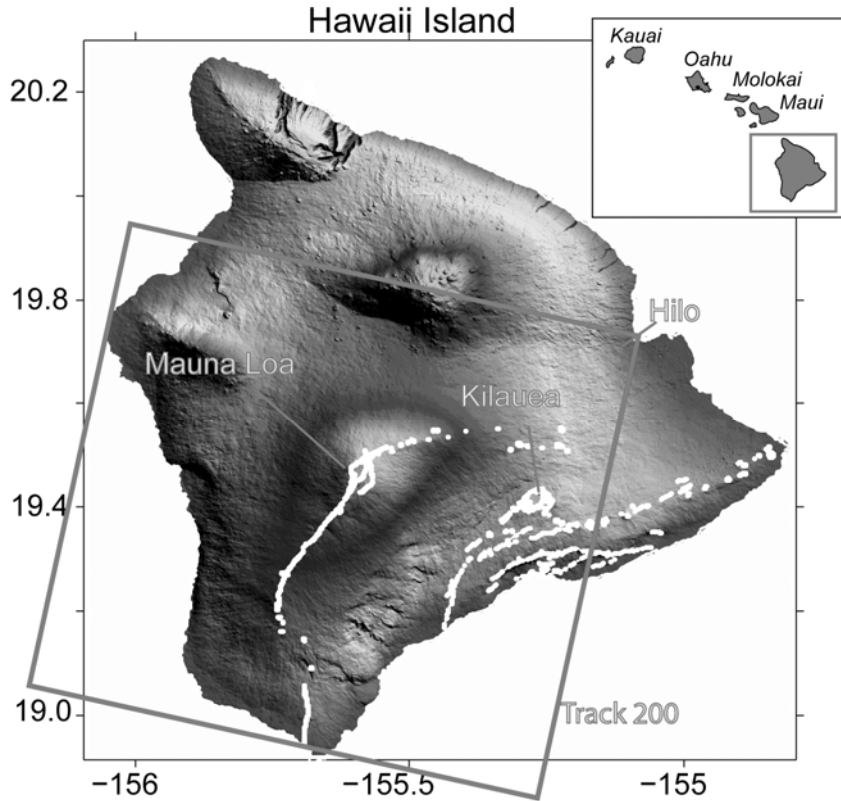


Figure 2.4. Overview of the study areas, Hawaii Island, the Shuttle Radar Topographic Mission (SRTM) is used. The white dashed lines mark the approximate location of active faults. The information of the used radar images and the type of orbit is shown.

Figure (2.5) shows two examples of generated interferograms (ENVISAT track 200) together with associated amplitude and coherence maps over Hawaii Island, spanning almost one year and 2.5 years. The topographic phase is calculated and subtracted using precise orbit ephemeris and a reference DEM (e.g., SRTM DEM of 90-m resolution). An increase of the number of the fringes (each fringe equal to a ~ 2.8 -cm displacement in LOS) over Mauna Loa and Kilauea may imply the evolution of the deformation over time. Moreover, 1-2 fringes are visible elsewhere on the island and might be due to surface deformation or due to artifacts. Note that a signal is backscattered in some areas over the ocean and also on land where vegetation is dense; it is most likely that the phase observations are distorted because the amplitude and coherence maps show very low values. This example illustrates that the pixels may carry very noisy information. In this study, we apply the seven steps of interferometry, pixel selection and the suite of wavelet-based filters to reduce environmental artifacts as described earlier.

2.3.1. WabInSAR processing

a) Interferogram formation: To apply WabInSAR, we employ a data set of 27 radar images acquired by the ENVISAT European satellite spanning the period of 2003 - 2008. The data geometry is descending orbit, track number of 200 and swath of I2 (i.e., $\theta \approx 23^\circ$). Using this data set, we formed about 190 interferometric pairs with spatial and temporal baseline smaller than an arbitrary chosen threshold (here, $B_{\max}^\perp = 600m$ and $B_{\max}^T = 3yr$). The processing was carried out following a multi-looking step with 4 looks in the range and 20 looks in the azimuth. This multi-looking step leaves us with a pixel size of about $80 m \times 80 m$ and enables investigation of many interferograms with a reasonable (1 week) computation effort on a conventional PC. The general topographic phase is subtracted using satellite ephemeris and an available DEM. Before starting the pixel selection step, to reduce the amount of the data we eliminated pixels with coherence below 0.02.

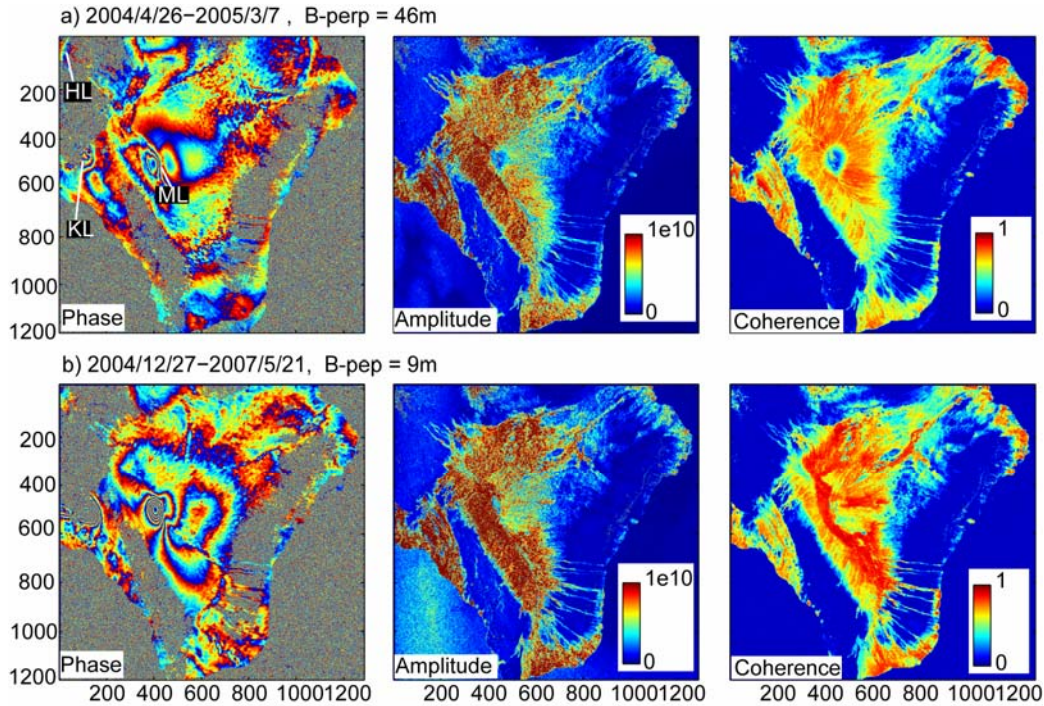


Figure 2.5. Two examples of the formed interferograms together with associated amplitude and coherence maps, a) spans one year and b) spans about two year and half.

b) Elite interferogram and elite pixel identification: Elite interferograms and elite pixels were chosen at the 95% confidence level. We implemented Daubechies wavelet of order 5 (db5) in 3 levels of decomposition. Because we are interested also in localized deformation components, the db5 was selected. Db 5 presents a balance between effective window width and smoothness; hence, it was identified by us to be a good candidate. However, we must note that according to our ongoing investigations, applying other wavelets such as Coiflet [Daubechies, 1992] leads to very similar results.

Applying a combined wavelet multiresolution and Wiener filter, the complex interferometric noise history for each pixel was obtained. Figure (2.6) shows the estimated total average error and standard deviation for this data set for the real and imaginary part of the complex interferometric phase, respectively. By applying equations (2.10) and (2.13) we obtained about 170 elite interferograms and about 650,000 elite pixels (Fig. 2.6f).

In the following, phase unwrapping was done in 2D for each interferogram. Afterwards, the unambiguous deformation field was obtained and could be used for analysis or further filtering as exemplified below.

c) DEM inaccuracy correction: To reduce errors in the digital elevation model, the LPW wavelet was initialized with parameters as used for the synthetic test (see appendix A), except that for the maximum DEM error that we considered 15 m here. Figure (2.7a) shows the average corrected DEM error. The largest correction was applied to the area of the Kilauea caldera rim and the Kilauea northeast rift zone where the topography is frequently modified by eruptions, intrusions and mass movements. Figure (2.7b) shows a bivariate plot giving the normalized deformation velocity versus the corrected average DEM error. About 93% of these two components are independent, which implies that reduction of the DEM error did not induce additional components.

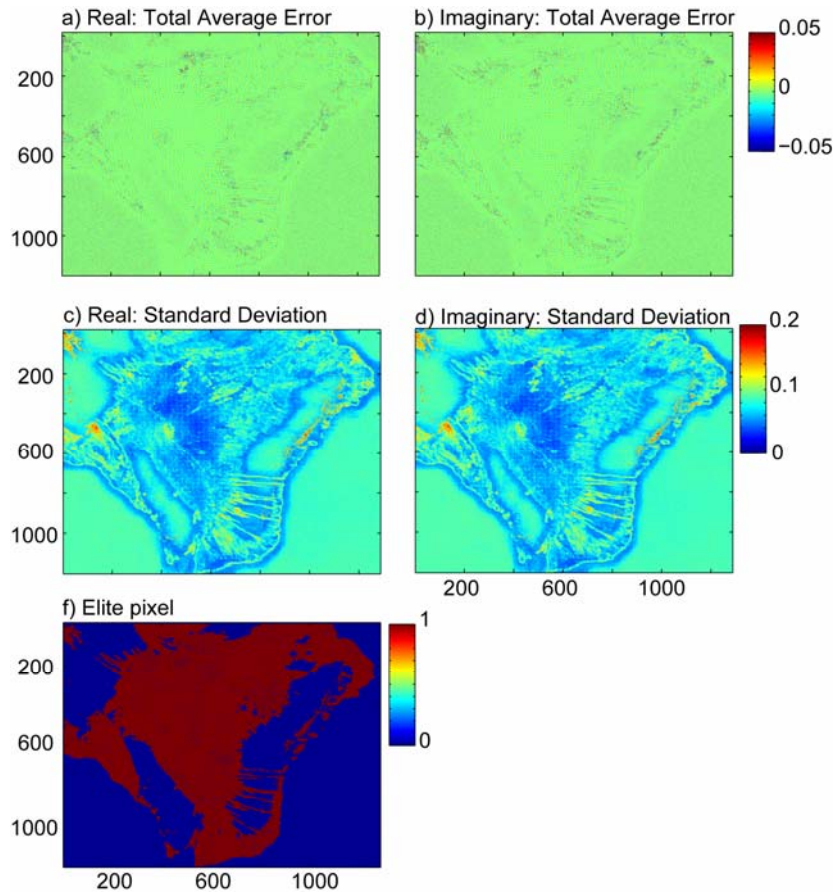


Figure 2.6. Estimated phase noise and the associated standard deviation using the wavelet-Wiener based filter to identify elite pixels, a, b) total average phase noise for real and imaginary part of phase observation, c, d) standard deviation of the phase noise for real and imaginary part of phase observation, f) location of the identified elite pixels.

d) Time series generation: Following the DEM error reduction, we inverted the differential deformations in each unwrapped and corrected interferogram in order to generate a time series of deformation at the location of each pixel using the aforementioned BLUE approach. We estimated, moreover, the variance-covariance of the time series, which is an indicator for the precision of the result.

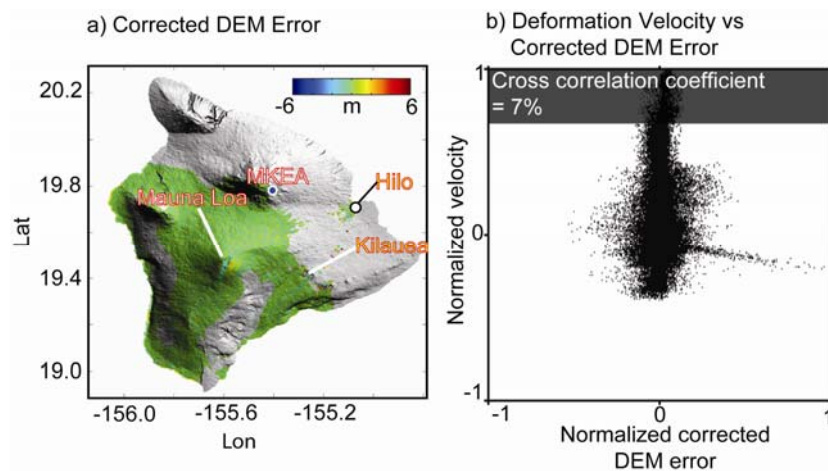


Figure 2.7. a) the average corrected DEM error b) Bivariate plot, showing the amount of correlation between corrected DEM error and deformation velocity filed.

e) Atmospheric delay correction: Given the spatial and temporal deformation field history, we reduced the effect of atmospheric delay by applying a 3D spatiotemporal wavelet based filter (see 2.5). For reducing the atmospheric delay, we chose continuous wavelets. Moreover, for direct comparison between temporal wavelet coefficients and assumed frequencies of the atmospheric delay, we estimated the pseudo frequencies equivalent to continuous wavelet scales [Torrence and Compo, 1998]. To make sure that the extracted temporal components result from the atmosphere, we considered the spatial information as well, which means the extracted temporal component and generated by atmospheric delay was also correlated in space within a certain range. Because specifying this range is not trivial and might vary from hundreds of meters to a few kilometers [Zebker et al., 1997], we chose Coiflets wavelet [Daubechies, 1992] with 5 levels of decomposition to provide an effective window length between 100 m and 5000 m for the pixel size of 80 m. This range covers the expected spatial correlation length of atmospheric delay over Hawaii Island [Foster et al., 2006; Zebker et al., 1997]. Because we had access to the supporting data for Hawaii Island [Foster et al., 2006; Zebker et al., 1997], we used DOG order 10 and the Coiflets wavelet with 5 levels of decomposition to form temporal filters.

f) Temporal noise reduction: After applying spatial and temporal filters using a linear dynamic Kalman filter, we decreased the temporal noise of the time series and estimated the final variance-covariance matrix of the deformation field and deformation linear velocity field. The resulting filtered result mean displacement map is shown in Figure (2.8) and further described below.

2.3.2 Reference point selection

The temporal pattern of the deformation field is nonlinear, though for illustration purposes we present the linear deformation velocity for the Hawaii Island (Fig. 2.8a). The reference point of this deformation field is ‘MKEA’ GPS station located at the flank of the Mauna Kea Volcano. Mauna Kea is dormant and does not show any sensible deformation activity as seen in the continuous GPS data shown in Figure (2.8b) with respect to SNARF (Stable North American Reference Frame). The cGPS data used were sampled at rate of 30 seconds, and they were processed by Bernese 5 [Dach et al., 2007] to solve the daily coordinate of the station.

Regardless of the linear trend visible in horizontal components resulting from plate tectonic drift, there is no significant fluctuation from zero displacement. In the period of 2003 – 2008, the most significant seismic activity that might have affected MKEA was the October 15, 2006 Mw 6.7 earthquake occurring on the Kohala coast, about 60 km away (http://www.agu.org/meetings/fm06/pdf/fm06_lateBreakingSessionSched.pdf). However, at this date we see very slight fluctuation falling in the uncertainty range of observation and unlikely resulting from the seismic event. Therefore, MKEA might be considered as a suitable stable point.

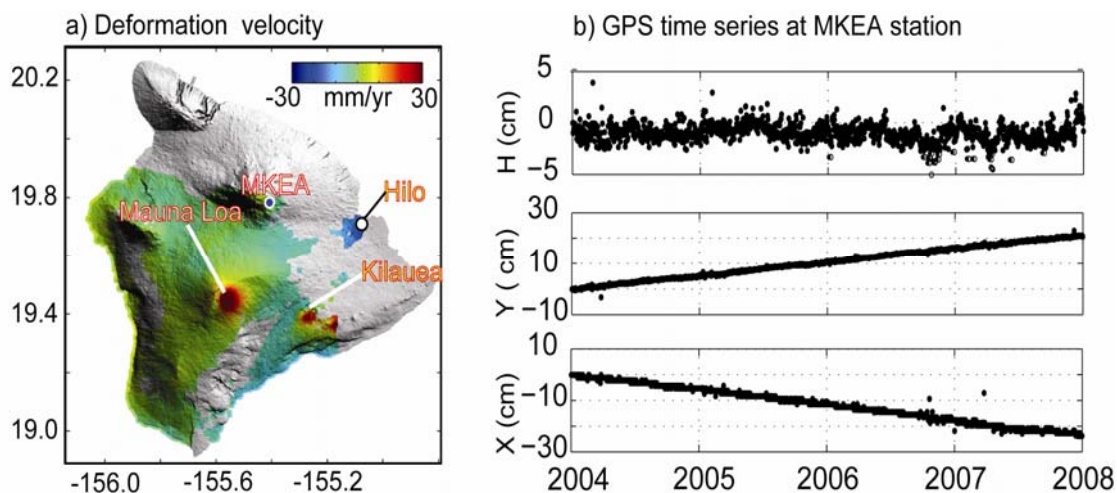


Figure 2.8. a) WabInSAR velocity field, b) cGPS time series of the deformation at MKEA GPS station in SNARF reference frame showing that this point is relatively stable to built a local reference frame.

2.3.3 Spatiotemporal deformation field and validation over Hawaii Island

With respect to MKEA, four significant deforming areas are visible (Fig. 28a). These were found to be located at Mauna Loa summit, at the Kilauea caldera, at the Kilauea east rift zone, and in the region of the Islands' capital Hilo city. The maximum uplift reaches up to 4 cm/yr in LOS. The non-linearity and complexity of the signal is found in the data time series. In Figure (2.9), the full spatiotemporal time series of the surface deformation obtained over Hawaii Island is shown. This Figure shows different episodes of activity at volcanic and tectonic systems.

The temporal evolution of the surface deformation obtained by WabInSAR agrees with the cGPS data available at 9 stations (Fig. 2.10). These cGPS data were processed by Bernese 5 [Dach *et al.*, 2007] in the ITRF2005 reference frame. The precise orbit data were obtained from IGS. The adjustment approach was a minimum constraint solution [Hofmann-Wellenhof *et al.*, 2000] by fixing the MKEA reference station to zero displacement so that the time series of the cGPS data was obtained in a local coordinate system established based on an MKEA fixed point, which makes the projected cGPS data on the LOS of the satellite comparable to the WabInSAR time series.

To achieve this comparison, we made a spatial averaging of the WabInSAR data in a circle centered at each cGPS station with arbitrary radius (here 250 m). This averaging is done for each data point of the time series and results in a WabInSAR time series that can now be compared to – and validated with – the cGPS data. In all evaluations, we considered an *accuracy* of 0.5 - 1 cm for the WabInSAR time series, which is in agreement with earlier works.

Figure (2.10a-j) shows that there is a very good agreement between both the amplitude and the trend of the cGPS and our WabInSAR data sets at all stations. To further quantify this, for each station we estimated the difference between the cGPS and WabInSAR time series and the associated uncertainty (Fig. 2.10k). The average difference between cGPS and WabInSAR data sets for each station is less than 0.5 cm, and the average difference for whole data sets is about 0.13 cm. This comparison demonstrates the capacity of the WabInSAR to retrieve time series of the deformation at high precision.

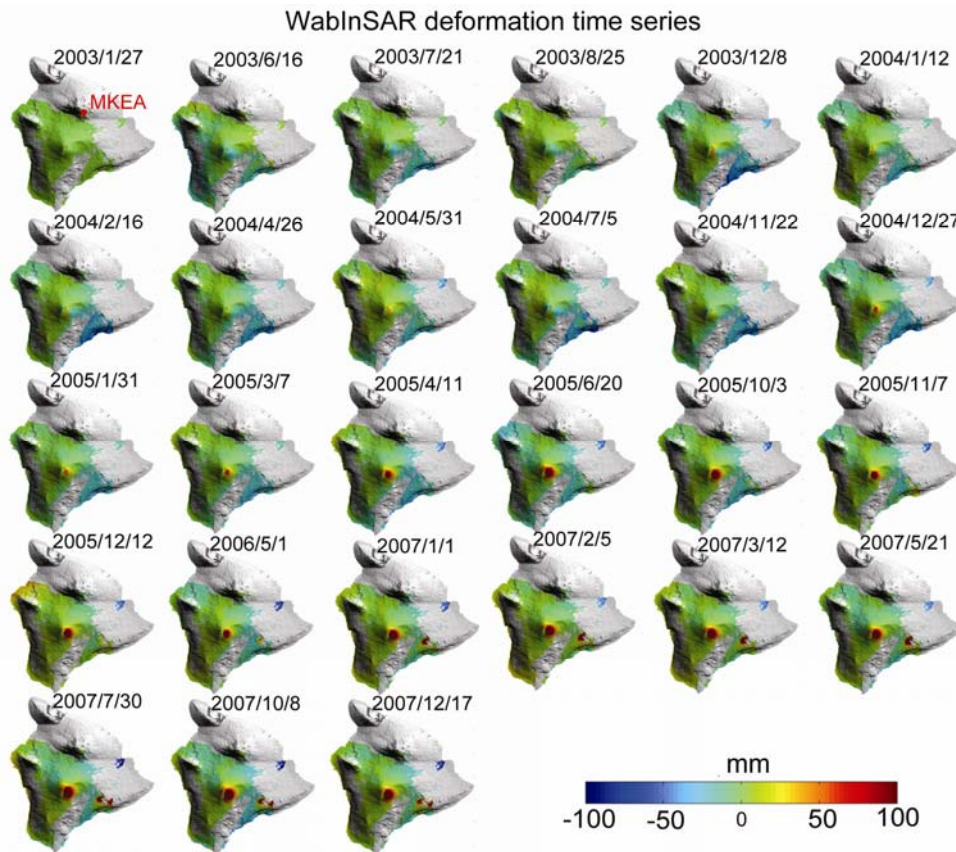


Figure 2.9. Full time series of the deformation obtained by WabInSAR over Hawaii Island in respect to MKEA station and the image acquired at 27 January 2003.

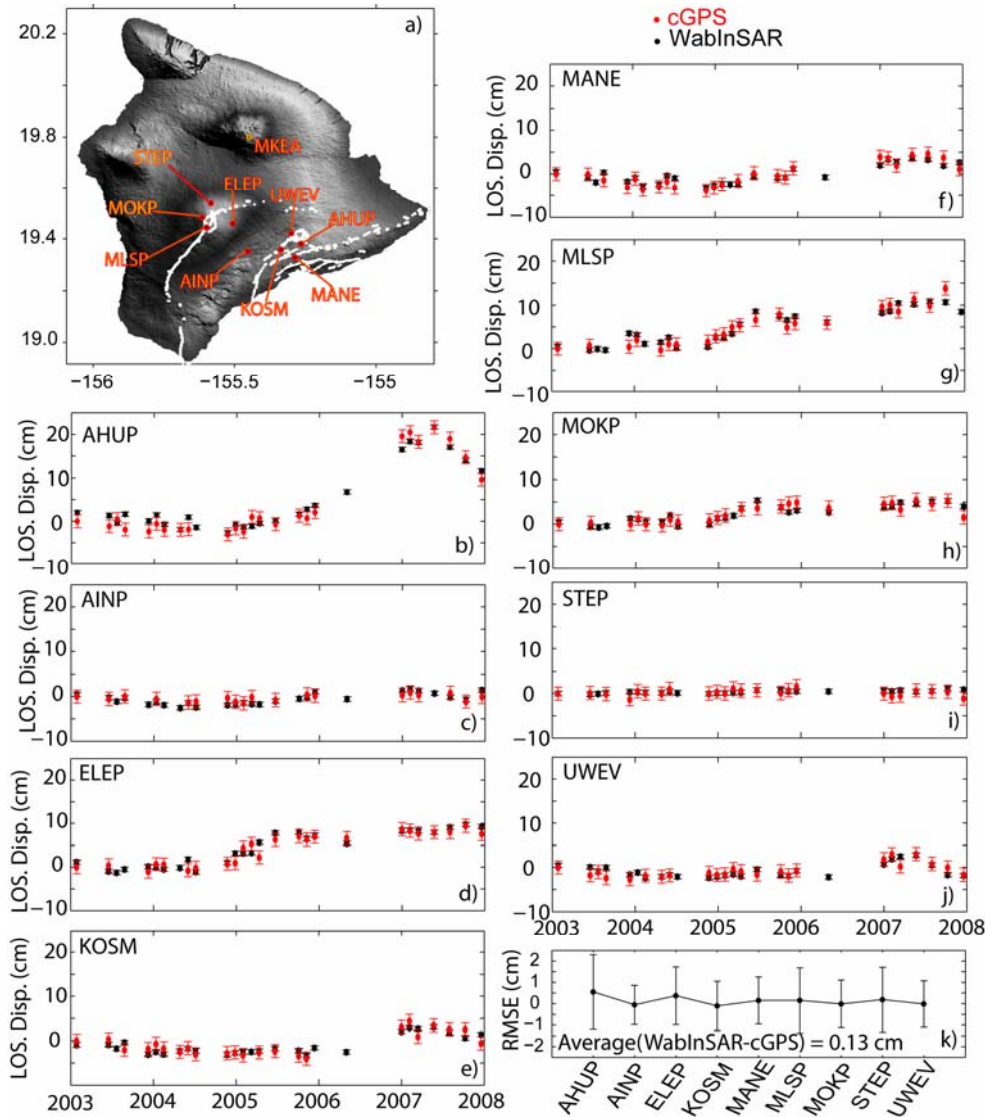


Figure 2.10. WabInSAR evaluation, a-j) presents the location of 9 cGPS stations and the comparison between cGPS time series (red dot) and WabInSAR time series (black dot), k) quantitative evaluation of the difference between WabInSAR and cGPS data sets for each station also the total average error considering whole stations which shows the average precision of 0.13 cm for the WabInSAR time series.

2.4. Discussion

WabInSAR is an approach that can generate an InSAR time series entirely free of any assumption about the temporal behavior of the deformation. It relies on multi-master interferometry and employs a variety of wavelet based, Wiener and Kalman filters to reduce major sources of artifacts. Further noise can be reduced pixel by pixel for all those areas that exhibit reliable interferometric phase information. In this work, we present WabInSAR as a wavelet-based processing package and flowchart, but we underline that only parts of the method have merit for other InSAR approaches and advancements. In the following, we discuss different aspects of WabInSAR.

2.4.1. Why are wavelets chosen for WabInSAR?

WabInSAR mostly relies on the combination of several filters designed based on wavelet transforms. Wavelets are dominant in the transient world and may be considered as base functions for the space

domain, generated by scaling and translating a single function [Daubechies, 1992]. In reality, most of the geologic phenomena (if not all) have a transient and, consequently, a wavelet structure. In crustal deformation processes, low frequency waves are often followed by high frequency components and vice versa. The wavelet theory can localize and identify such complex deformation behaviors and helps to better understand their reasons. Wavelets enable us to decompose a complicated signal and distinguish several simpler segments, each of which can be studied separately. This advantage applies not only to the deformation signal but also to elite interferograms and elite pixel selection as well as various environmental filtering techniques. Because the wavelet theory is based on a local frequency representation, it is different than Fourier and spectral analysis and appears to be more suited for InSAR data that are to be analyzed in multiple dimensions.

2.4.2 The user problem

Wavelets provide the user with a very large degree of freedom to choose the mother function, which is an advantage for identifying and studying complex signals. However, this large freedom requires very careful application of these mathematical transforms. For appropriate implementation of wavelet families, the user needs to be aware of 1) the characteristics of the signal that should be analyzed and 2) the properties of the implemented mother wavelet. These answers help to choose the most suitable wavelet families that efficiently deal with a specific part of a desired signal.

2.4.3 Data filtering or data loss?

Careless data filtering in general might be associated with a significant loss of important information. Distinguishing the latter from the noise is one of the main aims of our work. For instance, in the elite pixel selection step, the Wiener filter used is implemented here in a combination with wavelets for the following reason. The Wiener filter alone is designed to be efficient for noise reduction. This assumption, however, is valid only as long as the signal is not blurred or the signal and noise spectra are independent. In real scenarios these assumptions are usually violated. A combination with wavelets can identify both noise and signal and overcome the Wiener filter limitation. Due to the use of the wavelet-based approach, the data loss by filtering is therefore reduced rather than enhanced. Furthermore, the DEM error correction is achieved using a spatial low pass filter designed based on Legendre polynomial wavelets. Earlier workers implemented temporal low pass filters, which require an assumption about temporal behavior of the deformation field. These approaches also need to consider a constant DEM error at each pixel over the observation period. The wavelet implementation led us to apply spatial low pass filters. The wavelet coefficients are simply the value of the cross correlation between the signal and the scaled and translated wavelet function. The higher the correlation, the more similar the shape of the signal and the wavelet function in the time/space domain are. This similarity also allows representation of most of the DEM error using a sum of a finite number of wavelet terms, which provides us with an effective low pass filter that can be applied to an individual unwrapped interferogram in space. However, we should mention that this filter may extract other effects similar to the DEM error such as thermal noise and unwrapping discontinuities. Because DEM errors are commonly largest in regions of geologic activity, the DEM error correction has to be applied with care.

2.4.4 Atmosphere: Reduction of the largest error source in volcanic and tectonic terrains

Assume that the bulk of the atmospheric contribution is introduced by changes over various time scales, many of which are shorter than the satellite revisit time. Changes of the pressure, temperature and water vapor in the troposphere as well as variances of the total electron contents (TEC) of the ionosphere significantly affect the radar signal. Associated errors appear over Hawaii as large as several fringes in individual interferograms (see Fig. 2.5). The temporal frequency of atmospheric delay might be assessed as follows. Naturally, we may assume that the most of the atmospheric

contribution in repeat pass InSAR is introduced by rapid turbulence lasting hours and by gradual changes occurring within days and seasons. However, due to the present low satellite revisit times, our observations are under-sampled. Therefore, they may influence the deformation time series similar to a random temporal noise. The shortest period that we may detect in the Hawaii case has a length of about two months (for our ENVISAT data sets). Therefore, we apply a temporal filter to detect components with a frequency of about one year and also those with rapid and transient behavior. However, the deformation signal sometimes contains a sort of seasonal behavior [*Schmidt and Bürgmann, 2003*]. In this case simply removing the annual component suspected for atmospheric delay may lead to a loss of important information. This brief introduction highlights the difficulties we face when dealing with atmospheric delay. For reducing the effect of atmospheric delay, we applied a filter in a combination of a 2D spatial filter based on discrete Coiflets (in 5 levels) and a 1D temporal filter based on continuous DOG wavelets. To test the impact of the spatial part of the filter, we tested two scenarios: 1) applying filter using Coiflets wavelet with 3 levels of decomposition and 2) applying only the temporal part of the filter. As long as the temporal part (i.e., the continuous wavelet) provides a high frequency localization property (DOG of higher order ~ 30), the results of all applications remain very similar at the expense of a higher computation time. It means that in the absence of a spatial part, by implementing many temporal decomposition levels, we increased the temporal resolution and extract transient components precisely. Therefore, in cases where there is no auxiliary information, by spending more time on computation, this algorithm can produce reasonable results.

2.4.5 WabInSAR applied to Hawaii

As a case study, WabInSAR was applied to a data set of radar images over Hawaii Island acquired in the period of 2003 - 2008 using the ENVISAT satellite. The majority of the deformation was observed at Mauna Loa and Kilauea volcano calderas and their rift zones. Hence, our work confirms earlier studies [*Amelung et al., 2007; Montgomery-Brown et al., 2009a; Segall et al., 2006; Wright and Klein, 2006*]. Moreover, the trend and amplitude of WabInSAR time series over Hawaii is in good agreement with cGPS data with an average error of about 0.13 cm. The geophysical interpretation of the observed signal may include dike intrusion events and multiple fault movement, which will be further explored in a dedicated publication. The good agreement between our results, earlier work and GPS data supports the effectiveness of WabInSAR for the analysis of the deformation associated with volcanic and tectonic activities.

2.4.6 Future developments

Most of the concepts of WabInSAR are independent of the number of masters and mostly deal with single pairs, so it might be a relevant extension to single master interferometry, which has advantages in terms of computation time. Currently, we are working to implement the concept of WabInSAR in the framework of single master interferometry to lead to a wavelet based permanent scatterer. So far, we implemented standard wavelet families (such as Daubechies and Coiflet), which may fulfill the requirement of an InSAR time series analysis. An open question regards the analysis of a non-stationary deformation time series using adaptive wavelets that are constructed based on the segments of the time series considered. This question is key for more realistic and accurate deformation time series generation. Answering this question leads to the design of specific wavelet functions dedicated to studying individual sites such as volcanic and tectonic sites as well as man-made activities. By obtaining the optimum configuration of the wavelet filters, a filter selection dedicated to distinct study areas is achievable.

2.5 Conclusion

We have presented a new InSAR time series algorithm that is fully free from model assumptions concerning the deformation behavior. Because many of the data selection, identification and denoising are based on wavelets, we named the approach '*WabInSAR*'. WabInSAR is an advanced and

alternative view to the problem of InSAR time series generation and aims to revise and exploit the benefits of traditional time series approaches. As shown in this work, this method can distinguish between different components of phase difference, such as volcano surface deformation and environmental artifacts. A wavelet based statistical approach can identify elite pixels by utilizing the full spatial and temporal information available. Further wavelet based filters were successfully applied to reduce the effect of environmental artifacts such as the DEM inaccuracy and atmospheric delay, and a Kalman filter was found to be a sophisticated tool for reducing temporal noise.

This approach can be applied to a few images because, theoretically, pixel selection can be done for a minimum of two interferograms (3 radar images), DEM error reduction is done for each interferogram, and for precise atmospheric correction using 3D wavelet transforms five images might be enough. However, having a larger data set of radar images may help to better simulate and subtract environmental artifacts.

As a case study WabInSAR was applied to a data set of radar images acquired over Hawaii Island within 2003 - 2008, exhibiting large nonlinear deformation dynamic contaminated by significant atmospheric artifacts. The comparison of the WabInSAR time series and cGPS data proofed the ability of the presented approach to retrieve a dynamic deformation field with a precision of a few millimeters.

Appendix A: Synthetic test for DEM error correction

Because of the unknown characteristics of the DEM errors for each individual site, the following synthetic test considers the DEM error as a pixel-to-pixel high frequency noise with a spatial correlation. This scenario simulates the most significant part of the DEM error in InSAR data. Other effects such as slope and bias appear to be either negligible or might be considered in terms of orbital error and treated separately. We consider a deformation field that is the result of a magmatic inflation, simulated as a Mogi-type source [Mogi, 1958] at depth of 5 km with a volume change of 0.01 km^3 . This deformation is shown as an unwrapped phase, which is obtained at a grid with resolution of $80 \text{ m} \times 80 \text{ m}$ (Fig. A2.1.a). To simulate the DEM error in a more realistic way we add a sinusoidal component with a long period of 100 km and a random amplitude of up to 1.5 cm, which is equivalent to a maximum DEM error of up to 10 m for an interferogram with a perpendicular base line of 500 m, formed by radar images acquired by ENVISAT (Fig. A2.1.b). This procedure may allow testing the contributions of both spatially correlated and uncorrelated error components in the DEM. The unwrapped phase contaminated by the DEM inaccuracy is obtained by superimposition of the panels a and b in Figure (A2.1) and demonstrated in Figure (A2.1.c).

The LPW is initialized with Legendre polynomials of orders 1 to 3 and one level of decomposition at each order (in this way the effective window width is in the range of the pixel size, see section 2.2.5). Following the multiresolution analysis of the simulated observation, the corrected unwrapped phase and extracted DEM error (see above for detailed steps) are retrieved and presented in Figure (A2.1.d, e), respectively. To allow a direct comparison between the original and the corrected data, we show the difference between these two in Figure (A2.1.f). Clearly the difference is at the level of 0.1 cm, which shows the capacity of the LPW filter for reducing DEM error.

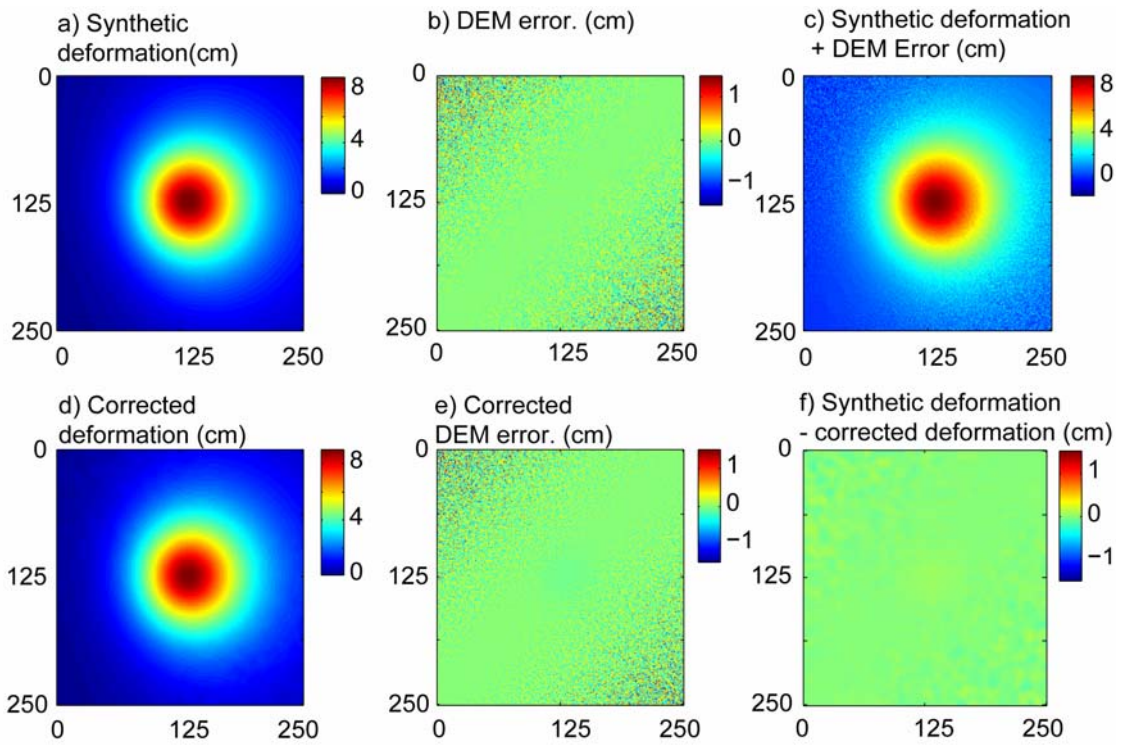


Figure A2.1: *a-f) Synthetic test showing the effectiveness of the LPW for reducing DEM error, a) simulated unwrapped phase using an inflating Mogi source, b) simulated DEM error using a sinusoidal wave with period of 100 km and random amplitude of 1.5 cm, c) superposition of the simulated unwrapped phase and DEM error, d) corrected unwrapped phase, e) corrected DEM error, f) separation between corrected unwrapped phase and simulated unwrapped phase.*

Chapter 3

Satellite orbital error reduction using wavelet based robust regression applied to InSAR deformation data¹

M. Shirzaei and T. R. Walter

Section 2.1, Dept. Physics of the Earth, GFZ German Research Centre for Geosciences, Telegrafenberg, 14473 Potsdam, Germany

Abstract

Satellite radar data analysis is often performed on the basis of repeated acquisitions. Errors in orbital determination, however, transfer to the data analysis and may even entirely obscure resulting interpretation. Therefore, orbital error correction approaches have been developed, which may affect both, noise and signal, however. Orbital error reduction remained difficult, because, InSAR data may contain a large deformation rate, atmospheric delay, topography error, low coherence and orbital error. Therefore only a robust approach for estimating the orbital ramp allows discriminating the contributions of the other components. In this work, we present a wavelet multiresolution analysis that allows, distinguishing between orbital error and other components (e.g. deformation signal). Moreover we perform a robust regression that simulates the properties of the L_1 -norm minimization for estimating the orbital ramp.

The novel orbital error estimation approach is first explained in theory, and then validated based on a synthetic test and finally applied to an interferogram formed over Tehran area in north Iran. The validation test shows that the orbital ramp can be estimated by a precision of 1 - 3 mm. therefore similar precision may be obtained for a more difficult real data set over Tehran area that shows that the signal may partly be filtered out using standard approaches, where the multiresolution and robust regression approach succeed. Our approach is moreover suitable for time series application, such as persistent scatterers or small base line subset approaches.

3.1 Introduction

The Differential Interferometric Synthetic Aperture Radar (InSAR) is the procedure that interferes two overlapped radar images acquired from similar viewing geometry and subtracts the geometrical phase contributions using satellite orbital ephemeris and a reference Digital Elevation Model (DEM) [Ferretti *et al.*, 2007]. The resulting interferogram contains information about ground displacement. However, it may also contain contributions from DEM inaccuracy, atmospheric artifact, the satellite state vector error or simply orbital uncertainties [Ferretti *et al.*, 2007].

The error in the satellite state vector can be attributed to an along track, cross track and a radial component [Hanssen, 2002]. The along track component is usually accounted once two radar images are coregistered [Hanssen, 2002]. The cross track and radial components both generate orbital fringes,

¹ MS developed the approach and processed the data. All authors were involved in discussion and writing the paper.

the so-called phase ramp, which is often parallel to the satellite track. In presence of an error in the satellite flight velocity, perpendicular fringes are feasible, too [Massonnet and Feigl, 1998]. The orbital error causes an incorrect so-called flat-earth phase to be subtracted [Hanssen, 2002]. Therefore in the real case, orbital fringes may have any pattern and orientation.

For reducing the residual fringes resulted by orbital error, for the case of topography height estimation, one way is to use tie-points or ground control point (GCP) for constraining the reference phase at certain points in each interferogram [Hanssen, 2002; Massonnet and Feigl, 1998]. To apply this GCP-approach one should ensure that the observation at the selected points is not tainted by any other contributions such as atmosphere and ground motion. Usually, however, the GCPs are affected by phase changes, therefore this approach may be too simplified and provide biased results.

Kohlhase and colleagues suggested to reduce the orbital artifacts using the improved short-arc estimates [Kohlhase et al., 2003]. This approach is found applicable to well correlated interferograms where orbital fringes are clearly countable. However, the interferograms should not be affected by significant topography and atmospheric disturbances; mainly its application is problematic in many mountainous or volcanic regions.

Another now widely used approach is to approximate this artifact using a planar phase ramp in range and azimuth direction [Hanssen, 2002] with the following form;

$$\varphi^{orbit}(\eta, \xi) = a + b\eta + c\xi \quad (3.1)$$

where, η is azimuth and ξ is range in radar coordinate system. The unknowns a , b and c can be estimated in the least square sense. In the absence of atmospheric and topographic artifacts and high deformation rate using the linear approximation, a maximum phase error of 0.35 rad may remain in the interferogram after correction [Hanssen, 2002]. However, in the case that no other component contributes to the interferometric phase, a quadratic approximation even performs better, particularly for topography generation [Hanssen, 2002]. Nevertheless, in real case our observations remain tainted, and applying a quadratic approximation may lead to filtering out the signal, too.

In practice the observation in an interferogram may be formulated as following [Ferretti et al., 2007];

$$\varphi^{int}(\eta, \xi) = \varphi^{def}(\eta, \xi) + \varphi^{atm}(\eta, \xi) + \varphi^{topo}(\eta, \xi) + \varphi^{orbit}(\eta, \xi) + \varphi^n(\eta, \xi) \quad (3.2)$$

where, φ^{def} , φ^{atm} , φ^{topo} , φ^{orbit} and φ^n are surface motion, atmospheric delay, topography error, orbital error and decorrelation noise contributions to phase observation in an interferogram, respectively.

Approximating the orbital error using equation (3.1) by a least square error approach is valid only if other terms of equation (3.2) behave randomly with a normal distribution function [Mikhail, 1976]. However, practically, this condition is often not fulfilled.

In this study we present a new approach for reliably estimating the planar phase ramp in an interferogram contaminated by atmospheric and topographic artifacts, decorrelation noise and subject to a high deformation rate.

3.2 Method

One may consider a data set with a minimum of two radar acquisition, from which by complex multiplication an interferogram is generated. After subtracting the reference geometrical phase contribution and unwrapping the phase, first we decompose the unwrapped phase using a 2-D wavelet multiresolution analysis [Mallat, 1989]. The purpose of this decomposition is to discriminate between components contributed to the observed signal in the interferogram. The orbital error has a relatively low spatial frequency that affects the entire interferogram [Hanssen, 2002] while the atmospheric and topographic artifact and decorrelation noise may have a much shorter wavelength with different amplitude than orbital error (see [Gorokhovich and Voustianiouk, 2006; Hanssen, 2002]). The situation for surface displacement may differ, as it may, by chance, show a similar behavior to the orbital error with a near constant phase gradient. However, as we are selecting interferograms larger than the area subject to deformation, this conflict might be identified before ramp removal.

We specify the number of levels for wavelet decomposition in the way that the effective wavelet window size is about the maximum wavelength of surface deformation, atmospheric delay,

topography error and decorrelation noise. This maximum wavelength might be estimated either visually or based on independent studies. The effective window size is twice of the root mean square radius (RMSR) of the wavelet function that may be calculated via following equation [Goswami and Chan, 1999];

$$rmsr = \frac{1}{\|\Omega\|} \left[\int_{-\infty}^{+\infty} (x - x^*)^2 |\Omega(x)|^2 dx \right]^{\frac{1}{2}} \quad (3.3)$$

$$x^* = \frac{1}{\|\Omega\|^2} \int_{-\infty}^{+\infty} x |\Omega(x)|^2 dx$$

$$\|\Omega\| = \left[\int_{-\infty}^{+\infty} |\Omega(x)|^2 dx \right]^{\frac{1}{2}}$$

where, $|\cdot|$ is the absolute value and Ω is the wavelet mother function [Daubechies, 1992; Goswami and Chan, 1999]. Figure (3.1) shows the wavelet mother function and associated RMSR in five levels of decomposition for three different wavelet families, Coiflets (CF), Daubechies (DB) and Symlets (SYM) of order 1 till 5. All of these families have a compact support and can be used in a discrete or continuous form [Daubechies, 1992]. Coiflets and Symlets both have a symmetric shape while Daubechies is a-symmetric [Daubechies, 1992]. The number of vanishing moments and support width for Daubechies and Symlets wavelets of order N are of 2N-1 and N, respectively, while similar values for Coiflets of order N are 2N-1 and 6N-1, respectively [Daubechies, 1992].

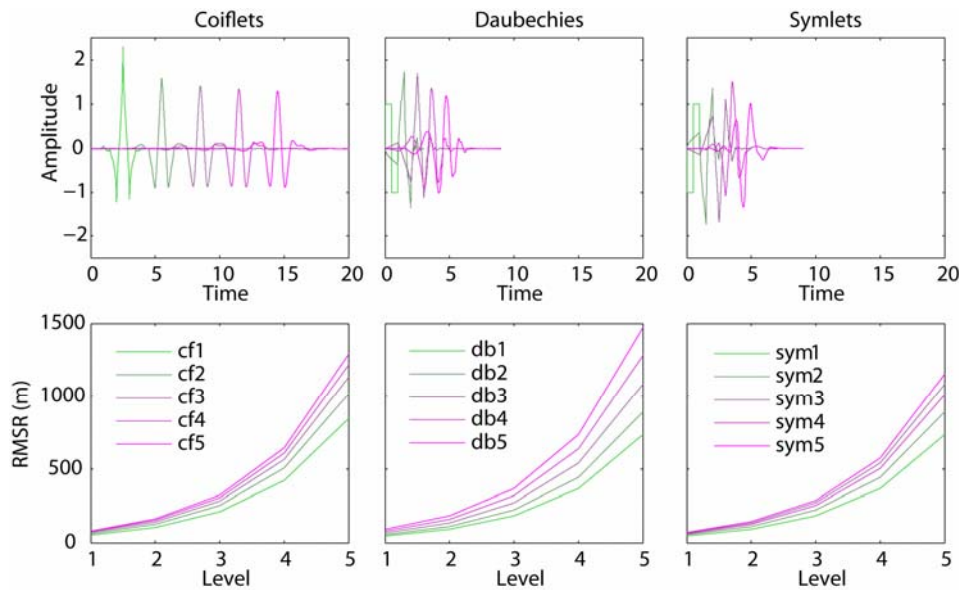


Figure 3.1. Comparison between different wavelet family and estimated root mean square radius for the pixel size of $80 \times 80 \text{ m}^2$ in five scales.

Following decomposing the signal and subtracting higher frequency components mostly the orbital error contribution remains. Now we are able to apply equation (3.1). But still the requirements for applying a least squares approach might not be fulfilled. This is, because a) a variety of unknown environmental artifacts may contribute and b) some components which arise from the applied processing algorithm may not be taken into account. These contributions act as outliers (or gross errors), thus the main assumption of a standard least squares (LSQ) is violated [Mikhail, 1976]. The reason is that LSQ tends to distribute errors evenly between observations. This effectively may avoid distinguishing the observations that are affected only by orbital error than others. As an alternative, using a more robust approach such as the L_1 norm minimization, the sample median is yielded instead of the mean (the case for LSQ) [Brown and Bethel, 1991; Fuchs, 1982]. Implementing the L_1 norm

requires rigorous mathematical calculations that lead to a linear or quadratic programming problem using Gauss-Markov models [Amiri-Simkooei, 2003; Marshall and Bethel, 1996].

A simpler way to simulate the properties of the L_1 norm is to implement the concepts of a robust regression [O'leary, 1990]. This approach employs the iterative weighted least squares, with observation reweighing as a bisquare function of the residuals from the previous step [O'leary, 1990]. The advantage is that this algorithm allows reducing the weight of those observations that are contaminated by an artifact.

Assuming A^n remains after n level decomposition of the signal with size of p and q along range and azimuth, respectively, the mathematical model might be written in terms of matrix algebra as following;

$$L_{pq \times 1} + \varepsilon_{pq \times 1} = B_{pq \times 3} X_{3 \times 1}$$

$$L = [A_{pq}^n]^T, \quad B = \begin{bmatrix} 1 & \eta_{pq} & \xi_{pq} \end{bmatrix}, \quad X = [a \quad b \quad c]^T \quad (3.4)$$

where, ε is the observation error. The weighted least square solution for equation (3.4) can be expressed as following [Mikhail, 1976];

$$\hat{X} = (B^T P B)^{-1} B^T P L \quad (3.5)$$

where, $P_{pq \times pq}$ is the diagonal weight matrix. Inhere we define P using an interferometric coherence map as following;

$$P_{ii} = \frac{Vec(C)_i}{\sum_{p,q} C_{p,q}} \quad (3.6)$$

where, C is the coherence map and $Vec(C)$ is an operator that generates a column wise vector with a size of $pq \times 1$ by putting the columns of C under each other. The residuals for observations are $V = L - B\hat{X}$. To start the iterative reweighted least squares problem we define a new weighting function as following;

$$Q^j = W^j P, \quad j = 1, 2, \dots \quad (3.7)$$

$$Q^0 = P$$

The W^j is the weighting function at iteration of j and is defined here as following [O'leary, 1990];

$$W^j = \frac{1}{1 + R_j^2} \quad (3.8)$$

$$R_j = \frac{V_{j-1}}{(T \times \sigma_{j-1} \times \sqrt{1-h})}$$

$$\sigma_{j-1}^2 = \frac{V_{j-1}^T Q^{j-1} V_{j-1}}{r}$$

where, T is tuning factor (inhere 2.385 after [Holland and Welsch, 1977; O'leary, 1990]), h is the leverage value, and r is the degree of freedom [Holland and Welsch, 1977; O'leary, 1990].

The new parameters can be obtained as following;

$$\hat{X}^j = (B^T Q^j B)^{-1} B^T Q^j L \quad (3.9)$$

$$V^j = L - B\hat{X}^j$$

The statistical properties of this estimation is further detailed in [Huber, 1981]. The procedure of calculating the new weight and updating parameters is repeated until a predefined stopping criteria reached. The stopping criteria used here is as follows;

$$|\hat{X}^j - \hat{X}^{j-1}| < \delta \quad (3.10)$$

where, δ is a small number (e.g. 10^{-7}). Obtaining the optimum parameters, we subtract the plane $\hat{a} + \hat{b}\eta + \hat{c}\xi$ from A^n and reconstruct the signal using the corrected component of the multiresolution analysis. In this way we more confident that the component extracted is due to orbital error, whereas

other phase contributions are not affected by this estimation. In the following section we evaluate this approach on a synthetic test.

3.3 Synthetic test

For analogy to our real case study (section 3.4) we generated a simulated scenario with a spatial dimension of $100 \text{ km} \times 100 \text{ km}$. We have generated a synthetic interferogram using the superposition of the effect of four deflating point sources [Mogi, 1958] at depth of 3, 5, 4 and 6 km and a volume change of -0.01, -0.01, -0.03 and -0.04 km^3 , respectively, in elastic half space medium. For simulating a real scenario we added white noise with standard deviation of 50 degree and a colored noise to represent a random atmospheric phase signal with maximum correlation length of 2 km following [Hanssen, 2002; Hooper and Zebker, 2007]. Figure (3.2a) shows the simulated interferogram. The orbital error is simulated using a planar phase ramp (Fig. 3.2b) and the final signal containing large deformation amplitude, atmospheric delay, noise and orbital error is demonstrated in Figure (3.2c). The used coherence map for the synthetic test is the map shown in Figure (3.3e) for the real case study and the areas with coherence less than 0.1 are masked out (marked with arrow in Figure 3.2c). As shown in Figure (3.3c) the spatial extend of the area subject to large deformation is about 50 km, which is considered to be the maximum wavelength in the data set.

The multiresolution analysis is done using Daubechies wavelet family of order 5 in 9 level of decomposition. The re-weighted least square is applied to the ‘approximate’ component in level 9. After 5 iteration the stopping criteria reached.

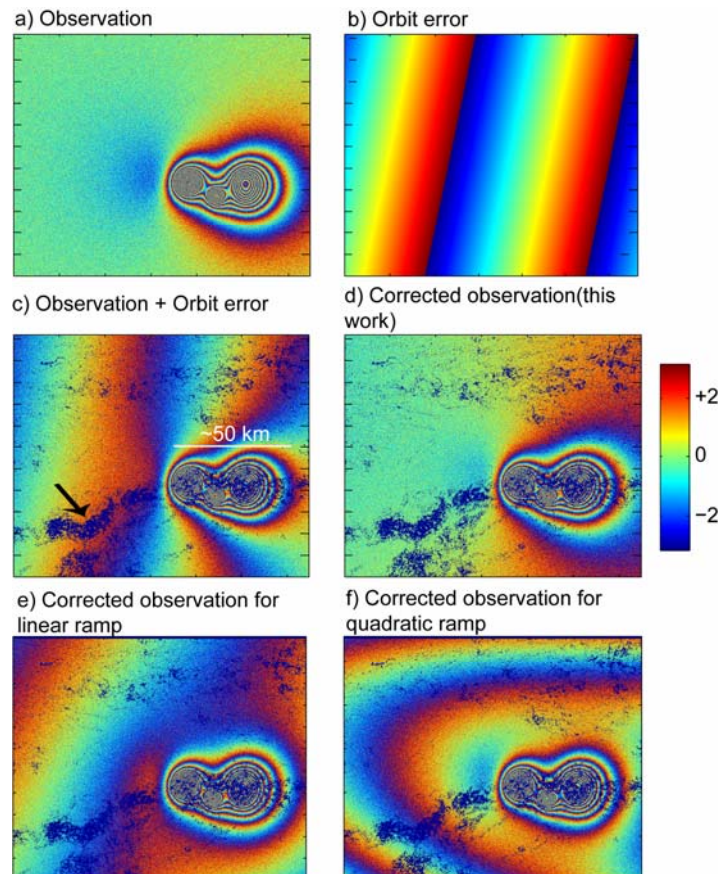


Figure 3.2. Synthetic test, a) simulated surface deformation using a superposition of the effect of four deflating point sources at depth of 3, 5, 4 and 6 km and volume change of -0.01, -0.01, -0.03 and -0.04 km^3 , and including noise and atmospheric artifact, b) the simulated orbital ramp, c) the examined simulated interferogram including orbital ramp, deformation and noise, d) the corrected interferogram for orbital ramp using our proposed method of wavelet analysis and robust regression, e, f) the corrected interferogram using standard approach for linear and quadratic ramp estimation.

The obtained corrected interferogram is presented in Figure (3.2d). As seen the signal associated to the surface deformation is preserved while the orbital ramp is corrected. The average orbital error of 0.7 rad remains after applying our correction, which is equivalent to 1-3 mm error in estimating deformation field. For comparison purposes in Figures (3.2e, f) we presented the result of applying a standard approaches [Hanssen, 2002] for estimating a linear and quadratic ramp, respectively. As seen the standard approach in this case performs much worse than our novel technique. We note that even a quadratic approximation does not perform significantly better (Fig. 3.2f). Therefore, this synthetic test shows the merits of our approach for reliable estimating the orbital error.

In the next section we apply this approach to an interferogram formed over an area of Tehran in north Iran.

3.4 Case study

We use a data set of two radar images acquired by ENVISAT radar satellite in descending mode over Tehran city, the capital of Iran with ~ 13 Mio inhabitants. The information of the interferogram is summarized in Table (3.1). This interferogram maps one year of phase difference in the satellites line-of-sight. Figure (3.3a) shows the study area and in Figure 3.3b the geocoded interferogram overlaid on SRTM DEM is presented. In the geocoded interferogram several areas apparently undergo deformation in terms of concentrated fringes, affecting western part of Tehran city. Also several sub parallel fringes forming a ramp like pattern extending from NE to SW are observed. Figure (3.3c-f) illustrates the interferometric phase, amplitude, coherence and unwrapped phase, respectively, in radar coordinate system. Clearly the area of the city exhibits high coherence and amplitude, while the area subject to rapid deformation is poorly coherent.

Table 3.1. Interferometric parameters of the pair used in the real case study

Master acquisition date	2003.8.3
Salve acquisition date	2004.8.22
Master orbit	7446
Salve orbit	12957
Perpendicular base line	96.75 m
Doppler shift	-13.45 Hz

As seen this interferogram encounters a high deformation rate with relatively large spatial coverage, decorrelation processes and sort of sub parallel fringes that partly or entirely might be due to orbital error. For correcting the orbital error, we apply the same procedure and parameters as we applied to the simulated test. The stopping criterion was reached after seven iterations. For illustration purpose, we re-wrapped the final corrected interferogram to compare it with uncorrected interferometric phase (Fig. 3.3g). As seen in Figure (3.3g) most of the ramps are corrected. Also most of the localized deformations are preserved, while other local effects become better visible. However, as marked by arrows in Figure (3.3g), one ramp-like fringe left. By comparing to Figure (3.3b) we realize that this ramp-like fringe takes place at the intersection of the mountain and the plain, and has a spatial frequency property that is different from the other ramps. Therefore this ramp-like fringe may have a different origin, where the fringe at the mountain edge may be due to ground displacement. Figure (3.3h) presents the corrected orbital ramp.

3.5 Summary and discussion

We have presented a new approach for orbital ramp correction by combining a wavelet multiresolution analysis and a robust regression. Wavelet multiresolution allows discriminating between orbital error components and other contaminants. Furthermore using a robust regression approach to simulate the properties of a L_1 -norm minimization, providing a reliable estimation of the orbital ramp. Using this approach, only the maximum phase error of 0.35 - 0.7 rad may remain in the interferogram after correction. This may cause about 1 – 3 mm error in the estimation of the deformation, which is

equivalent to random noise for independent SAR pairs. Therefore combining several corrected interferograms and generation of a time series of deformation may further guaranty an even more significant reduction of the orbital error and lead to high precision maps of the surface deformation field.

The advantages of this approach are hence; 1) it is applicable to very noisy data containing large decorrelation, 2) it is applicable to data set subject to large surface displacement and/or atmospheric artifact, 3) there is no need to have countable orbital fringes to identify its contribution and direction.

However, in the case that surface displacement has a very large spatial wavelength and a low rate (for instance in the case of extension tectonics in eastern Africa), which occupy the entire radar image with a similar pattern as the likely orbital ramp; applying such techniques may not be useful.

Our approach classifies the unwrapped phase into its building blocks and only applies ramp estimation operator to those classes, which are most likely affected by orbital error. In this way, the orbital ramps are not obscured by the existence of large surface motion, atmospheric artifacts, topography error and decorrelation noise. Our approach of orbital ramp estimation provides the orbital correction by 1-3 mm accuracy which is useful to identify slow tectonic processes, applied in special for precise InSAR time series generation approaches.

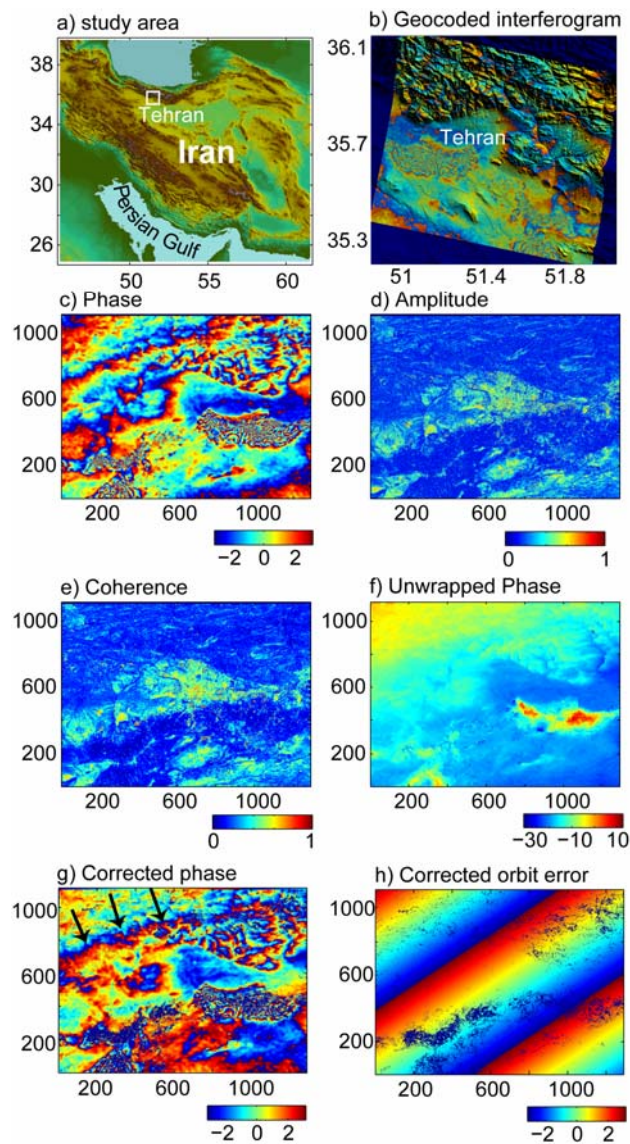


Figure 3.3. Real case study Tehran plain, a) study area, b) geocoded interferogram overlaid on SRTM DEM, c-f) interferometric phase, amplitude, coherence and unwrapped phase, respectively, g) interferogram with corrected orbital ramp, h) extracted orbital ramp.

Chapter 4

Wavelet analysis of InSAR time series reveals block-like movement and activity of the Hilina fault, Hawaii¹

M. Shirzaei and T. R. Walter

Section 2.1, Dept. Physics of the Earth, GFZ German Research Centre for Geosciences, Telegrafenberg, 14473 Potsdam, Germany

Abstract

The Hilina Fault System (HFS), located on the southern flank of Kilauea volcano, is thought to represent the surface expression of an unstable edifice sector. Despite its structural and kinematic importance for landslide initiation processes, the fault activity has not been detected by means of modern space geodetic data.

In this study we present surface deformation data obtained by an InSAR time series between 2003 and 2010 over the HFS. We observe a smooth deformation affecting most of the Kilauea south flank. Because more complex and transient signal may be hidden in this deformation pattern, we apply a novel decomposition technique. We combine continuous wavelet transforms and piecewise cubic hermite interpolation integrated with a Monte Carlo error estimation and variance-covariance matrix propagation to carefully qualify wavelet analysis coefficients of the InSAR time series. The wavelet analysis reveals that the frequency content of the deformation time series over the HFS is temporally and spatially variable. The variability of the wavelet spectrum observed at the southern Kilauea flank suggests movements of blocks that are bounded by the segments of the HFS and implies the contribution of transient and local movements at this fault zone. Since the HFS is the source of the largest earthquakes that occurred at the south flank of Kilauea, our finding may provide new insights for a more realistic assessment of the instability process and associated hazards at Hawaii Island.

4.1 Introduction

The recurrence intervals of large earthquakes ($M > 7$) at the Hilina Fault System (HFS) is estimated to be $\sim 80 - 260$ years [Cannon and Bürgmann, 2001]. In historic time the HFS has experienced several major events, the latest large earthquake occurred in 1975, i.e. $M_s 7.2$ Kalapana earthquake [Ando, 1979], which generated tsunami waves of up to 15 m height [Goff *et al.*, 2006].

The depth of the HFS is not well constrained, possibly being either a shallow structure (< 3 km) that is active during major earthquakes [Swanson *et al.*, 1976b], and/or representing the surface trace of a major and deep structure connected to the basal decollement at ~ 9 km depth [Parfitt and Peacock, 2001]. As most of the recorded seismicity beneath the HFS locates deeper than 5 km [Wolfe *et al.*, 2007] the shallow segments may be either temporally locked or displacing aseismically. Because the unstable flank a) may lead to destructive earthquakes, b) is occurring in association with magmatic

¹ MS developed the approach and processed the data. All authors were involved in discussion and writing the paper.

activity, c) may entirely or partly fail to generate tsunamis, therefore, characterising the deformation behaviour of the southern Kilauea flank is of great importance. In the next sections we first briefly explain the InSAR deformation time series as well as the tools we develop to analyze the time series, followed by a detailed description and discussion of the temporal and spatial occurrence of the fault activity and apparent aseismic flank movement.

4.2 InSAR deformation field

To study the spatiotemporal deformation field over the HFS on the southern flank of the Kilauea volcano, we used a data set of 44 radar images acquired in the period 2003 - 2010 in descending mode (track 200) by ENVISAT satellite. The data catalogue is almost complete; with an average sampling rate of 0.16 yr. We generated a dataset including ~520 interferograms with spatial and temporal baselines smaller than 450 m and 4 years, respectively. The topographical phase has been simulated and removed using satellite precise orbits and a reference Digital Elevation Model (DEM). To obtain the unambiguous differential deformation field, each interferogram has been unwrapped using a well tested minimum cost flow approach applied to those pixel containing less decorrelation noise [Costantini and Rosen, 1999]. The method for identifying less noisy pixels is derived from earlier works [Berardino *et al.*, 2002; Hooper *et al.*, 2007] based on interferometric coherence map. The unwrapped phase difference values are inverted using the approach of general unbiased estimate [Bjerhammar, 1973] to generate a time series of the deformation field [Schmidt and Bürgmann, 2003]. Finally, using the spatiotemporal information, which relies on the fact that atmospheric contributions are temporally decorrelated and spatially correlated, we apply a high pass filter in time and a low pass filter in space [Berardino *et al.*, 2002]. Thus we assume that the effect of atmospheric delay was reduced. However, the filtered data are only used for estimation linear velocity as well as visualization and further analysis is done based on unfiltered time series to preserve all components (signal, systematic error and noise) of the deformation time series.

Figures (4.1a) shows the linear velocity field. This data displays a rather diffuse deformation region, where no local faulting activity is visible at the HFS. However, as we will show further below, a local faulting activity may be hidden due to the complexity of the overlaying signal.

Figures (4.1b, c) demonstrate the non-linearity of the deformation field at several selected points. Figure (4.1b) presents the time series of the deformation field at Kilauea caldera and the northeast rift dike. As seen, both show a similar behaviour until the dike intrusion occurred at the northeast rift in June 2007. The intrusion lasted June 17 - 19 and was accompanied by deflation at the Kilauea magma chamber. The physical process of this event has been well studied by several workers [Brooks *et al.*, 2008; Montgomery-Brown *et al.*, 2009b], thought to be related to combined dislocation of the south flank, rift zone and shallow magma chamber.

Figure (4.1c) shows the InSAR time series of deformation at several points chosen on different fault blocks of Hilina. The general trend is movement toward the satellite, possibly as a result of rift intrusions and gravitational loading [Denlinger and Okubo, 1995; Dieterich, 1998]. However, several local fluctuations are apparent which we investigate in more details in the next sections.

4.3 Signal decomposition

To further explore the “diffuse deformation region” and analyze the hidden signal components in irregularly sampled InSAR data, we first develop a scheme relying on interpolation. In this regard we estimate the interpolation error and later on we combine this approach with the continuous wavelet transform for identifying hidden deformation signals.

4.3.1 Data interpolation and error estimation

InSAR observations are usually irregularly sampled in time. In contrast, most of the mathematical transforms are applicable to evenly sampled data sets [Pollock, 1999]. One way to construct a time series of regularly sampled observations within a range of a discrete set of points is to use

interpolation. Various methods are used for interpolating a discrete set of points, such as linear, quadratic, piecewise cubic Hermite polynomial (PCHP) and cubic Spline (CS) interpolation [Fritsch and Carlson, 1980]. PCHP and CS are often preferred because the interpolation error is usually small and also avoids an oscillatory behaviour of the interpolator. This may preserve the accuracy of the interpolation for monotone and smooth enough signals. The procedure for calculating PCHP and CS is similar, but the PCHP only guarantees the continuity of the first derivatives while CS provides a continuity condition to the second derivative, too. This means CS is more accurate for smooth data while PCHP leads to less oscillation for non smooth data sets [Fritsch and Carlson, 1980]. PCHP is generally less expensive to compute and applicable to large data sets. Herein we hence concentrate on PCHP and try to devise a framework for careful applying to time series.

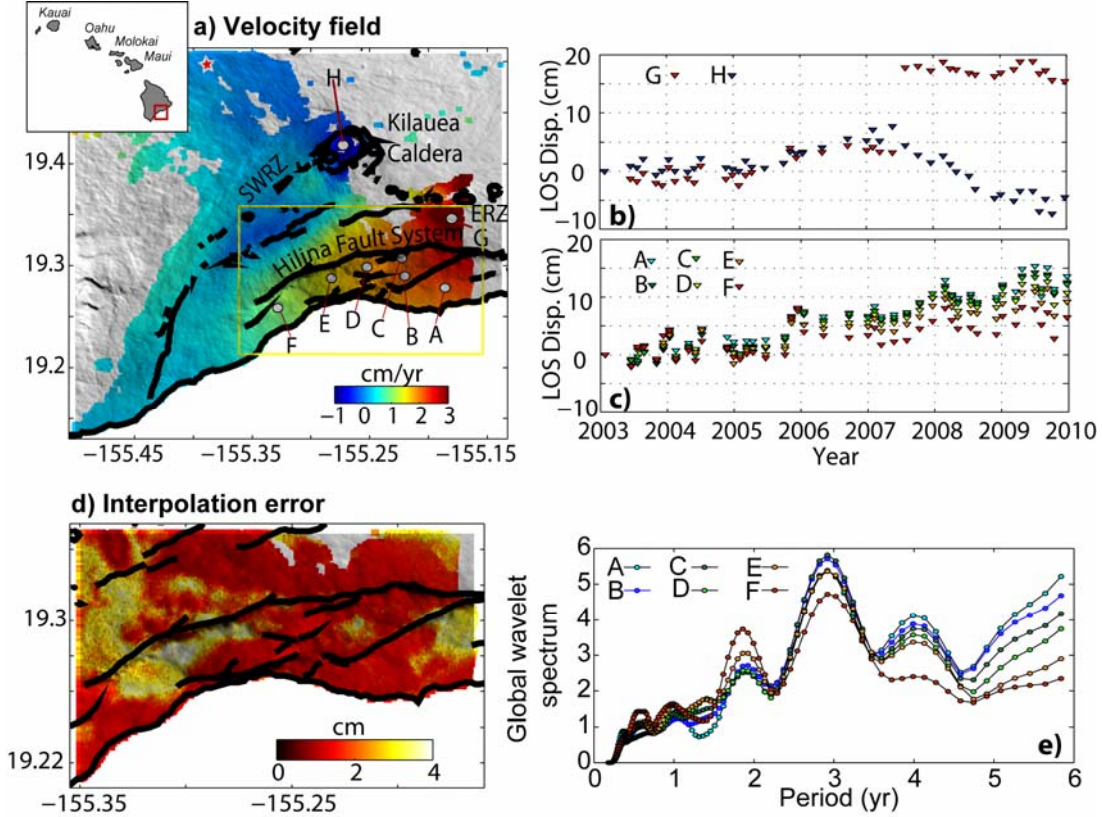


Figure 4.1. Kilauea south flank, a) study area and linear velocity field, geological faults and the location of the selected point for presenting the deformation time series. Red star depict location of the fixed reference point, and yellow box showing the area of HFS. b) InSAR time series of the deformation at Kilauea caldera and southeast rift, c) InSAR time series of the deformation at different points of the HFS. d) Interpolation error estimated for the HFS zone, e) Global wavelet spectrum obtained by analyzing the InSAR time series given in panel (c).

The main concern is the accuracy of the interpolated data sets, an unsolved issue generally without external controls. Herein, by employing the concept of “check point” in a statistical manner, we are estimating the quality of the interpolation as follows. Assume, given n irregularly sampled points in time $T = \{t_n\}_{n=1..N}$ with distinct values of $X = \{x_n\}_{n=1..N}$ there are two PCHP, i.e. P_T and P_j , that uniquely approximate $X = \{x_n\}_{n=1..N}$ and $X = \{x_n\}_{n=1..N, n \neq j}$, respectively. For P_j we excluded the j th component (i.e. the check point) from $X = \{x_n\}_{n=1..N}$ and subsequently estimate it using P_j as $x_j^{P_j}$. The interpolation error may be stated as $e_j = x_j^{P_T} - x_j^{P_j}$. If we repeat the procedure for n' random points, a more robust estimate of the interpolation error is obtained via $\bar{e} = 1/n' \sum_{j=1}^{n'} e_j$.

Using a Monte Carlo scheme, including a randomly iterated removal, evaluation and restore steps, we obtain an error distribution function likely in the Gaussian form. This Gaussian function is

characterized by two parameters, mean and variance, that both provide an estimation of the interpolation error over the intervals that the time series remains monotone. For a comprehensive validation test the reader is referred to the supplementary material.

4.3.2 Hidden signal detection using wavelet transforms

The continuous wavelet transform (CWT) of a time series $X(n) = \{x_n\}_{n=1..N}$ with a time step δt can be defined via convolution with a scaled normalized wavelet function (ψ_0) as following;

$$W(a, n) = \psi^T(n, a) * X(n) \quad (4.1)$$

where a is a scaling parameter, $(^T)$ is the complex conjugate, $(*)$ is the convolution operator. Following *Torrence and Compo*, [1998] we may write;

$$\psi(n, a) = \left(\frac{\delta t}{s}\right)^{1/2} \psi_0\left(\frac{n\delta t}{a}\right) \quad (4.2)$$

Equation (4.1) can be re-written in the following form;

$$W(a, n) = \Psi(n, a)X(n) \quad (4.3)$$

where Ψ is a $n \times n$ circulant matrix, ψ is the first row of Ψ and each row vector is rotated by one element forward relative to the preceding row vector.

Equation (4.1) can be efficiently calculated using the convolution theorem in the Fourier domain [*Torrence and Compo*, 1998]. We further explore the linear equation (4.3) in order to propagate the full variance-covariance matrix of the time series to the wavelet coefficients.

Having an time series $X(n) = \{x_n\}_{n=1..N}$ with a variance-covariance matrix of Q_{xx} (including the interpolation error) the variance-covariance matrix of a wavelet coefficient at scale a is expressed as following;

$$Q_{W_a W_a} = E(W(n, a) - E(W(n, a)))(E(W(n, a) - E(W(n, a))))^T \quad (4.4)$$

Substituting equation (4.3) in (4.4) and following some algebraic calculations we obtain;

$$Q_{W_a W_a} = \Psi(n, a)Q_{xx}\Psi(n, a)^T \quad (4.5)$$

This equation presents the variance-covariance matrix of the wavelet coefficients based on a variance-covariance matrix of the time series.

The global wavelet spectrum (GWS) at scale a is defined as following;

$$G(a) = \frac{1}{N} \sum_{n=1}^N |W(a, n)| \quad (4.6)$$

Regarding the linearity of the equation (4.3), both the wavelet coefficients and the time series have a similar probability density function. Therefore by assuming a normal distribution function for the time series the following statistics for the GWS is derived from [*Vanicek and Krakiwesky*, 1982];

$$\frac{W(a, n) - G(a)}{\left(\frac{N-1}{N}\right)^{1/2} S} \sim t_{N-2} \quad (4.7)$$

where, t is the t-student probability function and S is the standard deviation of the wavelet coefficients at scale a . This statistic might be used to build a $(1 - \alpha)\%$ confidence interval to identify an outlier as following;

$$G(a) - S\left(\frac{N-1}{N}\right)^{1/2} t_{N-2, 1-\alpha/2} < W(a, n) < G(a) + S\left(\frac{N-1}{N}\right)^{1/2} t_{N-2, 1-\alpha/2} \quad (4.8)$$

If this test fails, the wavelet coefficient is considered to be an outlier and not further considered.

This approach for hidden texture detection can be applied to any geophysical time series. Inhere we apply these tools to analyze the InSAR time series of the deformation field over the HFS.

As we mentioned before, we examine the original InSAR time series without applying any atmospheric filtering. The atmospheric artefact is independent from other components in terms of their spatiotemporal frequency properties. Therefore, the result of InSAR time series wavelet decomposition is unaffected by atmospheric filtering.

4.4 Application to Hilina fault system deformation time series

The hidden signal detection at the HFS may reveal activity at several associated fault segments. Figure (4.1d) shows the interpolation error with the average and maximum values of ~ 1 cm and 3 cm, respectively. The area with larger interpolation error indicates where the InSAR time series violates the assumption of being monotone, showing that for most of the south flank the approach is appropriate. As seen in Figure (4.1c), the InSAR time series at several points of the volcano flank are characterized by various fluctuations, which are better assessable in the global wavelet spectrum (GWS) plots (Fig. 4.1e).

At all data points the GWS plots are obtained by applying equation (4.1) in the Fourier domain using the Derivatives of Gaussian (DOG of order 30) as the wavelet function. The covariance matrix was obtained by using equation (4.5). A 95% confidence region is considered by implementing equation (4.8) to identify reliable wavelet coefficients. Using those reliable coefficients the final GWS is calculated and illustrated in Figure (4.1e).

Figure (4.1e) presents several periods in which the GWS is fluctuating at different sub-regions of the Kilauea south flank. To identify the spatial distribution of those frequency-dependent components we classified the normalized GWS at different time intervals as shown in Figure (4.2). The variances of these intervals are estimated using equation (4.5) and further detailed in electronic appendix. The interval with a period of 0 - 0.2 years presents the largest detectable frequency in our data set and is interpreted to be due to a very rapid change in the deformation time series e.g. intrusion events. Moreover, the period of 0.9 - 1.1 years showing very significant effect that might be associated with atmospheric delay based on the assumption that seasonal variability is the main source of change in the pressure, temperature and water vapour content of the troposphere.

Figure (4.2a) shows the effect of very rapid changes in the deformation time series and reveals the presence of a high GWS in the southeastern part of the flank, which locally is bounded to geological structures. We note, however, that this frequency interval is highly sensitive to the observation noise. In Figure (4.2b) two zones of high GWS are visible in the southeast and southwest. We find that both of them are clearly bounded by known pre-existing fault traces of the HFS. In the frequency interval 0.5 - 0.9 years the south-western block is similarly moving (Fig 4.2c), while now the southeastern blocks appear stable.

Figure (4.2d) presents the components that are probably associated with atmospheric delay, which has a smooth spatial pattern and is similar to the estimated atmospheric artefacts in other studies [*Williams et al.*, 1998; *Zebker et al.*, 1997]. Figures (4.2e, f) show again areas of relatively high GWS, in their updip controlled by segments of the HFS. Figures (4.2g, h) demonstrate that the zone of the HFS experiences approximately uniform low GWS for the intervals of 2 - 3 years. The last Figure (4.2i) presents the longest period considered (i.e. 6-7 years) showing a very low GWS throughout the HFS. Larger periods could not be extracted using the available data set.

In summary, the results of the wavelet decomposition of the InSAR time series reveal that isolated areas of the Kilauea south flank deform. These isolated areas are delimited by faults. The faults therefore define individual blocks, which are moving at specific frequencies. This suggests a spatially and temporally heterogeneous block-wise deformation field, which might be the complex surface expression of a continuously seaward movement of the south flank of Kilauea as further discussed below.

4.5 Discussion

Motion of the discrete blocks at Kilauea unstable flank have been postulated on a large scale before [*Bryan and Johnson*, 1991]. Our work shows the first InSAR evidence of a block-wise movement at the HFS. Using a frequency dependent InSAR analysis, we explore hidden signals in geodetic time series. We could find that the HFS segments bound discrete block-wise movements, which is also confirming paleomagnetic constraints on fault motions [*Riley et al.*, 1999].

Foster and colleagues, using conventional InSAR, observed a deformation at HFS but interpreted it to be influenced by atmospheric changes. As noted by the same authors, the atmospheric model MM5 (NCAR-Penn State Mesoscale Model Version 5) could not explain this signal, however [Foster *et al.*, 2006]. The reason for the apparent disagreement between the MM5 model and the observation might be the resolution and incompleteness of the MM5 model for explaining very local effects, or the contribution of hidden deformation signals such as a motion of the HFS blocks. Because the HFS consists of several normal faults with scarps up to 500 m height, the influence of both deformation and the variable troposphere's properties should be taken into account [Zebker *et al.*, 1997]. Because, in wet regions such as Hawaii Island, a 20% change in the humidity may lead to ~10 cm displacement error [Zebker *et al.*, 1997]. Consequently, the segments of the HFS may trap local anisotropies, in particular water vapour, and cause a artefactual phase change in the observed radar phase that can be mis-interpreted as surface deformation.

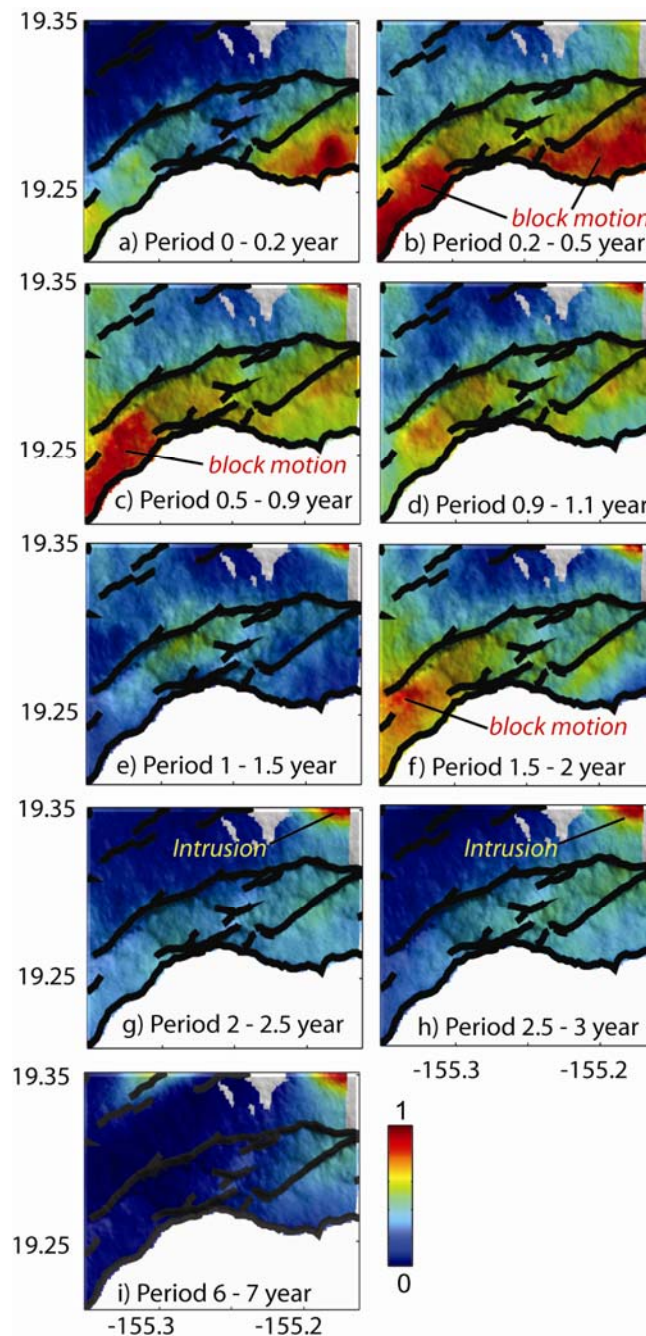


Figure 4.3. Frequency classification of the global wavelet spectrum, a - i) present the averaged and normalized GWS in different frequency classes.

The wavelet analysis of a signal deals with transient components as well as elements with mid- and long- term periods. Considering any deformation signal to be a result of many different superimposed components the wavelet analysis is able to identify and classify the building blocks upon their frequency properties.

The assumption for applying the Monte Carlo interpolation approach is that the signal is monotone. This assumption, however, is not always fulfilled. In the case of the fully non-stationary and unevenly sampled time series, we emphasize that, there is no confident method yet to fill gaps and estimate the associated quality.

After wavelet analysis of the HFS data set (Fig. 4.2a-f) we found that different frequency classes up to 2.5 years reveal isolated areas of the HFS to be moving at different scales. The analysis shows significant GWS areas bounded by geological structures. As these match with the areas of the HFS blocks, this study shows the deformation activity at these faults.

In contrast as seen in Figure (4.2d) (the components of 1 year interval associated with seasonal effects) there are local smooth effects bounded by sharp HFS morphology while being indifferent to the internal minor geological structures. Therefore we conjecture that the interpreted deformation is true. Because of a lack of seismicity at the shallow zone we may speculate that the faulting activity is aseismic.

This finding has a significant importance for hazard assessment on Hawaii Island, because since the last great earthquake occurred in 1975, no geodetic or seismic evidence for activity of these shallow faults has been evidenced. As, in particular, the study of the relation between the surface moving sequence and the downdip fault geometry is of interest for flank instability assessments; now, this study provided new line of evidence for aseismic block-wise movement which similarly can be tested and applied to other deforming volcanic and tectonic areas.

4.6 Conclusions

We presented and analyzed a 7-year InSAR time series over the south flank of Kilauea to study the local activities at the HFS. The motivation was to extract hidden information probably obscured by other signal components. To this aim we developed an approach for wavelet analysis of unevenly sampled data. It is based on a Monte Carlo approach for interpolation error estimation and variance-covariance matrix propagation through the wavelet transforms. We also provide a statistical test for evaluating the significance of wavelet coefficients.

The frequency classification revealed a block-wise movement at the Kilauea south flank, characterized by different frequency properties at the HFS segments. As shown at higher frequencies specific fault segments are locally active. In the low frequencies, in turn, the entire south flank behaves similarly, possibly, influenced by slow flank spreading. The evidences of a frequency-dependent block-wise fault movement are of importance because of the lack of seismicity at the shallow fault zone, and the requirement for identifying the partially locked or aseismically slipping Hilina segments.

4.7 Auxiliary material

4.7.1 Evaluating Data interpolation and error estimation approach via Synthetic test

To evaluate the approach for estimating accuracy of interpolation we employ a synthetic test. Figure (S1b) demonstrates the simulated data set in filled black circles and also the original analogue function in solid line. Herein, $n = 20$, $n' = 5$ and number of iteration is 1000. Figure (S1b) shows the misfit histogram for this test that has Gaussian form. The mean and variance for this Gaussian shape distribution are -2.3 and 7.1, respectively.

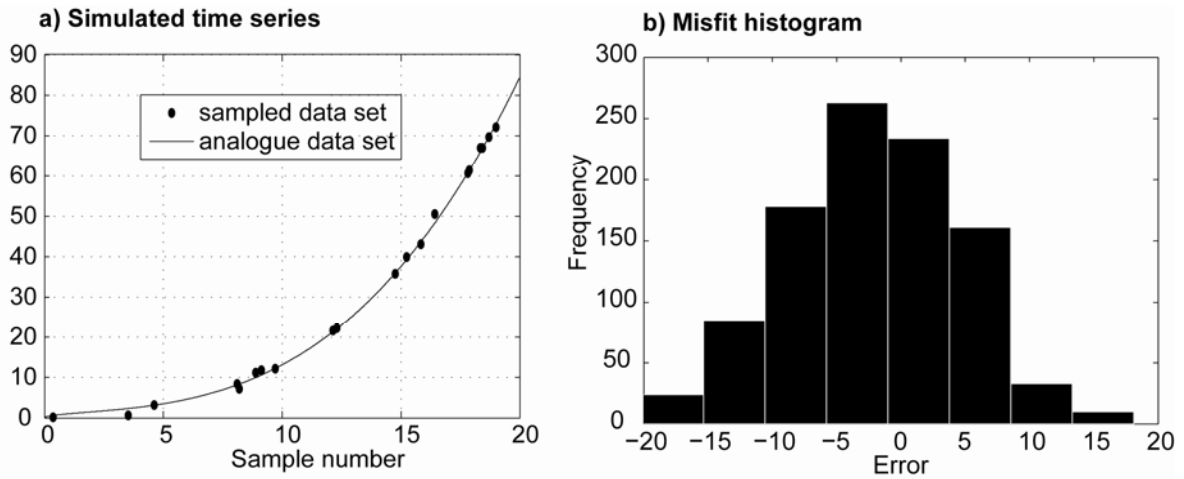


Figure S4.1: synthetic test, a) original data set and sub-sampled irregularly spaced data set, b) misfithistogram of the Monte Carlo simulation showing the distribution of the interpolation error.

4.7.2 Global wavelet spectrum variance

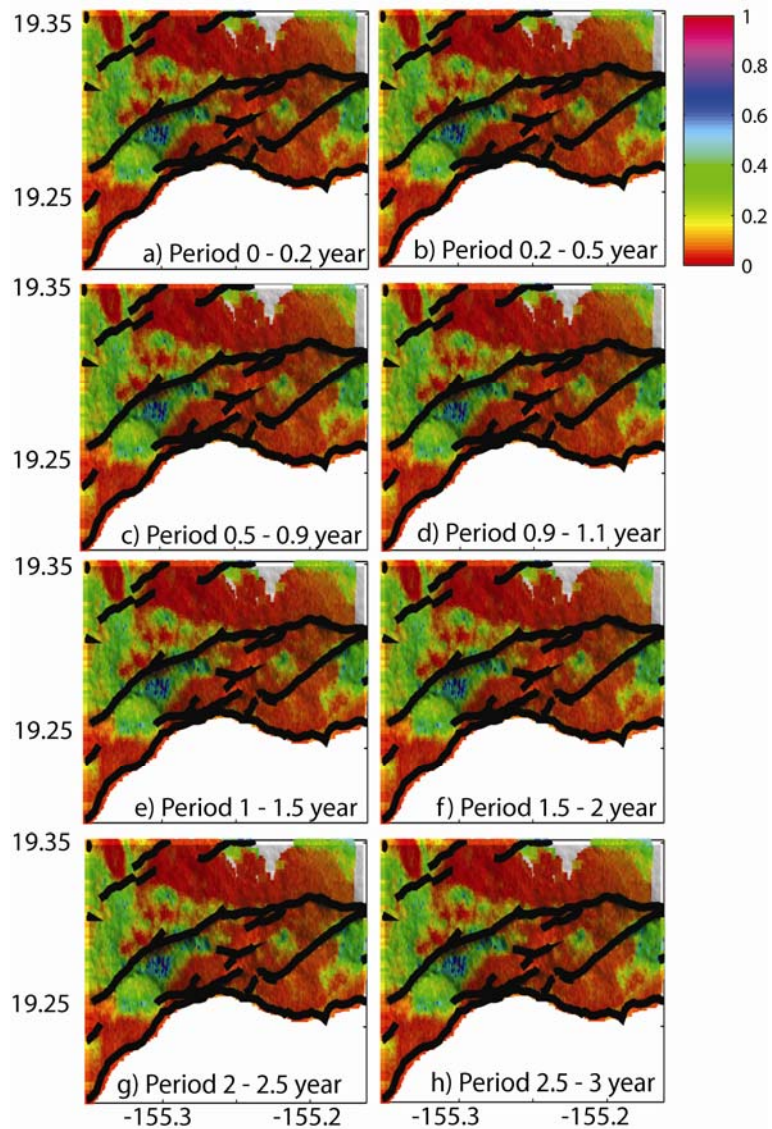


Figure S4.2. The normalized GWS variances obtained by propagating interpolation error through wavelet transform. The classes are the same as Figure (4.3).

Chapter 5

Randomly Iterated Search and Statistical Competency (RISC) as powerful inversion tools for deformation source modeling: application to volcano InSAR data¹

M. Shirzaei and T. R. Walter

Section 2.1, Dept. Physics of the Earth, GFZ German Research Centre for Geosciences, Telegrafenberg, 14473 Potsdam, Germany

Abstract

Modern geodetic techniques provide valuable and near real time observations of volcanic activity. Characterizing the source of deformation based on these observations has become of major importance in related monitoring efforts. We investigate two Random Search approaches, Simulated Annealing (SA) and Genetic Algorithm (GA), and utilize them in an iterated manner. The iterated approach helps to prevent GA in general and SA in particular from getting trapped in local minima and it also increases redundancy for exploring the search space. We apply a statistical competency test for estimating the confidence interval of the inversion source parameters, considering their internal interaction through the model, the effect of the model deficiency, as well as the observational error. Here, we present and test this new Randomly Iterated Search and Statistical Competency (RISC) optimization method together with GA and SA for the modeling of data associated with volcanic deformations. Following synthetic and sensitivity tests, we apply the improved inversion techniques to two episodes of activity in the Campi Flegrei volcanic region in Italy observed by the InSAR technique. Inversion of these data allows derivation of deformation source parameters and their associated quality, so that we can compare the two inversion methods. The RISC approach was found to be an efficient method in terms of computation time and search results, and may be applied to other optimization problems in volcanic and tectonic environments.

5.1 Introduction

High resolution mapping of spatiotemporal deformation fields can provide important information about earthquake and volcanic source geometries and associated physical processes. Utilizing numerical and analytical modeling techniques, detected deformation signals can be theoretically reproduced, and, for instance, the specific characteristics of a magma chamber being determined. The inferred characteristics of the magma chamber (or “source”) can include diverse geometric parameters such as location, and volume pressure and change. These physical variables are especially important for hazard assessment, including volcano monitoring or fast response teams.

¹ MS developed the approach and inverted the data. All authors were involved in discussion and writing the paper.

Since the relation between surface deformation and magmatic sources of Japanese volcanoes was investigated via an analytical formulation of an inflating point source in an elastic half space [Mogi, 1958], many other developments in the field of analytical models and their applications have been achieved to constrain magmatic source parameters specifically based on surface deformation data. Okada [1985] presented a closed formulation to explain parameters of a rectangular dislocation source causing surface deformation in an elastic half space. This model is applicable to volcanic deformation as well and earthquake simulation, treating the source as a finite rectangular fault that is either subject to opening or subject to strike and dip slip motions. Shortly afterward, Davis [1986] presented an analytical expression of an ellipsoidal inflating cavity buried in an elastic half space that causes deformation at the surface and enables us to explore the surrounding stress field. This research was ground for other developments, such as an analytical expression of finite sphere in half space [McTigue, 1987] and pressurized dipping ellipsoidal source [Yang *et al.*, 1988]. Despite their simplicity, these models have successfully explained observed deformation fields resulting from volcanic and tectonic activities over the past 60 years [Dzurisin, 2006], which together with independent geophysical and geological evidence demonstrated the validity of this kind of analytical expression to define the geometrical and mechanical parameters of the source of volcanic deformation. The procedure for obtaining the parameters of an analytical model from an observed displacement field is an inverse problem. From a mathematical point of view, there are many different techniques for solving an inverse problem, and to investigate magma chambers processes (see Table 5.1). A sophisticated inversion (optimization) technique requires a balance of *robustness* and *efficiency*. Geophysical solutions presented in the literature often provide details about the location and/or strength of a deformation source without knowing the sensitivity of the data and/or the model, which are directly related to the quality of the result. In order to evaluate the robustness of an inversion, the sensitivity of source parameters to the observations has to be evaluated first. Moreover, because space geodetic datasets are spatially and temporally increasingly large, the handling of this quantity of data together with their full variance-covariance matrix reflecting observation quality and relative weight has become a major difficulty in optimization problems. Several algorithms have been proposed to downsample such large datasets, including either sophisticated approaches such as Quadtree sampling [Jónsson *et al.*, 2002] or simple methods such as uniform sampling. Although these methods principally downsample the observation field, some important data may be lost. Therefore, as an alternative, improved and faster inversion algorithms may allow use of a more complete or even full data set.

Table 5.1. Summary of selected optimization methods used in different branches of geosciences

Method	Main idea	Application	Advantage	Disadvantage
Least-Squares	Gradient based	[Lundgren <i>et al.</i> , 2001] [Jónsson <i>et al.</i> , 2002] [Battaglia <i>et al.</i> , 2003; 2006] [Lanari <i>et al.</i> , 2004]	Very fast for convex search space	May get trapped in local minima.
Monte Carlo	Randomly samples the parameters space	[Keilis-Borok and Yanovskaja, 1967]	Gradient free	Slow. May miss the global solution.
Neighborhood Algorithm*	Generate new samples with density function related to previous step samples	[Sambridge, 1998; 1999a; 1999b] [Amoruso <i>et al.</i> , 2007]	Gradient free	Slows down very significantly when the number of parameters increases.
Simulated Annealing*	Motivated by analogy between annealing in solids and optimization problems	[Cervelli <i>et al.</i> , 2001b] [Chevrot, 2002] [Jónsson <i>et al.</i> , 2002] [Amelung <i>et al.</i> , 2007]	Gradient free, fast	Slows down when the number of parameters increases. Success depends on the cooling schedule. May find a solution in the vicinity of the global solution.
Genetic Algorithm*	Motivated by analogy between biological evolution and optimization problems	[Currenti <i>et al.</i> , 2005] [Gottsmann <i>et al.</i> , 2006] [Carbone <i>et al.</i> , 2008]	Gradient free, fast	Slows down when the number of parameters increases. May find a solution in the vicinity of the global solution.

* These methods are basically inspired by Monte Carlo search approach and fall into the same class

In this paper, we investigate the robustness and efficiency of optimization techniques with a focus on two sophisticated commonly used methods: the Simulated Annealing (SA) and Genetic Algorithm (GA). In comparison to other optimization techniques, SA and GA have been shown to be excellent methods for finding global solutions in complex search spaces [Sambridge and Mosegaard, 2002], which stimulate researchers in various geophysical disciplines to use these methods for optimization

(Table 5.1). We evaluate the advantages and disadvantages of these methods and find that GA, in general, and SA, in particular, may get trapped in local minima. Therefore, we suggest including a new iterative approach and statistical competency test to elude local traps and to estimate the reliability of the solution, thus improving the quality of the result.

The paper is organized as follows. First, in synthetic tests, we consider analytical models of different sources as an effective component governing the interaction of observation and inversion parameters. The investigated sensitivity allows us to estimate how a model may affect the precision and accuracy of inversion results. Second, we explain SA and GA optimization methods and show which parameters are important for the algorithm to successfully find a global solution. Third, we apply a randomly iterated search approach in order to avoid local minima and reduce the effect of the “cooling schedule”. We suggest that a Statistical Competency (SC) approach, considering both observation uncertainty and model deficiency, may allow estimation of the source parameters and their quality. We finally demonstrate the robustness and efficiency of our improved algorithms via synthetic tests and apply the two different methods to periods of uplift (2000-2001) and subsidence (2001-2002) at the Campi Flegrei caldera volcano, Italy.

5.2 From data to dislocation model

In the last two decades, the GPS and InSAR technique have provided nearly continuous observation of deformation fields in time (case for GPS) and in space (case for InSAR). With precision better than 1 cm, these techniques have increased the ability to develop a reasonable interpretation of geodetic data and also to analyze physical processes. One of the most common applications of these observations is to numerically or analytically simulate the source of the deformation. Three widely used analytical models for simulating the source of deformation events are the point source [Mogi, 1958], including four parameters (two horizontal locations, depth, and strength), the ellipsoidal source [Yang *et al.*, 1988], including eight parameters (two horizontal locations, depth, semi major and semi minor axes, plunge and strike angle of major axis, and pressure change), and the rectangular source [Okada, 1985], including ten parameters (two horizontal locations, depth, length, width, dip, strike, and three dislocation components). The first two source types are commonly used specifically for volcano and reservoir modeling, while the last is applicable to both volcanic and earthquake events. All of these models are usually implemented in an isotropic, linear, homogeneous, elastic half space. Despite their simplicity, in many examples these models can explain surface deformations very well and are used as standards in modern geodesy (Table 5.1). However, their sensitivity has been only partly investigated [Dawson and Tregoning, 2007] and for volcanic sources not characterized in detail. In the next sections, we will summarize the mathematical relations to obtain model parameters based on surface observation and perform a sensitivity analysis to test the effect of the three source parameters on the surface deformation field.

5.2.1 Dislocation problem and optimization

The stochastic model relating surface deformation data to dislocation source parameters is:

$$L + v = F(S) \quad (5.1)$$

where L is deformation observation, F is a function that provides a mathematical relation between deformation data and source parameters S , and v is the observation residual. As m is the number of observations and n is the number of source parameters, usually $m > n$. In this case, the number of unknowns is $m + n$, which means that equation (5.1) has many solutions. We are interested in a solution that minimizes a function of v . Based on this approach, to estimate the source parameters we solve an optimization problem:

$$C(v, P) \rightarrow \min \quad (5.2)$$

where $P = \sigma_0^2 C_l^{-1}$ is a weight matrix of the observations, C_l is variance-covariance matrix of the observations, σ_0^2 is the primary variance factor, and C is a function of P and v constraining the

solution space [Vanicek and Krakiwesky, 1982]. The most frequently used cost function in optimization problems is the weighted second norm of the residuals, given by:

$$C(v, P) = v^T P v \quad (5.3)$$

The advantages of this cost function are an unbiased estimation of the source parameters [Bjerhammar, 1973] and chi-square probability density function of $v^T C_i^{-1} v$, which may be used for evaluating the result [Vanicek and Krakiwesky, 1982]. Because of the latter advantage, a confidence interval $\chi_{n-m, \alpha/2}^2 < v^T C_i^{-1} v < \chi_{n-m, 1-\alpha/2}^2$ in a confidence level of $(1-\alpha)\%$ can be defined. This test can be rejected from the right side or left side. Rejection from the right side may mean a defect in the model or observation. Left side rejection means the residuals are too small or the model is too good. This could be the case in modeling the source of crustal deformation, where the easiest and relatively unrealistic way to obtain a small residual is by adding more and more analytical sources (e.g., point sources) without any constraints or auxiliary information. In this case, despite having an excellent fit to the observations, the analytical model may be completely wrong. For example, a point-wise observation of ground displacement (e.g., by GPS) can be perfectly fitted by defining dislocation sources of the deformation field at each of the observation points, even though the physical sense of such a model is questionable. As a result, during the optimization one should be aware of possible model defects as well as observation defects, keeping in mind that the model with the best fit is not always the realistic solution. In the following, we use this property to assess the quality of the results and the models.

5.2.2 Sensitivity analysis of three different analytical models

The mutual effect of dislocation parameters and deformation field observations is studied by a model sensitivity analysis. A *sensitivity analysis* is herein referred to a study of the two-way relationship between observations and parameter variations that are related via an analytical model. Using a Taylor series in matrix format, equation (5.1) can be expressed as:

$$\hat{L} = G S \quad (5.4)$$

where $\hat{L} = L + v$ and $G = \partial F / \partial s$ is a coefficient matrix reflecting the model effect [Vanicek and Krakiwesky, 1982]. The relationship between a change in the parameters ΔS and a change in the observation ΔL is obtained from $\Delta L = G \Delta S$. Using the definition of the generalized inverse and norm for matrices, $\|\Delta S\| \leq \|G^{-}\| \|\Delta L\|$, where $\|G^{-}\|$ is inverse of G . Dividing both sides of the latest inequality by $\|\hat{L}\|$ yields a relation between parameters and observation relative error;

$$\frac{\|\Delta S\|}{\|S\|} \leq \|G\| \|G^{-}\| \frac{\|\Delta L\|}{\|\hat{L}\|} \quad (5.5)$$

where $\|G\| \|G^{-}\|$ is the condition number of the coefficient matrix (considering the Euclidean norm, the condition number is equal to the ratio of largest to smallest singular value). Equation (5.5) provides an upper bound for the relative error of the parameters or a lower bound for the relative error of the observations.

In other words, when the condition number is small, $\|\Delta S\| / \|S\|$ would be small if $\|\Delta L\| / \|\hat{L}\|$ is small, and, when the condition number is large, $\|\Delta S\| / \|S\|$ can be large even if $\|\Delta L\| / \|\hat{L}\|$ is small. Equation (5.5) shows that observation and parameter error influence each other and also that this mathematical relationship may play an important role in the propagation and estimation of the error. Knowing these interactions between the model, observations, and parameters, we examine the three aforementioned types of analytical dislocation sources having 4, 8, and 10 parameters to be resolved, respectively. For this purpose, we assume a reference state for the source parameters (Table 5.2) and study the effect of parameter fluctuations on observations through forward modeling. In order to simulate a realistic scenario and to compare the results to the real data sets in section 5, observations are displayed along

Line of Sight (LOS) of the ERS Radar satellite (descending orbit, incidence angle 23° , azimuth 190°) shown along an east-west profile in Figures (5.1-3). By choosing east-west profile we investigate the highest level of sensitivity which results from the satellite geometry. The reader can expect less sensitivity for directions other than the east-west one. In each panel, only one parameter is altered, and the rest are fixed at the reference value. The relative error of observation (reference value minus calculated value divided by reference value) is presented as a function of the parameter relative error and distance; i.e., a high percentage of relative change ($>50\%$) means high sensitivity of the parameters to observation fluctuation and vice versa.

Table 5.2. Parameters of three different deformation source-types (point, ellipsoidal, and rectangular) used in synthetic tests, after Mogi (1958), Yang (1998), and Okada (1985). X, Y = horizontal coordinates, $Depth$ = depth to source center (for Mogi and Yang sources) or depth to upper edge (for Okada source), $Vol. Ch$ = volume change for Mogi source, $Pr. Ch$ = pressure change for Yang source, Op = opening for Okada source, $Length$ = length of Okada plane, $Maj. Ax$ = major axis of Yang source, $Width$ = width of Okada plane, $Min. Ax$ = minimum axis of Yang source, Dip = dip angle for Okada plane or Plunge angle for Yang source, $Strike$ = strike angle of Okada plane or strike angle of Yang source major axis.

	X (km)	Y (km)	$Depth$ (km)	$Strength$ $Vol.Ch(km^3)$ $Pr.Ch(GPa)/Op(m)$	$Length Maj.Ax$ (km)	$Width Min.Ax$ (km)	$Plunge (^\circ)$	$Strike$ ($^\circ$)
MOGI (point)	0	0	5	0.01	-	-	-	-
YANG (ellipsoid)	0	0	5	0.01	2	1	45	45
OKADA (rectangular)	0	0	5	2	3	2	45	135

For a Mogi-type point source (Fig. 5.1), we find a direct relation between observation and parameter changes. A large change of location (X, Y, Z) and a large volume change (dv) causes large changes in the observation and vice versa. This effect is symmetric for Y, Z , and dv ; however, the effect for X appears distorted because of the observation geometry. We found an exception in the result for parameter X (Fig. 5.1a), where large alterations in the X coordinate (~ -5 km) did not influence the LOS observations at distances of about 1.8 km from origin. This poor interaction between the parameters and the observations is the result of a defect in the analytical model (poor condition number). In another exceptional behavior, observed in Figure (5.1c) where the interaction between parameter Z and observations is investigated, a positive depth alteration (i.e., shallower source) significantly influenced the observations located around the origin. This behavior is probably because of the invalidity of modeling shallow deformation sources as point sources, which can be categorized in terms of model deficiency. The sensitivity test of a Mogi source model thus suggests that, for reliable estimation of the parameter locations and volume changes, good coverage of the observation field is required in addition to precise and accurate observations.

For an ellipsoidal Yang-type source (Fig. 5.2), we show the sensitivity test for the eight source parameters. We find that most parameters show a direct and almost symmetric relation to observation error. Positive errors on depth lead to the same effect as positive errors on the depth of Mogi models which may imply that this model is valid for deep sources as discussed by Yang, et al. [1988]. In the case of the plunge and strike angle (Fig. 5.2g, h), a change of parameters by about 50% has very little effect on the near field observations. The plunge and strike angle can only be constrained by a few percent in the far field. The sensitivity test of the Yang-type source thus suggests that a very broad observation field is required to reliably estimate the ellipsoidal source parameters, including data from the near-field (to constrain location and strength) and the far-field (to constrain plunge and strike). Note that the definition of the ‘near field’ region is case dependent; for example, for a deeper source, this region will be broader than shown in this example.

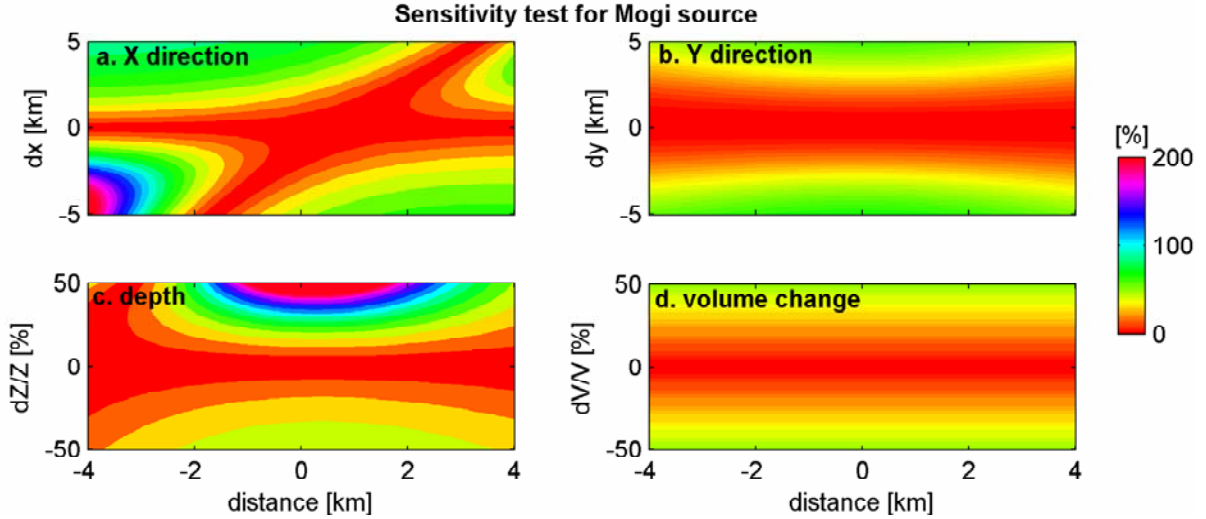


Figure 5.1. Sensitivity test of the Mogi-type dislocation source parameters to observed deformation perturbation in the LOS direction of ERS Radar images in descending mode. We considered a profile in the west-east direction and calculate the LOS observation due to relative changes of the selected source parameters. In each panel, the x-axis is the horizontal distance from the source, and the only parameter changed while the rest are fixed at the reference value (Table 5.2). Observation relative error is presented versus the relative error of the parameters at different distances (ordinate). Shown is the mutual effect of LOS displacement change and a) X coordinate perturbation, b) Y coordinate perturbation, c) source depth relative perturbation (over/under estimation), and d) source volume relative change (over/under estimation).

The sensitivity tests for a rectangular Okada-type source are shown in Figure (5.3). Considering only opening mode dislocations leaves us with 8 parameters to be tested for sensitivity. The situation is generally similar to the above described Yang-type source, showing a symmetric and direct relationship between the observation and parameter error. The parameter width W (Fig. 5.3e) shows a small sensitivity to LOS observation. For the chosen simulations, the strike angle has no effect on the near field observation. The sensitivity test for the Okada plane thus shows that good sensitivity is obtained for the coordinate, length, opening, and dip angle parameters. Moreover, it suggests that both good coverage and observation accuracy are necessary for reliable estimate the source parameters. The parameters width and strike cannot be resolved uniquely unless additional datasets (such as far field geodetic or seismic data) are included.

Considering the three sensitivity tests, we can summarize that the source parameters are affected differently by the precision and spatial distribution of the observations, which are important in qualifying the result. In the sensitivity test, the influence of the observation precision could be drawn by considering equation (5.5), where observation precision (ΔL) is related to parameters error (ΔS). By having high precision observation (small ΔL) we are able to constrain slight changes in parameters (small ΔS), even though the problem is governed by poor condition number. For reliable and precise source inversion, therefore, good coverage including both near- and far-field data is necessary in order to obtain adequate sensitivity. On the other hand, increasing the number of data, e.g., by considering two satellite viewing geometries (e.g., ascending and descending) may only lead to somewhat improved results and may leave some of the model parameters non-unique (see electronic appendix). With this knowledge of the limitation of simple analytical models, we are able to test the influence of different inversion algorithms on source parameter estimation in the following section.

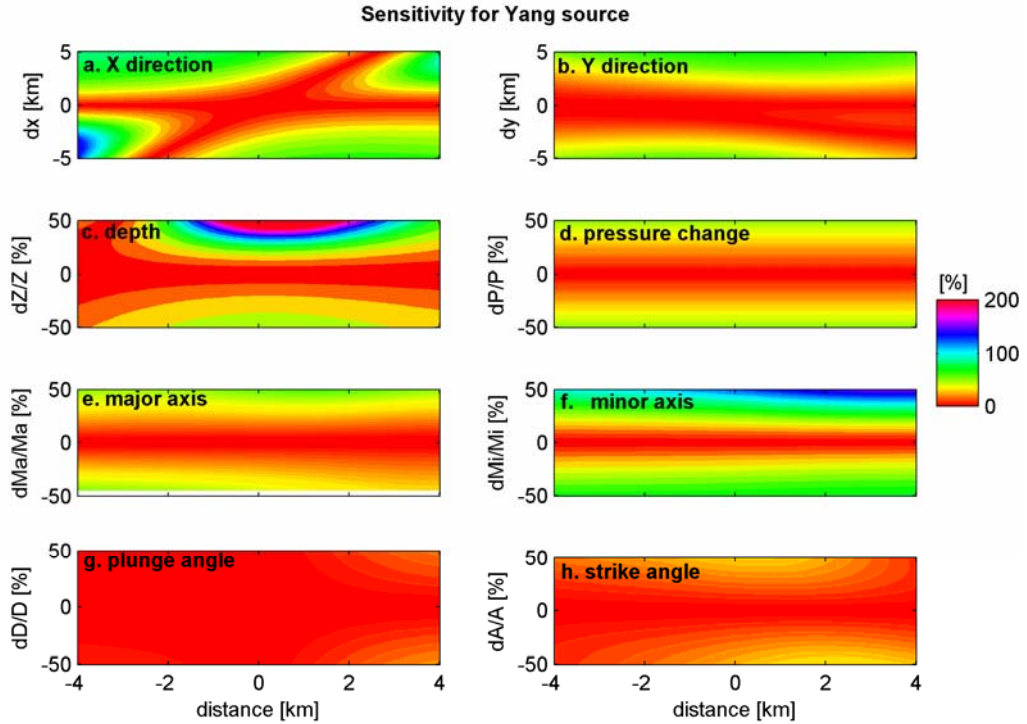


Figure 5.2. Sensitivity test of the Yang-type source parameters and observed deformation perturbation in the LOS direction of ERS Radar images in descending mode. Profile in the west-east direction shows LOS observation for the parameters given in Table 5.2. In each panel, the x-axis is horizontal distance from the source, and all parameters but one are fixed at the reference value; i.e., the graphs show relative changes with respect to the reference situations. Shown is the interaction of the LOS displacement relative change and a) X coordinate perturbation, b) Y coordinate variations, c) source depth relative undulation (over/under estimation), d) source pressure relative change (over/under estimation), e and f) source semi-major/minor axis relative variations, g and h) source plunge/strike angle relative perturbation

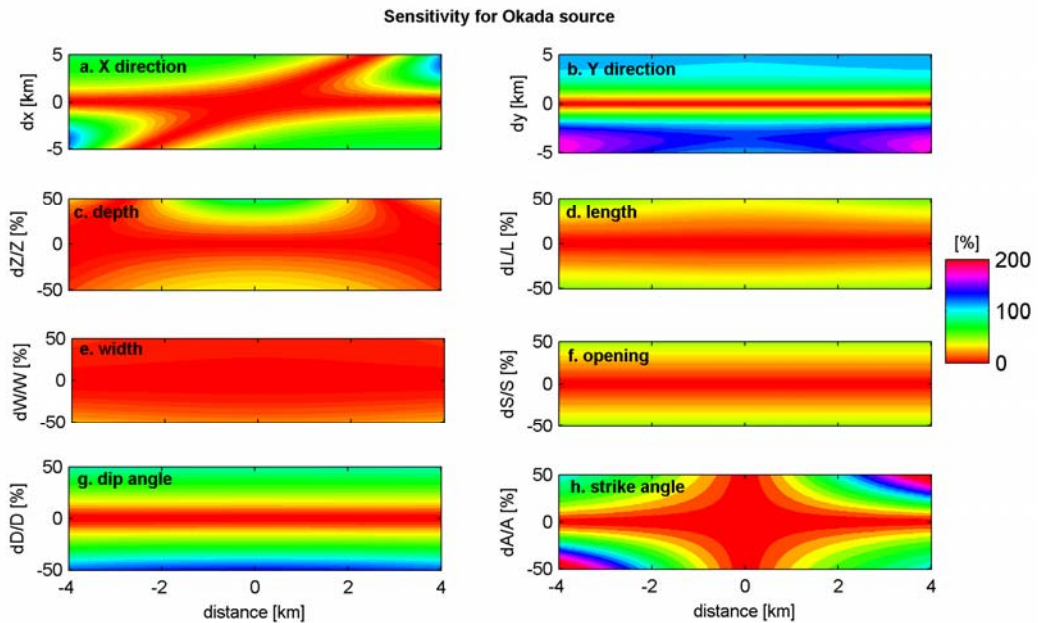


Figure 5.3. Sensitivity test of the Okada-type source parameters and observed deformation. Profile in the west-east direction shows the LOS observation for the parameters given in Table 5.2. In each panel, the x-axis is the horizontal distance from the source center, and all parameters but one are fixed at the reference value, i.e., graphs show relative changes with respect to the reference situations.

Shown is the interaction of the LOS displacement change and a) X coordinate perturbation, b) Y coordinate perturbation, c) Source depth relative undulation (over/under estimation), d) Source length relative perturbation, e) Source width relative perturbation, f) Source opening relative perturbation, g and h) Source dip/strike angle relative perturbation.

5.3 A comparison of sophisticated optimization methods

In the case of early warning and semi-real time hazard assessment of crustal deformation activities, a fast and reliable evaluation of deformation sources is very important. Considering this demand, an inversion tool that is gradient free (i.e., free from initial values), reliable, efficient, and flexible enough to include other complementary information is required. Over the past almost 30 years, the optimization methods Simulated Annealing (SA) and Genetic Algorithm (GA) have been used with increasing frequency for data inversion purposes (Table 5.1). This is because SA and GA are gradient free (i.e. free from initial value), which is important for fast source assessment (case for early warning systems), and because of their success in solving a large variety of optimization problems in different branches of the geosciences [Sambridge and Mosegaard, 2002]. Apart from those optimization methods addressed in Table (5.1), recently many other novel optimization methods have emerged. However, among all, the so called Covariance Matrix Adoption Evolutionary Strategy (CMA-ES), which is a stochastic method for optimization of non-linear and non-convex functions is showing merits for solving optimization equations with few (<100) number of parameters [Igel et al., 2007]. However, the choice of initial parameters play a significant role for the success of this method. Moreover, the diversity of the search operator to explore the search space critically depends on the settings of the normal distribution function, which often is problem dependent.

In the next section, we briefly explain the concepts and disadvantages of these two most commonly used optimization methods, GA and SA and then propose an improved algorithm that allows joint estimation of the uncertainty of the parameters. The proposed algorithm may be applied to other optimization methods as well.

5.3.1 Simulated Annealing (SA)

This Simulated Annealing (SA) algorithm is motivated by an analogy to annealing in solids [Metropolis et al., 1953], which has been applied to optimization problems for the last 25 years [Kirkpatrick et al., 1983]. Generally, SA starts with a random initial value of parameters, with an associated score based on the cost function, and a *cooling schedule* that includes the initial temperature, the reduction rate of temperature, the number of generated events at each temperature, and a final temperature to stop the algorithm [Kirkpatrick et al., 1983]. A commonly used cost function has been presented in equation (5.3). The orders of major steps in SA are introduced by different temperatures. At each temperature, small random changes are added to the parameters, and the resulting change in cost (Δc) is computed. If $\Delta c \leq 0$, the change is accepted; otherwise, the change is treated probabilistically. The Probability Density Function (PDF) of Δc at the current temperature T , with the Boltzmann coefficient K_B , is $PDF(\Delta c) = e^{-\Delta c / K_B T}$ [Kirkpatrick et al., 1983]. If $PDF(\Delta c)$ is greater than a random number uniformly selected in the interval (0,1), then the change is accepted.

The success of SA at finding a global solution critically depends on the cooling schedule [Basu and Frazer, 1990; Cervelli et al., 2001a; Rothman, 1985]. Although a slow cooling schedule at the expense of computation time might be useful, the difficulty is that the cooling schedule is substantially problem-dependent, and it seems impracticable to develop a global remedy for all problems. For overcoming those limitations, SA is sometimes combined with other optimization techniques [Cervelli et al., 2001a]. Another shortcoming is that an estimation of the parameters' quality is missing.

5.3.2 Genetic Algorithm (GA)

The Genetic Algorithm (GA) was introduced by [Holland, 1975], and further improved by many subsequent workers [Davis, 1987; Goldberg, 1989; Rawlins, 1991; Whitley, 1994] that have provided comprehensive summaries on the theory and applications.

In the basic form of GA [Holland, 1975], a key aspect is the binary encoding of the parameters. The search begins by defining a cost function and initializing the GA parameters, and it ends when a stopping criterion, such as the defined number of iterations, is reached. GA always deals with a set of solutions without any special emphasis on a particular solution. So, if the initial population consists of m independent solutions, each solution includes n variables, and each variable can be presented by q bits, then the initial population is constructed randomly by $n \times (m \times q)$ zero/ones. To evaluate the cost function, we need the decimal values of the variables obtained by [Haupt and Haupt, 2004]:

$$p_q = \sum_{i=1}^q g(i)2^{-i} + 2^{-(i+1)} \quad (5.6)$$

$$p = p_q(u_b - l_b) + l_b \quad (5.7)$$

where l_b and u_b are lower and upper limits and p is the corresponding decimal value of the binary variable g . Because in many problems we have prior knowledge about the variables, equations (5.6) and (5.7) allow entering this kind of auxiliary information into an inversion procedure by setting the limits for the variables during decoding.

During the algorithm progress, the initial population is subject to several random changes but systematically approaches the best solution among many investigated solutions. Selection, Pairing, Mating, and Mutation are major GA operators that allow modification of the population to explore solution space, and they are thoroughly explained in the literature [Holland, 1975; , 1992; Michalewicz, 1994].

Despite remarkable successes in solving very complex optimization problems, GA does not provide any information about the quality of the result. Some researchers have implemented approaches to estimate a symmetric PDF of the model variables after optimization [Zhou *et al.*, 1995]. However, the assumption of symmetry is true only when the relation between the observation and model parameters is linear. In another work, Carbone *et al.* [2008] used the approach presented by Deb *et al.* [2000] to estimate a confidence region for parameters free of any primary PDF assumptions. Quality estimation in this approach relies on the inversion residuals. The success of this approach depends on the freedom of the search operator to explore the vicinity of the optimum solution. Therefore, mutation rate and population size may play a significant role in the reliability of the result. Additionally, these approaches do not consider the effect of a model on the optimization result. Therefore, careful assessment of the result quality is still missing.

In brief, the main shortcomings of the SA and GA are; a) getting trapped in local minima and b) lack of estimation of the quality of the parameters. Therefore, in the following, we introduce and test the hybrid *Randomly Iterated search (RI) and Statistical Competency (SC)* approach.

5.3.3 Randomly iterated search (RI)

In order to diminish the importance of the cooling schedule (case for SA) and to increase the freedom of the search algorithm to explore the solution space (case for SA and GA), which is a necessity in statistical approaches for estimating the confidence interval, we present and apply a Randomly Iterated Search. The idea is to repeat the optimization with different initial random values in order to begin the search from a starting point close to the global solution. Here, we explain a combination of a Randomly Iterated Search (RI) with SA. Via synthetic test, we show the improvement of RI-SA compared to the standard SA. We then compare our random approach to the standard SA presented by Kirkpatrick *et al.* [1983]. Both algorithms are initialized with the same cooling schedule. As shown in Figure (5.4), the cost function is a mathematical function including many local minima, but only one global minimum of 0 at coordinate (0, 0). Using the coordinates (0.6, 0.6) as a starting point, Figure (5.4c) shows the trace of the standard SA that is searching for a global minimum but ultimately misses it and converges to a local minimum at coordinate (1, 1). In contrast, the RI-SA (Fig. 5.4d) initiates at

various random starting points (here 20, Figure 5.4d) with the same cooling schedule and finally converges to the global minimum even in this difficult synthetic test. Thus, RI-SA is able to find a global solution, while the other solutions in its vicinity can be used for qualifying the solution as detailed below.

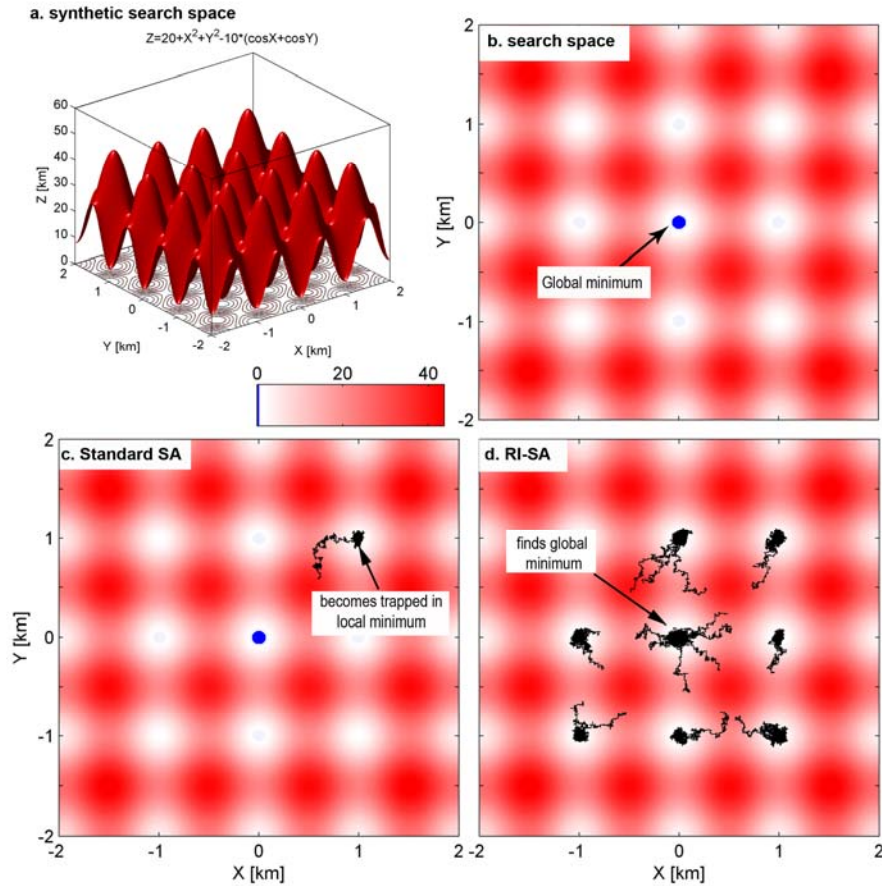


Figure 5.4. Synthetic search space to test local and global minima trapping and advancements of the RI approach. Standard SA and Randomly Iterated (RI) SA are both initialized with the same cooling schedule. a) 3D mesh of the synthetic search surface which has many local minima but only one global minimum of 0 at (0, 0), b) plan view of the search space; the global minima is depicted by blue point and color (see color bar), c) the trace of a standard SA test is converging to a local minima at (1, 1) and fails to find the global minimum, d) the trace of RI-SA is initialized iteratively at random starting points and finally finds the global minimum.

5.3.4 Statistical Competency (SC)

To test the Statistical Competency (SC) of the result of the SA, the optimization algorithm may be repeated p times starting from p initial points $\{I_1, I_2, \dots, I_p\}$ selected randomly between a lower and upper limit. These limits can be specified based on auxiliary information provided by other disciplines such as geologic measurements or earthquake hypocenters. Note that theoretically, the auxiliary information only facilitates the speed of convergence but will not affect the final result. In the RIS-SA, we save all acceptable solutions with their associated cost. After sorting acceptable solutions based on increasingly cost value in each repetition, we select the $q_i (i:1 \dots p)$ best solutions to yield p subsets $\{S_1\}, \{S_2\}, \dots, \{S_p\}$ with an average cost of $\mu_{s_i} (i:1 \dots p)$ as representative. The threshold can be specified either as a certain portion of the observations, based on the chosen cost function, or simply as a random number. The solution with the minimum cost among the subsets approaches the global solution μ . Each representative has a standard deviation σ_{s_i} and $E\{\mu_{s_i}\} = \mu$ (E is expectation

operator). In order to construct a confidence interval for μ when the variance is unknown, we may utilize the following statistic [Vanicek and Krakiwesky, 1982]:

$$\frac{\mu_{s_i} - \mu}{\sigma_{s_i} / \sqrt{q_i}} \quad (5.8)$$

Equation (5.8) has a t-distribution function [Vanicek and Krakiwesky, 1982], and, by specifying a significance level α (or confidence level, $1 - \alpha$), the confidence interval for μ can be expressed as:

$$\mu_{s_i} - \frac{t_{\alpha/2, (n-m)}}{\sigma_{s_i} / \sqrt{q_i}} \leq \mu \leq \mu_{s_i} + \frac{t_{\alpha/2, (n-m)}}{\sigma_{s_i} / \sqrt{q_i}} \quad (5.9)$$

If this test fails, the solution is rejected. If this test is accepted, the solution in the vicinity of the best solution is used to construct the confidence interval. After testing all solutions in equation (5.9), the accepted solutions contain a confidence interval for unknowns and thus allow evaluation of the result. The same successful approach can be also applied to other algorithms, as detailed in the following for GA.

To achieve a Statistical Competency (SC) test of the result of GA, we consider a large population size with random members for optimization in p iterations (Randomly Iterated Search (RIS)) and select $q_i (i:1 \dots p)$ to be the best solutions in each generation. After satisfying the stopping criteria, there are p sets: $\{S_1\}, \{S_2\}, \dots, \{S_p\}$. Each set has q_i chromosomes with an average cost of $\mu_{s_i} = (i:1 \dots p)$ as a representative. The solution with minimum cost among all the subsets is termed μ . Then, each μ_{s_i} has a standard deviation σ_{s_i} and $E\{\mu_{s_i}\} = \mu$. The rest of the algorithm to build up a confidence interval is comparable to equations (5.8) and (5.9). One should note that the statistics is built upon the residuals after evaluating in the cost function (equation 5.3), and the required independency for the t-distribution is preserved by a random error tainted the observations. However, to assure this independency and preserve diversity of the solutions in the vicinity of the global solution the mutation rate should be large enough (>0.5) and repeated generations are eliminated from each sets. In summary, for both RISC-SA and RISC-GA, we simultaneously consider the effects of observation variance via a weight matrix and observation blunder, together with model deficiencies through defined statistics. In the next section, we shall show that the solution is precise (with small dispersion around the average) and accurate (the average is close to the true value).

5.4 Application to synthetic InSAR data

The reliability and efficiency of the described optimization techniques are first investigated in synthetic tests (section 5.4) and then applied to real observations (section 5.5). To organize the simulated data sets, we consider the same source types as in the sensitivity tests of section (5.2) (point, ellipsoidal, and rectangular source). In reality, observations are tainted by different random and systematic errors, but, in the current test, we assume that the observations are free of systematic errors. To consider the effect of random noise, we add a normally distributed component with a variance of 0.5 cm to the observation. This variance is comparable to the real variance of modern radar interferometric methods [Berardino *et al.*, 2002]. Figure (5.5) shows a synthetic surface deformation at 5000 randomly distributed points calculated for a point source (Mogi, Figure 5.5a), an ellipsoidal source (Yang, Figure 5.5b), and a rectangular source (Okada, Figure 5.5c). We invert these three data sets using the inversion algorithms detailed in section 5.3 and discuss the results. The MATLAB script utilized for this test can be found in the electronic data supplement.

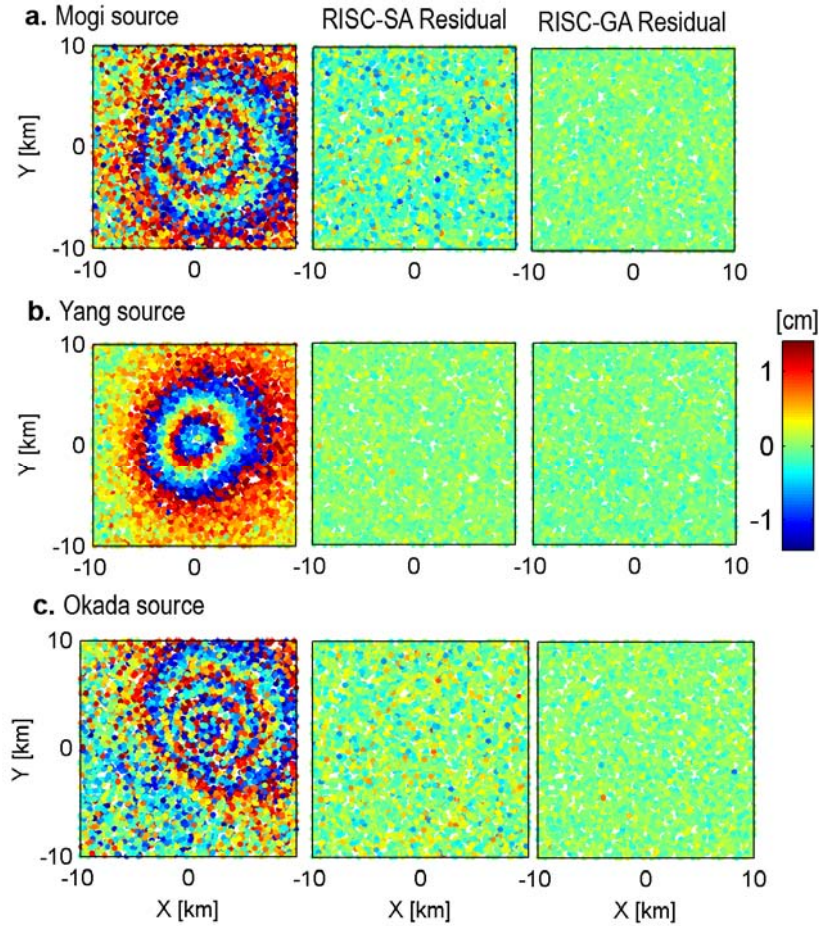


Figure 5.5. Synthetic test to show the reliability and efficiency of the Randomly Iterative Search and Statistical Competency (RISC) SA and GA and to compare their result. Source parameters are given in Table (5.2) for three different source-types. The observations are in the LOS direction of the descending ERS radar images, and a noise component was added with normal distribution (0, 0.6). Left column shows the models, center column shows the residuals of the RISC-SA, and the right column shows the residuals of the RISC-GA. a) Mogi type source deformation field, b) Yang type source deformation field, and c) Okada type source deformation field.

For the Mogi model (Fig. 5.5a), we run the optimization algorithm in a limited search space to explore the solution area. This information can be obtained either from other disciplines like geological and seismological data or from some trade-off free equations that give a rough estimate of the parameters directly from the observed displacement field. Here, we estimate the relation between volume change occurring at the source in elastic half-space (Poisson ratio of 0.25), and observed LOS displacement with an incidence angle $\theta = 23^\circ$ for a Mogi source according to (see electronic appendix for mathematical proof):

$$\Delta v = 0.72 \iint_{R^2} LOS dx dy \quad (5.10)$$

Equation (5.10) is independent of the source depth and provides an estimate of the volume change based on LOS observations. In a real case, we would have access only to a small part of the displacement field; hence, this estimate might be considered as a lower limit for the volume change in the optimization process.

Based on equation (5.10), the approximate volume change is $6 \times 10^{-3} \text{ km}^3$. The RISC-SA parameters are initiated with a starting temperature of 1, temperature reduction of 0.5, maximum iteration and maximum success in each temperature of 500 and 200, respectively, and a final temperature of 10^{-10} . The RISC-GA parameters are initiated with an initial population size of 40, mutation rate of 0.5, selection rate of 50%, and number of iterations of 100. The results of the RISC-SA and GA are shown in Table (5.3) and Figure (5.5). The two inversion algorithms produce the original observation almost

perfectly, and residuals are in a range of about ± 6 mm. We observe a slight difference between the estimated confidence intervals, which are systematically narrower for the RISC-SA than for the RISC-GA. This means that either the precision of the RISC-SA result is higher than RISC-GA or the freedom of RISC-SA to explore the vicinity of the global solution is lower than RISC-GA, but, when considering the amount of observation noise, both of them are reliable and hence acceptable. To compare the computation duration, we tested all calculations in this paper using MATLAB 7.1 software in a standard windows XP platform and a 3.4 GHz processor. The computation times are summarized in Table (5.4) and show that RISC-GA is efficient and able to treat large or even full data sets.

Table 5.3. Inversion results of the synthetic deformation field. Estimated parameters of three source-types (Mogi, Yang, and Okada). The confidence regions are calculated at the 95% confidence level

	Parameter	Simulated Algorithm		Genetic Annealing	
		Inversion Result	Confidence interval (95%)	Inversion Result	Confidence interval (95%)
MOGI	X (km)	-0.02	(-0.14, 0.16)	0.33	(-0.72, 0.12)
	Y (km)	-0.04	(-0.26, 0.29)	-0.02	(-0.39, 0.45)
	Depth (km)	5.05	(-0.32, 0.34)	4.93	(-0.32, 0.64)
	Volume Change (km ³)	0.0101	(-0.0009, 0.0009)	0.0099	(-0.0016, 0.0023)
YANG	X (km)	0.05	(-0.44, 0.05)	0.14	(-0.57, 0.34)
	Y (km)	-0.08	(-0.31, 0.43)	0.18	(-0.58, 0.4)
	Depth(km)	4.84	(-0.33, 0.41)	4.95	(-0.2, 0.53)
	Pressure Change (GPa)	0.0138	(-0.0065, 0.0007)	0.0078	(0, 0.0102)
	Major Axis (km)	1.90	(-0.37, 0.45)	2.18	(-0.41, 0.01)
	Minor Axis (km)	0.88	(-0.005, 0.23)	1.06	(-0.4, 0)
	Plunge (°)	46.48	(-10.23, 6.57)	43.33	(-8.96, 11.51)
OKADA	Strike (°)	51.31	(-12.08, 2.13)	43.09	(-5.32, 13.28)
	X (km)	0.23	(-0.74, 0.13)	0.10	(-0.51, 0.2)
	Y (km)	0.12	(-0.43, 0.17)	0.08	(-0.36, 0.3)
	Depth (km)	4.83	(-0.18, 0.31)	5.1	(-0.64, 0.1)
	Opening (m)	1.98	(-0.03, 0.03)	1.99	(-0.04, 0.02)
	Length (m)	3.02	(-0.23, 0.09)	2.96	(-0.26, 0.15)
	Width (m)	2.01	(-0.3, 0)	2.01	(-0.4, 0.09)
	Dip (°)	50.01	(-8.69, 1.53)	43.11	(-3.64, 9.01)
Strike (°)	139.38	(-18.94, 0)	132.65	(-6.63, 7.25)	

Table 5.4. Comparison of the computation time for the synthetic test using RISC-SA and RISC-GA

Source type	RISC-SA CPU-time (sec)	RISC-GA CPU-time (sec)
MOGI	832	38
YANG	1520	393
OKADA	3982	832

For the ellipsoidal Yang source, we have implemented exactly the same parameters as before and show the inversion results in Table (5.3) and Figure (5.5b). Although we added a high amount of noise, the results are considered to be quite good and are close to the initial model value (Table 5.3). Additionally, the inversion residuals are within the range of the observation noise. Although we are considering a broad deformation area (sides are 10 times the Yang semi-major axis), the confidence length of the plunge and strike angle is considerably larger than the others, which shows the high uncertainty in estimating these parameters.

In the third synthetic test, we inverted the surface deformation field caused by a rectangular dislocation source. The results are shown in Table (5.3) and Figure (5.5c). Although the inversion model reproduces the actual observation well and the inversion residuals are in the range of the observation noise, the uncertainty of the strike angle and width is clearly larger than the others.

To summarize after these three tests: 1) both RISC-algorithms can retrieve the initial model almost perfectly, even with the addition of high noise, 2) the presented algorithm for simultaneous confidence interval estimation works properly in both algorithms, and 3) for equal conditions, RISC-GA appears

to be more efficient in terms of computation time. In the following, we use a real database from one of the most actively deforming volcanic system.

5.5 Application to real InSAR data from the Campi Flegrei caldera volcano

Campi Flegrei (CF) is a caldera with a long documented history of unrest, and it is also in one of the most densely populated regions in Italy, including part of the city of Naples, with about one million inhabitants. The historical period of deformation at CF last culminated in 1158 and in 1538 A.D. [Bodnar *et al.*, 2007]. The dominant type of historical deformation in CF is subsidence, at a rate of 1.5-1.7 cm/yr with occasional periods of uplift [Troise *et al.*, 2007]. The last major periods of uplift occurred in 1969-1972 and 1982-1984 [Barberi *et al.*, 1984] and have been observed by triangulation and trilateration networks [Troise *et al.*, 2007]. After the development of space geodetic techniques, especially InSAR, the monitoring value of measuring deformations broadly increased. Subsidence at CF was already detected by InSAR method by Avallone *et al.* [1999], who observed subsidence of up to 2.5 cm/yr in the period 1993-1996. By using a gradient-based inversion method for an inflating Mogi-type point source, the same authors estimated the depth of the deformation source to be around 2.7 km. Lundgren, *et al.* [2001] studied a longer InSAR time series and found continuing subsidence in the period 1993-1998. The estimated mean subsidence rate in this period is about 3.5 cm/yr [Lundgren *et al.*, 2001]. To assess the source of the deformation, Lundgren and colleagues implemented a Levenberg-Marquardt nonlinear global optimization algorithm and investigated parameters of three different volcanic deformation sources (Mogi, Yang, Okada). They found source depths of about 2.5-3.0 km. Subsidence continued until 2000 and then changed to uplift, as shown by Lanari *et al.* [2004]. To model the source of deformation, they adapted a nonlinear least squares inversion for ellipsoidal (Yang) and rectangular (Okada) source parameters in an elastic homogeneous half-space and estimated a magma chamber depth of about 2.7-3.0 km. In other studies, such as Troise *et al.* [2007], Battaglia *et al.* [2006], and Gottsmann *et al.* [2006], different kinds of geophysical observations and inversion methods, such as gradient-based approaches for source parameters in an elastic homogeneous half-space, have been applied and estimated the deformation source similarly to be at a depth of about 2.5-3.0 km. In a recent study, Amoruso *et al.* [2002] discussed another uplift period lasting from 2004-2006 and modeled this phenomenon in a horizontally layered half space. They obtained an estimate of 3.5 km depth for a crack type deformation source.

However, seismic studies suggest a more complex story about the 3D location of the hydrothermal and magma chamber. Based on the seismic tomography, two low velocity zones can be inferred at depths of 2.7 km and 7.5 km [Zollo *et al.*, 2008]. The shallower zone might be interpreted as a thermo-metamorphic rock assembly, while the deeper one is interpreted as a magma body with an area of less than 30 km² and thickness of 1.2- 1.5 km [Zollo *et al.*, 2008].

In the following, we test the two improved RISC methods on the episodes of uplift (2000-2001) and subsidence (2001-2002). Utilizing both Genetic Algorithm and Simulated Annealing, we estimate the deformation source parameters as well as their uncertainty.

5.5.1 Data set

The data set used here is extracted from the geodetic time series obtained by a Small Base Line Subset (SBAS) approach for measuring ground displacement using differential SAR interferometry [Lanari *et al.*, 2004]. This SBAS technique selects data pairs with a small baseline to establish differential interferograms for achieving time series analysis. The advantages of this method are in overcoming spatial decorrelation and in eliminating atmospheric artifacts, as detailed in Berardino *et al.* [2002].

The time series of a long period of subsidence from 1992 until 2002, with a cumulative displacement of 25 cm in the center of the caldera, was presented by Berardino *et al.* [2002]. The subsidence episode reversed into uplift in 2000. The uplift episode lasted one year, accumulating about 4 cm of displacement. Another subsidence episode followed in 2001 and continued to the end of the time span considered here. We now compare the source parameters of the 1 year uplift and 1 year subsidence

periods and consider observation error and model deficiency. We calculate a confidence interval for all parameters as well as their best estimates.

5.5.2 Model uplift period 2000-2001

To initialize RISC-SA and RISC-GA, we follow the same procedure as detailed in the synthetic simulations in section 5.4 and define upper and lower bounds in search space. For both deformation periods (uplift and subsidence) and for all types of model sources, the considered bounds of depth range is assumed to be somewhere between 2 and 5 km, as suggested in previous publications (e.g. [Battaglia *et al.*, 2006; De Natale *et al.*, 1997]). Equation (5.10) allows us to estimate the lower bound of the volume change, which is $5 \times 10^{-4} \text{ km}^3$. The Mogi-type source volume change lies between 5×10^{-4} and $5 \times 10^{-2} \text{ km}^3$, and the horizontal location could be at any point in the observation plane. Tables (5.5, 6) summarize the results and computation times for RISC-SA and RISC-GA, and a graphical representation is given in Figure (5.6). The Root Mean Square Error (RMSE) for both methods is about 0.3 cm (i.e. similar to observation error) and shows that the model reproduces the observations very well. The depth and volume change differ slightly in RISC-SA and RISC-GA. However, considering their confidence intervals, we note that both inversions are consistent, covering a similar range of uncertainty.

The second source is a Yang-type. As in the previous case, we start with a broad bound for the parameters, with an assumed pressure bound between 0 and 0.01 GPa, a semi-axis between 0 and 3 km, a dip angle between 0 and 90 degrees, a strike angle between 30 and 150 degrees, and the horizontal location at any point in observation plane. The RMSE for both RISC-SA and RISC-GA is again about 0.3 cm, which shows that the models precisely reproduced the observation field. The best fitting source is elongated east-west, and the estimated depth is in the range of 2.5 - 3.3 km.

As a third model, we consider an Okada-type source. The model parameters are bound by a 0-2 km length and width, a 0-90 degrees dip, a 30-150 degrees strike, and a 0-2 m opening. Again, this source model can reproduce the deformation field very well, with an RMSE below 0.3 cm. The Okada source is elongated east-west, and the associated depth varies between ~2.4 km and ~3.3 km.

Table 5.5. Inversion results of the uplift at Campi Flegrei observed by InSAR over the period 2000-2001. Parameters of three source-types (Mogi, Yang, and Okada) are estimated. The confidence regions are calculated at the 95% confidence level

2000-2001 uplift period					
	Parameter	Simulated Algorithm		Genetic Annealing	
		Inversion Result	Confidence interval (95%)	Inversion Result	Confidence interval (95%)
MOGI	X (km)	426.20	(-0.1, 0.08)	426.22	(-0.36, 0.24)
	Y (km)	4519.45	(-0.41, 0.31)	4519.65	(-1.34, 0)
	Depth (km)	2.41	(-0.3, 0.31)	2.29	(0, 0.92)
	Volume Change (km^3)	0.00091	(-0.0002, 0.0003)	0.00073	(0, 0.0007)
YANG	X (km)	426.05	(-0.3, 0.29)	426.54	(-1.42, 0)
	Y (km)	4519.80	(-0.58, 0.37)	4519.66	(-0.74, 0.57)
	Depth(km)	2.84	(0, 0.5)	2.89	(-0.36, 0.4)
	Pressure Change (GPa)	0.00074	(0, 0.0009)	0.00069	(0, 0.0047)
	Major Axis (km)	2.68	(-0.75, 0.08)	2.77	(-0.52, 0.02)
	Minor Axis (km)	1.43	(-0.18, 0.01)	1.46	(-0.81, 0)
	Plunge ($^\circ$)	82.40	(-14.47, 0)	87.98	(-19.13, 0)
Strike ($^\circ$)	91.71	(-0.14, 21.49)	113.39	(-22.12, 0)	
OKADA	X (km)	426.16	(-0.96, 0)	425.86	(-0.31, 0.63)
	Y (km)	4518.17	(-0.9, 1.17)	4518.47	(-0.85, 0.53)
	Depth (km)	3.26	(-0.88, 0)	3.02	(-0.47, 0.09)
	Opening (m)	1.08	(-0.45, 0)	0.84	(-0.12, 0.8)
	Length (m)	0.44	(0, 0.52)	0.69	(0, 0.89)
	Width (m)	1.45	(0, 0.22)	1.51	(-0.69, 0.04)
	Dip ($^\circ$)	62.39	(-3.15, 20.87)	76.29	(-37.62, 0)
Strike ($^\circ$)	103.86	(-32.34, 0)	118.52	(-43.91, 0)	

Table 5.6. Comparison of the computation time for inverting the uplift period deformation date set using RISC-SA and RISC-GA

Source type	RISC-SA CPU-time (sec)	RISC-GA CPU-time (sec)
MOGI	283	13
YANG	677	26
OKADA	1354	51

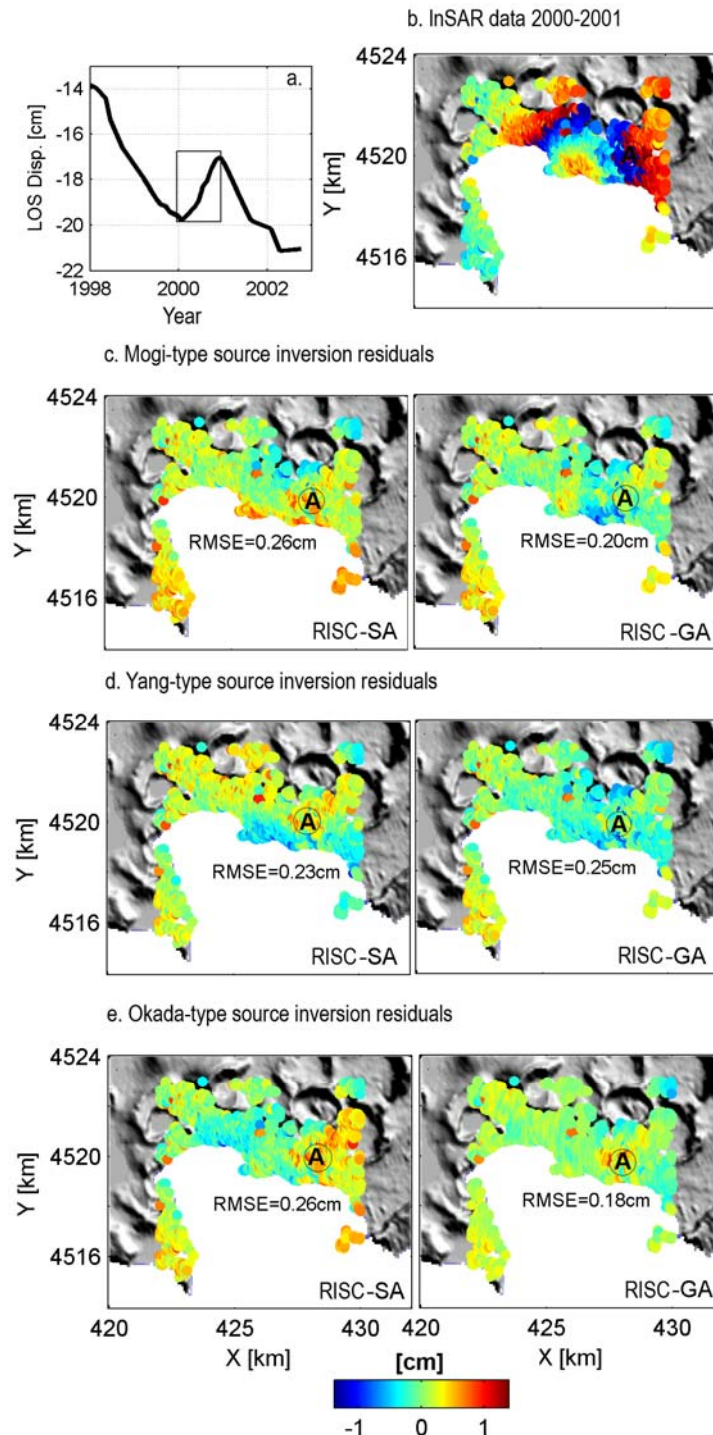


Figure 5.6. Application of the algorithm to real data from Campi Flegrei caldera, Italy. a) A period of uplift occurred from 2000-2001 and is tested herein. b) Uplift observation in the LOS direction of ERS Radar images in descending mode wrapped into 2.8 cm fringes, c) residuals for Mogi-type source inversion by RISC-SA and RISC-GA, d) residuals for Yang-type source inversion, and e) residuals for Okada-type source inversion. All source-types provide very good solutions with residuals below 1 cm. (A = the location of local hydrothermal activity in Solfatara)

5.5.3 Model subsidence period 2001-2002

To initiate RISC-SA and RISC-GA, we considered a bound between 5×10^{-4} - 5×10^{-2} km³ for a Mogi-type volume change, and the whole observation plane for horizontal location. The results are provided in Table (5.7) and Figure (5.7). The RMSE is about 0.5 cm; thus, the model well reproduces the InSAR observations. Because the numbers of observation points and optimization parameters are exactly the same as for the uplift case, the computation times remain similar. We use similar parameter bounds as in the above described inversion method of the subsidence scenario.

The estimated depth for the source is between ~ 2.1 and ~ 2.4 km for RISC-SA and between ~ 2.2 and ~ 2.8 km for RISC-GA, while the optimum solution is found at 2.3 km depth for both.

The RMSE for the Yang-type is larger than for the Mogi-type source, which may be due to the low sensitivity of the source parameters (section 5.2). The Yang source is elongated east-west and the depth range is ~ 2.4 ~ ~ 2.9 km for both RISC-SA and RISC-GA. Comparing this depth with the uplift, the inversion suggests that the source is shallower than for the inflation period.

The Okada-type results show a better fit than those for the Yang-type source because of the higher sensitivity of the Okada parameters. The estimated depth for RISC-SA is between ~ 2.2 and ~ 3.0 km and between ~ 2.3 and ~ 3.1 km for RISC-GA.

5.6 Discussion

In a sensitivity test, we investigated the influence of an analytical model on the quality of the inversion result. We find that a poor analytical model may lead to unreliable results. Devising a gradient-free, fast and reliable optimization method, which is necessary for semi-real time hazard assessment, we consider two sophisticated optimization approaches, simulated annealing (SA) and genetic algorithm (GA). We utilize their advantages and suggest a method to overcome their disadvantages, by including a hybrid randomly iterated search and statistical competency approach (RISC). To show the reliability and efficiency of the RISC-approach, we performed synthetic and real case tests. In the following, we discuss different theoretical and practical aspects of the presented approach.

Table 5.7. Inversion results of the subsidence at Campi Flegrei observed by InSAR over the period 2001-2002. Parameters of three source-types (Mogi, Yang, and Okada) are obtained. The confidence regions are calculated at the 95% confidence level

2001-2002 subsidence period					
	Parameter	Simulated Algorithm		Genetic Annealing	
		Inversion Result	Confidence interval (95%)	Inversion Result	Confidence interval (95%)
MOGI	X (km)	426.54	(-0.05, 0.05)	426.57	(-0.46, 0)
	Y (km)	4519.34	(-0.23, 0.27)	4519.80	(-0.76, 0.15)
	Depth (km)	2.31	(-0.2, 0.12)	2.32	(-0.12, 0.53)
	Volume Change (km ³)	-0.00106	(-0.0002, 0.0002)	-0.00097	(-0.0006, 0)
YANG	X (km)	426.03	(-0.35, 0)	426.31	(-0.25, 0.47)
	Y (km)	4518.51	(0, 0.14)	4519.53	(-0.75, 0)
	Depth(km)	2.41	(0, 0.15)	2.38	(0, 0.52)
	Pressure Change (GPa)	-0.00224	(-0.0036, 0)	-0.00305	(-0.0023, 0)
	Major Axis (km)	2.43	(0, 0.45)	2.09	(0, 0.38)
	Minor Axis (km)	1.00	(-0.39, 0)	0.73	(-0.08, 0.23)
	Plunge (°)	63.50	(0, 11.61)	88.38	(-23.24, 0)
OKADA	Strike (°)	117.73	(-23.05, 0)	111.88	(-17.19, 0)
	X (km)	426.42	(-0.19, 0.2)	426.44	(-0.49, 0.16)
	Y (km)	4519.04	(-0.56, 0.33)	4518.97	(-0.88, 0)
	Depth (km)	2.66	(-0.43, 0.31)	2.88	(-0.56, 0.22)
	Opening (m)	-1.51	(-0.36, 0.49)	-1.49	(-0.14, 0.4)
	Length (m)	0.98	(-0.41, 0.27)	0.86	(-0.07, 0.35)

	Width (m)	0.53	(0, 0.3)	0.70	(0, 0.31)
	Dip ($^{\circ}$)	73.97	(-21.47, 2.62)	73.97	(-21.47, 2.62)
	Strike ($^{\circ}$)	118.04	(-19.47, 0)	115.27	(-18.25, 0)

5.6.1 Sensitivity analysis

In sensitivity tests, we considered the mutual effects of parameters and observation errors (in the same geometry as the ERS satellite image in descending mode). We suggest that the reliability of the parameters not only depends on the observation quality but is also strongly affected by the observation distribution because of model sensitivity. As a result, we recommend in such inversion problems the use of an entire data set including near and far field observations with suitable relative weighting. For instance, weighting of the far field improves the quality of the plunge angle, whereas weighting the near field improves the quality of the pressure change in the case of a Yang-type source.

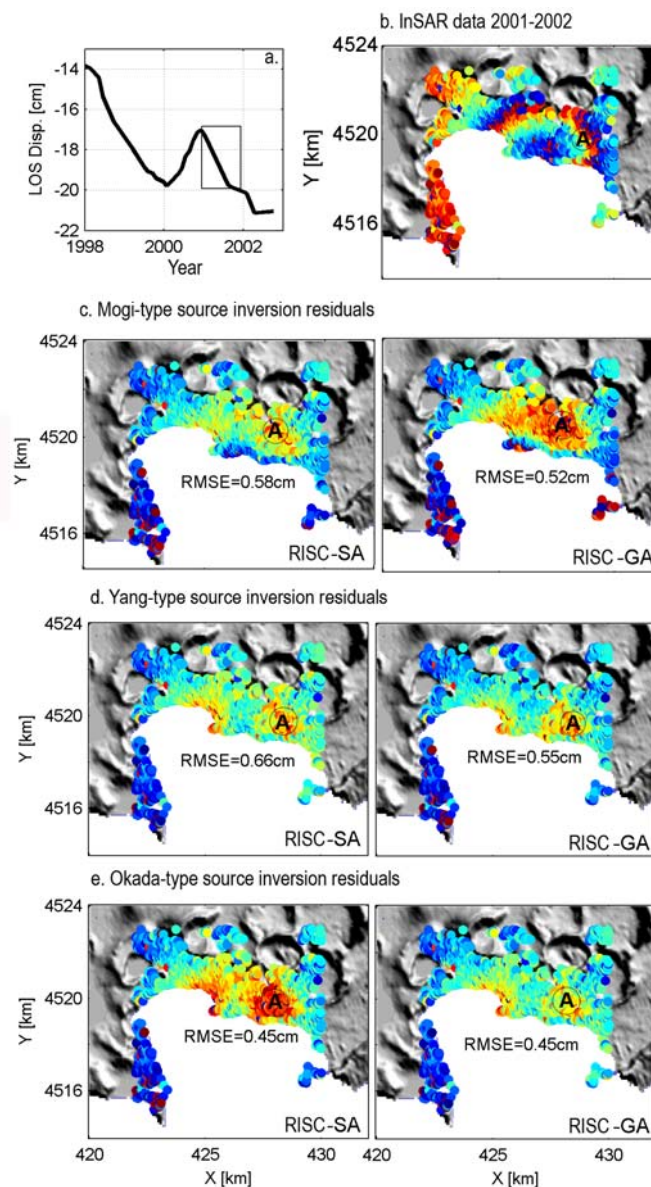


Figure 5.7. Application of algorithm to real data from Campi Flegrei caldera, Italy. a) A period of subsidence from 2001-2002. b) Subsidence observation in the LOS direction of ERS Radar images in descending mode (cf. Fig. 5.6), c) residuals for Mogi-type source inversion by RISC-SA and RISC-GA, d) residuals for Yang-type source inversion, and e) residuals for Okada-type source inversion. All panels are wrapped into 2.8 cm fringes. All source-types provide good solutions, with smallest residuals for the Okada-type.

It has been shown by Dieterich and Decker [1975] that the source geometry and depth using vertical deformation data alone can not be reliably resolved and that the full 3D displacement field is needed. Because InSAR observations are only a projection of the 3D displacement field, some of the source parameters may not be resolved reliably. However very often in the InSAR applications, we are able to carry out joint inversions by combining observations obtained from different satellite geometries. To see how these extra observations influenced the quality of the parameters, we set up two other sensitivity tests, the results of which are illustrated in the electronic appendix. The first test considered the ERS satellite image geometry in ascending mode, and the second test considered the norm of the 3D displacement field obtained, for instance, by combining InSAR, GPS, and leveling data. We find a moderate improvement of the sensitivity of the model parameters in comparison with previous results. In the case of the Okada-type source, the width and strike angles remain non-unique, while the quality of the other parameters is clearly improved. Considering the sensitivity test for ascending and descending geometry, together with the norm of the 3D displacement field, we suggest that the analytical model sensitivity (termed condition number after equation 5.5) might be a significant foundation for occasional poor observations and parameter interactions. Therefore, even though we can set up joint inversion of different geometries, good coverage of deformation in the near and far field and/or independent geophysical data (seismicity, gravity) still seems necessary.

5.6.2 Advances of the RISC approach

We proposed the RISC approach as a novel technique to answer the demand of practical optimization problems for obtaining a reliable and fast solution. Nevertheless, a valid question is whether other optimization methods (listed in Table 5.1) are not able to find the optimal solution equally well? From mathematical point of view it has been proved that all those optimization techniques are able to reach a global solution, though at expense of CPU time (because in many scenarios the computation time approaches infinity, and definition of a unique search criteria that is large enough is difficult). In practical optimization problems the CPU time is limited, the search criteria are problem-dependent and priority information is poorly available. Therefore any of those standard techniques may fail in finding the global solution; a failure that is not defined inherent but is rather a result of our poor knowledge about search space and CPU time constraint. Therefore in practical cases it seems reasonable to be aware of this shortcoming. The herein presented RISC approach is trying to answer the request of practical problems for reliable and efficient estimation of the global solution. In the RISC approach, the optimization problem can be initialized with reasonable values based on available information and user experiences; the algorithm converges to a good approximation of the global solution. In fact the RISC approach is not a stand-alone optimization technique, rather further strengthens available search techniques, with the aim to improve reliability and efficiency of the optimization process. Herein we exemplify a combination with GA and SA but may be adapted as well for any other algorithms such as Covariance Matrix Adoption Evolutionary Strategy [Igel, et al., 2007] or Neighborhood approach [Sambridge, 1999b].

The main limitation of the existing algorithms is becoming trapped in a local minimum because, for example, of an inappropriate cooling schedule. An improvement is shown by combining the standard SA with a randomly iterative (RI) approach. The same approach could be applied to the simple GA, especially when dealing with a complex search space. Another important aspect is obtaining a confidence region for the parameters by implementing a statistical competency (SC) approach. The statistic used here considers observation quality and model deficiency together. Combining RI and SC, we presented a sophisticated inversion algorithm. This approach can be applied to any other heuristic search algorithm to improve the performance of the search operator. The MATLAB codes for both RISC-SA and RISC-GA are included in the electronic appendix.

5.6.3 Model implication for Campi Flegrei volcano

The presented InSAR time series shows a general trend of subsidence from 1992-2002, temporarily interrupted by the 2000 uplift period. The uplift reached up to 4 cm between 2000 and 2001 and was

followed by subsidence up to 5 cm in 2002. A model that best fits both episodes is obtained by an Okada-type source, although also the other models reproduced the observed deformation field well. We find that during the subsidence period, the source of deformation is systematically shallower and the volume change is larger than during the uplift episode (see Fig. 5.8). The source separation is on average about 0.6 km. Regarding our sensitivity test showing 50% change in the average depth compromising by almost 200% change in the surface observation, we are confident that this separation (~ 0.6 km equivalent to 25% change in the observed deformation field) is not because of poor observation precision or the applied inversion method. Moreover this result is similar to what Battaglia *et al.* [2006] obtained based on inverting geodetic and gravity data for uplift period of 1980-1984 and subsidence period of 1990-1995. The source depth in our model, however, is slightly deeper. Table (5.6) compares RISC result and other published studies, showing that the independent studies are agreeing well. Based on previous sensitivity tests, we note that the location and strength parameters are well constrained, whereas the strike and dip parameters can not be uniquely determined. Considering model deficiency and observation variance via a statistical approach, we calculated the confidence region for the parameters. For instance, the uncertainty of the source depth is between 2.1 and 3.3 km for the uplift and between 2.1 and 3.0 km for the subsidence period. This range covers most of the estimates using the elastic homogeneous assumption in the Campi Flegrei region (Table 5.8).

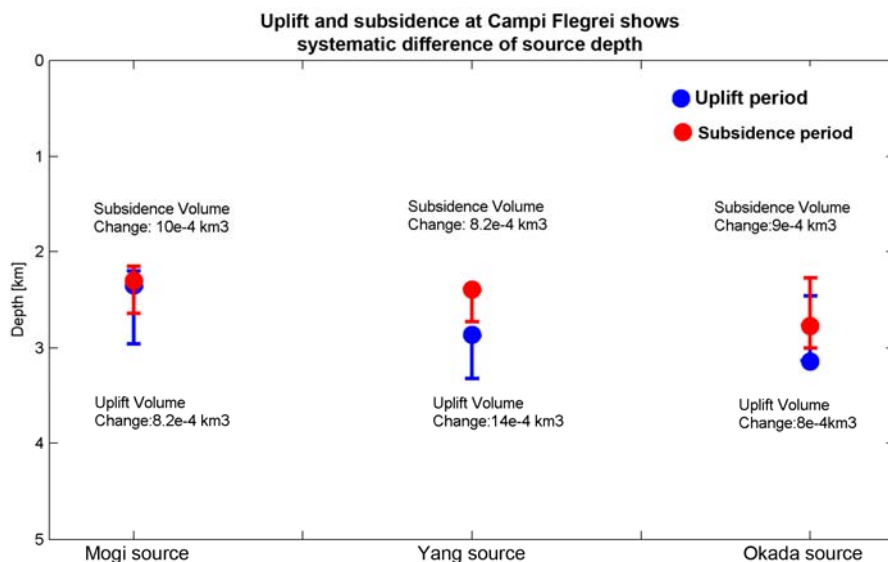


Figure 5.8. Synthesis of the Campi Flegrei test. Comparison of the absolute depth, associated confidence interval and volume change of different deformation source-types (Mogi, Yang and Okada) for the two periods of uplift (2000-2001) and subsidence (2001-2002). The uplift period is systematically associated with a deeper source than the subsidence period.

Table 5.8. Comparison between the depths of different deformation sources obtained in this study using RISC-SA and RISC-GA approaches and earlier studies

Source type	reference	Depth (km)	Inversion method
Mogi	This study	2.1-3.2	RISC-GA/SA
	[Lundgren et al., 2001]	2.5	Levenberg-Marquardt
Yang	This study	2.1-3.2	RISC-GA/SA
	[Avallone et al., 1999]	2.7	Gradient search
	[Lundgren et al., 2001]	2.1	Levenberg-Marquardt
	[Lanari et al., 2004]	2.4-3.2	Least square
<i>Prolate spheroid</i>	[Battaglia et al., 2006]	1.9-2.2	Least square
Okada	This study	2.4-3.3	RISC-GA/SA
	[Lundgren et al., 2001]	2.9	Levenberg-Marquardt
	[Lanari et al., 2004]	2.4-2.8	Least square
	<i>Penny shaped crack</i>	[Battaglia et al., 2006]	2.5-3.5

Nevertheless, our estimate is not completely consistent with the seismically inferred reservoir, where two zones can be inferred at depths of 2.7 km and 7.5 km [Zollo *et al.*, 2008]. This discrepancy might be due to material heterogeneity and observation uncertainty or because of an oversimplified base model. The effect of reactivated steeply dipping ring faults may explain such a discrepancy [De Natale *et al.*, 1997]. Another source of the difference may be found in the simplified half space assumption. Amoruso, *et al.*[2002] studied the unrest period of 1982-1984 at CF caldera using a crack model embedded in the layered elastic half space. The obtained PDF for the depth of the best model as a quality criterion is between 2 and 5 km. This broad estimate includes the estimated confidence region in this paper. Therefore, the slight differences between various models might be due to differences either in observation quality or model assumptions. Although our base model is very simple, our inversion approach is applicable to more complex or simple scenarios and significantly improves data resolution and computation time, and thus the efficiency and robustness of geodetic data interpretations.

5.7 Conclusions

We applied a Simulated Annealing and Genetic Algorithm for estimating deformation source parameters based on surface displacement data. The work was aimed at developing a fast and reliable inversion technique that allows utilization of large datasets with confidence. Therefore, first we showed that the important parameters for precision and accuracy of the results are not only the quality of the observations but also the distribution of the observations. We further improved the optimization methods, by applying a hybrid random iterated search and statistical competency approach (RISC). The RISC approach prevents SA from getting trapped in local minima. Moreover, this approach allows an estimation of the quality of the results at a certain confidence level. We extend the similar idea to the GA for estimating the confidence interval of parameters. Similarly RISC can be applied to different optimization methods. To indicate the efficiency and robustness of our methods, we performed synthetic tests utilizing three commonly used volcano deformation sources, including Mogi, Yang, and Okada sources. We find that the two algorithms can retrieve noisy synthetic field parameters as well as a meaningful confidence region for the results. Therefore, the statistical approach combined with an inversion algorithm has been shown to be a large improvement to the standard techniques commonly used. Considering computational time, we find that GA is much faster than SA and also more flexible in accepting limits for parameters, which is useful in hybrid and constrained optimization and allows consideration of full InSAR sets.

We applied the two developed optimization methods to investigate the source of deformation periods at Campi Flegrei volcano, Italy. The observations are a time series obtained based on SBAS interferometry. The displacement series shows that an uplift period occurred in 2000-2001 and a subsidence period occurred in 2001-2002. As a result, for the uplift and subsidence periods the depth of the deformation source is constrained between 2.1 and 3.3 km and 2.1 and 3.0 km, respectively. Comparing the source parameters for the uplift and subsidence periods shows that the source location is systematically deeper for the uplift period. We utilize an approach to validate the model parameters considering two different sources of uncertainty, model deficiency and observation errors.

5.8 Auxiliary material

5.8.1 Relation between observed LOS displacement and volume change of Mogi source

Delaney and McTigue (1994) presented a relation between 3D volume change at the surface of elastic half space and volume change of the Mogi-type model, which is;

$$\frac{\partial v_s}{\partial v_c} = 2(1 - \mathcal{G}) \quad (\text{A5.1})$$

Where \mathcal{G} is Poisson ratio, ∂v_s and ∂v_c are volume change at the source and at the surface, respectively. In perfect elastic material ($\mathcal{G} = 0.5$) the volume change at the source is equal to the

change at surface. In the common case ($\mathcal{G} = 0.25$) the volume change at the source is 1.5 times the change at the surface. Knowing a 3D surface displacement field we are able to use this equation, but in many cases this formulation is not applicable. For instance InSAR data is an observation that only includes the projection of the 3D deformation field on the dimension of the line of satellite (LOS) direction. Therefore herein we derive an alternative equation which is applicable to LOS observation. The 3D surface displacement due to a point source buried in elastic half space with Poisson ratio \mathcal{G} can be obtained by following equations (Mogi,1958):

$$\begin{aligned}
U_x &= \frac{1-\mathcal{G}}{\pi} \frac{x}{(d^2 + x^2 + y^2)^{3/2}} \Delta v_s \\
U_y &= \frac{1-\mathcal{G}}{\pi} \frac{y}{(d^2 + x^2 + y^2)^{3/2}} \Delta v_s \\
U_z &= \frac{1-\mathcal{G}}{\pi} \frac{d}{(d^2 + x^2 + y^2)^{3/2}} \Delta v_s
\end{aligned} \tag{A5.2}$$

Where Δv_s and d are source volume change and depth and x and y are horizontal coordinates, respectively. The relation between 3D displacement field and LOS observation field by knowing satellite orbit azimuth and incidence angle is (Hanssen, 2002):

$$LOS = c_x U_x + c_y U_y + c_z U_z \tag{A5.3}$$

Where U_x , U_y and U_z are the three components of a displacement field, and c_x , c_y and c_z are three projection coefficient that may vary by azimuth and incidence angle (Hanssen, 2002). Equation A5.3 is not reversible which means having only InSAR observation does not allow us to calculate a 3D displacement field. Therefore equation A5.1 is not applicable in such cases. So we used a new formulation to estimate source volume change directly based on LOS observation.

The volume beneath LOS surface is calculated by two times integration on x and y :

$$\begin{aligned}
\iint_{R^2} LOS dx dy &= \\
& c_x \iint_{R^2} U_x dx dy + c_y \iint_{R^2} U_y dx dy + c_z \iint_{R^2} U_z dx dy
\end{aligned} \tag{A5.4}$$

Due to symmetry of U_x and U_y , two of the integrals become zero;

$$\iint_{R^2} U_x dx dy = 0, \iint_{R^2} U_y dx dy = 0 \tag{A5.5}$$

Then

$$\begin{aligned}
\iint_{R^2} LOS dx dy &= c_z \iint_{R^2} U_z dx dy \\
&= c_z \iint_{R^2} \frac{1-\mathcal{G}}{\pi} \frac{d}{(d^2 + x^2 + y^2)^{3/2}} \Delta v_s dx dy = \\
& \frac{(1-\mathcal{G})\Delta v_s c_z}{\pi} \iint_{R^2} \frac{d}{(d^2 + x^2 + y^2)^{3/2}} dx dy
\end{aligned} \tag{A5.6}$$

On the other hand

$$\iint_{R^2} \frac{d}{(d^2 + x^2 + y^2)^{3/2}} dx dy = 2\pi \tag{A5.7}$$

namely independent of depth then

$$\iint_{R^2} LOS dx dy = 2\pi \frac{(1-\mathcal{G})\Delta v_s c_z}{\pi} = 2(1-\mathcal{G})\Delta v_s c_z \quad (A5.8)$$

Finally Δv can be obtained by

$$\Delta v_s = \frac{\iint_{R^2} LOS dx dy}{2(1-\mathcal{G})c_z} \quad (A5.9)$$

5.8.2 Ascending mode sensitivity test of the parameters of three source-types.

Observed deformation perturbation is shown in the LOS direction of ERS Radar images in ascending mode. This allows comparison to the sensitivity test shown in Figures (5.1-3). All other conditions are the same as Figure (5.1-3).

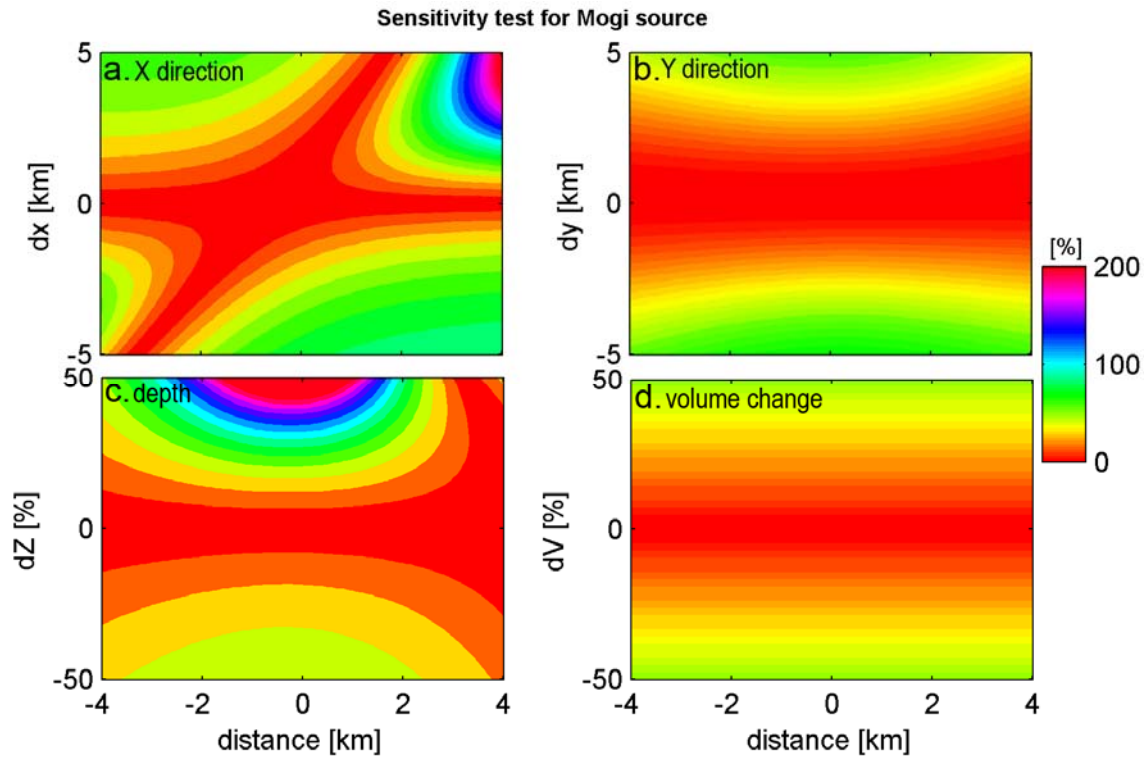


Figure A5.1. Sensitivity test for Mogi-type source

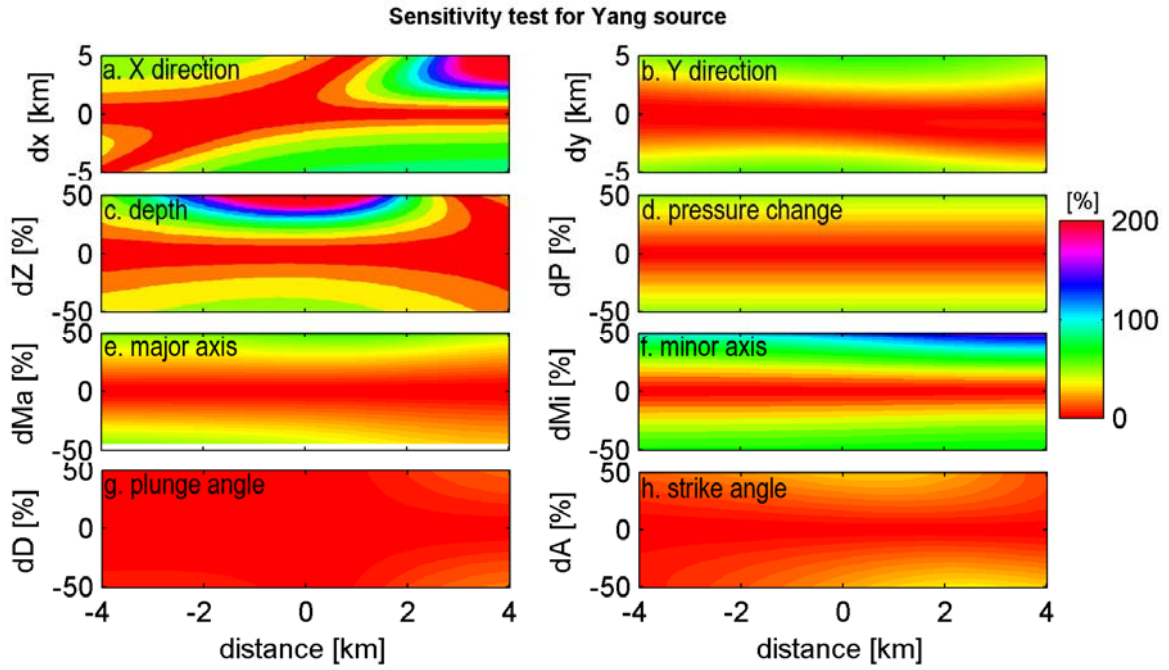


Figure A5.2. Sensitivity test for Yang-type source

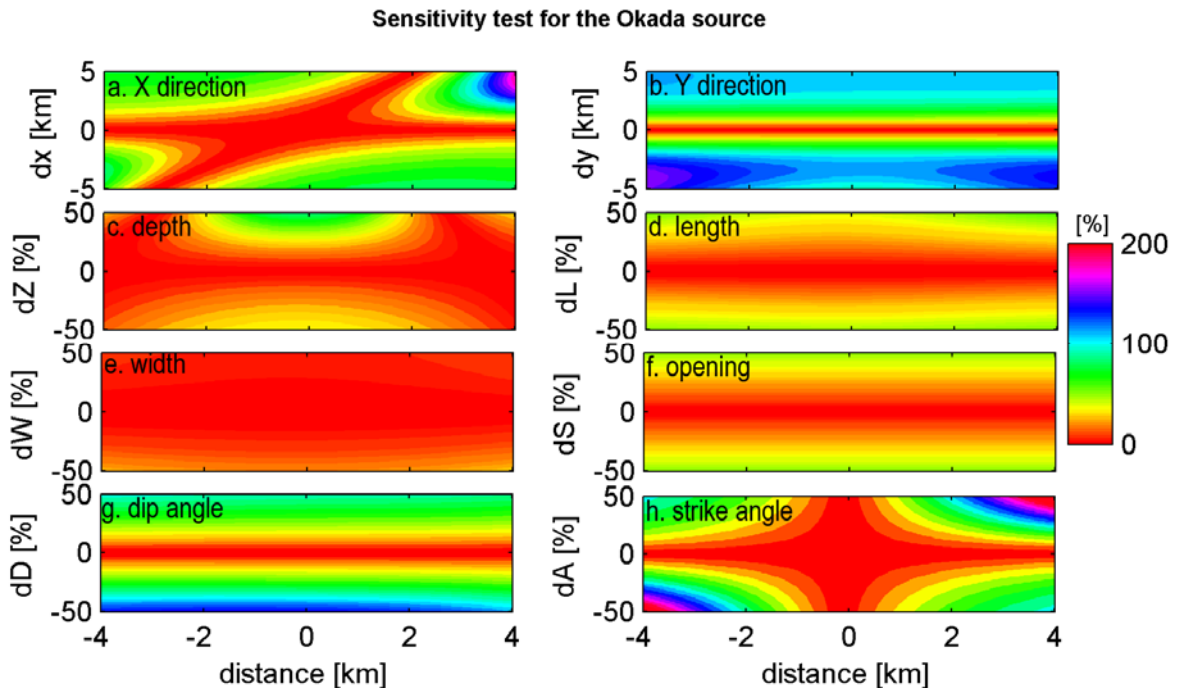


Figure A5.3. Sensitivity test for Okada-type source

5.8.3. Sensitivity test of the parameters in a fully constrained 3D deformation field, obtained from, for instance, a combination of ascending and descending together with GPS and leveling data. We considered the same condition as in Figures (5.1-3).

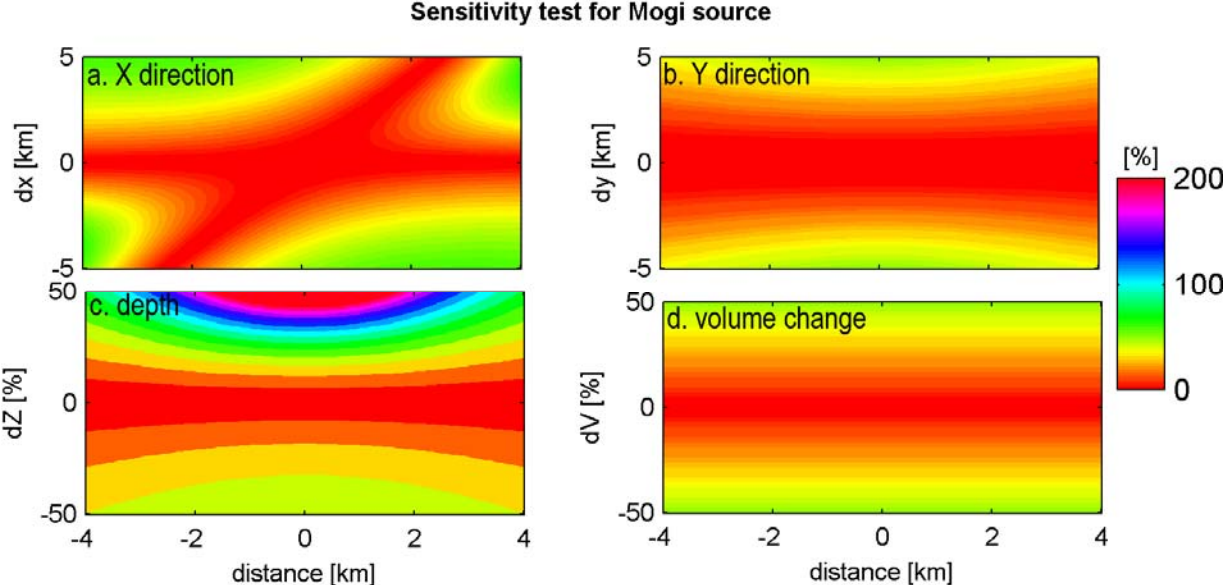


Figure A5.4. Sensitivity test for Mogi-type source

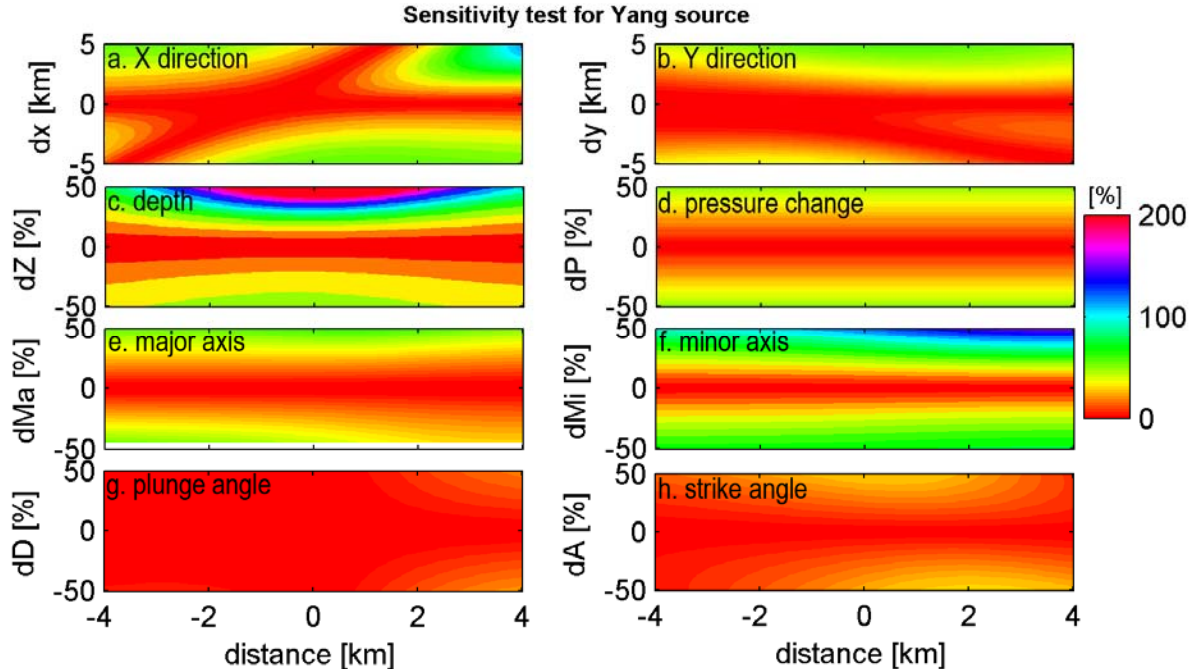


Figure A5.5. Sensitivity test for Yang-type source

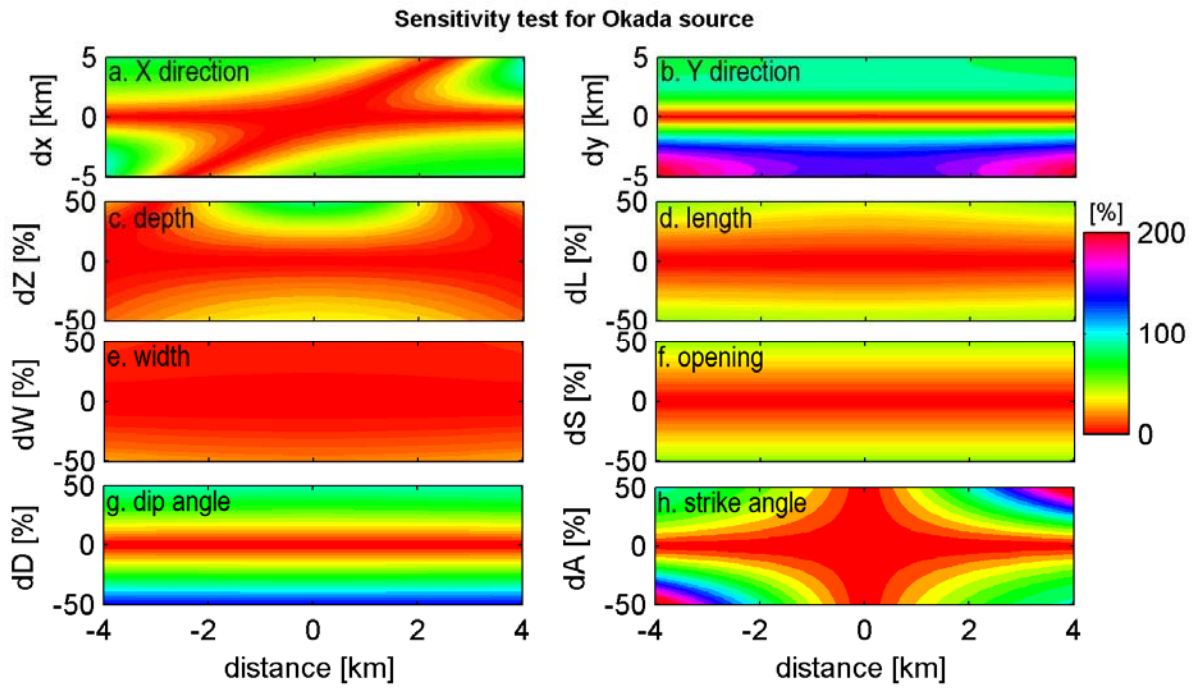


Figure A5.6. Sensitivity test for Okada-type source

Chapter 6

Time-dependent volcano source monitoring using InSAR time series: A combined Genetic Algorithm and Kalman Filter approach¹

M. Shirzaei and T. R. Walter

Section 2.1, Dept. Physics of the Earth, GFZ German Research Centre for Geosciences, Telegrafenberg, D – 14473 Potsdam, Germany

Abstract

Modern geodetic methods allow continuous monitoring of deformation fields at volcanoes. The acquired data contributes significantly to the study of the dynamics of magmatic sources prior to, during and after eruptions and intrusions. In addition to advancing monitoring techniques, it is important to develop suitable approaches to deal with deformation time series.

Here, we present, test and apply a new approach for time-dependent, nonlinear inversion using a combination of a Genetic Algorithm (GA) and Kalman Filter (KF). The GA is used in the form presented by *Shirzaei and Walter*, [2009] and KF implementation now allows for the treatment of monitoring data as a full time series, rather than as single time steps. This approach provides a flexible tool for assessing unevenly sampled and heterogeneous time series data and explains the deformation field using time-consistent dislocation sources.

Following synthetic tests, we demonstrate the merits of time-consistent source modeling for InSAR data available between 1992 and 2008 from the Campi Flegrei volcano in Italy. We obtained multiple episodes of linear velocity for reservoir pressure change associated with parabolic surface deformation at the volcano. This may be interpreted via differential equations as a linear flux to the shallow reservoir and provides new insight into how both the shallow and deep reservoirs communicate beneath Campi Flegrei.

The synthetic test and case study demonstrate the robustness of our approach and the ability to track and monitor the source of systems with complex dynamics. It is applicable to time-dependent optimization problems in volcanic and tectonic environments in other locations and allows physical process to be understood in a temporal and quantitative way.

6.1 Introduction

In past years, there has been significant technical development in the detection of spatiotemporal surface deformation fields. Dense, continuous Global Positioning System (GPS) networks [*Segall and Davis*, 1997] and Interferometric Synthetic Aperture Radar (InSAR) time series [*Berardino et al.*, 2002; *Ferretti et al.*, 2001b] provided valuable information about the temporal evolution of

¹ MS developed the approach and inverted the data. All authors were involved in discussion and writing the paper.

deformation fields. These new developments yield daily and monthly deformation measurements with millimeter precision over regional scales [Dixon *et al.*, 2006; King *et al.*, 1995; Segall and Matthews, 1997; Tizzani *et al.*, 2007].

Inverse modeling is a strategy used to understand the source of the deformation field. A number of different modeling algorithms for inverting deformation data can currently be found in the literature (see e.g., Shirzaei and Walter [2009]). However, these are commonly applied to either short or selected periods, and therefore provide merely a “snapshot” of a particular stage of a system. Modern developments in the field of deformation time series require appropriate progress in the inversion tools to address the full spatiotemporal capacity of the observations. To address this issue, a Kalman Filter (KF) technique is introduced into the field of deformation time series analysis. This technique is a sophisticated advancement from previous, common approaches.

KF has a recursive formulation that is applicable to irregularly sampled data. In its original form, KF is applicable to linear dynamic systems as well [Grewal and Andrews, 2001; Kalman, 1960]. In the static case, KF corresponds to a sequential least squares adjustment [Hofmann-Wellenhof *et al.*, 2000]. In the geosciences, the linear dynamic Kalman filter (LKF) has already been applied to better understand spatiotemporal variations in fault slip rates, dike intrusion and fault creep history [Fukuda *et al.*, 2004; Ozawa *et al.*, 2004; Segall *et al.*, 2000; Segall and Matthews, 1997].

While this linear approach is valid for some problems, many dynamic systems are inherently non-linear. Non-linearity is especially common in the field of geosciences, with processes such as fault slip rates or volcanic deformations. For example, a volcano may be inflating prior to an eruption, undergo rapid collapse during an explosion or be affected by periodic flank movement. Therefore, an extension of KF to include slightly nonlinear problems has been applied (e.g., [Grewal and Andrews, 2001]). One widely used extension requires linearization of the equations about the estimated parameters for every time step [Grewal and Andrews, 2001; Welch and Bishop, 2001]. The extended Kalman filter has been used for time-dependent estimation of stress field, slip rate, and aquifer modeling [Leng and Yeh, 2003; McGuire and Segall, 2003; Miyazaki *et al.*, 2006]. This method only performs well, however, if the equations are locally linear. Because of the recursive nature of KF, when this assumption is violated the errors may be distributed and this may lead to biased results.

The Kalman filter technique has been combined with other techniques to overcome this limitation. One recent application combines KF with unscented transforms (UT) to propagate the mean and covariance information through a nonlinear function [Julier and Uhlmann, 1997; Julier and Uhlmann, 2004; Wan and Van Der Merwe, 2000]. The result is free from derivatives and relies on the fact that approximating a probability distribution is more feasible than approximating an arbitrary nonlinear function [Julier and Uhlmann, 2004].

Recently, Fournier *et al.* [2009] implemented this idea using dynamic models of the magmatic source at the Okmok volcano. The crucial issue to consider, however, is the initialization task and the selection of so-called hyperparameters, which are generally problem-dependent and only manageable by trial and error ([Julier and Uhlmann, 2004]; personal communication with Fournier [2009]). The power and importance of the KF for time series assessment is well understood, but a sophisticated implementation free from assumptions and limitations has unfortunately not yet been elaborated.

As an alternative to overcome these limitations, combining KF with other tools, such as Monte Carlo, artificial neural network and wavelet transforms [Chou and Wang, 2004; Fukuda *et al.*, 2004; Kato *et al.*, 2009], is a promising approach.

Along these lines, this study presents a novel, time-dependent, non-linear inversion tool by combining KF and the GA techniques. The KF utilizes the simple form of Kalman [Grewal and Andrews, 2001] and the GA is implemented in an iterated manner combined with a statistical competency test [Shirzaei and Walter, 2009]. By using a sophisticated confidence estimation, we are able to combine the strength of a confident inversion tool with the robustness of a linear Kalman Filter (LKF). The implementation of a standard LKF makes this approach relatively easy to apply and makes optimization of the algorithm parameters very straightforward.

We begin by briefly summarizing the GA and LKF approaches. Later, these two methods are combined and the capacities of a statistic inversion tool and a time varying filter are combined to estimate the dynamics of the system.

We demonstrate the robustness of our approach using a synthetic test and apply it to a long deformation time series obtained by SBAS-InSAR between 1992 and 2008 at the Campi Flegrei volcano in Italy. A new understanding of the physical process of occurring at this volcano is obtained and the source of deformation is monitored through time.

6.2 Methods

The concept of both the applied inversion and filtering approaches is described, followed by a description of the combination of these two approaches.

6.2.1 Randomly Iterated Search and Statistical Competency Genetic Algorithm (RISC-GA)

The Genetic Algorithm (GA) was recently identified as a powerful inversion tool that has the potential to process large data sets in full resolution [Shirzaei and Walter, 2009]. The GA was introduced by [Holland, 1975] and has been further improved by many subsequent researchers who provided comprehensive summaries on the theory and applications (see e.g., [Davis, 1987; Goldberg, 1989; Haupt and Haupt, 2004; Rawlins, 1991; Whitley, 1994]). Despite remarkable successes in solving extremely complex optimization problems, the original form of the GA does not provide any information about the quality of the result. Therefore, several researchers made efforts to determine the quality of the parameters optimized by the GA (e.g., [Carbone et al., 2008; Deb et al., 2000; Zhou et al., 1995]). Recently, Shirzaei and Walter [2009] introduced a sophisticated extension to the GA. This extension is named *Randomly Iterated Search and Statistical Competency* (RISC), and it that allows the quality of the optimized parameters to be estimated. In the RISC approach, the optimization algorithm is initialized with reasonable values based on available information. With random repetitions, the degree of freedom and the chance for exploring the vicinity of the optimal solution increases. This statistical approach allows probability distributions, therefore, the confidence region for selected optimization parameters to be explored. RISC-GA was originally applied in binary format [Shirzaei and Walter, 2009]. To speed up the algorithm, however, we implement it here using continuous variables (for the GA with continuous variables, see e.g., [Haupt and Haupt, 2004]).

For the GA with continuous variables, if b_{lo} and b_{hi} are the lower and upper band of unknowns, the initial population (*Pop*) is generated by the following equation:

$$Pop = (b_{hi} - b_{lo})p_m + b_{lo} \quad (6.1)$$

where p_m is a random number uniformly chosen in the range [0, 1]. Comparable to the binary version of GA, other operators (such as pairing, mating and mutation) will guide the algorithm toward the optimum solution (see for details [Haupt and Haupt, 2004; Michalewicz, 1994]). The details for implementing the RISC approach with a continuous variable GA are the same as those explained for the binary version; the reader is referred to Shirzaei and Walter, [2009] for a more detailed explanation.

6.2.2 Linear Dynamic Kalman Filter (LKF)

LKF addresses the problem of estimating the parameters of a linear, stochastic system by using measurements that are a linear function of the parameters. According to the original form of the LKF, the system dynamic and measurement models, respectively, are formulated as follows [Grewal and Andrews, 2001]:

$$\begin{aligned} X_k &= \Phi_{k-1}X_{k-1} + w_{k-1} \quad , \quad w_k \sim N(0, Q_k) \\ Z_k &= H_kX_k + v_k \quad , \quad v_k \sim N(0, R_k) \end{aligned} \quad (6.2)$$

where X and w are $n \times 1$ vectors of unknowns and the associated noise with Gaussian distribution; Z and v are $l \times 1$ vectors of observations and the associated noise with Gaussian distribution; Φ and H are $n \times n$ and $l \times l$ matrices, respectively [Grewal and Andrews, 2001; Kalman, 1960]. A

recursive solution for the system of equations (6.2) might be performed as follows (see Table 4.3; *Grewal and Andrews, [2001]*):

$$\begin{aligned}
\widehat{X}_k^+ &= \widehat{X}_k^- + \overline{K}_k [Z_k - H_k \widehat{X}_k^-] \\
P_k^+ &= [I - \overline{K}_k H_k] P_k^- \\
\widehat{X}_k^- &= \Phi_{k-1} \widehat{X}_{k-1}^+ \\
P_k^- &= \Phi_{k-1} P_{k-1}^- \Phi_{k-1}^T + Q_{k-1} \\
\overline{K}_k &= P_k^- H_k^T [H_k P_k^- H_k^T + R_k]^{-1}
\end{aligned} \tag{6.3}$$

In equation (6.3) \widehat{X}_k^+ is the posterior estimate, P_k^+ is the covariance, \widehat{X}_k^- is the priori estimate, P_k^- is the variance and \overline{K}_k is the Kalman gain matrix.

6.2.3 Combining RISC-GA and LKF for time-dependent nonlinear inversion

The evaluation of a sophisticated, combined inversion tool using a KF and the GA to explain deformation time series and estimate the associated source parameters responsible for the deformation is detailed below.

The approach of a combined RISC-GA and LKF method is best explained by an example. Assume a spatiotemporal observation $L_k(x, y)$ is sampled at times $k=1, \dots, T$ and is simulated by a forward model $F(X_k^1, \dots, X_k^n)$ using the following equation:

$$L_k(x, y) + r_k(x, y) = F(X_k^1, \dots, X_k^n) \tag{6.4}$$

where, in terms of crustal deformation, F is an analytical solution for a rectangular dislocation source [*Okada, 1985*], an inflating point source [*Mogi, 1958*], a pressurized spherical source [*McTigue, 1987*], or any combination of those; (X_k^1, \dots, X_k^n) are n time-dependent dislocation source parameters; L_k is the surface deformation observation obtained by either continuous GPS data or InSAR time series; and r_k is the time-dependent observation error.

The aim of this method is to reproduce and explain a time series of source parameters, (X_1^i, \dots, X_k^i) with $i=1, \dots, n$, such that the mean of the squared error is minimized.

The rationale for our approach combining RISC-GA and LKF is composed of three main steps:

Step (1): Static, non-linear inversion of the surface observations at each time j ($j=1, \dots, k$) using RISC-GA. In this step, equation (6.4) is inverted to obtain the parameters (X_j^1, \dots, X_j^n) , regardless of the observations before and after time j . First order information about the parameters is required to specify the initial population using equation (6.1) (further detail about RISC-GA initialization may be found in *Shirzaei and Walter [2009]*). After repeating this step T times (i.e. number of samples), we obtain the dislocation source parameters responsible for the observed surface deformation. In addition, this statistical approach provides associated confidence intervals at T time steps. This estimation is optimized at each time step in terms of the spatial mean of squared error but not necessarily in terms of temporal mean square error. In order to also address the temporal error, a further step is necessary, which is detailed below and accomplished based on the LKF method.

Step (2): To perform LKF, we introduce a system of equations based on the previous inversion step. Assuming a time series of the i -th parameter and an associated half-length of the confidence region as $\{_{rg} X_1^i, \dots, _{rg} X_k^i\}$ and $\{_{rg} \sigma_1^i, \dots, _{rg} \sigma_k^i\}$, respectively, we may establish the dynamic system model as:

$$\begin{bmatrix} _{kf} X_k^i \\ \overline{V}_k^i \end{bmatrix} = \begin{bmatrix} 1 & \Delta t \\ 0 & 1 \end{bmatrix} \begin{bmatrix} _{kf} X_{k-1}^i \\ \overline{V}_{k-1}^i \end{bmatrix} + \begin{bmatrix} X W_{k-1}^i \\ V W_{k-1}^i \end{bmatrix}, \quad X W_k^i \sim N(0, Q_X^i), \quad V W_k^i \sim N(0, Q_V^i) \tag{6.5}$$

and the measurements model as

$$[_{rg} X_k^i] = [1]_{kf} [_{kf} X_k^i] + [v_k^i], \quad v_k^i \sim N(0, R^i), \quad R^i = Q_X^i \tag{6.6}$$

where

$$\begin{aligned}
Q_X^i &= 1/k-1 \sum_{p=1}^k ({}_{rg} \sigma_p^i - {}_{rg} \bar{\sigma})^2 \\
Q_V^i &= 1/k-1 \sum_{p=1}^k (V_p^i - \bar{V}^i)^2 \\
{}_{rg} \bar{\sigma} &= 1/k \sum_{p=1}^k {}_{rg} \sigma_p^i \\
\bar{V}^i &= 1/k \sum_{p=1}^k V_p^i \\
V_k^i &= \frac{{}_{rg} X_k^i - {}_{rg} X_{k-1}^i}{t_k - t_{k-1}}
\end{aligned} \tag{6.7}$$

Comparing equation (6.6) with (6.2), it can be seen that the observations are a result of the inversion at step 1. Because the system of equations is linear, we are able to use LKF. Each dislocation source parameter is considered a particle with constant velocity subject to random velocity perturbations. This assumes that the fluctuation of the inversion result over the time is caused by random noise. The new solution for the parameters in equations (6.5 - 7) can be obtained via equation (6.3). This new solution is obtained such that it minimizes the mean of the squared temporal error. We note, however, that it is likely that the new solution may not perfectly replicate surface deformation observations. This means that the solution is not optimum in terms of the mean of the squared spatial error, which requires another step in the process.

Step (3): To minimize both the spatial and temporal error, we repeat step (1) with a slight modification, namely that the initial population is divided into two parts. Part one is the *priori population* (P_{pr}) and initialized using the same bounds as step (1). Part two is the *posterior population* (P_{po}), which is initialized using bounds based on the result of step (2). The bounds are described as:

$$\begin{aligned}
{}_{kf} b_{lo}^i &= {}_{kf} \hat{X}_k^{i+} - P_{11_k}^{i+} N_{1-\alpha/2} \\
{}_{kf} b_{hi}^i &= {}_{kf} \hat{X}_k^{i+} + P_{11_k}^{i+} N_{1-\alpha/2} \\
P \left[{}_{kf} \hat{X}_k^{i+} - P_{11_k}^{i+} N_{1-\alpha/2} < {}_{rg} X < {}_{kf} \hat{X}_k^{i+} + P_{11_k}^{i+} N_{1-\alpha/2} \right] &< 1 - \alpha
\end{aligned} \tag{6.8}$$

where $P_{11_k}^{i+}$ is the posterior variance of the estimated parameter ${}_{kf} \hat{X}_k^{i+}$ and $P[\cdot]$ is the normal probability density function. Equation (6.8) is defined by the $(1-\alpha)\%$ confidence interval for the posterior parameters. We use the assumption of a normal probability distribution with bounds defined by the upper and lower limits of the confidence interval. After initialization of the RISC-GA with these two subpopulations, the first based on our priori information and the second based on LKF, we run the RISC-GA again. The GA control parameters (cross over, pairing and mating) may allow for random combinations of population members and lead to a result that minimizes both the spatial and temporal mean square errors.

Steps (1-3) are repeated until specified stopping criteria are reached, which may be defined as:

$$\begin{aligned}
\left| \frac{RMSE^{itr} - RMSE^{itr-1}}{RMSE^{itr-1}} \right| &< \varepsilon \\
\left| \frac{\sum_{i=1}^n \left[({}_{kf} \hat{X}_k^{i+})^{itr} - ({}_{kf} \hat{X}_k^{i+})^{itr-1} \right]}{\sum_{i=1}^n \left[({}_{kf} \hat{X}_k^{i+})^{itr-1} \right]} \right| &< \varepsilon
\end{aligned} \tag{6.9}$$

where ε is a small arbitrary number, $|\cdot|$ is the absolute value operator and itr denotes the number of iterations. Note that reaching only one of those stopping criteria is sufficient to estimate optimality of the solution.

6.3 Synthetic test and validation

To examine the abilities of RISC-GA-LKF and to ensure that it can improve the stability of the model parameters, we now look at a synthetic test demonstrating its performance. The purpose of the synthetic test is simple. The test requires that five parameters of a dynamic, pressurized, spherical magmatic source be estimated [McTigue, 1987] in an elastic homogenous half space. The dynamic models of source depth (D), radius (R) and pressure change (P) are given as:

$$\begin{aligned}
 D &= 4 - 0.7 \sin(0.5t) \\
 R &= 0.5\sqrt{t} \quad t = 1:1:10 \\
 P &= \begin{cases} 0.1 - 0.01t & , t \leq 6 \\ P(6) - 0.01t & , t > 6 \end{cases}
 \end{aligned} \tag{6.10}$$

As seen in Figure (6.1), the synthetic models simulate fully nonlinear deformation dynamics, which challenge the ability of RISC-GA-LKF to track such a system. The observation area is a $20 \times 20 \text{ km}^2$ grid with 1 km spacing, and the source location is fixed at coordinate (0,0). To simulate a more realistic scenario, we include random noise with a variance of 1 cm as measurement error. The time-dependent deformation is inverted as follows.

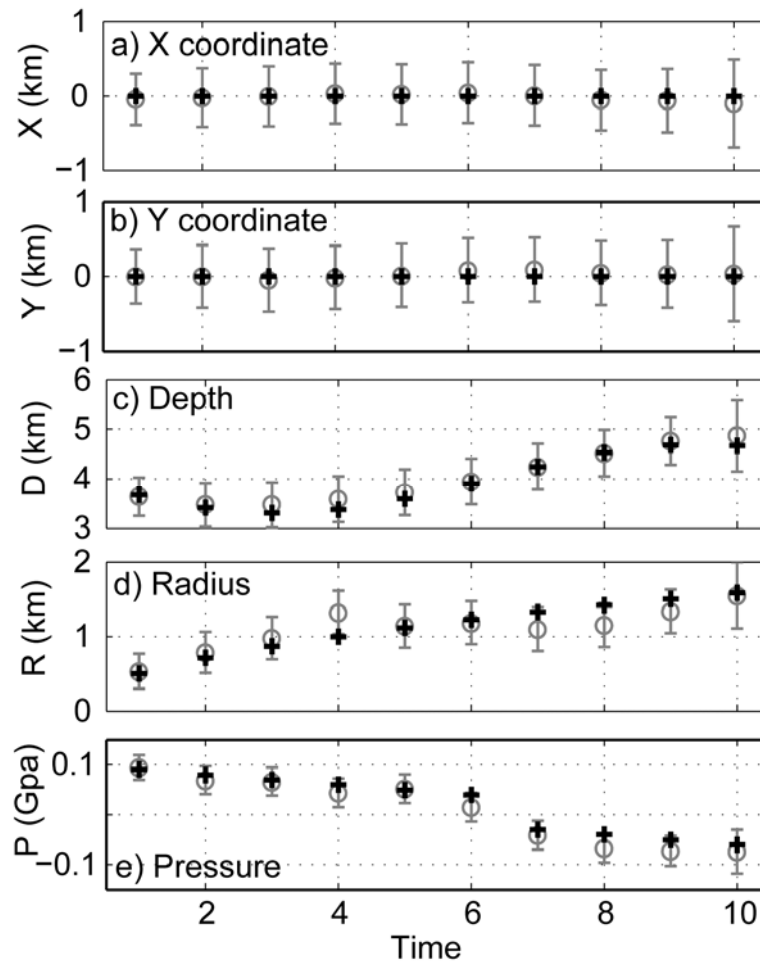


Figure 6.1. Evaluating RISC-GA-LKF for a synthetic scenario. This shows the comparison between the inversion results (open circles with error bars) and the true values (cross). a) easting, b) northing, c) depth, d) radius and e) pressure change of a pressurized, spherical, magmatic source buried in an elastic half space.

To start the inversion, the RISC-GA is initialized with a population size of 80, mutation rate of 0.7, selection rate of 0.5 and a maximum iteration of 200 (after [Shirzaei and Walter, 2009]). The ratio

between priori (P_{pr}) and posterior (P_{po}) population size is chosen randomly such that P_{pr} plus P_{po} is equal to the total population size. We use the second relation shown in equation (6.7), with $\varepsilon = 0.01$ as a stopping criterion. The upper and lower bounds were chosen to be (-2 km, 2 km) in the horizontal direction, (2 km, 6 km) for depth, (0 km, 2 km) for radius and (-0.2 GPa, 0.2 GPa) for the pressure change. These values appear realistic for Silicic magmatic systems.

The stopping criteria were reached after three iterations of the algorithm. Figure (6.1) shows a comparison between the inverted source parameters and the original source parameters. The error bars for the estimated parameters are plotted in the 95% confidence interval. We find there is good agreement between the original and the estimated parameters. This test shows the merits of RISC-GA-LKF for both tracking systems with nonlinear dynamics, and also for resolving the trade off between source parameters such as source radius, pressure change and depth. Note that the pre-selected parameter bounds are merely accelerating the algorithm convergence. If broader bounds are chosen, the algorithm iterations increase at the expense of computation time. However, the final result is mostly independent from the initialization procedure. This is a significant advantage of the optimization technique compared to other approaches. Therefore, the initial conditions have no effects on the final result accuracy and lead to correct results.

6.4 Application to InSAR time series at the Campi Flegrei volcano

Campi Flegrei (CF) hosts a caldera with a long documented history of unrest. It is also in one of the most densely populated regions of Italy, partly including the city of Naples and its approximately one million inhabitants. The historical deformation at CF is governed by subsidence at a rate of 1.5-1.7 cm/yr, with occasional periods of uplift [Troise *et al.*, 2007]. The most recent large-scale uplift episodes occurred during 1969-1972 and 1982-1984 [Barberi *et al.*, 1984; Troise *et al.*, 2007].

The first observation of the deformation using InSAR at CF reported by Avallone *et al.* [1999] was associated with a subsidence rate of up to 2.5 cm/yr during the period 1993-1996. Later, using InSAR time series, Lundgren *et al.*, [2001] observed a subsidence rate of 3.5 cm/yr in the period 1993-1998.

Subsequently, further developments of the InSAR time series Small Base Line Subset (SBAS) approach allowed for precise spatiotemporal maps of the deformation field to be obtained [Berardino *et al.*, 2002; Lanari *et al.*, 2007]. Later, this deformation time series was extended to late 2008 [Manconi *et al.*, 2010].

Various episodes of the deformation at CF have been studied by many different researchers (see [Lanari *et al.*, 2007] and references therein). Although the time series data are available, the dynamics of the source have never been investigated in a temporal context. Thus, InSAR has remained a ‘snapshot’ tool. Utilizing long time series of the CF deformation field obtained by both the SBAS method [Lanari *et al.*, 2007] and by proposed approach for time-dependent source modeling (see above) we study the temporal changes of the reservoir underneath the Campi Flegrei caldera.

To simulate the source of deformation underneath the caldera, we consider a pressurized spherical source in an elastic homogenous half space (as used in synthetic tests) that evolves over time. The time series used here was provided by Lanari and colleagues at IREA, Napoli [Lanari *et al.*, 2007]. The data spans the period 1992-2008 and comprises 116 observation samples with an average sampling rate of 45 days (Fig. 6.2). The deformation field is obtained in the Line of Sight (LOS) of the satellite with descending orbit and incidence angle of 23° and azimuth angle of 190°. The data were thoroughly validated by comparison to ground truth data, including leveling and GPS data. For data validation, we refer the reader to Lanari *et al.* [2007].

As seen in Figure (6.2), the general deformation pattern shows subsidence up to 25 cm at the center; occasional uplift is apparent mainly from 2001-2002 and 2005-2007.

For initialization of RISC-GA, we began with 200 iterations, a mutation rate of 0.7, a selection rate of 0.5 and an initial population size of 100. The other parameters in the RISC-GA-LKF were the same as in the synthetic test and the a priori bound for the parameters is provided in Table (6.1) and are based on previous studies (see [Shirzaei and Walter, 2009] and references therein).

Table 6.1. *Priori bounds for the parameters of the pressurized spherical source used for simulating the magmatic source underneath CF*

Parameter	X (km)	Y (km)	D (km)	R (km)	P (GPa)
Lower bound	420	4515	2	0.5	-0.1
Upper bound	435	4525	5	2	0.1

After four iterations of the RISC-GA-LKF, the stopping criteria were reached and the time series of the magmatic source parameters was obtained. Figure (6.3) shows the time series of the source parameters (to compare this result with time series obtained by applying only RISC-GA see electronic appendix). The easting and northing of dislocation source position in the UTM map projection system are 425 ± 1 km and 425 ± 1.2 km, respectively.

Figure (6.3a) shows the root mean square error (RMSE) of the inversion for each data sample with an error bar showing the 95% confidence interval. The magmatic source with parameters found using the inversion is able to retrieve the observed deformation time series very well.

The cumulative pressure change time series (Fig. 6.3d) emphasizes the overall deflation period of the CF volcano since 1992. Deflation continues until 2000, when the onset of inflation gradually begins and lasts until 2001. After the inflation, another deflation period begins and lasts until late 2005. Beginning in 2006, the gradual deflation period ends and a period of slow inflation begins. Deformation remains positive, with slight undulations, until the end of the time series.

The magmatic source depth and radius (Fig. 6.3b, c) remain nearly stable at 3.1 ± 0.4 km and 1.3 ± 0.1 km, respectively. This is the first model obtained for Campi Flegrei with time-consistent parameters. The limitations and further implications of this approach and results are discussed below.

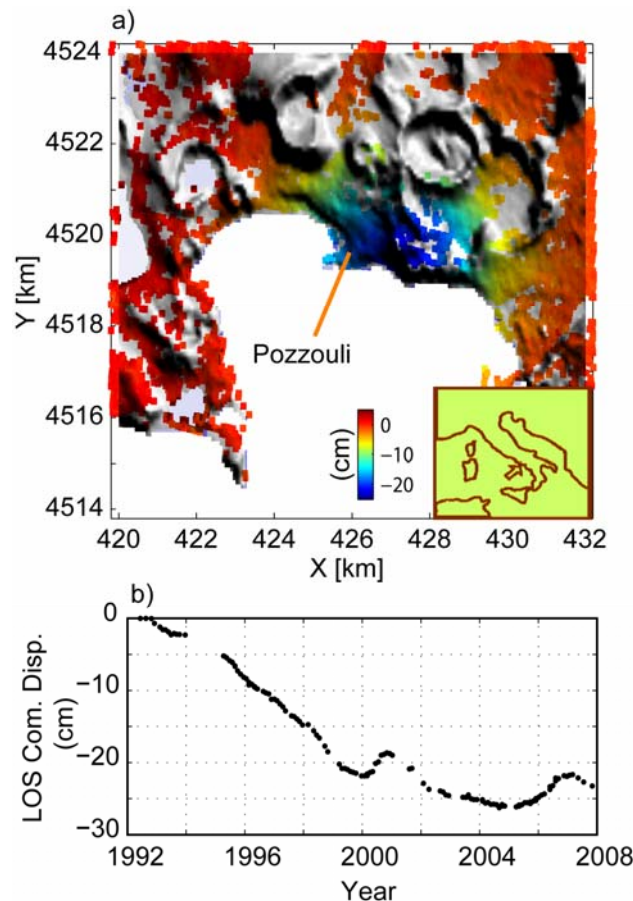


Figure 6.2. *a) The cumulative displacement of the surface over the study period obtained using the SBAS approach in LOS of a satellite with a descending orbit and a 23° incidence angle and azimuth of 190° [Lanari et al., 2007], b) example of the deformation time-series at the center of the caldera at Pozzouli.*

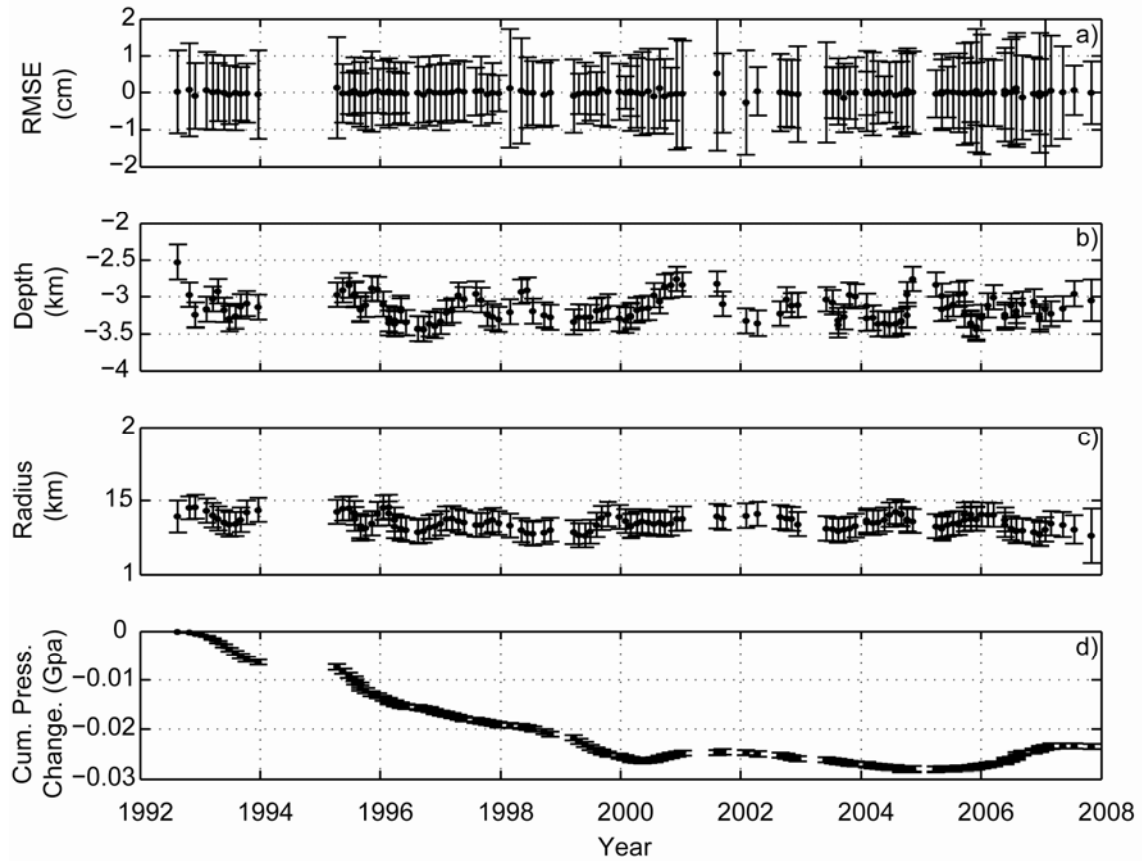


Figure 6.3. RISC-GA-LKF applied to a deformation time-series at the Campi Flegrei volcano. a) The inversion residual (observation - model) for each snapshot of the deformation time series, b) time series of the deformation source depth, c) time series of the deformation source radius, and d) time series of the deformation source cumulative pressure change. All the error bars are in the 95% confidence interval.

6.5 Discussion

We developed and tested a time-dependent, non-linear inverse modeling method using a combination of randomly iterated search and statistical competency Genetic Algorithm (RISC-GA) and a linear Kalman filter (LKF). This novel approach utilizes advantages of the GA for nonlinear inversion and the LKF for estimating dynamic source parameter changes in a volcanic system. After showing the merit of RISC-GA-LKF using a synthetic test, we applied it to a deformation time series for the Campi Flegrei caldera between 1992 and 2008, which was obtained using InSAR. Different aspects of this research might be approached as follows:

6.5.1 Time-dependent modeling as the key for volcano source monitoring

Modern geodetic techniques, such as the Global Positioning System (GPS) and Interferometric Synthetic Aperture Radar (InSAR) time series, provide a valuable tool for dynamic monitoring of volcanoes. This data, together with model simulations, allows for a better understanding of the volcanic process. Most modeling approaches use snapshots of the deformation rather than utilizing the full range of the deformation time series.

To address this question, the Kalman filter (KF) emerged in different forms such as the linear dynamic Kalman filter (LKF), the extended Kalman filter (EKF) or was combined with other tools like the Unscented Transform (UKF) [Grewal and Andrews, 2001; Kalman, 1960; Welch and Bishop, 2001] [Julier and Uhlmann, 1997; Julier and Uhlmann, 2004; Wan and Van Der Merwe, 2000]. Although the KF was broadly applied in different forms, specific limitations remained because the LKF is only

applicable to linear dynamic systems, the EKF is suitable only for locally linear systems and the control parameters are problem dependent for the UKF.

Our new approach combines the randomly iterated search and statistical competency Genetic Algorithm (RISC-GA) and the linear Kalman filter (LKF). The rationale for this combination includes the fact that the requirements of a LKF are good a priori estimation of the initial covariance matrix of the parameters and their initial value. We note that these inputs can be provided by any sophisticated optimization tool, which is able to provide a reasonable confidence interval for the parameters. Though we prefer the RISC-GA implemented here, one should be aware that other optimization techniques might also be applicable. For instance, instead of GA, other Monte Carlo approaches such as Simulated Annealing might be used if a precise assessment of the confidence region for the optimum parameters is obtained. In addition, one should ensure that the initial optimization procedure (step 1) is not trapped in local minima, which is the case for gradient base approaches.

The advantages of our approach are (1) it is applicable to nonlinear systems; (2) the ability for handling irregularly sampled observations; (3) the capacity to incorporate heterogeneous observations; (4) the recursive manner that allows for efficient assessment of new data sets and expanding time series; and (5) the ability to be less sensitive to initial values and the requirement of only a rough estimation of search space.

Moreover, RISC-GA-LKF allows for consideration of model deficiency and observation error, which may lead to a more realistic estimate of the confidence interval. This is an advantage when RISC-GA-LKF is compared to other approaches that usually overestimate the quality of the estimated parameters.

The KF implemented here is built based upon the assumption that the measurement and system noise behaves randomly. In the presence of colored noise, however, one may replace equation (6.3) with those explained by *Zimmerman* [1969] for the optimum gain, covariance and parameters that assess the effect of colored noise in a Kalman filter.

6.5.2 Applications for monitoring the source under the Campi Flegrei volcano

Using RISC-GA-LKF, we modeled the deformation source responsible for 16 years (1992-2008) of unrest underneath CF as a dynamic pressurized spherical source. The average depth and radius of the source are about 3 km and 1.3 km, respectively, in agreement with previous studies (see [*Shirzaei and Walter, 2009*] and references therein).

To estimate the impact of the trade-off between the parameters, we estimated the cross correlation coefficient between the source depth, pressure change and radius. Pressure change correlates to depth and radius by 2% and 18%, respectively. Radius correlates to depth by 12%. The correlation values are relatively low values and imply that the negative effect of trade-off between the source parameters is negligible.

The overall pattern of the cumulative pressure change verifies an apparent contraction period for the source. A reason for this contraction might be cooling or draining of a reservoir [*Natale et al., 2006*]. However, the presence of a single shallow reservoir may be too simplistic and may not explain the occasional inflations in the area, such as those seen in 2001 and mid-2006. Those uplift periods might be explained if hydrothermal activities or recharge of the very shallow reservoir are considered [*Battaglia et al., 2006; Gottsmann et al., 2006; Zollo et al., 2008*]. In our work, we didn't consider the presence of two sources, or layered or non-linear rheologies. Nevertheless, our results provide important new insight into how the reservoir pressure evolution works.

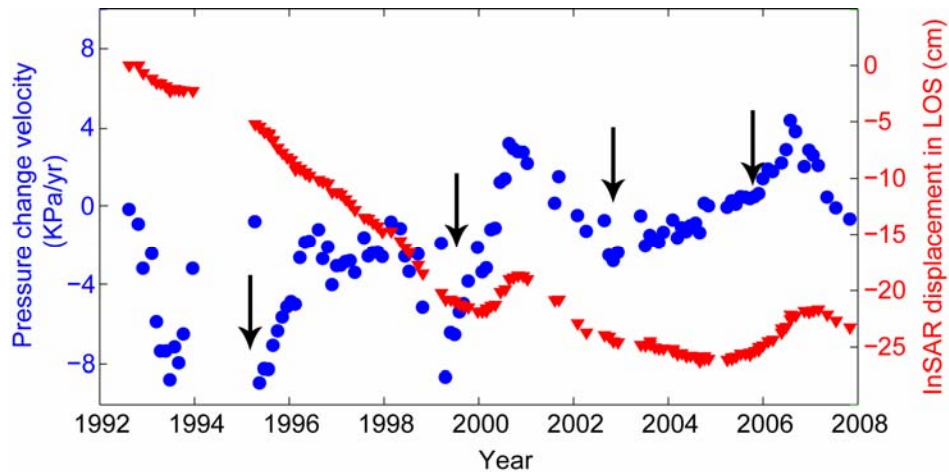


Figure 6.4. The deformation source pressure change velocity compared to the deformation time series. The major episodes of accelerated change are characterized by a linear trend with a similar slope; the timing of the magma flux is more easily distinguishable based on pressure change velocity than deformation time series.

Estimating the velocity of the pressure change indicates four major periods of accelerated change at the magmatic source (Fig. 6.4). The first major period starts from the beginning of the observation period and lasts until mid-1993. The second period of accelerated change occurred between 1995 and mid-1996. Both of these episodes are attributed to expedited subsidence at the surface. The next two periods of accelerated pressure change are associated with uplift episodes and took place between 1999 and 2001 and during 2006. These last two episodes of accelerated pressure changes are immediately followed by seismic swarms. For example, the micro seismic survey of the 2006 acceleration period shows a cluster of seismic events that occurred at 1.5-2.5 km [Saccorotti *et al.*, 2007]. Because the seismicity location is somewhat shallower than the inferred reservoir source, one may speculate whether they are due to reactivation of existing faults above a pressurized reservoir. Most interestingly, the major episodes of accelerated change are characterized by constant velocity change (i.e., constant acceleration), which exhibits a linear acceleration of about $4.5 - 7 \text{ kPa/yr}^2$ during the major periods of activity (Fig. 6.5a).

A similar linear magma flux was reported from in situ volcano observatory data. For instance, the Kupaianaha vent on the east rift zone of Kilauea showed a linear magma flux that was found to be associated with a parabolic change in surface deformation [Denlinger, 1997]. To investigate whether the Campi Flegrei episodes of linear velocity are associated with parabolic surface deformation, we fit a parabolic function to the deformation time series in a piece-wise manner, which is shown in Figure (6.5b). There is very good agreement between the deformation time series and the parabolic functions, which might imply that the periods of linear pressure change at the reservoir resulted in parabolic surface deformation. Assuming V is the reservoir volume and B is the bulk modulus, the following relation between reservoir pressure change dP and volume change dV holds [Denlinger, 1997]:

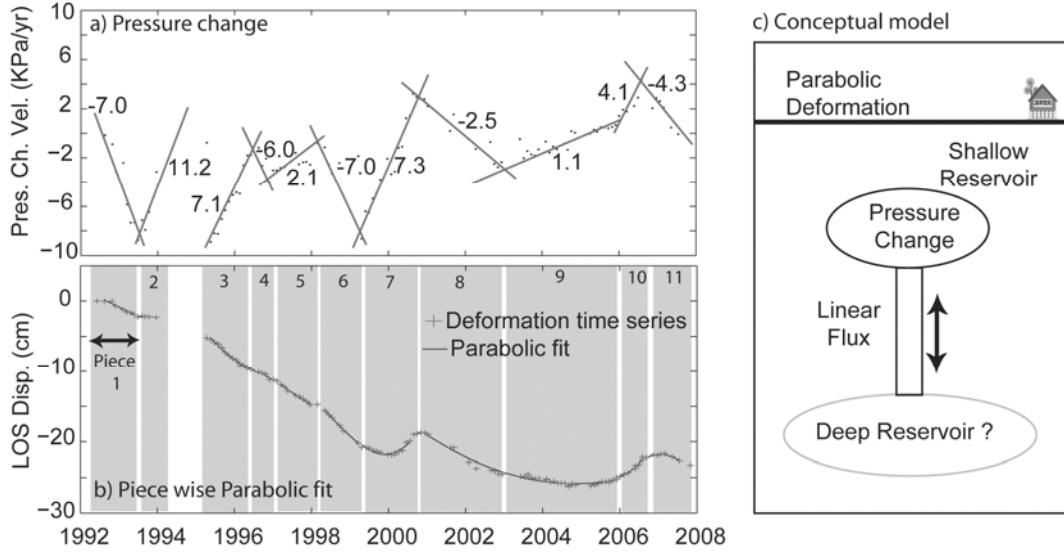


Figure 6.5. a) The linear velocity of the pressure change together with the estimated constant acceleration, b) piece-wise parabolic fit to the time series of the surface deformation at CF, c) conceptual model explaining the relation between the deep and shallow reservoirs underneath CF.

$$\frac{dV}{dP} = V/B \quad (6.11)$$

Assuming an occasional linear flux of bt into the shallow reservoir underneath CF at time t and a constant supply of $a = bt_0$ at time t_0 , the change in the reservoir pressure might be written as follows:

$$\frac{dP}{dt} = -\frac{bB}{V}(t - t_0) \quad (6.12)$$

Solving this differential equation for P yields:

$$P = P_0 - \frac{bB}{2V}(t - t_0)^2 \quad (6.13)$$

where P_0 is the reservoir pressure at time t_0 . Equation (6.13) shows that a linear flux into the reservoir through a feeder may cause a parabolic pressure change with linear velocity. Because the surface deformation is a linear function of the pressure change, it also follows a parabolic function. Therefore, the dynamics of long- and short-term uplift and subsidence periods may be controlled by a volume flux, possibly coming from a deeper reservoir into the shallow hydrothermal source.

Seismic tomography underlined the existence of a shallow reservoir and a deep magma chamber beneath CF [Zollo *et al.*, 2008]. However, the way that these two reservoirs communicate was not well understood. Our study suggests that the shallow reservoir at CF is occasionally fed through a vent by a linear flux of material and that the vent might be connected to a deeper reservoir. Figure (6.5c) presents a conceptual model visualizing this hypothesis. This model implies that the pulses of fluid, or magma flux, from the deeper source to the shallow reservoir are associated with the linear velocity of the pressure change and the parabolic surface deformation at the summit. The trigger might be an external source such as tectonic loading, or an internal component such as a pressure change at the deep magma chamber. Our observations are the consequence of these triggering mechanisms. This demonstrates that monitoring of surface processes may successfully lead to monitoring the source parameters as a function of time only if changes in the source parameters are physically well understood. New efforts for hazard assessment and early warning may emerge from this.

6.6 Conclusion

We developed and tested a new approach for time-dependent inverse modeling. This approach is a combination of Genetic Algorithm and Kalman Filter. Therefore, it encompasses the advantages of both in terms of efficiency and robustness. This integration allows for the consideration of very

heterogeneous observations, complex and nonlinear dislocation sources and efficient processing time that may also be applicable for early warning purposes.

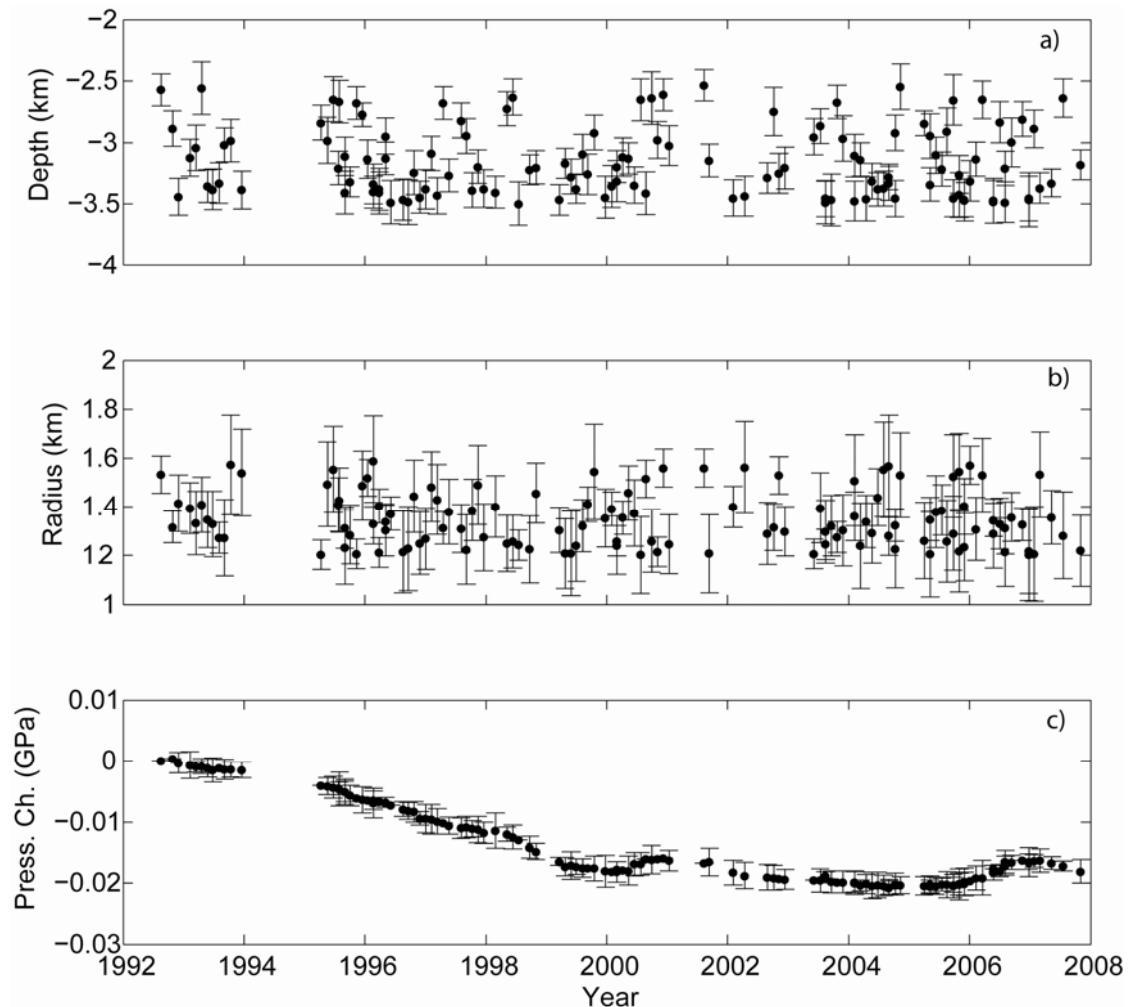
Validation tests were successfully performed and demonstrated based on a synthetic example. This simulation highlighted the capabilities of this approach for dynamic modeling of volcano-tectonic deformation sources.

Following the validation test, we applied this approach to a deformation time-series obtained at the Campi Flegrei caldera between 1992 and 2008 [Lanari *et al.*, 2007]. The most striking results of this study are the discovery of an approximately fixed source radius (~ 1.3 km) as a function of time. Upon inversion, the source pressure change is found to be responsible for a variable deformation field, which often shows different episodes of linear inflation and deflation associated with parabolic deformation at the surface. This linear pressure change and parabolic deformation, was interpreted using differential equations as a linear flux into the shallow reservoir from a deeper magma chamber. This provides new insight into how the deep and shallow reservoirs at Campi Flegrei communicate.

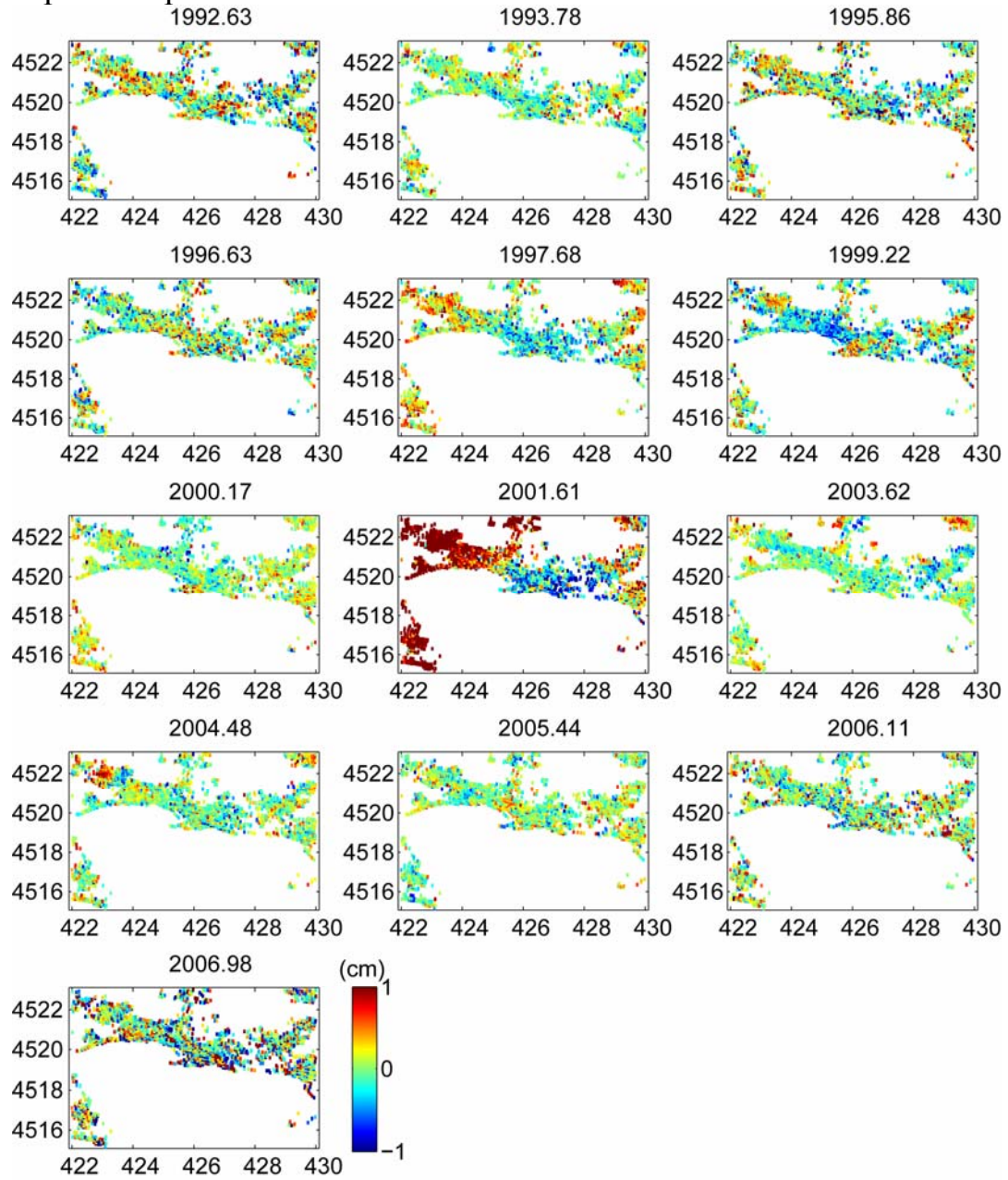
Consequently, we argue that the method presented here has advantages for time-series modeling, and it is well suited for source monitoring and further applications in volcanic and tectonic fast response systems.

6.7 Auxiliary material

6.7.1 Inversion result for the time series of deformation at Campi Flegrei using RISC-GA



6.7.2 Spatiotemporal distribution of the inversion residuals at selected time steps



Chapter 7

Interplay of deformation sources at Hawaii Island investigated through InSAR time series and time-dependent modeling¹

M. Shirzaei and T. R. Walter

Section 2.1, Dept. Physics of the Earth, GFZ German Research Centre for Geosciences, Telegrafenberg, D – 14473 Potsdam, Germany

Abstract

Volcanoes are known to closely interact with the tectonic environment. For instance they may be controlled by active regional-tectonic faults and erupt after earthquakes. Similarly, adjacent volcanoes interact with each other in time and space, as suggested for the Hawaiian volcanoes Kilauea and Mauna Loa. As shown herein by new satellite radar data, this interplay on Hawaii is even more complex than previously thought. It involves magma chamber pressure changes, dike intrusions, slow earthquakes and ground subsidence. The affected regions are the Mauna Loa and Kilauea volcano summits, their active rift zones, the island's unstable southeast flank and even the city of Hilo. Using data acquired by the European satellite ENVISAT, we present a five-year spatiotemporal InSAR analysis of the deformation signals recorded between 2003 and 2008. The data suggest that most of the deformation sources are acting in chorus. Magma intrusions at the Mauna Loa chamber and the intrusions into the Kilauea rift are correlated in time, and they also change with gravity-driven flank movement events. Some of the events occur silently underneath the Kilauea south flank, such as slow earthquakes that may largely affect all of the active magmatic systems and reverse their sign of correlation. This study of the interplay between multiple deformations shows that the sources are correlated, providing a better understanding of Hawaiian volcano activity. It may also lead to new methods for assessing the hazards that arise during volcano-tectonic activities elsewhere.

7.1 Introduction

Modern monitoring techniques, such as the Global Positioning System (GPS) and Interferometric Synthetic Aperture Radar (InSAR) time series, can provide a high precision map of the ground deformation field, and so hold great potential for detecting volcanic activity precursors. In combination with model simulations, such geodetic data allow a better understanding of, e.g., volumetric changes, intrusions and fracture propagations under active volcanoes [Dzurisin, 2006]. High precision volcano monitoring has also been used to investigate coupling, between magmatic and tectonic activity. For instance, complex interaction with tectonic earthquakes which may trigger the unexpected awakening of dormant volcanic systems [Amelung *et al.*, 2007; Darwin, 1840;

¹ MS developed the approach and processed and inverted the data. All authors were involved in discussion and writing the paper.

Eichelberger and Izbekov, 2000; Hildreth and Fierstein, 2000; Nostro et al., 1998. In some cases, the coupling of a volcano to its surroundings also involves neighbouring volcanoes, which show correlating activity changes or even erupt in chorus [*Walter, 2007*]. At Hawaii Island (Fig. 7.1), one of the most active and intensively studied of volcanic complexes, previous work suggests various modes of interaction, such as between the adjacent rift zones [*Jaggard and Finch, 1929*], between flank movements and eruptions [*Swanson et al., 1976a*], between the volcanoes Mauna Loa and Kilauea [*Miklius and Cervelli, 2003*], or between earthquakes and rift zone intrusions [*Walter and Amelung, 2006*].

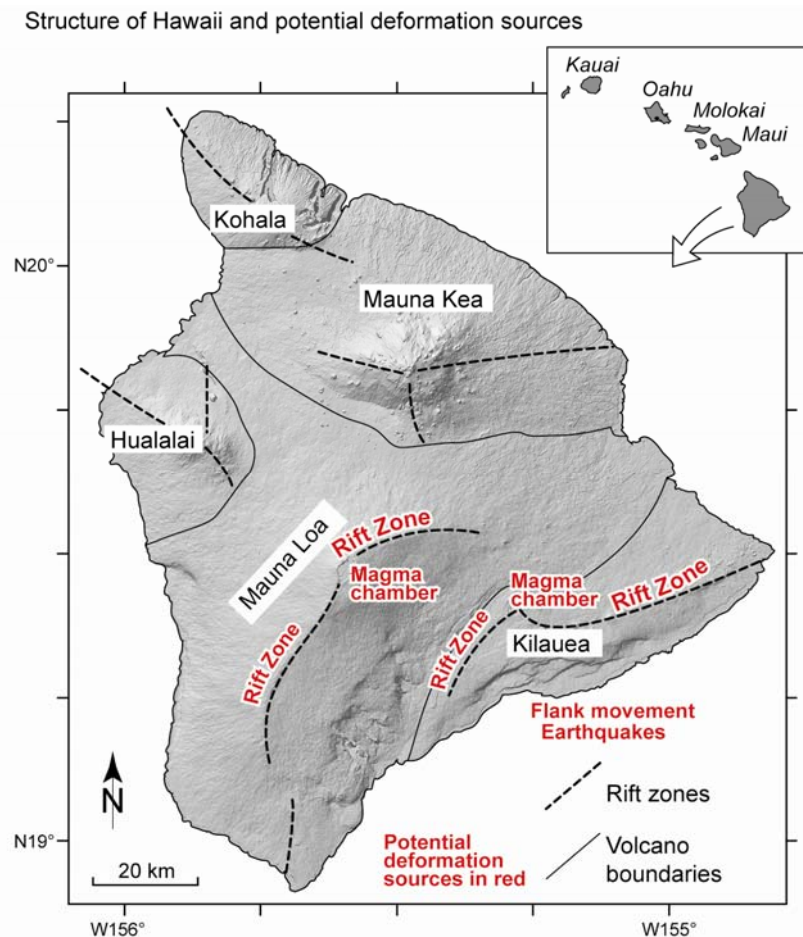


Figure 7.1. Overview of the study area, Hawaii Island, and its main volcanic and tectonic systems.

In this paper, we analyze the 2003-2008 Hawaii Island activity and deformation sources. First, we investigate the dynamics of each individual magmatic and tectonic source. Second, we explore the type and degree of mutual interaction between these sources. To achieve these goals, we utilize a high number of interferometric synthetic aperture radar data to generate a spatiotemporal time series of the deformation field. Using a time-dependent modeling approach, we then locate and quantify the dislocation sources responsible for the observed surface deformation. We thereby elucidate spatiotemporal details of the various adjacent deformation sources in Hawaii with the aim of better understanding magma dynamics and possibly even, identifying precursors for volcanic activity.

7.2 Tectonic and magmatic activity at Hawaii Island

Hawaii Island hosts five volcanoes (Fig. 7.1) with two of them, Mauna Loa and Kilauea, being amongst the most active volcanoes worldwide. The Island's southeastern flank is gravitationally unstable; the substratum is the location of intermittent large earthquakes.

Deformation at Kilauea and Mauna Loa was regularly measured already since the appearance of leveling and triangulation techniques and rapidly this observation became an important parameter for

routine monitoring [Decker *et al.*, 1966] by the U.S. Geological Survey at the Hawaiian Volcano Observatory [Dzurisin, 2006]. The potential for use of geodetic techniques as tools for forecasting was first shown through repeated electronic distance measurements across the Kilauea Caldera that demonstrated and quantified magma reservoir inflation prior to eruptions [Decker *et al.*, 1966]. These inflations were due to the interplay of magma intrusions at magma chamber and fissure eruptions, where, by intrusion first causes expansion of a magma reservoir before propagating into the rift zones. Improving time series resolution allowed demonstration that these events are associated and possibly temporally related to instability and the lateral movement of the southern flank of Kilauea [Dvorak *et al.*, 1983]. To increase and refine the data set, Dvorak and colleagues considered leveling, tilt and electronic distance measurement (EDM) data in joint dislocation inversion models, pointing to an interaction of the local deformation sources with earthquake activity or episodic block movements. The occurrence of the 1975 magnitude 7.2 Kalapana earthquake vividly demonstrated that flank instability may impact upon hazard potential, by releasing accumulated stress, by disrupting shallow magma pathways, and by influencing storage location, ascent rates, intrusion and eruption volumes [Dvorak *et al.*, 1994].

The emergence of space-based geodetic techniques since the mid 1990s has increased the understanding of the interplaying deformation processes. GPS data induced that the southern flank may be dislocating as individual segments [Owen *et al.*, 1995]. A significant improvement of the vertical deformation component was shortly afterwards achieved with satellite radar data, whereby interferograms of the reflected phase contribution yield a near complete data observation field with up to > 1 Million of observation points as defined by the pixel size [Rosen *et al.*, 1996]. The interaction between volcanism and tectonic events could be identified and investigated in much greater detail using these novel techniques [Amelung *et al.*, 2007; Cervelli *et al.*, 2002; Owen *et al.*, 2000; Segall *et al.*, 2001; Segall *et al.*, 2006]. Whilst, individual periods of eruptions and earthquakes on Mauna Loa and Kilauea have been investigated, a complete InSAR-based time series study of the different sources as well as their correlation remained to be made.

7.3 Methods

To investigate the deformation pattern, the responsible dislocation sources and their temporal correlation on Hawaii Island we applied (a) an InSAR time series with new filtering techniques that allow yielding high precision observations, (b) deformation data comparison to reliable and continuous GPS stations, (c) time dependent dislocation model simulations using Genetic Algorithm and Kalman filtering technique, and (d) a cross correlation analysis that shows directivity and temporal proximity of related events.

7.3.1 Wavelet based InSAR time series

Hawaii's deformation field was obtained by time series of InSAR images that measures differences in the phase of the electromagnetic waves returning to a satellite [Ferretti *et al.*, 2007]. The InSAR technique can measure sub-centimeter rate changes of the ground motion over time spans of days to years [Hanssen, 2002].

So far, two broad categories of InSAR time series methods have been introduced: Permanent Scatterers (PS) [Ferretti *et al.*, 2001a] and Small Baseline Subset (SBAS) [Berardino *et al.*, 2002; Schmidt and Bürgmann, 2003]. The PS method refers to the category that uses a single master interferogram and identifies individual pixels that are of high quality (so-called elite pixels) on the basis of their phase stability in time or space. In contrast, the SBAS method employs multi-master interferometry with a small spatial baseline and recognizes elite pixels based on spatial phase coherence. Both methods favor a sparse unwrapping approach to reduce the negative impact of noisy pixels and a filtering approach for reducing topographic and atmospheric artifacts [Berardino *et al.*, 2002; Ferretti *et al.*, 2001a; Hooper *et al.*, 2007]. Both time series methods allow investigation temporarily varying activities. Disadvantages are, however, that parts of the processing chains are based on an a priori model, which may introduce systematic artifacts in the displacement observation, and that a relatively large number of images are required. In the following, we employ the advantages

of PS and SBAS but we overcome systematic biases and wavelike disturbances by utilizing new filtering approaches. These new approaches are briefly summarized herein and are further detailed in the electronic appendix and fully explained and validated in *Shirzaei and Walter*, [2010b].

The applied suites of filters include spatiotemporal wavelets and Kalman-based approaches that we adjusted to reduce the error contributions from inaccuracy in the digital elevation model (DEM), from atmospheric delay and from temporal decorrelation noise. Wavelets have been shown to be sophisticated for recognizing hidden patterns in signal [*Kumar and Fofoula-Georgiou*, 1997; *Mallat*, 1989; *Torrence and Compo*, 1998]. In addition, we could evaluate the signal adaptively. For example for noise reduction, the wavelet filter parameters may be adjusted by using criteria obtained directly from the signal [*Donoho and Johnstone*, 1994].

The wavelets were used herein to identify elite pixels by statistically integrating all spatial and temporal information. The pixel selection step begins by estimating the noise of each pixel in all interferograms through a combination of Wiener filter and wavelet multi-resolution analysis [*Zha et al.*, 2008]. Having a noise history for each individual pixel allows probabilistic evaluation of the quality of individual pixels in respect to the population of all other examined pixels. This identifies less noisy (i.e. elite) pixels. Although the definition of elite pixels is relative, this approach helps to identify less corrupted pixels, leads to more accurate phase unwrapping and results in data refinement. Following identification of elite pixels, a sparse phase unwrapping approach is applied to estimate absolute phase values [*Costantini and Rosen*, 1999].

Other sources of environmental errors, such as DEM inaccuracy and atmospheric delay, were reduced by considering the problem as a non-stationary process. Therefore, we investigate different wavelet based filters. The contribution of DEM inaccuracy Δh in phase observation at a pixel located at a given coordinate (ζ, η) in an interferogram k may be formulated as following [*Hanssen*, 2002];

$$\phi_{\text{topo}}^k(\zeta, \eta) = \frac{4\pi}{\lambda} \frac{B_{\perp}^k}{R^k(\zeta, \eta) \sin \theta(\zeta, \eta)} \Delta h \quad (7.1)$$

where, R^k is slant range from satellite to pixel (ζ, η) , B_{\perp}^k is the perpendicular base line for interferogram k , θ is the local incidence angle and λ is radar wavelength. This equation may be expanded to Legendre polynomials as following;

$$\phi_{\text{topo}}^k(\zeta, \eta) = \frac{4\pi}{\lambda} \frac{\sqrt{2} B_{\perp}^k \Delta h}{R^k(\zeta, \eta)} \sum_{m=0}^{\infty} P_m(\cos^2 \theta(\zeta, \eta)) = A^k(\zeta, \eta) \sum_{m=0}^{\infty} P_m(\cos^2 \theta(\zeta, \eta)) \quad (7.2)$$

where P_m is the Legendre polynomial of the order m . Equation (7.2) shows that the DEM error not only affects the amplitude of observed deformation, but also has a frequency property in space. By applying a 2D filter based on Legendre polynomial wavelet, one can extract and even eliminate components with similar spatial frequency properties (for more detail see [*Shirzaei and Walter*, 2010b]).

To reduce the contributions of atmospheric delay, we developed a 3D filter as a tensor product of 2D discrete and 1D continuous wavelet transforms. We exploit the fact that the atmospheric delay holds a certain spatial and temporal decorrelation length while it is a non stationary process. This allows application of an adaptive wavelet-based filter with a variable window size and with the ability to extract such specific spatiotemporal components. Similarly, for an atmospheric correction, the 3D deformation field is decomposed with the 3D wavelet transform and the components that have specific spatial correlation length and temporal frequency [*Shirzaei and Walter*, 2010b]. Applying above mentioned filtering scheme assures us that most of environmental artifacts are reduced and only the temporal noise may remain. We treat that by implementing a Kalman Filter similar to the approach used in continuous GPS data processing [*Hofmann-Wellenhof et al.*, 2000].

WabInSAR Flowchart

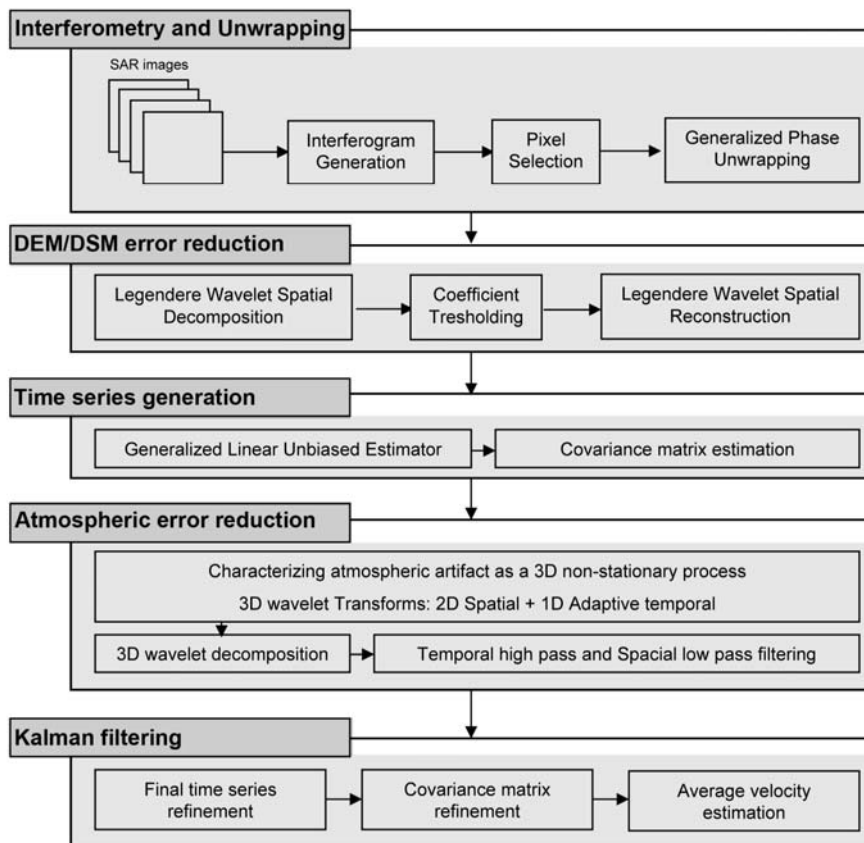


Figure 7.2. Flowchart of the wavelet-based InSAR approach, applied for generating a deformation time series and filtering significant environmental artifacts.

In summary, Figure (7.2) presents the flowchart summarizing the steps of our InSAR time series approach named ‘WabInSAR’. WabInSAR stands for Wavelet Based InSAR and comprises five major steps, beginning with standard interferogram generation, pixel selection and sparse phase unwrapping [Costantini and Rosen, 1999]. The phase unwrapping achieved here using two dimensional minimum cost flow [Costantini, 1998]. Then we apply the filter based on Legendere wavelets for DEM error correction. To generate a time series of the deformation field in the following stage, the unwrapped phase corrected for DEM error is inverted by using best linear unbiased estimate approach [Bjerhammar, 1973] applicable to full rank or rank deficient problems. The last two filtering steps are made to correct atmospheric delay and to reduce the temporal noise by using a Kalman filter [Hofmann-Wellenhof et al., 2000] (further details are presented in [Shirzaei and Walter, 2010b]).

7.3.2 GPS processing

The continuous GPS (cGPS) data used in this study (Fig. 7.3b, c) are all provided by UNAVCO, a non-profit, membership governed research consortium dedicated to supporting and promoting high-precision measurement techniques.

The cGPS data are sampled at the rate of 30 seconds. We used the Bernese 5 software [Dach et al., 2007] to solve the daily coordinate of the cGPS stations in ITRF2005 reference frame. The precise orbit data are obtained from IGS. To generate a time series of the displacement field for each GPS station we use a Kalman filter [Hofmann-Wellenhof et al., 2000]. In Figure (7.3b), c each GPS displacement point is the average coordinate of the station within 3 days that temporally spans the WabInSAR observation point and was projected to satellite’s Line of Sight (LOS) for comparison with InSAR time series.

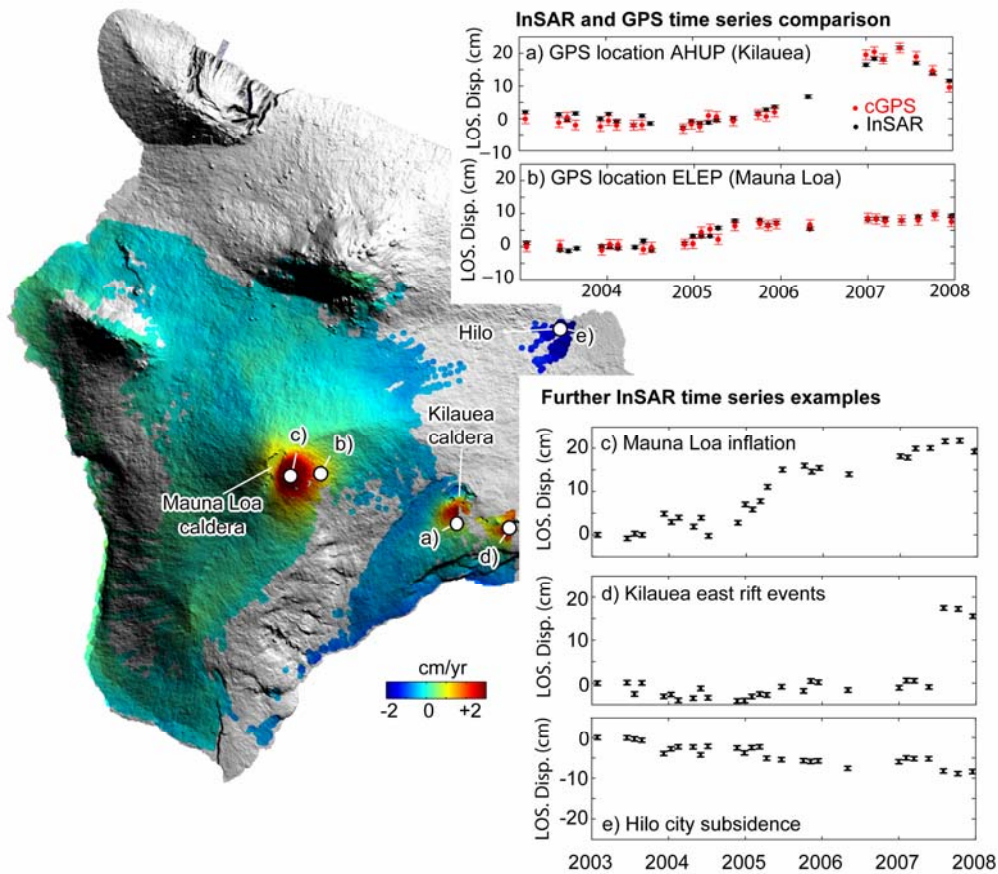


Figure 7.3. The deformation of Hawaii Island as seen from space. Main image shows the average change in the line-of-sight radar acquisition obtained via a five-year InSAR time series. The warmer colors show a movement of the ground towards the satellite at a rate of up to 4 cm/year. The satellite geometry is descending (azimuth $\approx 190^\circ$) with an incidence angle of 23° . a, b) InSAR time series at location of the cGPS stations are available. c-e) examples of InSAR time series at areas with significant displacement. All of the error bars reflect a 95% confidence level.

7.3.3 Time dependent inverse modeling

To understand the causes of the observed deformation, we developed a time-dependent non-linear inverse model simulation. This method consists of two main operators: (i) a non-linear inversion method, Genetic Algorithm (GA), as a minimum spatial mean error estimator [Shirzaei and Walter, 2009]; and (ii) a recursive filter, Kalman Filter (KF), to generate time series of the deformation source parameter as a minimum temporal mean square error estimator [Grewal and Andrews, 2001; Hofmann-Wellenhof et al., 2000]. These two operators are combined in an iterative manner [Shirzaei and Walter, 2010a].

To relate observation to deformation source parameters, the mathematical model comprises several laterally connected rectangular dislocation planes [Okada, 1985] mimicing the rift zones at Mauna Loa and Kilauea. In addition, two pressurized spherical sources [McTigue, 1987] are considered as magma chambers located underneath the caldera of Mauna Loa and Kilauea. Slip along the basal decollement beneath Kilauea's east flank and compaction underneath Hilo city was simulated using two sub-horizontal rectangular dislocation planes [Okada, 1985]. We assumed a homogeneous elastic half-space and initialized all model source parameters based on earlier works [Amelung et al., 2007; Cervelli et al., 2002; Okubo et al., 1997; Segall et al., 2006].

7.3.4 Cross correlation

After obtaining a time series of the dislocation source parameters, we estimate the linear correlation between two source parameters x (e.g. magma chamber pressure change) and y (e.g. dike intrusion volume) with associated variance-covariance matrix of Q_x and Q_y , respectively, by calculating the cross correlation coefficients (C_{xy}) as follows [Meyer, 1970];

$$C_{xy} = \frac{E[(x - E(x))(y - E(y))]}{\sqrt{E[(x - E(x))^2]E[(y - E(y))^2]}} \quad (7.3)$$

,where, $E[.]$ is the statistical expectation. The obtained value reflects the strength of a linear relation between each data pair and helps to understand their relationships in future.

To assess the quality of the correlation coefficients, we may reduce the problem to identifying the slope of a best fitting line to each data pair as follows;

$$y = ax + b \quad (7.4)$$

,where, a is slope and b is the y axis intersection. For instance, $\tan^{-1} a$ with values of 45° , 90° and 135° is equivalent to C_{xy} with values of 1, 0 and -1, respectively.

The main difference to the standard least square (SLS) regression is that inhere a method should be applied that takes the uncertainty of both the x and y axes into account. This problem is in a general way already formulated by [Deming, 1943], who suggested to minimize following cost function;

$$R = r_x^T p_x r_x + r_y^T p_y r_y \quad (7.5)$$

where $r_x = x - E(x)$, $r_y = y - E(y)$, $p_x = Q_x^{-1}$ and $p_y = Q_y^{-1}$. The problem of finding a and b with uncertainty in both x and y is the so-called *Total Least Square Problem* (TLSP) [Krystek and Anton, 2007]. In TLSP, minimizing equation (7.5) is equivalent to minimizing the orthogonal distance of the fitting line to both axes. More details of the concepts of TLSP, the analytical solution for the parameters a and b , and the associated variance-covariance matrix is given in [Krystek and Anton, 2007; Schaffrin and Wieser, 2008]. Analyzing TLPS allows us to assess the uncertainty of the correlation coefficient by considering the uncertainty of abscissa and ordinate data sets at the same time.

In the following, we are therefore able to analyze the results obtained for Hawaii Island, in terms of its deformation pattern, source parameters and source interplay analysis as a function of time.

7.4 Results

The European environmental satellite ENVISAT flies and acquires radar images over Hawaii Island every 35 days. For this study, we utilized 27 radar images acquired between 2003 and 2008 to process about 170 interferograms for generating a spatiotemporal map of the surface deformation. The obtained time series shows variations in the deformation velocity in the satellite's line of sight (LOS) as seen in Figures (7.3, 4).

7.4.1 Deformation field and data validation

Validation tests were performed by comparing InSAR time series and available cGPS data sets. To achieve this comparison, we made a spatial averaging of the WabInSAR data in a circle centered at each cGPS station with radius of 250 m. This averaging is done for each snapshot of the time series and results in a WabInSAR time series comparable to cGPS data.

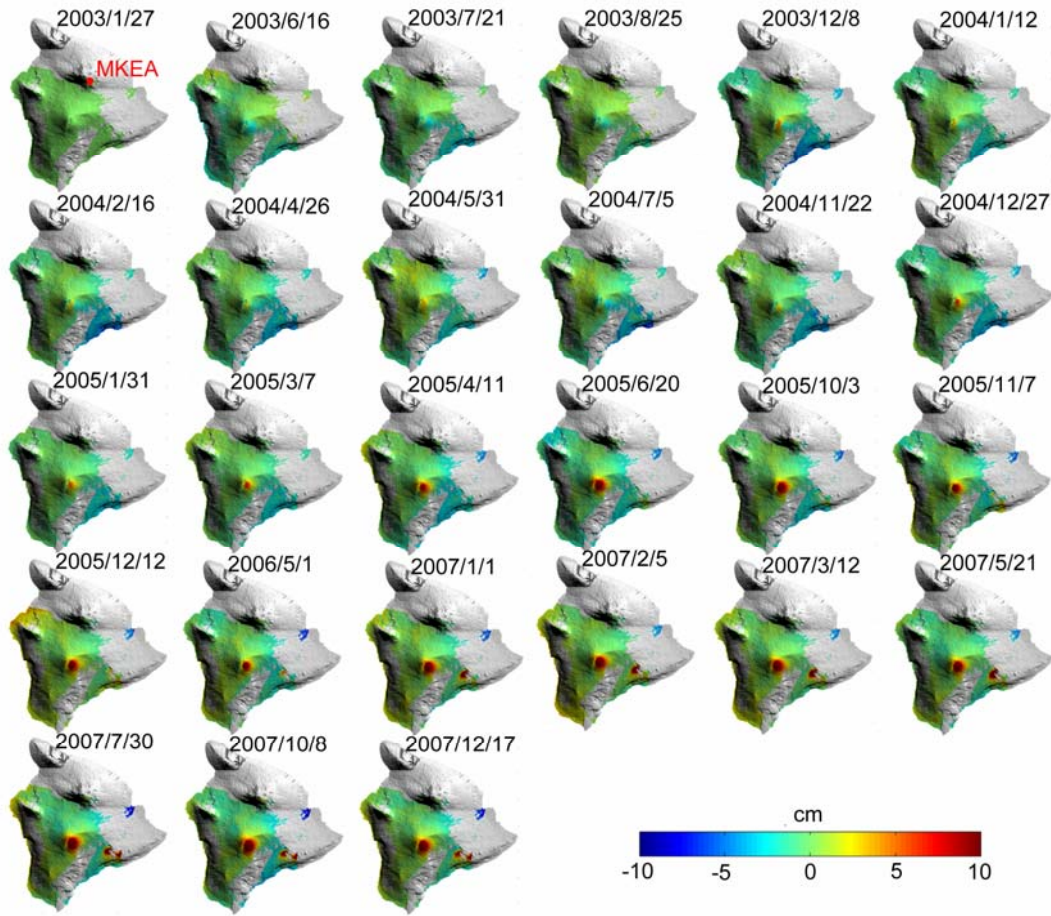


Figure 7.4. Spatiotemporal evolution of the deformation field over Hawaii Island, as obtained using WabInSAR. Each image presents the cumulative displacement since beginning of the time series in respect to the MKEA GPS station (filled circle) located at coordinate of $(-155.45, 19.80)$. For better illumination, the color-bar is saturated between -10 cm (i.e. away from satellite) and $+10$ cm (i.e. toward the satellite).

The average of n samples $\{l_1, l_2, \dots, l_n\}$ with variance of σ is \bar{l} with variance of $\bar{\sigma} = \frac{\sigma}{\sqrt{n}}$, hence is an unrealistically small value here, because of the high number of redundant observations for estimating σ and the large number of pixels in the vicinity of the cGPS station. Therefore, in all evaluations, we have considered an uncertainty of $0.5 - 1$ cm for the WabInSAR time series. These errors are considered by us to be more realistic than standard error propagation analysis. The precision of cGPS data is better than a few millimeters [Dach et al., 2007]. Nevertheless, after projecting components of the 3D displacement field into LOS, we may consider an uncertainty of $1-1.5$ cm in the 95% confidence region for cGPS data set.

The observations at the cGPS station *AHUP*, which is located south of the Kilauea caldera (Fig. 7.3a), show a small amount of deformation over the first three years and a pronounced uplift period at *AHUP* between 2006 and 2007. The time series of WabInSAR selected at the vicinity of *AHUP* site agrees well with the cGPS time series (Fig. 7.3a). Similarly, the other time series of WabInSAR is consistent with the cGPS observations (Fig. 7.3b). Assuming that the cGPS measurements provide the true values, the average accuracy of the InSAR time series is better than 0.5 cm (see [Shirzaei and Walter, 2010b]).

Thus, the main advantage of the satellite radar technique applied in this study is that we obtain deformation data from about $650,000$ coherent pixels with a resolution of $80 \text{ m} \times 80 \text{ m}$ and an accuracy of <0.5 cm. The obtained deformation time series enables us to further investigate Hawaii's deformation episodes. For instance, significant uplift was detected near the two central regions of

Mauna Loa and Kilauea (Fig. 7.3, 4), causing inflation in the volcano summits that increased during 2005 and 2006 (Fig. 7.4). Moreover, an unexpected finding was the continuous subsidence of the city of Hilo at the rate of 0.8 cm/yr (Fig. 7.3e, 4). In the next section, we describe the time dependent modeling designed to explore the causes of this complex deformation field.

7.4.2. Time dependent modeling of the deformation sources

For time dependent source modeling, the dislocation model parameters are constrained by using the parameters summarized in Table (7.1). The Genetic algorithm is initialized by population size of 100, iteration number of 500, mutation rate of 0.65 and selection rate of 50% (for detail see [Shirzaei and Walter, 2009]). By simulating the strength, geometry and location of the dislocations as a function of time, the InSAR and GPS displacement data at all pixels and stations could be reproduced with a spatial root mean square error better than 0.5 cm (Fig. 7.5b).

Table 7.1. The initial bounds for dislocation source parameters

	Parameter	Lower bound	Upper bound
Rift dikes	Coordinates (km)*	Rift trace - 5	Rift trace + 5
	Depth (km)	6	14
	Width (km)	6	14
	Dip (deg)	70	110
Magma chamber	Depth (km)	2	7
	Radius (km)	0.1	Depth lower bound
	Horizontal location (km)*	Maximum deformation location - 5	deformation location + 5
Basal decollement	Coordinates (km)	Rift trace - 10	Rift trace + 10
	Depth (km)	6	14
	Width (km)	10	30
	Dip (deg)	-10	10
Hilo plane	Coordinates (km)*	Subsidence area - 5	Subsidence trace + 5
	Depth (km)	1	6
	Width (km)	1	6
	Dip (deg)	-10	10

* the location was constrained approximately, and freedom of ± 5 km was allowed for the source

The deformation occurring at the volcano summits of Mauna Loa and Kilauea was best explained by magma chambers located 4 ± 0.5 km and 3.8 ± 0.8 km below the surface, respectively. Similar reservoir depths have been constrained by earlier studies based on other independent data. The reservoir depth under Kilauea is thought to be between 2.5 and 5 km depth [Cervelli and Miklius, 2003; Johnson, 1992; Okubo et al., 1997; Rowan and Clayton, 1993; Wright and Klein, 2006; Yang et al., 1992]. Under Mauna Loa, earlier GPS and InSAR studies constrained the depth to the range of 3.5 – 5 km [Amelung et al., 2007; Okubo et al., 1997], being slightly offset from the summit caldera to the southeast. Thus our results on source locations and depths are well in agreement with these earlier findings.

Additionally, we found that the rift zones opened at a depth between 1 and 10 ± 2 km. At this stage, we did not consider distributed slip models. The plan view of the geometry of the segmented rift zone in the model follows the morphological expression of the rift zone. Although being simplified, the rift zone model results are again well in agreement with previous works and suggest rift zone activity from the surface down to the lower depth of the edifice at 8-12 km [Amelung et al., 2007; Segall et al., 2006]. Furthermore, we reproduced the movement of the south flank by slip along a decollement plane located at an average depth of 10 ± 1 km, which is again in agreement with independent studies [Rowan and Clayton, 1993; Segall et al., 2006]. The subsidence of the city of Hilo was simulated by considering a compacting layer; the location of this layer was found by the inversion technique, and the average depth was 3.7 ± 1.5 km, in agreement with the depths of the soft hyaloclastite layers identified by a deep scientific borehole near the city (ICDP website, Hawaii Scientific Drilling Project, <http://hawaii.icdp-online.org>).

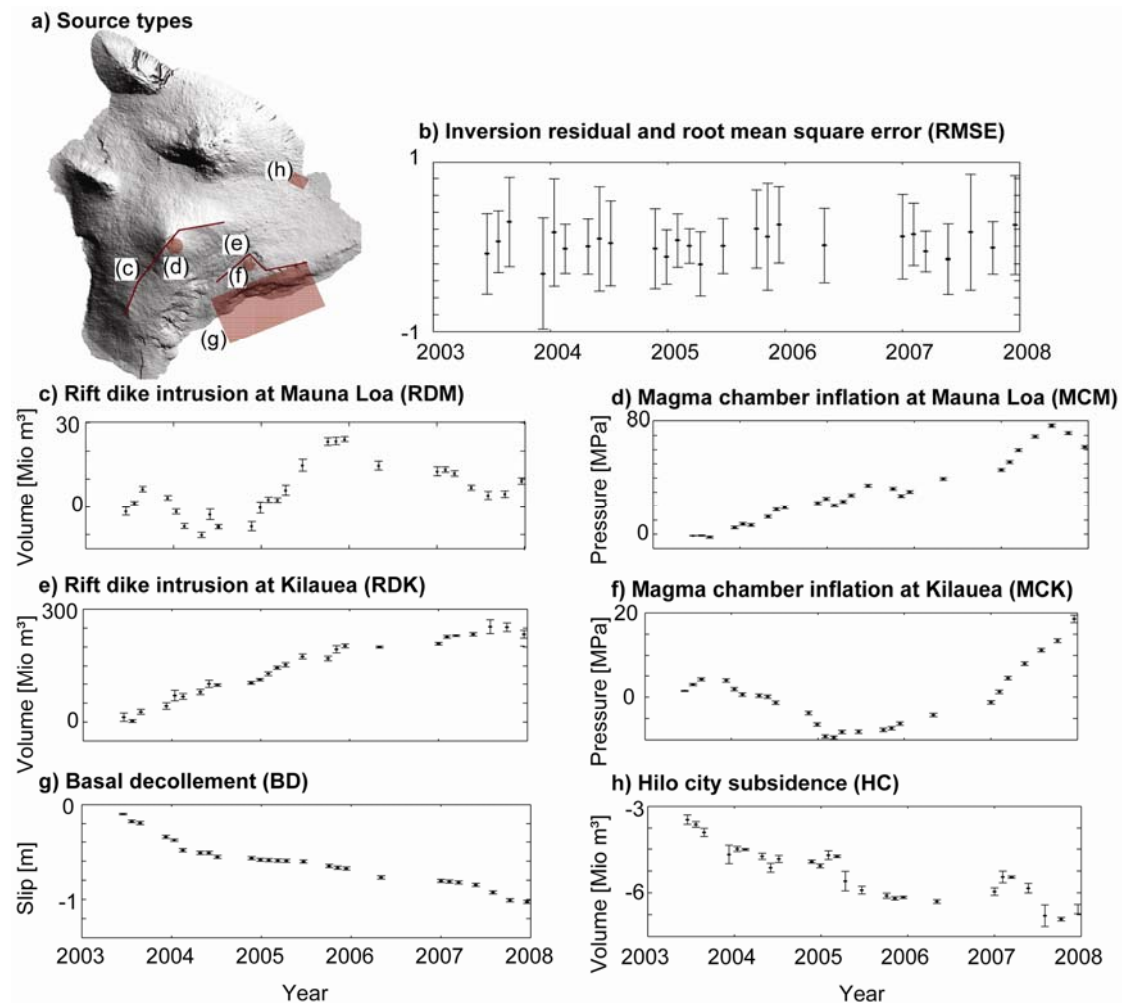


Figure 7.5. Evolution of source parameters for the modeled magma chambers, rift zone dikes, flank slip and city subsidence. *a)* schematic view of the position of simulated dislocation sources, *b)* inversion residuals and root mean square error for each date of the time series and *c-h)* the strengths of the deformation source parameters obtained by non-linear time-dependent data inversion. Here, we used a mathematical formula that relates the simulations to the measurements and we consider several laterally connected dike-like dislocation planes [Okada, 1985], following the rift zone strike directions at Mauna Loa and Kilauea. The spherical pressurized sources [McTigue, 1987] correspond to the Mauna Loa and Kilauea magma chambers. Moreover, sub-horizontal dislocation planes [Okada, 1985] were employed to simulate the possible basal decollement slip at Kilauea and the substratum compaction underneath Hilo city. All of the simulations were performed in a linear elastic half-space with a Poisson's ratio of 0.25 and a shear modulus of 10 GPa. All of the error bars reflect a 99% confidence level.

7.4.3 Identifying volcanic and tectonic interactions on Hawaii Island

All of the detected magmatic and tectonic deformation sources showed temporal variations (Figs. 7.5c-h). At the Mauna Loa rift dike, large fluctuations in the volume flux were found (Fig. 7.5c), possibly related to dike opening (2005-2006) and dike closure (2006-2007). At the same time, the Mauna Loa magma chamber displayed a nearly linear increase in pressure (Fig. 7.5d). Thus, at first glance, it appears that the sources were acting independently. However, by examining shorter periods and the temporal distribution of the rate changes, we found that most of the sources were acting together. For instance, the 2007 pressure increase of the Mauna Loa magma chamber occurred at the same time as the pressure increase of the magma chamber beneath Kilauea, which may imply the beginning of an augmented phase of magmatic activity at both of the Hawaiian volcanoes. As induced by our models, the total volume of intruded magma at the Kilauea rift dike was almost 20 times the

volume at the Mauna Loa rift dike, while the volume of magma in the magma chamber was 4 times smaller. A comparison of the relative intruding volumes hence shows that the magma chamber at Mauna Loa currently plays a more important role in magma storage than the Kilauea magma chamber. To study the relationship between the different deformation sources, we investigated their linear cross correlation and associated uncertainty (Fig. 7.6a, b). A correlation coefficient with an absolute value close to 1 indicates a significant correlation and the uncertainty close to 0 means the high precision of the estimation. This statistical test shows that the Kilauea rift dike intrusions are correlated in the long-term (over the five years) with both Mauna Loa magma chamber inflation and basal slip underneath the Kilauea flank (Fig. 7.6a). Hence, the long-term correlation test confirms interactions between both Mauna Loa and Kilauea [Miklius and Cervelli, 2003] and the rift dikes and flank movement [Cayol *et al.*, 2000; Dieterich *et al.*, 2000].

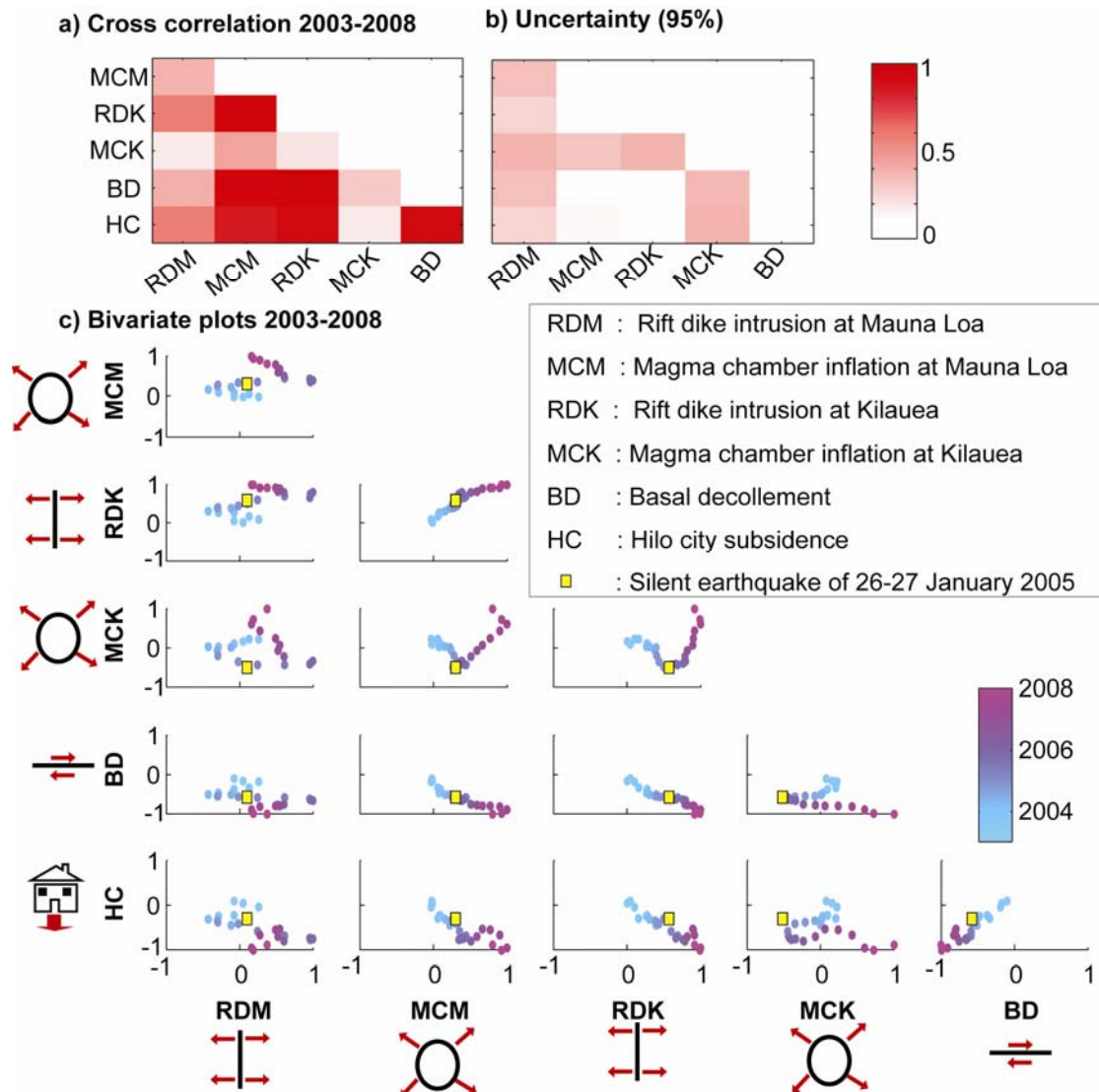


Figure 7.6. Correlation analysis suggesting interplaying sources. a) Long-term cross-correlation coefficients indicating the degree of linear dependency between the strengths of the sources; b) the cross-correlation coefficients' uncertainty obtained via TLSP analysis in 95% confidence region, c) bivariate plots of the relationships between the strengths of the sources as a function of time, which also indicate the degree and pattern of the relationship. The coordinate of each point represents two values; for instance, the abscissa represents the normalized volume of magma intruding into the Kilauea dike system (RDK), and the ordinate represents the normalized pressure change in the Mauna Loa magma chamber (MCM). We use a color scale to assign a date to each point. In each panel, the image acquired immediately after the silent earthquake (31/1/2005) is marked by a square. Since the silent earthquake often appears as a reversal point (opposite slopes before and after the square), the long-term and short-term correlations may be different and may even reach zero.

In order to investigate the correlation on shorter time scales (< 2.5 year), we estimated the sign and degree of the correlation via bivariate plots (Fig. 7.6c). An increasing trend with time means that the correlation is positive (e.g., the magma volume is increasing at both sources), whereas a negative trend indicates an anti-correlation (e.g., the volume of one system is increasing, whereas that of the other system is decreasing). The results show that the magma chamber inflation periods are anti-correlated with dike intrusion periods (Fig. 7.6b). For instance, in 2007, Mauna Loa began to undergo an augmented period of inflation that was related to a rapid pressure increase within the magma chamber. Then, by mid-2007, the pressure dropped within the chamber, which was associated with a new intrusion into the Mauna Loa rift zone (see Fig. 7.5). This observation is in agreement with previous report on the deformation of the Kilauea volcano [Dvorak *et al.*, 1983], in which intrusions of magma into the rift zone appeared to be preceded by summit inflation. Similarly, a strong correlation is observed for the magma chamber pressures and the amount of decollement slip. Furthermore, the rate of subsidence at Hilo city occasionally appears to be affected by volcanic activity and movements of the unstable volcano flank, implying the presence of a system that is sensitive to very small fluctuations in the crustal deformation field.

7.5 Discussion

In this study, we investigated the spatiotemporal deformation field over Hawaii Island as obtained by a new wavelet-based InSAR (WabInSAR) time series method. Following the time-dependent inverse source modeling and cross correlation coefficient estimation, we investigated the behavior of deformation sources individually and in chorus. The main sources of deformation in this period are interpreted as (a) dikes that opens or close and are located along the rift axes of Mauna Loa and Kilauea volcano, (b) magma chambers that inflate and deflate and are located beneath or slightly offset from the summit calderas, (c) a basal decollement that accomodates south-directed slip of the Kilauea flank and that is located at the interface between the volcano edifice and the oceanic crust, and (d) a compacting layer underneath Hilo city. All model sources are well constrained and explain the data well. Our study showed that all of these sources also partially interact with each other. We hereafter discuss different aspects of these findings.

7.5.1 Improvements and limitations of WabInSAR

The major improvements of WabInSAR are: 1) freedom from model assumption, and 2) requirement of relatively smaller number of images. For instance, a polynomial assumption for simulating a deformation behavior to reduce possible topography error is not required. WabInSAR is an effort to overcome such limitations and to improve the accuracy of existing deformation time series methods. The approach treats signals by using the available information directly associated to its building blocks, i.e. surface deformation, atmospheric delay, DEM inaccuracy and decorrelation noise. For instance, artifacts that resulted from inaccuracy in the DEM can be treated using Legendre wavelet filters, because of their specific characteristics that resemble the spatial behavior of Legendre polynomials.

To reduce or even eliminate atmospheric artifacts, information about the spatiotemporal behavior of the troposphere pressure, temperature and humidity might be required, although using the default values may lead to a reasonably good result (for more detail see [Shirzaei and Walter, 2010b]). The a priori information comprises a spatial and temporal decorrelation length of atmospheric delay, which is incorporated into our 3D wavelet filter via spatial and temporal window sizes. In other words, various root mean square radii of wavelet mother functions are utilized at different wavelet scales [Goswami and Chan, 1999] (for more detail see [Shirzaei and Walter, 2010b])

Regarding limitations of the current version of WabInSAR, implementation of a 3D unwrapping algorithm is required. However, by the time we prepared this manuscript, we have developed a new approach for 3D phase unwrapping based on combination of artificial intelligence and minimum cost flow and will be available in a separate publication soon. Moreover, to obtain accurate results, a careful application of the wavelet concept is required. The wavelets provide a very large variety of

analyzing functions with different advantages and limitations. Misuse of them may lead to filtering out of part of the signal.

7.5.2 Time dependent modeling

Most modelling studies of volcano deformation processes consider individual events or averaged data. A deformation time series, as presented herein, requires time dependent modeling approaches that provide (analytical) source solutions that may be variable in strength but consistent in time. For instance, an active fault can not jump laterally by many kilometers as the deformation proceeds. Such temporal undulations in the source parameters are usually produced by model deficiency and/or data deficiencies. The approach devised here for inverting the deformation time series incorporates the advantages of the Genetic algorithm [Shirzaei and Walter, 2009] and the robustness of the Kalman filter [Grewal and Andrews, 2001]. This approach integrates the entire spatial and temporal information to generate a time series of the dislocation source parameters. This inversion approach has the further advantage of handling irregularly sampled observations while preserving nonlinearity of the observations. It is also capable incorporating heterogeneous observations. Moreover, because the Kalman filter is implemented recursively, it allows for considering new data sets in efficient manner which suites for early warning systems (for more detail see [Shirzaei and Walter, 2010a]).

We note, again, that the dislocation sources are simulated in an elastic homogeneous half space medium, which is a simplification of the real space. In other studies it was shown that mechanical heterogeneity and the effect of topography may influence the inferred depth of magma chambers [Manconi *et al.*, 2007] or of a basal decollement by few kilometers [Montgomery-Brown *et al.*, 2009a]. Nevertheless, the position of all dislocation sources described by us is in agreement with earlier works. Although we had access to about 10 GPS station, we used only InSAR data for time dependent modeling. This is because, whilst incorporating more data may increase the accuracy of the result, the issue of relative weighting of GPS data at few stations in respect to thousands of InSAR points is not yet fully solved. Future works will need to test the effect of integrating independent datasets on the model result.

7.5.3 Deformation source correlation

Our results show that the long-term source correlations differ from the source correlations in shorter time scale. Some of the observed relations might be useful as precursors for future eruptions. The relation between a silent earthquake and the Kilauea magmatic activity has been explored for the dike intrusion event of 17- 19 June 2007 [Brooks *et al.*, 2008]. However, a closer investigation of the bivariate plots suggests that silent earthquakes at the Kilauea south flank, such as the 26-27 January 2005 slow slip event [Segall *et al.*, 2006], have a much broader affect on the most of magmatic systems at Hawaii Island. Following the 2005 silent earthquake, the sign of the correlation between the magmatic sources reversed (Fig. 7.6c). For instance, the magmatic process at Kilauea correlates negatively with magmatic activity at Mauna Loa magma chamber before the 2005 silent earthquake, while after the event the type of their correlation shifted to a significant positive value. Furthermore, additional reversal points occur at the same time as silent earthquakes, e.g., in 7/2007 [Montgomery-Brown *et al.*, 2009a]. To validate this relationship, we calculated the cross-correlation coefficient and associated uncertainties for the time series before and after the large silent earthquake that occurred in 2005 (Fig. 7.7a, b). Both periods show that the magmatic sources were strongly correlated, either before or after the 2005 silent earthquake. This observation emphasizes the impact of flank movements and, especially, silent earthquakes acting together with the magmatic sources, as well as the need to investigate the time series of a volcano in order to understand the physical processes and activity changes. Comprehension of the dynamic interactions is of importance for evaluating hazards at the volcano itself and associated with flank failure and tsunami generation.

Other correlating processes on short time are as follows: magma chamber at Kilauea correlates with magma chamber at Mauna Loa and rift dike at Kilauea, also basal decollement slip is correlates with magmatic activity at Mauna Loa.

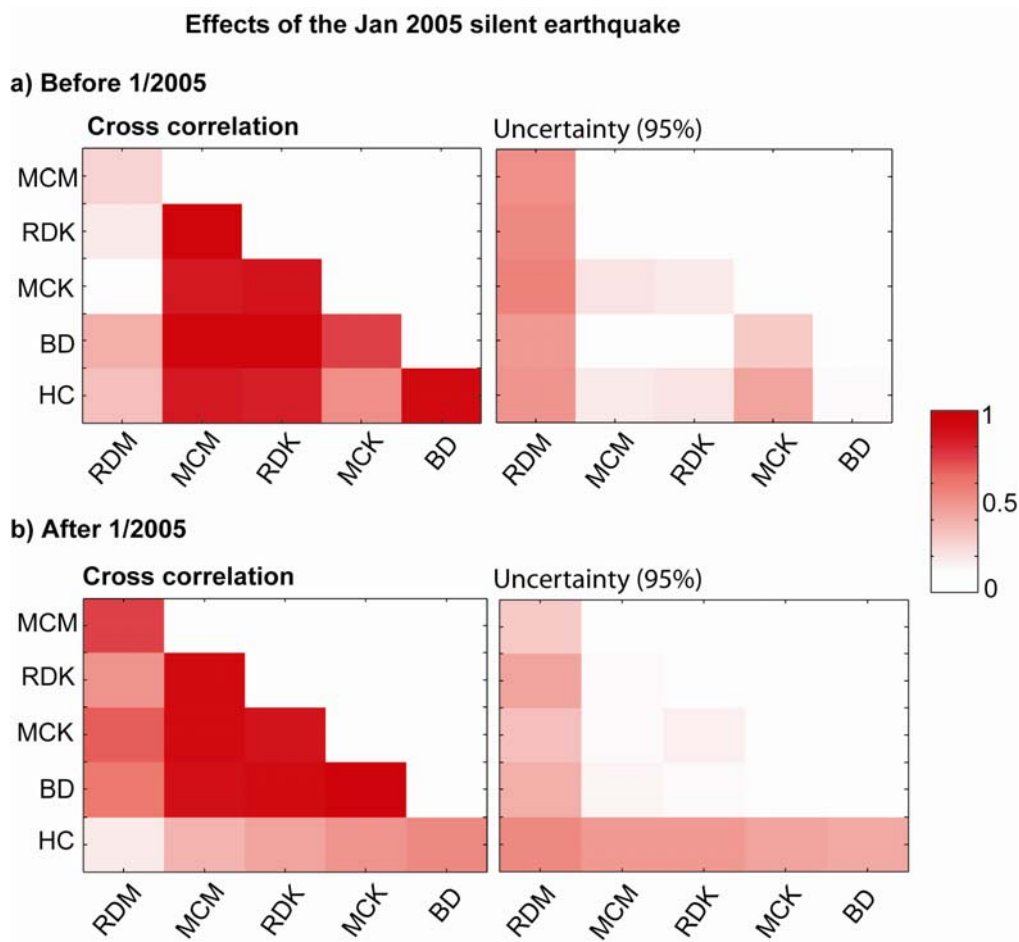


Figure 7.7. a, b) Graphical representations of the short-term source strength cross-correlations for 2003-2005 and 2005-2008 together with the cross-correlation coefficients' uncertainty obtained via TLSP analysis in a 95% confidence region. The abbreviations are explained in Figure (7.6).

Three main conceptual models can be used to explain the correlations observed in this study. First, it has already been proposed that small changes in the shallow crustal stress field trigger the interaction between the Kilauea rift dike intrusions and decollement slip events [Cayol *et al.*, 2000; Dieterich *et al.*, 2000]. Second, the short-term correlation between the magma chamber pressure changes and the dike intrusions is in agreement both with a hydraulic connection model [Dvorak *et al.*, 1983] and related past eruptive activities that indicate competition for the same magma source [Klein, 1982]. Third, an external source, such as meteorological forcing may change loading and friction condition of faults, and even triggers flank movements [Cervelli *et al.*, 2002]. Since most of the changes to the mutual interaction process over time occurred in relation to the south flank slip events, this study implies that the flank mobility is an important proxy. Future work will need to address the reasons for this interaction, and explore the quantity and directivity of stress changes as a function of time and space. In particular, the timing of silent slip events need to be considered as an important occurrence during which most, if not all, of the other deformation sources on the island alter in both the long-term and short-term.

7.5.4 Hilo Subsidence

We discovered various spatial and temporal deformation patterns affecting not only the volcanic centers rift dikes, magma chambers and a basal decollement are the main sources of deformation. In addition, we discovered an important subsidence signal of 0.8 cm/yr underneath Hilo city. Hilo city is known to subside at a rate of 0.4 ± 0.5 mm/yr with respect to Honolulu on the Oahu Island. [Caccamise II *et al.*, 2005], but the rate observed here is much faster (~20 times). The difference between these two values may have several reasons. Our observation is obtained with respect to the

location of MKEA GPS station in a local coordinate system. In contrast, earlier estimations considered the great Pacific fixed reference frame and obtained in respect to Honolulu on Oahu Island. As Oahu Island is unstable, we consider the local reference frame to be a better choice. The reference chosen here, MKEA GPS station, is a member of IGS (international GNSS network), and its precision and reliability has been repeatedly validated (see the station information at <http://igsb.jpl.nasa.gov/network/site/mkea.html>). This station is located at the flank of Mauna Kea volcano, and daily solutions of the station position show only very slight fluctuations (see also electronic appendix and [Shirzaei and Walter, 2010b]).

The factors that may have affected the magnitude of this observed subsidence mainly are unwrapping error and uncompensated orbital error. As seen in Figure (7.3,4) the pixels over the Hilo are isolated from the rest of data set. This might imply existence of a phase jump, leading to an improper phase unwrapping. However, closer investigation of the interferograms makes us confident that our interpretation is valid for two reasons: 1) there is a local phase gradient (concentration of fringes) over Hilo city that proves a local deformation gradient at the given scale; and 2) a phase change over the nearby area displays a smooth pattern, that makes existence of a phase jump unlikely. As a result, we consider the unwrapping solution presented here to be valid. Also, we rule out an uncompensated orbital error for the following reason. The general pattern of orbital error (orbital ramps) is reduced using a planar assumption (see for instance [Hanssen, 2002; Kampes, 2005]). The uncompensated part is expected to have a random pattern in time and to be much smaller in amplitude than the observed subsidence. However, as the presented Hilo trend is large and systematic, we also rule out the significant contribution of orbital ramps. In this way, we argue that this new line of evidence for accelerated subsidence underneath Hilo city is robust.

Nevertheless using tide gauge data, *Moore and Fornari* [1984] suggested an absolute subsidence rate of ~ 3 mm/yr for Hawaii Island. Moreover other researchers using the Small Base Line Subset (SBAS) approach have observed a similar subsidence rate at Hilo [Bertran Ortiz et al., 2009]. This observed subsidence rate might be an indicator for a) sinking Honolulu, or b) a reference frame that is not really fixed and encounters a slight motion that may influence observations, or c) simply that Hilo's sinking rate has increased.

7.6 Conclusion

We have presented first island wide InSAR spatiotemporal map of the deformation, spanning 5 years of activity over the Hawaii Island. A complex spatiotemporal deformation field at all of the volcanic and tectonic systems has been revealed. To explain the sources contributing to the deformation field we have developed a time dependent inverse modeling approach by combining a Genetic algorithm and a Kalman filter. This approach provides a unique time series of the dislocation source parameters as a minimum spatial and temporal variance component. The statistical analysis of the time series of the source's parameters reveals different states of interaction over Hawaii Island between volcanic and tectonic systems at different time scales. Moreover, we found that the interaction between silent or slow earthquakes at the Kilauea south flank and magmatic systems is much more complex than it was thought before. The silent events have significant impact on the magmatic systems and alter the type of correlation between them. This finding may lead to new methods for assessing the hazards that arise during volcano-tectonic activities.

Chapter 8

Gravity-driven deformation of Damavand volcano detected through InSAR time series¹

M. Shirzaei*, T.R. Walter*, H. R. Nankali⁺, E. P. Holohan*

*Section 2.1, Dept. Physics of the Earth, GFZ German Research Centre for Geosciences, Telegrafenberg, 14473 Potsdam, Germany

⁺ Geodesy and Geodynamics Department, National Cartographic Center, PO Box 13185-1684, Meraj Av., Tehran, Iran

Abstract

The detection and monitoring of volcano spreading is of vital importance for understanding volcanic hazard. This however has been achieved geodetically at several large active volcanoes. In this study, we present a first InSAR deformation time series at a dormant volcano Damavand in northern Iran over the periods of 2003 through 2008. Our data show a lateral extension of the volcano at the relative rate of up to ~8 mm/yr accompanied by a subsidence at the rate of up to ~5 mm/yr at the volcano summit. Lateral motion of the east flank is more significant than that of the west flank. Our observations supported by understanding from spreading volcanoes elsewhere therefore reveal a first line of evidence that Damavand volcano is undergoing slow, probably gravity-driven, spreading. As gravitational spreading may episodically accelerate can control the location of sector collapses and flank eruptions, the detection and study of this effect might therefore be a key element in realistic hazard assessment at Damavand volcano.

8.1 Introduction

Volcano deformation commonly results from the inflation or deflation of magmatic bodies. These processes produce uplift and outward flank motion or subsidence and inward flank motion, respectively [Dzurisin, 2006]. Other processes causing volcano deformation may be entirely or partly gravity driven, and include landslides, sector collapses, and edifice spreading. The latter of these is characterized by subsidence of the volcano summit, lateral extension of the upper flanks, as well as lateral contraction and uplift of the volcano's lower flanks [Borgia, 1994]. Spreading may lead to flank failure and debris avalanche generation [Van Wyk de Vries and Francis, 1997] and it may cause (or be caused by) magmatic and volcanic activity [Froger *et al.*, 2001; Siebert, 1992].

Geodetic methods have long been used to reveal deformation induced by magmatic bodies at many volcanoes around the world [Dzurisin, 2006]. In only a handful of instances, however, have such methods revealed deformation associated with gravity driven processes like volcano spreading. Moreover, these instances have been restricted to historically-active volcanoes whose hazard potential is consequently well-advertised.

As this study shows, gravity-driven processes may also characterize deformation at volcanoes thought to be dormant or inactive. Surface displacement data that we have obtained by advanced InSAR time

¹ MS processed the data. All authors were involved in discussion and writing the paper.

series approaches reveal previously undetected but ongoing deformation at the ostensibly dormant Damavand volcano in Iran. We argue that this deformation field primarily reflects a gravity-driven slow spreading process. In the following we discuss different sources that may contribute in the observed process such as topographic and (un)buttressing effects, a weak core, dipping substrata, deep flexure or some combination of these. Our results highlight the possibility of long-lived hazard from gravity-driven processes at dormant or inactive volcanoes and underscore the importance of remote sensing and other geodetic techniques in their detection and monitoring.

8.2 Damavand tectonic setting and volcano geology

Damavand volcano is located in the Central Alborz Mountains of northern Iran (Fig. 8.1a), and it lies 50 km north of Tehran, the capital city with ~13 Mio inhabitants. This large snow-capped volcanic edifice (~ 400 km³) reaches an elevation of 5,670 m above sea-level and is the highest peak in the Middle East (Fig. 8.1b). Damavand is also of great significance in Persian mythology (the ‘Persian Mount Olympus’).

At Damavand area, the regional slope is about 0.5°-2.5° to the East and the basement under Damavand volcano comprises Palaeozoic-Mesozoic siliciclastic, carbonate and evaporite sequences, overlain by Palaeogene-Neogene tuffs, lavas, and sediments [Allenbach, 1966]. These units are deformed within an east-west trending structural grain of large folds and major thrusts and/or strike-slip faults. Presently these faults accommodate ~5 mm/yr north-south shortening and ~4 mm/yr left lateral west-east motion [Vernant *et al.*, 2004a] and have generated several destructive earthquakes [Ambraseys and Melville, 1982].

The edifice of Damavand volcano is mainly made of trachy-andesite lavas, as well as several compositionally-identical fall-out tuffs and at least one ignimbrite [Allenbach, 1966; Davidson *et al.*, 2004]. Geochronological and field evidence indicates an older cone constructed since at least 1.8 Ma and a younger cone constructed since 0.6 Ma [Davidson *et al.*, 2004]. The youngest preserved eruptive products are lava flows dated to c. 7 ka. Damavand is thought to be dormant, although fumarolic activity still occurs near the summit [Davidson *et al.*, 2004].

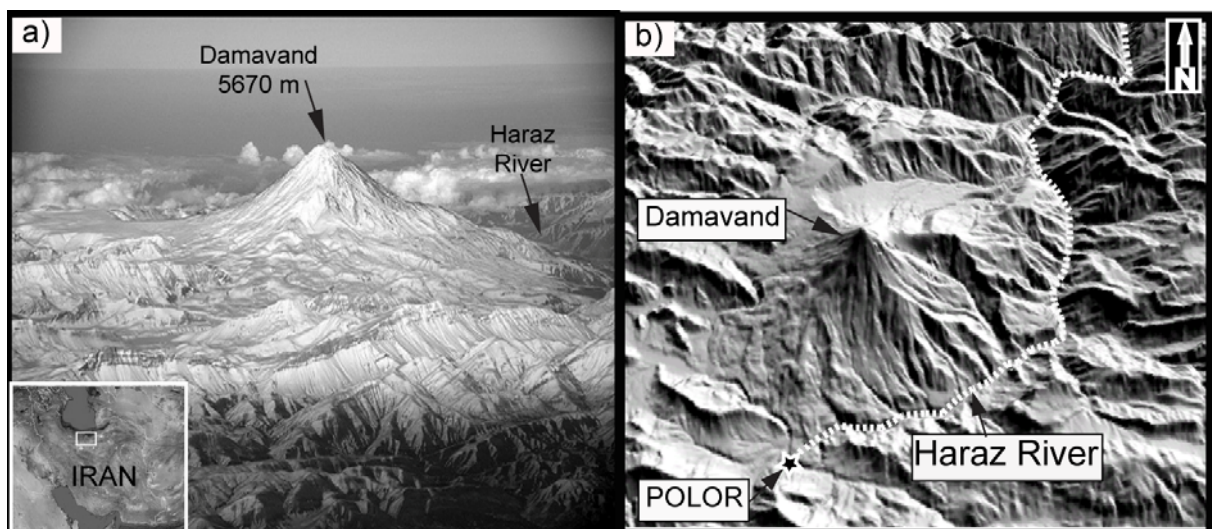


Figure 8.1. a) Photo of Damavand, as viewed from south, taken by Shreyans Bhansali on 10 January 2007. b) An oblique view of the topography of the Damavand area in northern Iran. The location of the Polor city and Haraz River are depicted.

The Haraz River flows south-to-north along the eastern side of the volcano (Fig. 8.1b). In this area, the spatial developments of the river and volcano are thought to be intertwined. The river erodes the eastern volcano flank and the adjacent topography; the volcano’s growth has locally altered the river’s course [Davidson *et al.*, 2004]. The volcanic history indicates potential hazard from eruption, sector collapses, debris avalanches and mud flows. Evaluation of such risks at this volcano, which is now

very poorly monitored, is therefore of great importance. In the next section, we present evidence that Damavand volcano is actively deforming.

8.3 Deformation field at Damavand volcano

To detect and characterize the deformation field at Damavand volcano, we used multiple radar images acquired by the European Space Agency satellite ENVISAT. The data set includes 20 images in descending orbit (track 106) and 25 images in ascending orbit (track 285), and it spans the period of 2003 through 2008. Using these data sets, we generated 153 and 77 interferograms in ascending and descending mode, with maximum spatial and temporal baselines of 450 m and 4 years, respectively. To obtain unambiguous phase changes, we unwrapped the modulo 2π phase observations of each interferogram using a 2D minimum cost flow algorithm [Chen and Zebker, 2001; Costantini, 1998]. Phase unwrapping is applied only to those pixels exhibiting low decorrelation noise [Costantini and Rosen, 1999]. The algorithm for identifying low-noise pixels was derived from earlier works [Berardino et al., 2002; Ferretti et al., 2001b; Hooper et al., 2007]. The differential phase changes of the interferograms were inverted [Bjerhammar, 1973] to generate a time series of the deformation at each pixel [Schmidt and Bürgmann, 2003]. The filter for reducing the atmospheric phase screen is derived following Ferretti et al. [2001b] and was applied by using a time frequency analysis [Daubechies, 1992].

Figure (8.2a, b) shows maps of the linear velocity field as seen in the satellite's 'Line-Of-Sight (LOS)' viewing geometry for the descending and ascending orbits. At the vicinity of the Damavand summit, a slight displacement of +2 mm/yr is detected in the descending viewing geometry (Fig. 8.2a), whereas a maximum displacement of -15 mm/yr is seen in ascending viewing geometry (Fig. 8.2b).

To validate the results of the InSAR time series and to estimate their accuracy, we compared this data against independent data sets. In the study area there are two continuous GPS stations equipped with Ashtech IGRS receivers and choke ring antennas ('PLOR' and 'ABSD' in Fig. 8.2a, b). These two high-quality stations are members of Iranian Permanent GPS Network (IPGN), which is maintained by the Iranian National Cartographic Center (NCC), and they are sampled every 30 s. Their daily observations are jointly adjusted with the observations of surrounding IGS stations using GAMIT and IGS precise orbits. GLOBK is used to combine daily solutions and generate time series of the deformation field by using a Kalman Filter approach [Hofmann-Wellenhof et al., 2000]. To reduce most of the regional effects whilst preserving the local components of the deformation at Damavand volcano, we considered the PLOR station to be fixed at zero displacement and referred other geodetic data to this point.

As seen in Figure (8.2c, d), the validation test presents a good agreement between InSAR time series and GPS data sets in both ascending and descending geometry, with an accuracy of ~ 2 mm and a precision of 0.5 mm/yr. Note that to make the InSAR and GPS data comparable, the GPS time series was projected onto the satellite LOS. Moreover, we considered an uncertainty of 1 cm for the projected cGPS time series in the 95% confidence region. This yields a high-precision time series of the deformation field at $\sim 100,000$ pixels.

The different viewing geometries of the radar satellites enable us to constrain the West-East (W-E) and Vertical (V) components of motion at Damavand volcano (Fig. 8.2e, f). Since the satellites' orbits are near-polar, the north-south component could not be measured. As its LOS projected component is smaller than 0.5 mm/yr, the N-S regional-tectonic shortening across the Alborz [Vernant et al., 2004a] is below the method's precision and is thus considered to have a negligible contribution to the calculation of the E-W and vertical components.

In general, the W-E component shows a pattern characterized by extension of the volcanic edifice either side of a line trending roughly NNE-SSW (Fig. 8.2f). The eastern flank moves eastward at an average velocity of 4 mm/yr, whilst the western flank moves westward at an average velocity of less than 1 mm/yr. In detail this pattern is not smooth, however. On the eastern flank of the volcano, for instance, the area immediately south of a prominent topographic scarp has a locally higher eastward velocity of up to 10 mm/yr (see arrow in Fig 8.2e). There are also some areas that represent anomalies to the general pattern. These are marked by letters (a), (b) and (c) in Figure (8.2e) and they show motion opposite to the general movement of the sector they occur in. The area marked by (c) at the

northern margin of Damavand may be an extension of areas further north-east and the area marked by red triangle in Figure (8.2a, b) are known to be subject to very rapid land slide [Peyret *et al.*, 2008], which generates significant decorrelation noise. The V component (Fig. 8.2f) shows a relatively smoother pattern characterized by an average subsidence of ~ 5 mm/yr at the summit. On the western flank the subsidence declines at a low rate towards the volcano base. On the eastern flank the subsidence declines at a faster rate towards the volcano base, where locally V becomes positive (i.e. there is uplift).

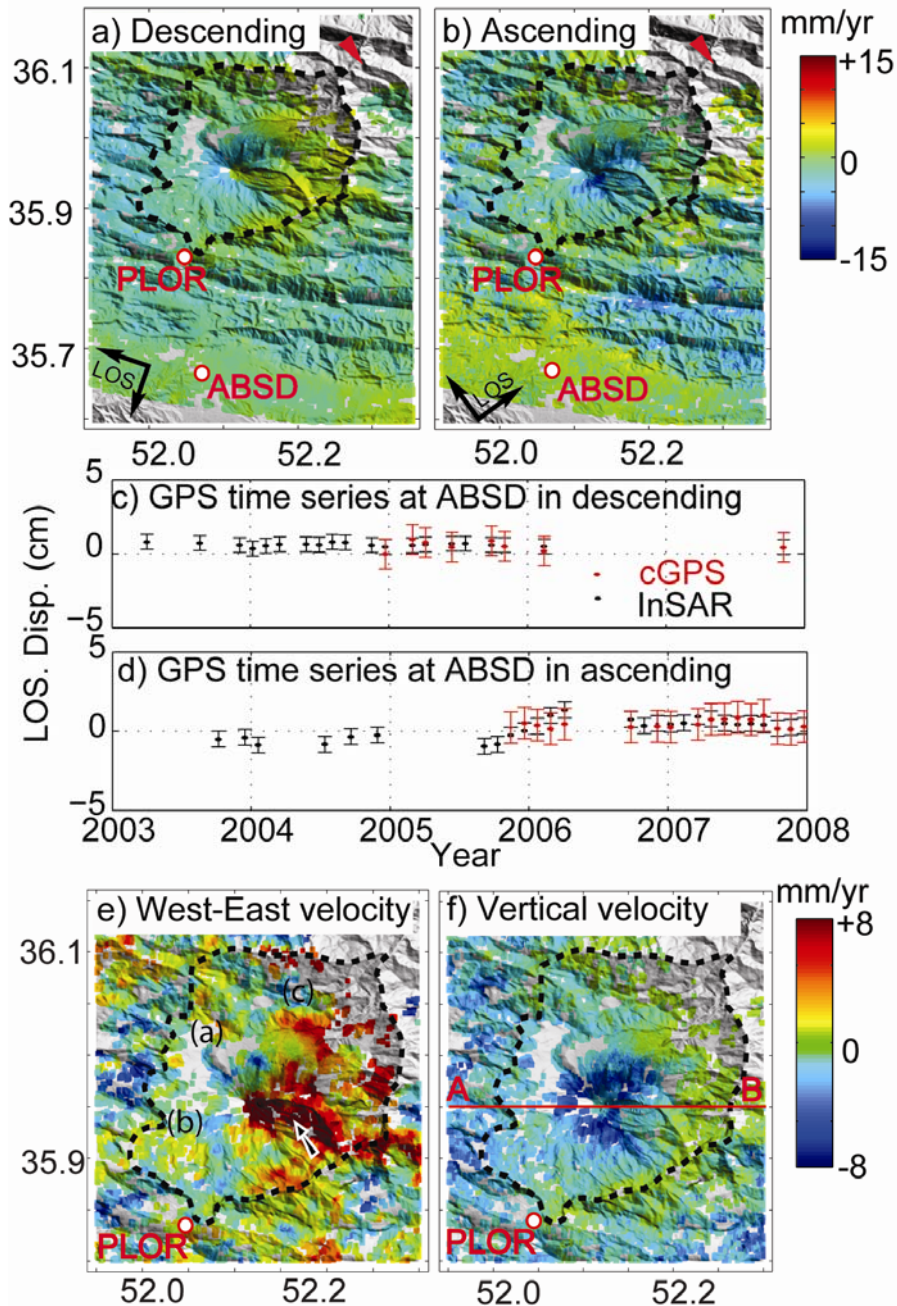


Figure 8.2. a, b) deformation field velocity in LOS direction of the satellite as obtained in descending and ascending viewing geometries, respectively. Area of Damavand volcano is marked by a black dashed line and the locations of the GPS stations at Polor city (PLOR) and (ABSD) depicted. The red triangles indicate areas subject to rapid land slide. c, d) comparison between InSAR time series and GPS time series at the ABSD GPS station. e, f) E-W and V velocity field. An area of rapid eastward motion is marked by the arrow in panel e. Letters (a), (b) and (c) denote anomalies to the general trend in the displacement field.

To better visualize the deformation field with respect to the volcano morphology, a west-east cross section is shown in Figure (8.3a). The profile passes just north of the prominent scarp on the volcano's eastern flank (Fig. 8.2). The displacement vectors at the profile surface are those measured from our InSAR data set. The western side of the profile shows a predominant subsidence and a slight westward component of motion. The eastern side shows a more heterogeneous deformation profile, and a main feature is the stronger component of horizontal motion (toward the east). At 22-25 kilometers on the cross section, step like features occur in volcano topography (Fig. 8.3a), where the sense of motion shifts from subsidence to uplift.

8.4 Discussion

At Damavand volcano, from an advanced InSAR deformation time series, we have observed a broad subsidence that decreases from the volcano summit area toward the flanks, toward the base of which there is localized uplift. This subsidence is accompanied by outward-directed lateral motions that are more pronounced on the eastern flank.

The surface displacements revealed here are not immediately compatible with any simple inflation or deflation of a magmatic body. Inflating(deflating) deformation sources generally cause a pattern of outward(inward) directed motion but with a broad uplift(subsidence), which is not observed at Damavand volcano. Even a vertically-elongated inflating body, such as a dyke, may generate the summit subsidence. However, the accompanied broad uplift on the flanks again is not observed, inhere.

The best scenario explaining the observed displacement field at Damavand volcano is a slow gravity-driven spreading that is more pronounced toward the east. Surface displacement fields associated with volcano spreading have been isolated and quantified in laboratory-based analogue models. Whether induced by a weak substratum or a volcano core [Cecchi *et al.*, 2005; Delcamp *et al.*, 2008], and directed by dipping substratum [Wooller *et al.*, 2004] or by direction of the regional slope [Francis and Wells, 1988] or by (un)buttressing [Borgia *et al.*, 1992] or by lateral inhomogeneities in the edifice or in its basement [Cecchi *et al.*, 2005], the displacement patterns for model volcano spreading are generally very similar, and characterized by subsidence with a maximum around the summit region and horizontal extension with a maximum around the volcano's mid or upper flanks (see Fig. 12 of Delcamp *et al.* [2008]).

Overall therefore, the surface displacements patterns associated with slow gravity-driven spreading, as constrained by controlled experiments as well by geodetic and structural data from volcanoes known to be actively spreading, closely mimic those detected asymmetric of the deformation at Damavand volcano in this study (Fig. 8.2e, f). This reveals first evidence of geodetically detected spreading at a dormant volcano while earlier evidence of spreading was observed geodetically at historically and currently active volcanoes, such as Mt Etna whereas the geodetic signals also contain contributions from magmatic sources [Froger *et al.*, 2001].

The asymmetric nature of the deformation at Damavand volcano, with more pronounced spreading on the eastern flank, might be induced by dipping weak substrata, regional slope, (un)buttressing of an edifice or a combination of those similar to Mt Etna [Borgia *et al.*, 1992]. At Damavand, there appears to be topographic buttressing to the west and 'erosional unbuttressing' to the east caused by the powerful Haraz River (cf. Fig. 8.1b), which down-cuts at a rate of ~1 km per Myr [Davidson *et al.*, 2004].

This asymmetry is a feature observed in many other spreading volcanoes. One exception is Nicaragua's Conception volcano where shown by structural mapping and GPS campaigns to be subject to radial symmetric spreading [Borgia and Van Wyk de Vries, 2003]. Partial spreading is more commonly observed at other active volcanoes, for instance at Kilauea [Morgan *et al.*, 2003], and Etna [Froger *et al.*, 2001], where only a discrete flank reveals significant movement.

Structures typically associated with an unstable volcano flank include normal faults on the upper flank, a main decollement underneath the flank, and basal thrusts and/or strike slip faults at the base of the flank [Borgia and Van Wyk de Vries, 2003; Merle and Borgia, 1996]. Although the presence of such structures is as yet unconstrained at Damavand volcano, a linear interpolation of the surface deformation field on a grid inside the volcano cone reveals the location of a potential decollement

where the displacement vectors become sub-horizontal (Fig. 8.3b). This occurs at a depth of about 2 km, which closely corresponds to the geologically-defined base of Damavand volcano [Allenbach, 1966].

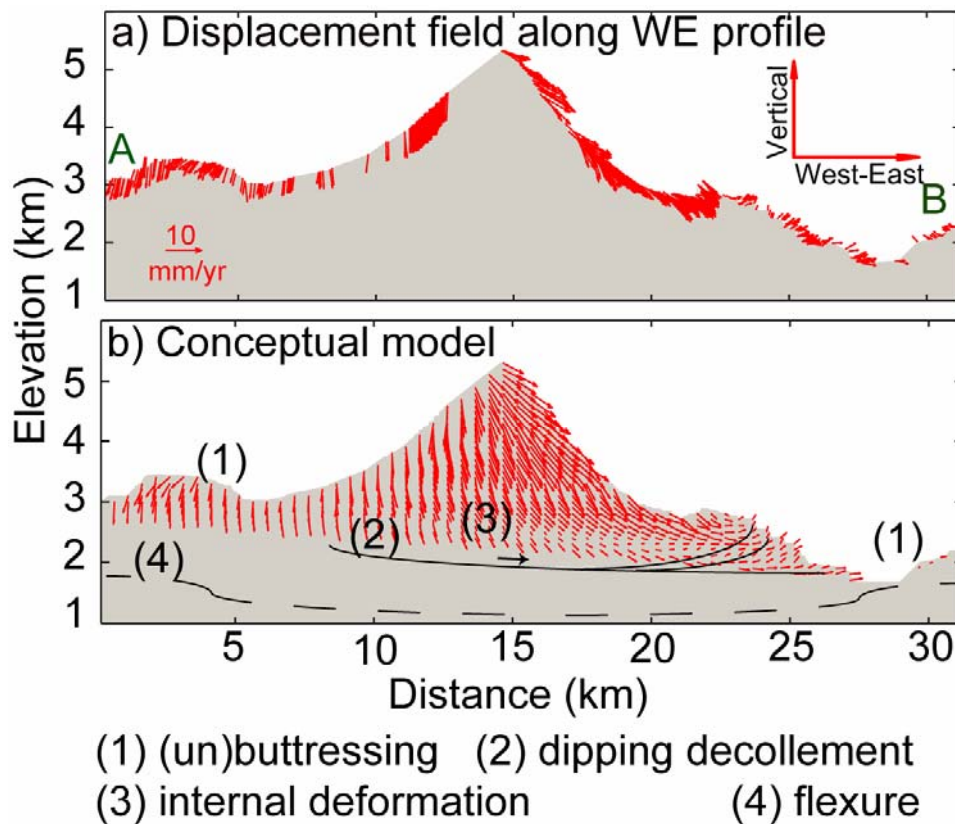


Figure 8.3. a) West-east profile of the observed deformation field with respect to volcano topography. This profile highlights that the volcano is slowly spreading eastward. b) Conceptual model obtained by interpolation deformation field inside the volcano. Possible driving mechanisms for the deformation are numbered and discussed further in the main text. Internal deformation includes effects such as weak core, magmatic cooling, hydrothermal activity, etc.

The irregular or more localized deformation within the general pattern of flank movements at Damavand volcano (see arrow and letters in Figure 8.2e) is reminiscent of heterogeneity within displacement fields of Mt Etna and Hawaii [Froger *et al.*, 2001]. Such heterogeneity at these volcanoes is linked to structured displacement of individual blocks within the moving flank. The displacement field heterogeneity at Damavand volcano may similarly relate to localized slip on block-bounding faults. Small slip events on regional fault segments and the activity of fast deforming mechanisms, such as land sliding, could also play a role, however.

Although we argue that asymmetric spreading plays the dominant role in the deformation field at Damavand, we cannot entirely preclude additional influences from other mechanisms. For instance, the dominant subsidence pattern could also contain contributions from internal deformation sources. There could potentially be an influence from lithospheric flexure caused by a dense body beneath Damavand volcano as detected in a past seismic receiver functions study [Sodoudi *et al.*, 2009]. Furthermore, a general limitation of the InSAR viewing geometry is that it does not allow us detect the south-north component of the deformation field and hence to resolve the full 3D displacement field. To overcome such limitations, and to better understand the dynamics of deformation at this volcano, supplementary GPS, tilt-meter, gravimeter, seismic and field observations observations are required. This study and new data will ultimately help evaluate the hazard potential of Damavand volcano. Volcano spreading may lead to sector collapses and debris avalanches, which may be accompanied by eruptions [Lipmann and Mullineaux, 1981; Siebert, 1992]. At Damavand volcano there is evidence for at least one large sector collapse that dammed regional drainage [Davidson *et al.*, 2004]. In addition to

affecting local population centres and those downstream along the Haraz river, the recurrence of such an event could pose major problems for populations further afield, specifically in Tehran city (~13 Mio inhabitants) much whose water is sourced from dams along the Harez river.

8.5 Summary and conclusion

In this study, we used InSAR time series to detect and characterize a deformation field for the first time at the dormant Damavand volcano in north Iran. We observed subsidence of the summit and predominantly eastward-directed spreading of the flanks. Several reasons, possibly combined, may explain these observations, including a dipping weak substratum, a weak volcano core, volcano base flexure, topographic buttressing in the west, and erosional unbuttressing in the east. Our results illustrate the potential for long-lived hazard from gravity-driven processes at dormant or inactive volcanoes and the importance of geodetic techniques in their detection and monitoring.

Chapter 9

The 12 Jan 2010, Haiti earthquake affected by aseismic fault creep¹

M. Shirzaei and T. R. Walter

Section 2.1, Dept. Physics of the Earth, GFZ German Research Centre for Geosciences, Telegrafenberg, 14473 Potsdam, Germany

On 12 Jan 2010 a destructive strike slip earthquake (Mw 7.1) occurred in the oblique convergence zone of Hispaniola. Over 222,000 were killed, most in Port au Prince, the capital city of Haiti at ~80 km eastward distance to the mainshock. The earthquake ruptured along a 50 km trace, which is only a part of the much larger Enriquillo Fault Zone (EFZ) that last broke in 1751 along a length of ~150 km. Assuming an average slip rate of 5-9 mm/yr[Manaker et al., 2008] the amount of slip deficit accumulated at the entire EFZ is estimated to be on the order of 1.5 – 2.5 meters[Ali et al., 2008]. This may imply that a much larger portion of the EFZ is ready for earthquake occurrences. Here we present results of a deformation field investigation in the period of 2004-2009 using ScanSAR data. The data and models reveal that the fault segment to the west of the 2010 earthquake was aseismically slipping for years, with a rate being similar as the interseismic long term slip rate. Therefore, this study shows that the accumulating stress was partly released by aseismic slip. Coulomb stress calculations suggest that this may have enhanced the occurrence of the 2010 earthquake disaster, similar as now another fault segment further to the east is stressed. The observed relation between aseismic slip and the 2010 earthquake confirmed the importance of aseismic slip in earthquake understanding and for seismic hazard mitigation.

Surface deformation observations suggest that aseismic slip may occur in the shallow crust along strike slip faults such as at the San Andreas or the Hayward Faults[Bürgmann et al., 2000; Rolandone et al., 2008; Schmidt et al., 2005]. The occurrence of aseismic slip may be explained by velocity strengthening fault friction[Barbot et al., 2009; Scholtz, 1998], sometimes lasting for years or even decades[Bürgmann et al., 2000; Rolandone et al., 2008; Schmidt et al., 2005]. The occurrence and dimension of aseismic slip at active faults is important to quantify, as it may trigger large earthquakes or, reversely, act as a slip barrier[Linde and Silver, 1989; Thatcher, 1982].

In Haiti, the 2010 earthquake was the first to occur after 259 years of apparent silence at this fault, partially releasing a significant slip deficit. Hence, although a magnitude ~7 earthquake was not a surprise to geoscientists[Manaker et al., 2008], a vital question now remain to be answered: Why did only a this relatively small segment of the EFZ ruptured in 2010 although the slip deficit is thought to have accumulated everywhere along this fault?

We studied the large scale deformation field using a data set of 43 ScanSAR radar images acquired in the period 2004-2009 by the European Space Agency satellite ENVISAT (see methods). Since the satellite radar images are obtained in different viewing geometries, by using a principal component decomposition approach we are able to retrieve the West-East (WE) and Vertical (V) long term

¹ MS developed the approach and processed and inverted the data. All authors were involved in discussion and writing the paper.

deformation rate (Fig. 9.1a, b). The WE component indicates aseismic eastward movement at a ~50-km-long fault segment located just to the west of the 2010 fault rupture. We observe an average slip rate that is comparable to the long term interseismic rate [Manaker *et al.*, 2008] (the velocity field quality in terms of the formal variance is shown in Fig. S9.2). The deformation amplitude decreases with normal distance from the fault trace, implying that the slip is occurring in the shallow brittle zone of the lithosphere. The surface data shows that the lateral transition boundary between slip deficit and aseismic slip is not spatially clear. The vertical component rather shows no significant perturbation from zero displacement except at the city of Port au Prince, there mainly illustrating a local subsidence (see 'A' in Fig. 9.1). Similar deformations in urban areas have been observed elsewhere [Dixon *et al.*, 2006], but maybe affected by data errors [Ghiglia and Pritt, 1998], too.

To investigate the kinematics of the aseismic slip we modeled the deformation field using a dislocation fault model [Okada, 1985]. The optimal location, dip, strike and depth of the fault model are obtained following a uniform slip model inversion. The best fitting model suggests an E-W trending sub-vertical sinistral strike slip fault extending to the depth of ~20 km. The geometry is in agreement with geological data and the downdip extent is comparable to inferred locked zone [Manaker *et al.*, 2008]. The fault area is then subdivided into a regular grid of 50 km² patches. Our model inversion provides us with the creep distribution prior to the 2010 Haiti earthquake (Table S9.2). Although this single fault model explains over 98% of the satellite radar data with a total root mean square error of 2 mm/yr, further associated fault branches or material heterogeneities may have locally contributed to the deformation signal (Fig. S9.4). At the fault we estimated up to 9 mm/yr dislocation with an average value of 6.5 mm/yr. Because during the same period no significant seismic energy was released, one may assume that most of the slip occurred slowly and aseismically. As our results imply that no slip deficit has accumulated along this segment, the loading that occurred was negligible too. Assuming that aseismic slip has continued since the last earthquake in 1751, it is explaining why this patch did not rupture in the 2010 seismic event, hence providing a pronounced segment boundary. Observation of the 2010 coseismic rupture revealed that it stopped where the aseismic segment begin to creep, probably interrupting even further westward rupture propagation. The role of such barriers are now well understood in terms of the initialization and stopping of an earthquake rupture [Aki, 1979; Halldorsson and Papageorgiou, 2005].

To further test the hypothesis whether the 2010 event has been affected by the aseismic slip, we calculate the Coulomb stress change [King *et al.*, 1994] on the EFZ (Fig. 9.1d), hypothesizing that the aseismic slip is constant over the time [Rolandone *et al.*, 2008] and that the receiver fault parameters [Ali *et al.*, 2008] are valid. The model implies that the aseismic slip increased the Coulomb failure stress along the EFZ by ~6 bars, which is a significant stress change. Maximum stress increase is found at the location of the 2010 earthquake zone, which confirms that the aseismic slip brought this segment closer to failure and even may have triggered the earthquake disaster. A similar stress increase may have occurred due to the 2010 earthquake [2010; Showstack, 2010], which may be a hint that the next event might be further to the east again. Therefore another earthquake, possibly reaching or even exceeding the 2010 event rupture, may occur near to the area of Port au Prince.

These results also have implications for realistic seismic hazard assessment in other areas, such as at the San Andreas and Hayward Fault where at the central part significant aseismic slip is measured [Bürgmann *et al.*, 2000; Rolandone *et al.*, 2008]. Such aseismic slip is locally reducing loading and earthquake potential [Bürgmann *et al.*, 2000]. Although the presence of an aseismically slipping fault segment locally relieves the stress, this study shows that adjacent fault segments receive a stress increase affecting the earthquake occurrence and dimension.

9.1 Methods

9.1.1 Satellite radar data

In a fast response the European Space Agency (ESA) provided satellite radar images on a virtual archive free to use (<http://supersites.unavco.org/>). In ScanSAR mode the satellite transmits so-called bursts including limited radar pulses and scans back and forth among five swaths (I2-I6) to image an area of 400km×400km. We used this dataset to explore phase changes by generating 35 radar

interferograms[Ferretti *et al.*, 2007] with spatial baselines smaller than 650 m and at least 30% burst synchronization. Further details are given in the supplementary material.

9.1.2 Principal component decomposition

Having $L_{ij}^k(x, y)$ the phase change between time t_i and t_j at a pixel located in the coordinates of (x, y) in each k -th interferogram, the principal component decomposition can be presented as [Aubrey and Emery, 1983; Savage, 1988; , 1995];

$$L_{ij}^k(x, y) = c_e(x, y) \times u_e(x, y) \times (t_j - t_i) + c_z(x, y) \times u_z(x, y) \times (t_j - t_i) + \sum_{p=1}^N [A_p \times [C_p(t_j) - C_p(t_i)] + B_p \times [S_p(t_j) - S_p(t_i)]] \quad (9.1)$$

where u_e and u_z are west-east and vertical velocity at each pixel, c_e and c_z are the unit vectors projecting the 3D displacement field to the radar's line-of-sight, $N + 1$ is the number of individual modes, A and B are the constant amplitudes for each mode and C and S are the sine and cosine functions defined at a discrete time t . The first mode is the long term horizontal and vertical slip rate, respectively, and the 2nd, 3rd and 4th modes constant periods of 0.5, 1 and 2 years are considered taking into account possible semi annual, annual and biannual effects (e.g. atmospheric delay). Each mode is the best approximation of the data after stripping off the contribution of the previous mode[Aubrey and Emery, 1983; Savage, 1988]. Inhere the first mode is the most important one and since it is obtained in a way similar as obtained during common data stacking we are confident that the atmospheric delay does not have a significant impact[Ferretti *et al.*, 2007]. The assumption is that the north-south component of velocity field is negligible. To first approximation this assumption is valid for an east-west trending strike slip fault (such as EFZ). However, the occurrence of local deformation types such as due to landslides processes are yet unlikely to influence the general pattern of the observed signal inhere. Further detail on decomposition approach is given in the supplementary material.

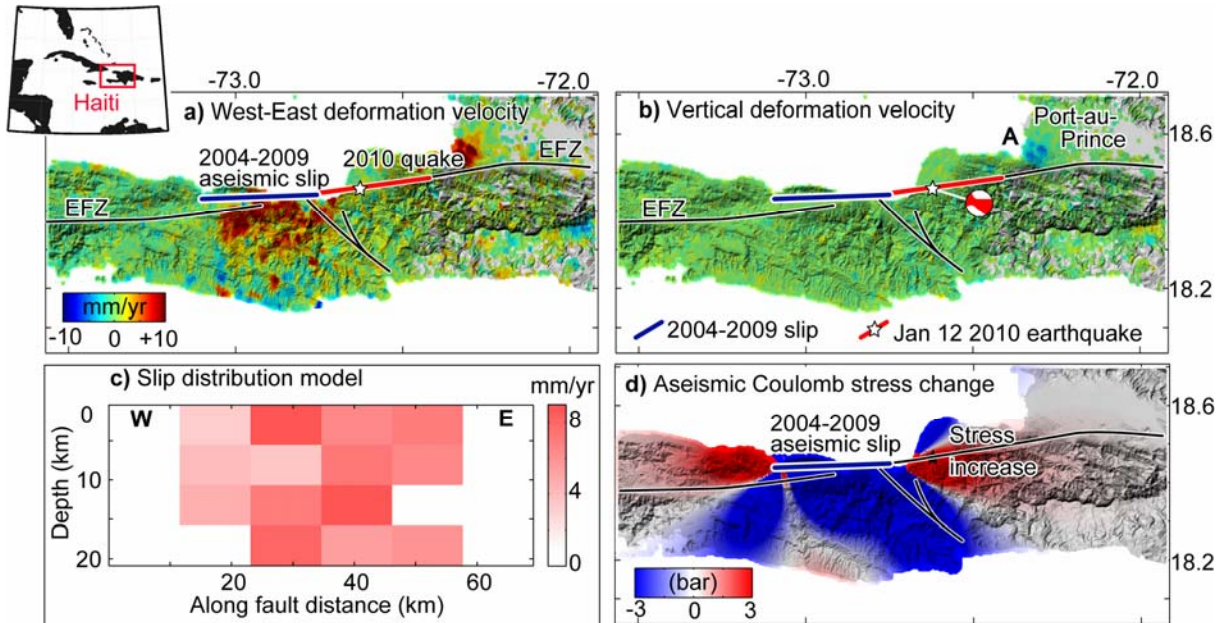


Figure 9.1. Haiti deformation field study based on ScanSAR satellite radar data.

a) West-East deformation velocity field shows a localized region of ground motion (reddish pixels) bounded by geologically inferred faults (solid black lines), implying horizontal fault motion. b) Vertical velocity field shows no major tectonic influence, implying that dip slip fault motion is inferior. Note subsidence in the city area of Port au Prince. c) Insert shows a cross-sectional view onto the fault. Left-lateral strike slip obtained in a distributed slip model inversion explains >98% of the

deformation signal. d) Coulomb stress change induced by the aseismic slip model on sub-parallel receiver faults suggests largest stress increase at the fault to the east. Red colors mean that fault is brought closer to failure. In all panels the approximate location of the Enriquillo Fault Zone (EFZ) is marked (source: www.bme.gouv.ht).

9.2 Auxiliary material

9.2.1 ScanSAR interferometry

To generate a large map of the deformation field we consider a large data set of 43 ScanSAR images acquired by the ENVISAT radar satellite between 2004 and 2009 and generated 35 interferograms (Table S9.1). The major steps before interferogram generation are azimuth scanning pattern synchronization, spectral shift filtering and Doppler centroid estimation [Holzner and Bamler, 2002]. To increase the interferometric correlation we corrected misalignments for each ScanSAR acquisition [Holzner and Bamler, 2002]. In order to reduce the data quantity, we process the data at $320 \text{ m} \times 320 \text{ m}$ pixel resolution. The topographical phase has been simulated and removed using satellite precise orbits and a reference Digital Elevation Model (DEM). To obtain the unambiguous differential deformation field, each interferogram has been unwrapped using a well tested minimum cost flow approach [Costantini, 1998] applied to those pixel [Costantini and Rosen, 1999] showing correlation larger than 0.4 in at least 65% of generated interferograms. The possible orbital ramp for each unwrapped interferogram is estimated and removed using a planar approximation [Hanssen, 2002].

The reference point utilized for calibrating the observed deformation field is (-73.908 , 18.136), located far from the deforming area. This selection allows studying the local effects such as urban subsidences, slow landslide and segment-wise creep at the EFZ.

We note that the eastward movement of the Port au Prince city (see ‘A’ in Figure 9.1a,b) should not be overinterpreted, as the same region has been the site of significant constructions and man made elevation changes, making the InSAR methodology difficult to apply if no independent data is available.

Table S9.1. *interferometric parameters of the generated ScanSAR interferograms*

Orbit No.		Track No.	Master			Slave			Perb. Baseline (m)
Master	Slave		Year	Mon	Day	Year	Mon	day	
11745	34791	Dsc-168	2004	5	16	2008	10	29	-513.86
11788	34834	Dsc-211	2004	6	1	2008	10	28	-634.93
12812	28844	Asc-233	2004	8	6	2007	8	19	-305.03
28593	33603	Dsc-483	2007	8	3	2008	8	7	140.83
28593	34104	Dsc-483	2007	8	3	2008	9	12	175.9
28593	34605	Dsc-483	2007	8	3	2008	10	19	120.36
28300	33811	Asc-190	2007	7	22	2008	8	27	122.76
28300	34312	Asc-190	2007	7	22	2008	9	30	-223.15
28300	34813	Asc-190	2007	7	22	2008	10	31	-37.38
28343	33854	Asc-233	2007	8	12	2008	9	21	103.79
28343	34355	Asc-233	2007	8	12	2008	9	25	-383.99
28343	34856	Asc-233	2007	8	12	2008	10	30	-34.27
26525	38549	Asc-419	2007	3	15	2009	7	15	-100.81
33603	34104	Dsc-483	2008	8	7	2008	9	12	34.88
33603	34605	Dsc-483	2008	8	7	2008	10	19	-20.47
34104	34605	Dsc-483	2008	9	12	2008	10	19	-55.86
33582	34083	Asc-462	2008	8	2	2008	9	6	373.42
33582	34584	Asc-462	2008	8	2	2008	10	11	-127.23
34083	34584	Asc-462	2008	9	6	2008	10	11	-501.32
33746	34247	Dsc-125	2008	8	13	2008	9	17	-280.52
33746	34748	Dsc-125	2008	8	13	2008	10	22	105.14
34247	34748	Dsc-125	2008	9	17	2008	10	22	385.7
33789	34290	Dsc-168	2008	8	20	2008	9	25	-119.42
33789	34791	Dsc-168	2008	8	20	2008	10	29	75.24
34290	34791	Dsc-168	2008	9	25	2008	10	29	195.3
33811	34312	Asc-190	2008	8	27	2008	9	30	-346.23
33811	34813	Asc-190	2008	8	27	2008	10	31	-160.47
34312	34813	Asc-190	2008	9	30	2008	10	31	185.38

33832	34333	Dsc-211	2008	8	19	2008	9	23	-31.96
33832	34834	Dsc-211	2008	8	19	2008	10	28	36.99
34333	34834	Dsc-211	2008	9	23	2008	10	28	68.98
33854	34355	Asc-233	2008	9	21	2008	9	25	-488.11
33854	34856	Asc-233	2008	9	21	2008	10	30	-138.39
34355	34856	Asc-233	2008	9	25	2008	10	30	349.18
34061	34562	Dsc-440	2008	9	4	2008	10	9	68.43

9.2.2 Principal component decomposition

Principal component decomposition (PCD) is a widely used technique for identifying patterns in data. PCD computes the most meaningful basis to re-express a data set, in order to filter out the noise and reveal hidden dynamics [Aubrey and Emery, 1983]. Herein the basis are chosen as linear and sinusoidal functions and the observation is the unwrapped, corrected and calibrated displacement field at those pixels that preserve a higher quality in all interferograms.

For solving equation (9.1) it is required to calculate the constant c_e and c_z per each pixel. These constant are functions of satellite heading and local incidence angles. Since the incidence angle varies significantly through the ScanSAR image ($\sim 20^\circ - 45^\circ$), this value was calculated for each pixel in all interferograms. Because incidence angle varies only linearly along range in radar coordinate system, this calculation is straightforward. Therefore, by having incidence angles in near and far range, the average value per each pixel can be obtained.

After calculating the constant unit vectors solving equation (9.1) for different modes is proceeding by steps. Each successive mode is the best approximation to the data with contribution of the previous modes subtracted. For estimating the first mode (i.e. linear approximation) equation (9.1) can be expressed in the matrix form as follows;

$$L + V = AX$$

$$L = \begin{bmatrix} L^1(x, y) \\ \cdot \\ \cdot \\ \cdot \\ L^k(x, y) \end{bmatrix}, V = \begin{bmatrix} V^1(x, y) \\ \cdot \\ \cdot \\ \cdot \\ V^k(x, y) \end{bmatrix}, A = \begin{bmatrix} c_e(x, y)\Delta t^1 & c_z(x, y)\Delta t^1 \\ \cdot & \cdot \\ \cdot & \cdot \\ \cdot & \cdot \\ c_e(x, y)\Delta t^k & c_z(x, y)\Delta t^k \end{bmatrix}, X = \begin{bmatrix} u_e(x, y) \\ u_z(x, y) \end{bmatrix} \quad (\text{A9.1})$$

where $\Delta t^k = t_i - t_j$ is the temporal baseline of each interferogram and V is the observation residual.

The data availability (i.e. the number of interferogram available per each pixel) is shown in Figure (S9.1), showing a large data set in the central and western part of the study area, and a poorer data coverage in the eastern part.

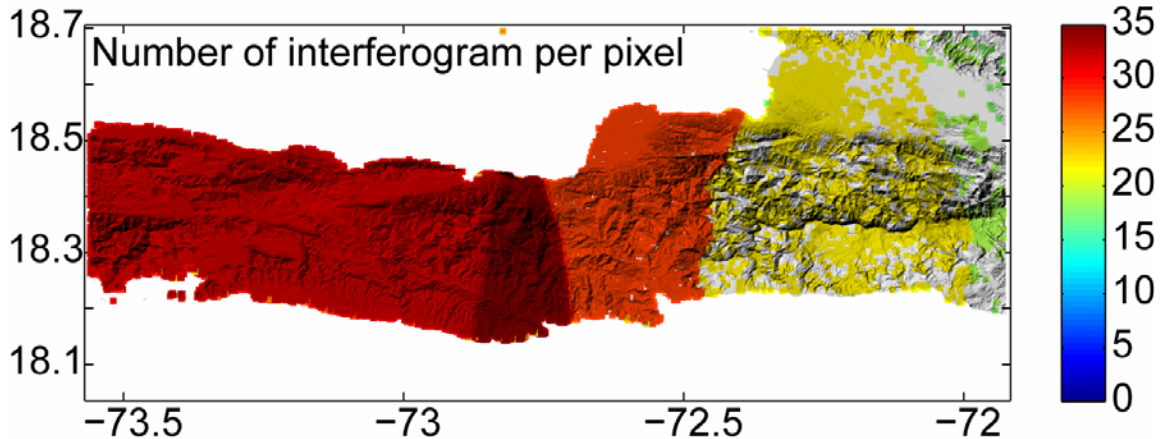


Figure S9.1: Schematic view of the number of available interferogram per each good pixel used in PCD.

For estimating linear velocity the equation (A9.1) is solved subject to the following condition;

$$V^T P V \rightarrow \min$$

$$P = \sigma_0^2 \begin{bmatrix} c_1 & 0 & 0 & 0 & 0 \\ 0 & c_2 & 0 & 0 & 0 \\ 0 & 0 & . & 0 & 0 \\ 0 & 0 & 0 & . & 0 \\ 0 & 0 & 0 & 0 & c_k \end{bmatrix} \quad (\text{A9.2})$$

$$c_i = \frac{C_i(x, y)}{\sum_{i=1}^k C_i(x, y)}, \quad i = 1, \dots, k$$

Where $C_i(x, y)$ is the interferometric coherence for each pixel and $\sigma_0^2 = V^T P V / df$ ($df = k - 2$, is degree of freedom). The solution of the equation (A9.1) subject to (A9.2) as well as the unknown's variance-covariance matrix can be obtained in an iterated manner[Mikhail, 1976]. Figures (9.1) and (S9.2) show the linear velocity field and the associated variance, respectively.

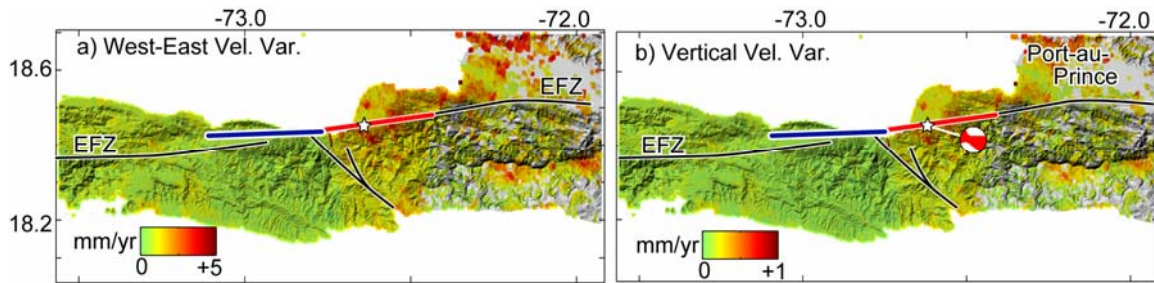


Figure S9.2: the formal variance obtained following principal component decomposition for the horizontal (a) and vertical (b) deformation velocity field. The area with few data coverage shows larger uncertainty. The approximate location of the Enriquillo Fault Zone (EFZ) is marked (source: www.bme.gouv.ht).

Having the horizontal and vertical velocity field one can estimate the velocity field in the line-of-sight of the radar satellite which is shown in Figure (S9.3).

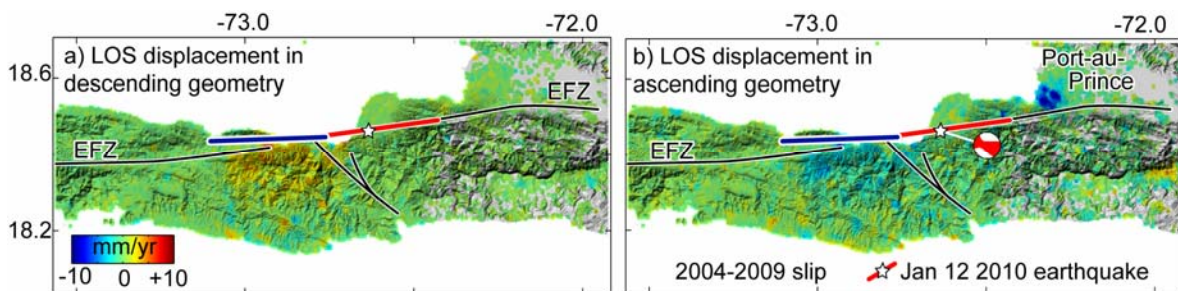


Figure S9.3: the linear velocity field in the Line-Of-Sight of satellite in descending (a) and ascending (b) orbit geometry. The approximate location of the Enriquillo Fault Zone (EFZ) is marked (source: www.bme.gouv.ht).

The other modes can be estimated in similar way after stripping off the contribution of the previous modes. The PCD implementation allows modeling more than 90% of the signal using a linear, semi annual, annual and biannual basis.

In this study we do not consider any covariance between observations. The covariance may facilitate the propagation of systematic errors from one interferogram to another one. Therefore uncorrected error may affect the estimated deformation time series. However, this is only the case if the sign of the error (for instance atmospheric delay) remain unchanged in the entire data set[Mikhail, 1976]. Fortunately this is not the case for many artifacts that encounter InSAR processing[Ferretti et al.,

2007]. This allows precise estimation of the mean velocity (i.e. data stack) without considering any covariance between observations. To reduce the effect of the observations corrupted by outliers and gross errors (such as significant atmospheric delay, unwrapping error and so on) a standard statistical test (so-called “Barda test”) has been applied[*Vanicek and Krakiwesky, 1982*].

9.2.3 Inverse modeling

To understand the kinematics of the aseismic slip we employ inverse modeling in two steps, 1) uniform slip inversion without any constraint, 2) slip distribution inversion with fixed fault geometry from first step.

The general location of the EFZ based on geology is not very well known. In the northwestern area of the aseismically slipping segment, about coordinate of (-73.127 , 18.413) as shown in recent geologic maps, a graben is expressed with a width of 2-4 km bounded to two faults in north and south. These faults can be either two deep parallel faults or a shallow expression of a deep fault. For constraining the general fault location and geometry we started the inversion procedure with a uniform slip model which provides us with the best dislocation source explaining most of the observed signal. The optimization method is the Genetic algorithm following the earlier works[*Shirzaei and Walter, 2009*]. Following the uniform slip model inversion, the optimum fault plane has the dip angle of $80.5 \pm 2^\circ$, the width of 17.7 ± 1.5 km and the location precision of ± 3 km. These parameters however provide a good approximation for the EFZ depicted by geology and seismology.

The next modeling step to investigate the distribution of the slip is done following the earlier works at the San Andreas Fault[*Rolandone et al., 2008*] by fixing the geometry of the EFZ upon the uniform slip model. At the San Andreas Fault, GPS data was inverted to retrieve the shallow aseismic creep as well as the deep interseismic strain accumulation. These authors showed that the deep interseismic slip varies by a few millimeters at the aseismic zone from the long term slip rate and differs slightly from the estimated shallow creep. Therefore the influence of the model resolution and data uncertainty is of great importance to validate this result.

We discretize the fault plane into patches of 50 km² down to depth of 20 km. We have tested the effect of patch size by considering finer grid. However it did not lead to better fit to data set. Furthermore we achieved a sensitivity analysis using an approach followed earlier works[*Shirzaei and Walter, 2009*] to tested the model resolution for the patches at depth larger than 20 km. we find, regarding the 1-2 mm/yr surface deformation precision, that the slip at these deep patches can not be constrained with precision better than 3-4 mm/yr. Table (S9.2) provide the slip distribution model.

Table S9.2: the parameters of the slip distribution rate together with geometry and location of each patch

Lon.start(°)	Lat.start(°)	Lon.end(°)	Lat.end(°)	Slip (mm)	Dip(°)	Top.depth(km)	Bot.depth(km)
-73.223	18.481	-73.114	18.480	0.000	80.611	0.400	5.522
-73.223	18.473	-73.114	18.473	0.000	80.611	5.522	10.644
-73.223	18.466	-73.114	18.465	6.541	80.611	10.644	15.766
-73.223	18.458	-73.114	18.457	0.000	80.611	15.766	20.888
-73.114	18.480	-73.005	18.480	3.362	80.611	0.400	5.522
-73.114	18.473	-73.005	18.472	4.020	80.611	5.522	10.644
-73.114	18.465	-73.005	18.464	4.710	80.611	10.644	15.766
-73.114	18.457	-73.005	18.457	0.000	80.611	15.766	20.888
-73.005	18.480	-72.896	18.479	9.578	80.611	0.400	5.522
-73.005	18.472	-72.896	18.471	3.459	80.611	5.522	10.644
-73.005	18.464	-72.896	18.463	6.987	80.611	10.644	15.766
-73.005	18.457	-72.896	18.456	8.100	80.611	15.766	20.888
-72.896	18.479	-72.786	18.478	6.355	80.611	0.400	5.522
-72.896	18.471	-72.786	18.470	7.227	80.611	5.522	10.644
-72.896	18.463	-72.787	18.462	9.210	80.611	10.644	15.766
-72.896	18.456	-72.787	18.455	5.335	80.611	15.766	20.888
-72.786	18.478	-72.677	18.477	6.884	80.611	0.400	5.522
-72.786	18.470	-72.677	18.469	0.000	80.611	5.522	10.644

-72.787	18.462	-72.677	18.461	0.000	80.611	10.644	15.766
-72.787	18.455	-72.677	18.454	5.957	80.611	15.766	20.888
-72.677	18.477	-72.568	18.476	0.000	80.611	0.400	5.522
-72.677	18.469	-72.568	18.468	0.000	80.611	5.522	10.644
-72.677	18.461	-72.568	18.460	0.000	80.611	10.644	15.766
-72.677	18.454	-72.568	18.453	0.000	80.611	15.766	20.888

Moreover, the inversion residual (observation - model) are given in Figure (S9.4). The residual analysis shows that about 98% of the data could be explained by such a simple model.

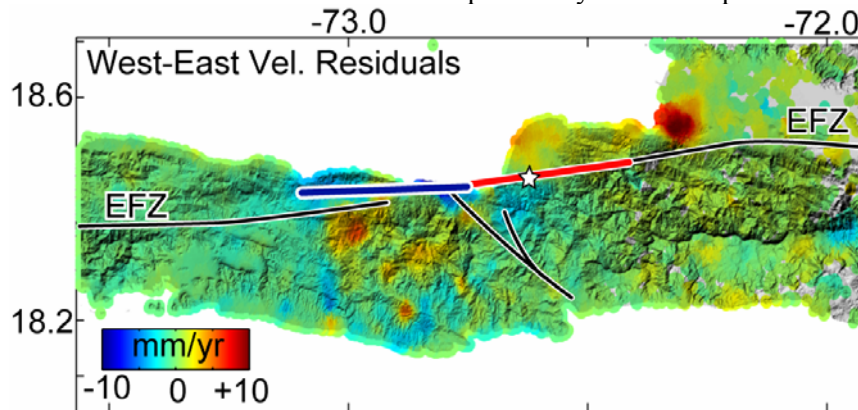


Figure S9.4. The residual velocity map (InSAR - Model) obtained following slip distribution inversion. The residual RMSE is ~ 2 mm/yr. We note that there are some areas of locally higher residual signal, which might be because of environmental and processing artifacts or the slip at other fault systems nearby the EFZ. The approximate location of the Enriquillo Fault Zone (EFZ) is marked (source: www.bme.gov.ht).

9.2.4 Cumulative Coulomb stress model

To identify the area capable for the next earthquake [2010] we estimated the cumulative Coulomb stress change induced by both the aseismic segment and the 2010 coseismic rupture. For the coseismic rupture we used the latest distributed slip provided by USGS (event id: us2010rja6). This model is only a first approximation and more precise coseismic fault model and slip distribution requires rigorous investigation of all available data, such as GPS, InSAR, seismic and geological data which can be subject of an independent study and out of scope of this article. However, the model simulation, assumes a ~ 100 km long fault dislocation, further transferring stress sideways (Fig. S9.5). Two zones of significant stress increase are found, one to the west of the aseismic segment and one to the east of the 2010 coseismic rupture. The eastern branch, in specific, is very close to the city centre of Port au Prince, underlining the area capable for the next left-lateral strike slip event. As noted by other researchers [2010; Showstack, 2010] and now supported by our data, though there was a destructive earthquake, yet, the EFZ is a major seismic threat. The eastward progression direction, starting from the creeping segment and followed by the 2010 rupture may be a hint that the next event might be further to the east again. Our data and model simulations thus suggest that another earthquake, possibly reaching or even exceeding the 2010 event rupture, may occur near to the area of Port au Prince.

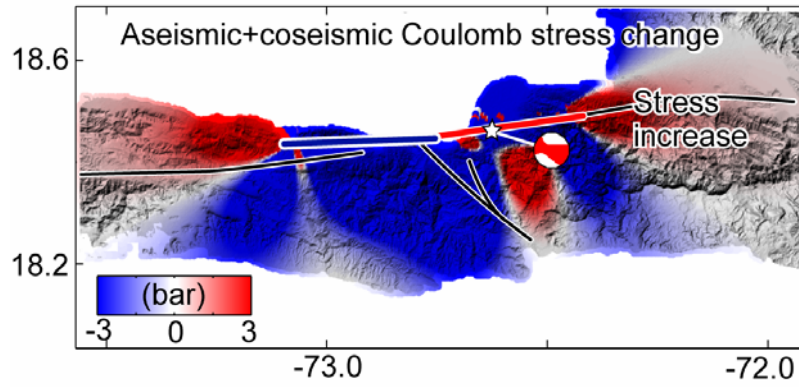


Figure S9.5. Cumulative Coulomb stress change induced by combined aseismic slip and the 2010 earthquake suggest even further eastwardly directed stress increase, now being close to Port au Prince. Red colors mean that fault is brought closer to failure. The approximate location of the Enriquillo Fault Zone (EFZ) is marked (source: www.bme.gouv.ht).

Chapter 10

Geodetic, seismic and Coulomb stress transfer analysis of the 2005 Qeshm earthquake: competing model interpretation¹

M. Shirzaei¹, T. R. Walter¹, F. Yamini-fard², A. Gholamzadeh²

¹Section 2.1, Dept. Physics of the Earth, GFZ German Research Centre for Geosciences, Telegrafenberg, D – 14473 Potsdam, Germany

²International Institute of Earthquake Engineering and Seismology (IIEES), Tehran, Iran

Abstract

The Zagros Fold Belt in southern Iran is subject to intense tectonic activity and deep basement faulting, as well as shallow folding and salt diapirism. On November 27th, 2005, a poorly understood thrust earthquake with a magnitude of M_w 5.9 occurred beneath Qeshm Island. Here we use (1) an extended InSAR data set acquired by different satellite viewing geometries, (2) a rapid response aftershock campaign dataset that contains about 1000 relocated events, (3) detailed Coulomb stress model simulations that were used to test the occurrence and focal mechanisms of the largest aftershocks, and finally (4) satellite optical images that suggest the earthquake events to be located beneath the surface expression of a fold or diapir structure. We test two interpretations, and find that a simple fault model is explaining InSAR data alone, and one more complex multi-patch fault model is explaining also geologic and geophysical data. Through stress field modelling we evaluate the two models, and find that a single fault model is causing a negative Coulomb stress change at the aftershock locations. The more complex fault model, in contrast, is well supported by the stress models. Our preferred data interpretation is hence that the earthquake triggered an upper circular deformation source that may geometrically resemble a fold or salt diapir structure. Important implications arise from this study, as it may show that diapir deformation can be triggered by tectonic events.

10.1 Introduction

The interaction of active tectonic faults with their environment has been the subject of a number of recent studies [Rundle *et al.*, 2006; Scholz, 2002; Walter, 2007]. Earthquakes and fault slips cause a transfer of the crustal shear stress, and hence interact with other fault zones [King *et al.*, 1994], volcanoes [Eggert and Walter, 2008; Walter, 2007], potential landslides areas [McGuire, 1996] and ice sheet loading or unloading [Hampel and Hetzel, 2008]. Also, the long term interaction between fault zones and salt diapirs has been shown to play an important role in nuclear storage systems [Jackson *et al.*, 1994]. However, the short term relationship between a tectonic earthquake and a deformed salt diapir has been poorly documented and understood.

¹ MS developed the approach and processed InSAR the data and achieved hybrid inversion of InSAR and seismic data. FZ and AG processed seismic data. All authors were involved in discussion and writing the paper.

The Zagros region is one of the most active tectonic areas in the world, hosting numerous active faults and shallow fold and diapir structures. In this paper we investigate an earthquake-deformation sequence and test possible physical and conceptual models. This paper is structured as follows: we begin with a short introduction of the study area; then we present the seismic and space geodetic data (InSAR) that we used to develop the models. We find that the InSAR data alone may be approximated by a single fault dislocation model. The aftershock data, however, suggests a more complex model as does the evaluation of stress transfer models. In the discussion section we elaborate the potential and limits of these modelling approaches as well as their interpretations.

10.1.1 The area of the November 27th, 2005 earthquake on Qeshm Island

The crustal deformation found in Iran is the result of plate convergence between Arabia and Eurasia [Jackson and McKenzie, 1984; 1988]. GPS studies show shortening at a rate of 22 mm/yr towards N8°E from south to north Iran due to the northward motion of the Arabian plate relative to the Eurasian plate [Vernant *et al.*, 2004b]. Zagros Mountain in southern and southwest Iran accommodates approximately 10 mm/yr of this shortening [Tatar *et al.*, 2002; Vernant *et al.*, 2004b]. Although this is one of the most seismically active regions in the Alpine-Himalayan belt, the majority of the deformation in the Zagros belt is still aseismic; i.e., the ratio of the seismic strain to geodetic strain is small [Jackson *et al.*, 1995; Masson *et al.*, 2005]. Due to the lack of surface evidence, it has been proposed that large tectonic earthquakes (> 5) occur on blind active thrust faults located [Berberian, 1995]. Apart from some events [Talebian and Jackson, 2004], the majority of large tectonic earthquakes are thought to occur beneath a sedimentary layer within the crystalline basement [Berberian, 1995]. The basement depth of the Zagros belt has been estimated by various studies; aeromagnetic studies estimated its upper limit to be at 16 km [Kugler, 1973; Morris, 1977], while microseismic data suggest a depth of about 11 km [Tatar *et al.*, 2004]. The sedimentary package overlaying this basement not only hosts blind faults and shallow folding, but also evaporite layers that gave rise to salt diapir formations [Bruthans *et al.*, 2006; Kent, 1970; Talbot *et al.*, 2000]. Presently, as seen in Figure (10.1) about 200 salt diapirs are known to be located in the Persian Gulf region [Bruthans *et al.*, 2006; Kent, 1970], some of which may have played a role in the recent Qeshm earthquake sequences.

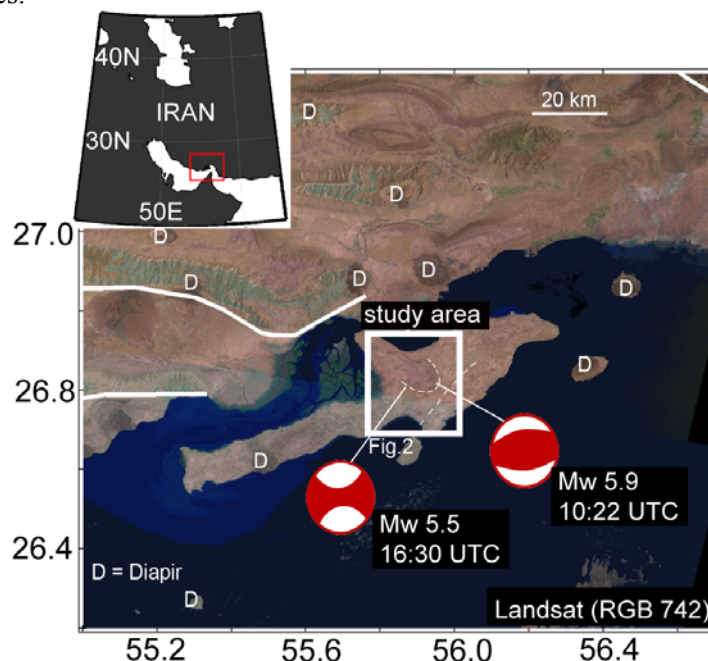


Figure 10.1. The Qeshm Island and Iranian coast, located in the tectonic collision zone of the Iranian and Arabian plate (upper left inset). The Landsat (band 742) image depicts the location of salt diapirs and the main geological features. The focal mechanisms are obtained using the Global CMT fault plane solution and correspond to the mainshock and the largest aftershock. The white box gives the area of the deformation, and aftershock observations are highlighted in Figure (10.2).

On November 27th, 2005 at 10:22 UTC, a M_w 5.9 earthquake occurred beneath Qeshm Island. The hypocenter was located at 26.66°N and 55.80°E (CMT catalog event 200511271022A). The corresponding seismic moment for this event was 1.03×10^{18} Nm. This mainshock event was followed by another large M_w 5.5 earthquake at 16:30 UTC located at 26.65N and 55.89E (CMT catalogue event 200511271630A). The Global CMT fault plane suggests a different mechanism for this aftershock than the mainshock: a strike slip along a vertical fault. The corresponding seismic moment of the event was 2.13×10^{17} Nm.

Deformation associated with these events was analyzed by means of InSAR data, showing an elliptically uplifted region [Nissen *et al.*, 2007]. Inverse source modelling as well as body wave modelling suggests a single shallow fault (4-8 km depth). As we will show below, more recent data and coulomb stress modelling suggest a possibly more complex fault system to be responsible for the 2005 events.

10.2 Data sets used for the conceptual models

First we considered the seismic fault plane solution and the moment of the mainshock and largest aftershock. Figures (10.1, 2a) illustrate the CMT solution for the mainshock ($M_w=5.9$, 10:22 UTC) and the largest aftershock ($M_w=5.5$, 16:30 UTC). The mainshock occurred along a thrust, while the aftershock was a strike slip event; both events show a non-double couple component that may imply a curved fault plane.

The aftershocks were observed by a local seismological network, including 17 three-component seismic stations that were temporarily setup during the 80-day period from December 2005 to February 2006 [Gholamzadeh, 2009]. During this observation period, 1082 events were recorded and analyzed. The relative locations were calculated by HypoDD software [Waldhauser and Ellsworth, 2000], and the velocity model is given in Table (10.1). Removing all teleseismic, regional and explosion events for the data set leaves us with 902 seismic events. From this data set we selected those events with hypocentral errors less than 2 km and recorded by at least 8 stations having horizontal and vertical locating error less than 2 km, azimuthal gap less than 180° and RMS values less than 0.2 s. This provide us with 648 seismic event with location precision better than 2 km.

Table 10.1. Velocity model used for locating aftershock events

Depth (km)	V_p (km/s)	V_s (km/s)
0	5.50	2.97
8	5.90	3.19
12	6.20	3.35

Figure (10.2a) shows the spatial distribution of the aftershocks of the November 27th, 2005 Qeshm earthquake, locations of the stations and the focal mechanisms of the selected events which represent the general pattern of the event's mechanism in each zone. The plan view of the aftershock distribution shows three patches arranged in a half-ring that is open to the northwest. The aftershocks were mainly located at a depth of 10 to 20 km (Fig. 10.2b,c) and thus mostly located within the assumed brittle basement.

The deformation on Qeshm Island was mapped by interferograms formed from SAR images provided by European Space Agency's (ESA) ENVISAT satellite. Figure (10.3) summarizes the investigated data set, which was acquired between March 2004 and February 2006, spanning the earthquake event. The average perpendicular baseline is 75 m. We selected interferograms with two geometries (ascending, image modes 6 and descending, image modes 2) to better constrain the displacement field, the source parameters and also to reduce atmospheric artefact by averaging the source parameters. All of the interferograms are coseismic including the effect of the mainshock and largest aftershock due to occurrence in the same day. In four of the interferograms, the master image was acquired 1-1.5 years before the mainshock, while one interferogram spans shortly before and after the mainshock, and one interferogram spans shortly before and about 8 months after the mainshock.

We processed the SAR data using ENVI Sarscape software (<http://www.sarmap.ch>) and used 20 cm precision orbital information that is provided by the University of Delft [Scharoo and Visser, 1998].

The topographic contribution to the slant range changes is simulated and removed using a SRTM 90 m digital elevation model.

Figure (10.4) shows six interferograms presented in a fringe format, with one fringe showing a 2.8 cm displacement in the line of sight (LOS). The general pattern of the displacement in the interferograms was characterized by an ellipse elongated in the east-west direction with a diameter of about 10 km for the long axis for the period from 2004 to 2006. Interferograms (10.4a-d) were formed from descending orbit tracks (images mode I2), and they show 6-7 fringes that are equivalent to 18-20 cm of deformation in the LOS toward the satellite. Interferograms (10.4e-f) were formed by ascending orbit tracks (images mode I6), and they show 4-5 fringes that are equivalent to 15 cm of displacement in the LOS toward the satellite.

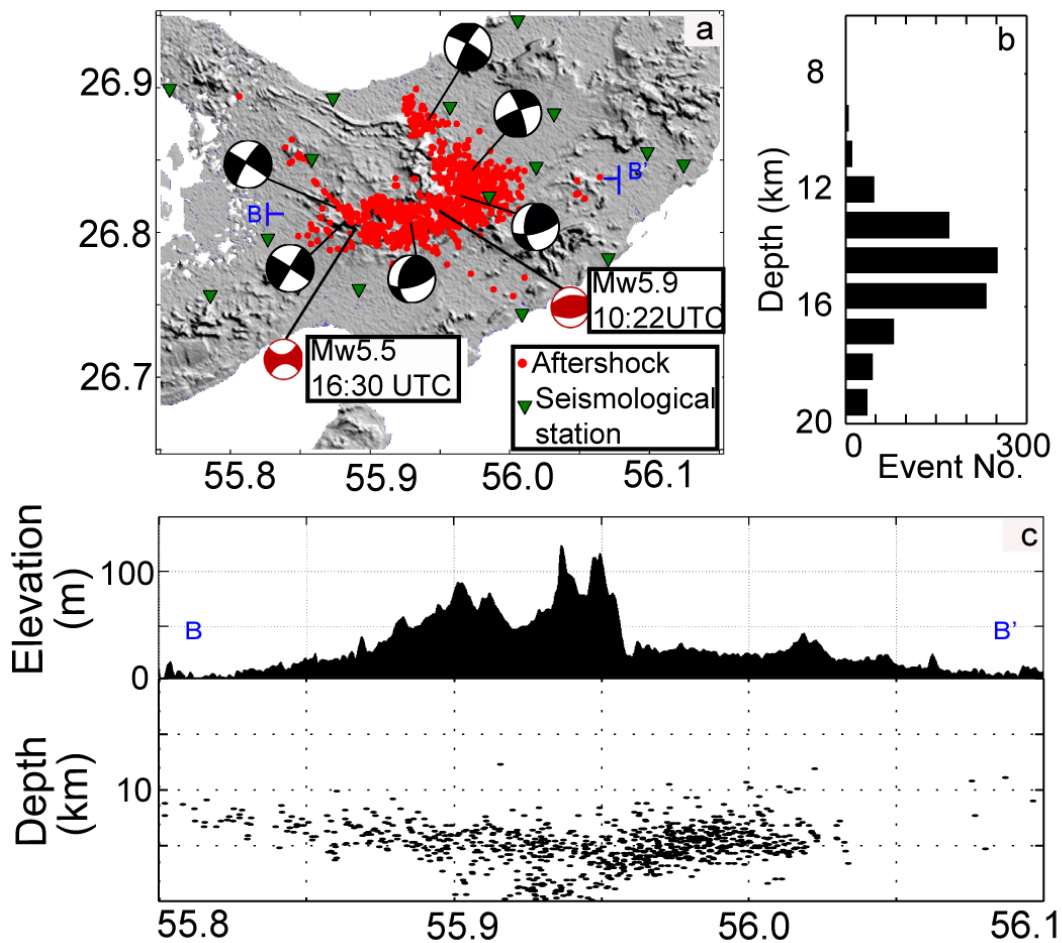


Figure 10.2. a) The spatial distribution of the aftershock data (red dot), the location of seismic stations (green triangles) and the focal mechanisms provided by the Global CMT solution and the focal mechanism of the representative aftershocks, b) the distribution of the depth of the aftershock events, c) The projection of the 3D location of aftershocks along the profile BB' on a surface of constant latitude; most of the seismicity is located under the sharp topography change.

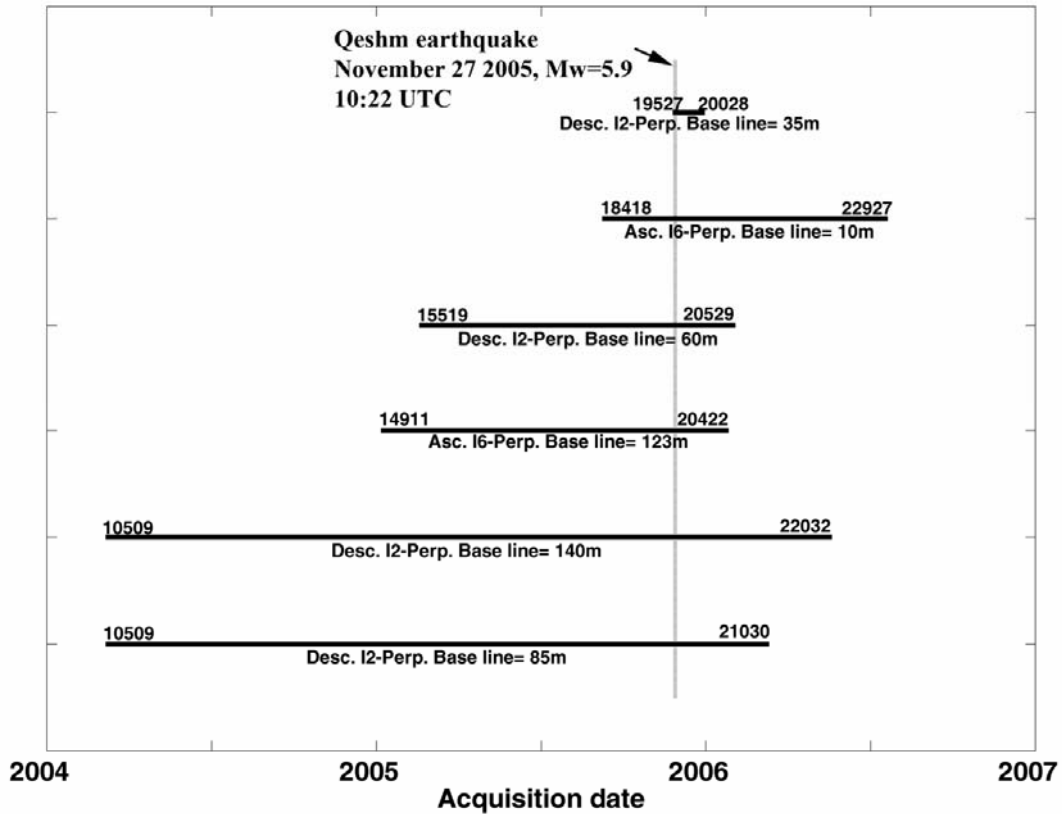


Figure 10.3. A summary of the Envisat SAR images used to produce interferograms. The horizontal bars represent the temporal baseline of the interferograms, and the vertical dashed line represents the time of main earthquake.

10.3 A single fault plane solution

To explain the source of the observed surface deformation data we use inverse modelling to estimate the parameters of a rectangular dislocating source [Okada, 1985] in elastic homogeneous half space medium. The same method was already used for the same earthquake by Nissen et al. [2007], though, herein we use a much larger InSAR data set from different viewing geometries. In analogy to previous work [Nissen et al., 2007] we use a single fault plane as responsible for the observed deformation and only use the InSAR data sets. During optimization, the source depth, width and dip angle were constrained at ranges of (2 km, 7 km), (2 km, 7 km) and (40°, 120°), respectively. The source location can be any point in the observation plane. To find the optimum source parameters, we use a binary constrained genetic algorithm (GA) in an iterative procedure [Shirzaei and Walter, 2009]. The InSAR data are sub-sampled uniformly to grid size of 400 m to decrease the amount of handled data.

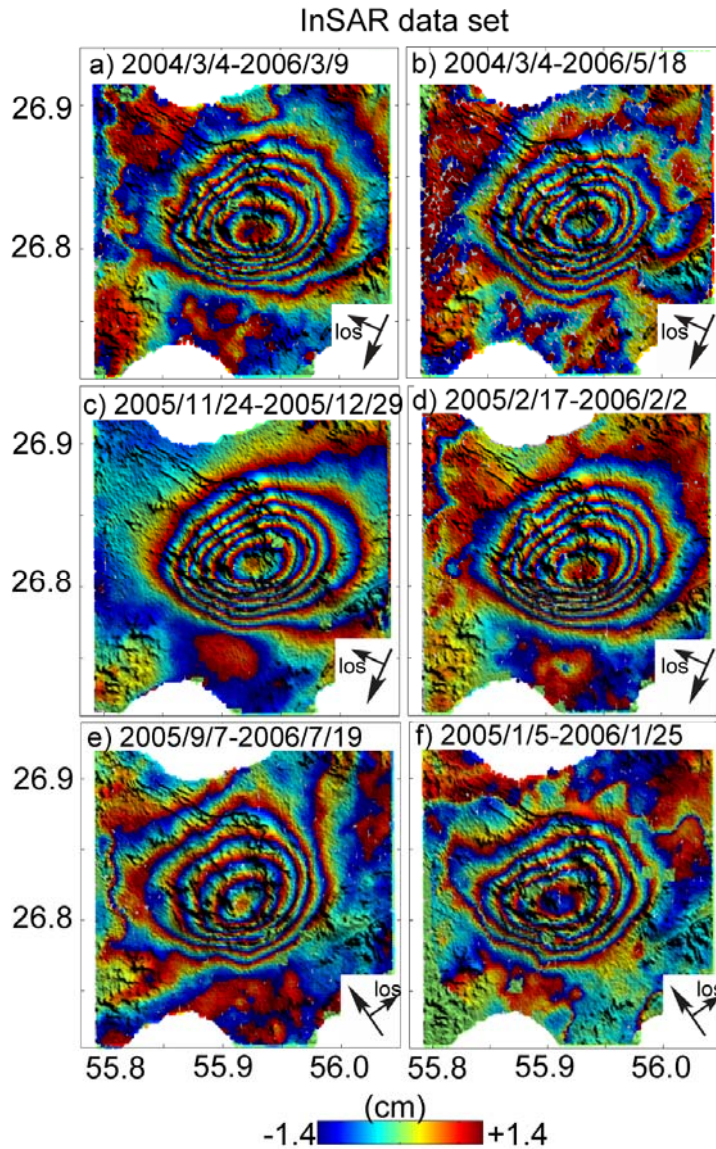


Figure 10.4. The interferograms used for this study, which show the displacement field. All of the panels are wrapped with adjacent fringe differencing by 2.8 cm along the LOS and overlaid on SRTM DTM. a-d) Interferograms formed from descending orbit images; mode 2. e-f) Interferograms formed from ascending orbit images; mode 6. For better illustration, a median filter with window size of 5×5 pixel has been applied to all panels.

The optimum solution for the fault plane has a width of 6.0 ± 0.62 km, length of 9.03 ± 1 km, depth of 4.3 ± 1 km, slip of 0.98 ± 0.19 m, dip of $55^\circ \pm 12$ and rake angle of 92.4° and strike angle of $254^\circ \pm 10$. The uncertainties are presented in 95% confidence region. Figure (10.5a, b) present the optimum model interferogram and the associated residuals (observed data minus modelled data). The equivalent moment release is 1.59×10^{18} Nm and thus consistent with energy release of an earthquake with magnitude of $M_w = 6.07$. Considering the uncertainty range of the parameters our result is in good agreement with the fault plane solution obtained by Nissen et al. [2007] as responsible for the mainshock event. Comparing to Nissen et al. [2007], including more data sets with different viewing geometry did not improve significantly the result.

In the residual plots about 0.5-1.5 fringes equivalent up to 4 cm misfit are visible (Fig. 10.5c-h). A similar misfit has been discussed by Nissen and colleague to be due to atmospheric artefact, or necessary model simplifications because use of elastic homogeneous medium and uniform dislocation [Nissen et al., 2007].

Figure 10.5. *The inversion result for single fault plane solution. a, b) obtained model interferogram in descending and ascending orbit. c-h) The residuals (observed minus modelled) of the inversion, in descending orbit (c-f) and ascending orbit (g and h). All of the panels are wrapped with adjacent fringe differencing by 2.8 cm along the LOS. For better illustration, a median filter with window size of 5×5 pixel has been applied to all panels. i) Coulomb stress change induces by simple dislocation model at the location of the representative aftershock events and receiver parameters are obtained using calculated focal mechanisms.*

As shown by Nissen et al. [2007], body wave modelling is not sensitive to minor depth variations. Therefore the uncertainty range of depth estimation using body wave modelling might be in the range of 6 – 9 km or even beyond. As a result the estimated depth using InSAR is in agreement with body wave modelling. We elaborated the locations of 902 aftershocks and find a significant disagreement between the single fault model and the aftershocks. As seen in Figure (10.2), most of the aftershocks are accommodated at large depth of 10 – 20 km. This depth is significantly deeper than the single fault plane determined by InSAR data. To test the possible link between the mainshock and the observed aftershocks we elaborated the static Coulomb failure stress [King et al., 1994]. We calculated the Coulomb stress change associated with the mainshock fault, utilizing with the parameters that we obtained by InSAR data set inversion. The considered receiver faults were the fault plane of the largest aftershock and the focal mechanisms of the representative aftershocks (shown in Fig. 10.2a). The parameters of this plane are estimated by Nissen et al. [2007] using body wave modelling (see Table 10.3 in Nissen et al. [2007]). However the location of this event based on CMT solution is not well constrained, nonetheless, because most of the event at the south-western side have very similar mechanism and depth to the largest aftershock we assume that this event occurred there. The effective coefficient of friction is assumed to be 0.4.

We obtain at depths of 11 km (i.e. the depth obtained by body wave modelling) and depth of 13 km (i.e. the depth of aftershock accumulation) mostly negative values of Coulomb stress changes (Fig. 10.5i). This may imply that the either the mainshock model is not satisfactory, or the aftershocks are wrongly located, or that the Coulomb stress concept does not apply here. As we will see in the next section, more complex fault geometry may explain these independent geophysical dataset and it is also consistent with Coulomb stress change model.

10.4 A complex dislocation source solution

By investigating the InSAR data with seismic constraints, we can estimate the source and type of deformation with even more complex pattern. We test a data interpretation scheme, based on a combination of Okada planes for investigating the source of the surface deformation data. Considering the available information on the parameters and the linearity of the elastic half space, the optimum source parameters are obtained using a Genetic Algorithm (GA) [Shirzaei and Walter, 2009].

10.4.1 Geometric arrangement of faults

An estimation of the approximate shape of the source and number of dislocation segments is necessary. For this purpose, we are considering three patches at depth of 8-20 km in agreement with the depth and pattern of aftershocks (Fig. 10.6a, b). This arrangement forms a half ring open to the NW (Fig. 10.6a). However, we obtain a very long wavelength in the simulated deformation field, thus are not able to reproduce the data by using deep dislocation planes: either the deformation field can not be explained or the seismic data remains questionable.

To resolve this discrepancy, for the next step, we expanded the half ring fault to shallower depth, which is reducing the deformation wavelength accordingly. This was achieved by placing a second half ring above the first ring at a depth of 0-8 km, thus extending the faults from 20 km depth to the surface.

During inversion all parameters of these dislocation patches have reasonable degree of freedom. The coordinates of the edges of each dislocation plane is preconditioned by the aftershock locations, but

allowed to be variable within a circle of radius of 3 km. The dip angle can vary from 30°-90°. The sense of slip was allowed to simulate both strike slip and dip-slip faulting.

The optimum dislocation sources are presented in Figure (10.6c-f). The Root Mean Square Errors (RMSEs) of the InSAR pairs for the dates (2004.03.04, 2006.03.09), (2004.03.04, 2006.05.18), (2005.01.05, 2006.01.25), (2005.02.17, 2006.02.02), (2005.9.7, 2006.07.19) and (2005.11.24, 2005.12.29) are 1.1 cm, 2.6 cm, 2.8 cm, 1.4 cm, 1.3 cm and 1.5 cm, respectively. The optimal model determined from constrained inversion is consistent with the seismic data. We found that this model explains more than 90% of the geodetic signal.

We compared the parameters of the dislocation planes to available data (Table 10.2, 3). The location, depth, strike and dip of the deep fault patches are in agreement with the aftershock pattern. By comparison of the inversion result to the solution from the Global CMT fault plane and body wave modelling, we find that the fault plane parameters are consistent. The geodetic moment (1.3×10^{18}), however, is larger than the seismic moment (1.0×10^{18}), which could be due to aseismic and time delayed deformations, material heterogeneity and the propagation of slip from other segments.

Table (10.3) shows the optimized geometry and uniform slip of the aseismic shallow structure for the 0-8 km range. Although this shallow structure apparently behaved aseismically, we find that a large part of the deformation signal (~47%) can be explained by these shallow dislocation sources.

Table 10.2. Fault plane solution for the seismogenic structure located at a depth of 8-16 km. The solution was found using the hybrid inversion of the InSAR and aftershock data. The structure was modeled as three segments: (a) the mainshock, (b) the largest aftershock, and (c) a third rupture plane; these segments were consistent with the aftershock pattern. For comparison, the Global CMT solutions are presented for the two largest earthquakes (a, b). The strike, dip and rake are defined in the study by Aki and Richards [1980]; top refers to the depth taken from the upper edge of the fault, and centroid gives the depth provided by Global CMT solver (main shock number 200511271022A and aftershock number 200511271630A)

Model		Strike (°)	Dip (°)	Rake (°)	Slip (m)	Top (km)	Width (km)	Length (km)	Moment (Nm)
a. Mainshock plane (central plane)	Hybrid inversion	241	55	101	0.87	9	6.7	7.4	1.3×10^{18}
	CMT	257	39	83	-	-	-	-	1.03×10^{18}
b. Aftershock plane (southwest plane)	Hybrid inversion	324	84	140	0.72	8.4	5.1	3.5	3.9×10^{17}
	CMT	308	88	183	-	-	-	-	2.1×10^{17}
c. Third eastern plane (northeast plane)	Hybrid inversion	147	80	20	0.34	9	6.5	7.6	5.1×10^{17}

Table 10.3. The optimized dislocation parameters [Okada, 1985], producing shallower, aseismic structure at a depth of 0-8 km. Top refers to the depth to the top edge of the fault.

Model	Strike (°)	Dip (°)	Rake (°)	Slip (m)	Top (km)	Width (km)	Length (km)	Moment (Nm)
Central plane	236	87	39	1.27	4.4	4.6	6.3	1.1×10^{18}
Northeast plane	151	62	13	0.50	3.8	4.4	7.0	4.5×10^{17}
South west plane	325	69	122	0.8	4.4	5.2	3.0	3.9×10^{17}

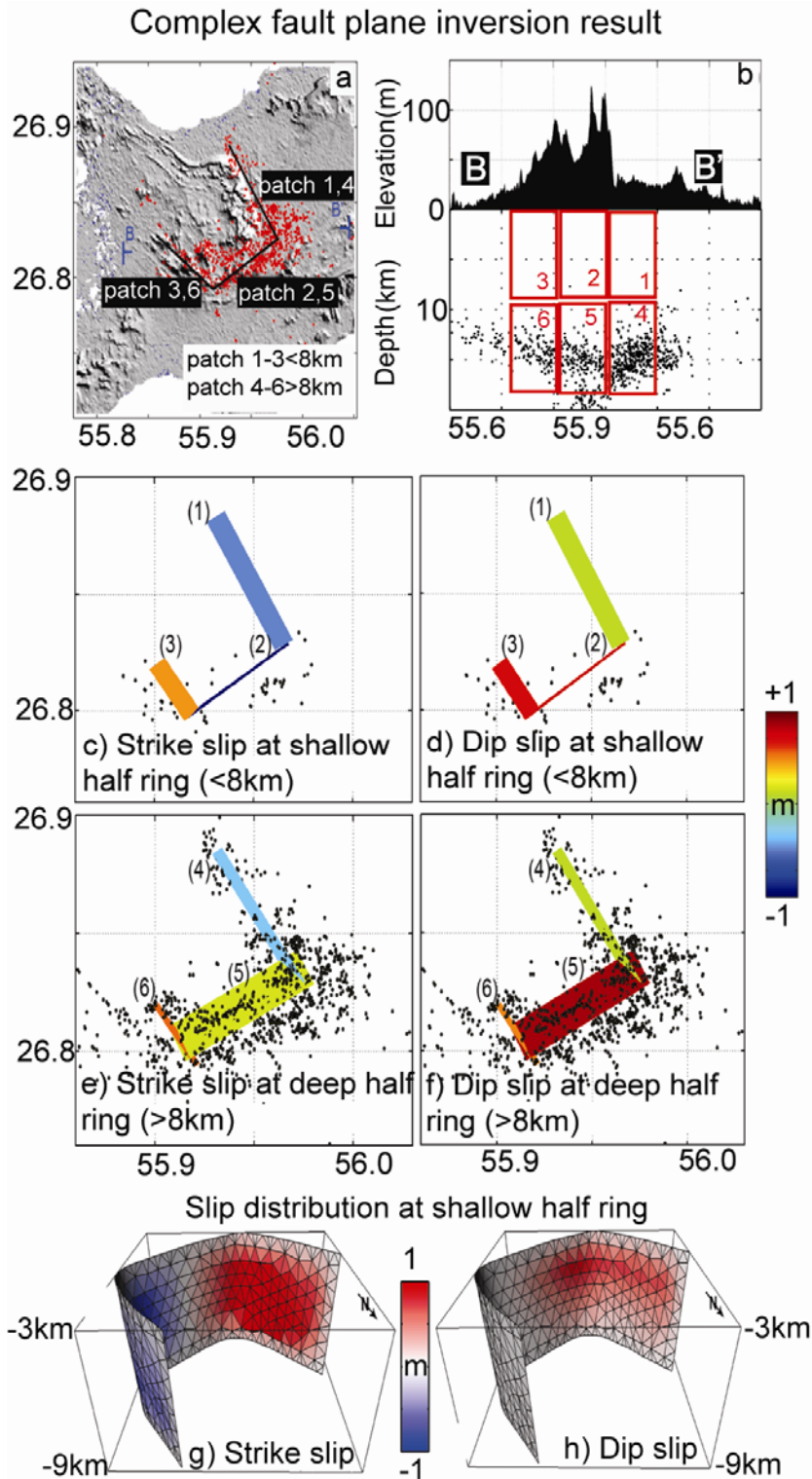


Figure 10.6. Complex multi source inversion model initialization (a, b), and the ultimate optimized model (c- f). The model setup conFiguRation is based on the seismic and morphologic data, two distinct half rings are shown: one is shallower than 8 km, and the other is deeper than 8 km. a) The horizontal view with aftershocks and b) the vertical view along the profile BB'. A plan view of the optimized uniform slip model, where c) and d) illustrate the strike and dip slip motion at the aseismic half ring (<8km); e) and f) show the strike and dip slip motion at the seismogenic half ring (>8 km). The dots indicate the locations of the aftershocks. g, h) distributed dip slip and strike slip models at the interface of the aseismic shallow half ring in a perspective view from the north.

10.4.2 Slip distribution

To obtain more information about the mechanism of the rupture located at a shallow depth, we evaluate the slip distribution around the shallower structure at a depth of 3-9 km. We use the boundary element code Poly3D, which employs a set of planar triangular elements of constant slip to model complex fault surfaces [Maerten *et al.*, 2005], in order to represent the half-ring-like fault. For this purpose, we use the approximate fault geometry that was obtained in the previous step. To make a mesh of triangles and to avoid edge effects, we enlarge the fault plane laterally, down-dip by 20% and discretize the area into 484 triangles, as determined by the Delaunay triangulation algorithm. The problem of slip distribution estimation is a linear inversion problem. All of the elements can have strike slip (left or right lateral) and dip slip motion, and to avoid an unreasonable slip pattern at the border elements, the slip is set to zero.

Figure (10.6g, h) shows the dip slip and strike slip distribution obtained for the shallow structure. In comparison with the uniform slip inversion model, the RMSE improves by about 30%, 35%, 42% and 40% for the pairs of dates (2004.03.04, 2006.05.18), (2005.01.05, 2006.01.25), (2005.02.17, 2006.02.02) and (2005.11.24, 2005.12.29), respectively. The RMSE becomes worse by 18% for the pair (2004.03.04, 2006.03.09), and for the interferogram (2005.09.07, 2006.07.19), there is no improvement in the RMSE. Compared to the uniform slip distribution solution (Fig. 10.6c, d), the general distributed slip pattern (Fig. 10.7a, b) shows similar amounts and locations of maximum slip located in the western and south-western parts of the half-ring structure. The maximum dip slip is 0.9 m and it is located in the western and south-western areas. The strike slip motion has two signs: positive (i.e., right lateral) and negative (i.e., left lateral). The magnitude of the maximum left lateral strike slip is 0.7 m in the south-eastern area, whereas the magnitude of right lateral strike slip is 0.9 m in the western and south-western areas.

The modelled interferogram in descending and ascending viewing geometry and residuals (observation minus model) shows that 95% of the signal was removed by the model (Fig. 10.7a-h). Although the residuals are generally less than 1 cm along the LOS, some of the residuals might be due to material heterogeneity that is not considered herein and/or observations that are tainted by other deformations (pre- and/or post-seismic) or atmospheric artifacts.

10.5 Did the tectonic earthquake trigger the shallower structures?

To address how the seismic dislocation and the aseismic dislocation interacted, we calculate their stress transfers based on calculated slip distributions. We assume that elastic medium was loaded by the mainshock and largest aftershock. Herein we compute the associated shear transfer. The Coulomb stress change can be calculated at any point along the aseismic dislocations [King *et al.*, 1994]. Each receiver fault has individual dip and strike angles. The associated rake angle is based on the type of slip distribution: 0° (or 180°) for left (or right) lateral strike slip motion and 90° for dip slip motion [Aki and Richards, 1980]. We repeated the calculations for different effective friction coefficients, ranging between 0 and 0.4. Changing the friction coefficient only slightly alters the result, which means that the shear stress is the effective part of the induced stress. Therefore, in Figure (10.7i, j), we only show the calculated shear stress for the dip slip and strike slip receiver faults. In our Figures, the positive and negative values of the stress are normalized to the maximum stress. The value of maximum positive stress for the dip and strike slip receiver faults are 3.2 bar and 7.0 bar, respectively, and the corresponding values for the negative stress are 2.9 bar and 3.5 bar, respectively. The models show very good agreement between the calculated shear stress and the fault patch displacement. Moreover, at points of zero slip the stress model predicts a negative shear stress change. Therefore, the displacement at the aseismic shallow ring fracture can be fully explained by the coulomb stress changes associated with the earthquake sequence. We find that most of the boundary elements confirm the results of the estimated slip distribution, as discussed in section 10.4.2. The mainshock sequence, therefore, probably triggered the displacement of the shallow aseismic half-ring structure.

As will be discussed in the following section, both, a single shallow and a complex half ring-like fault geometry may explain the geodetic data. Aftershocks, Coulomb stress transfer and geologic evidence, however, are supporting the half ring-like fault geometry.

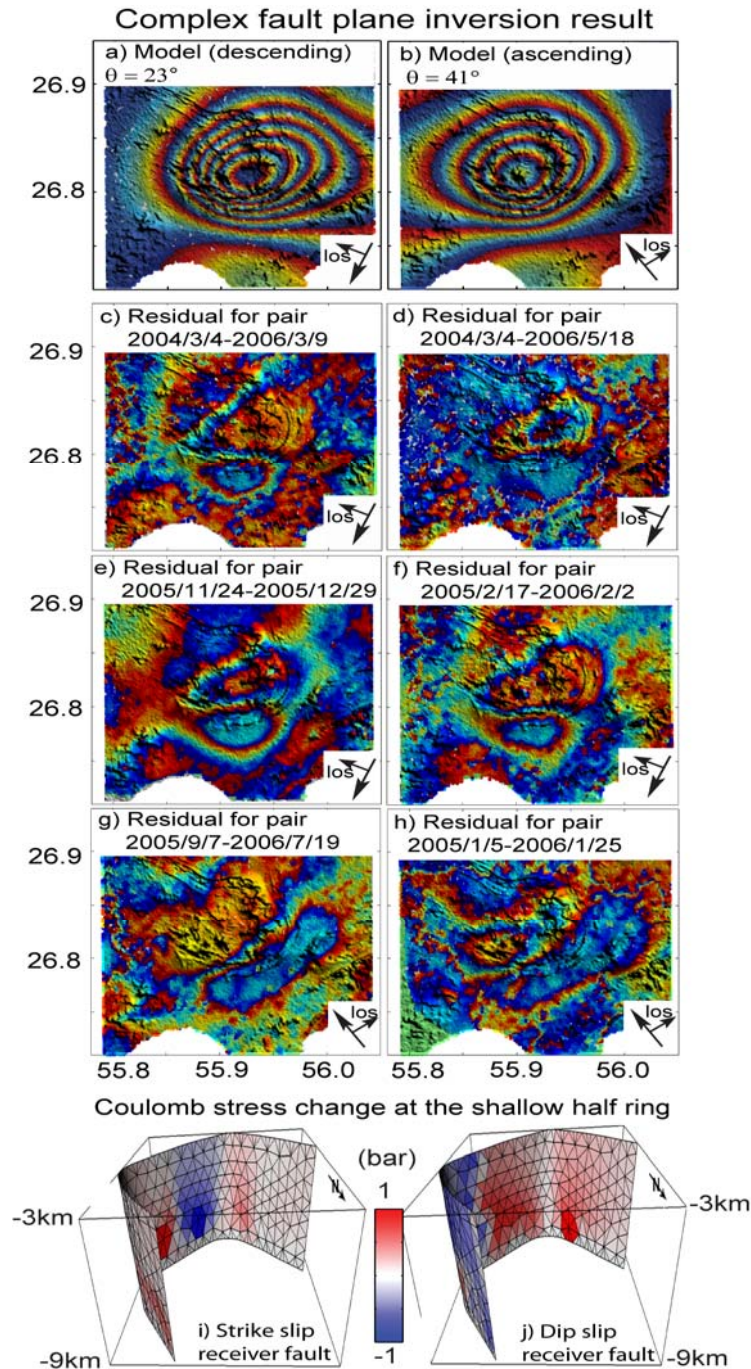


Figure 10.7. a,b) Modelled interferogram in descending and ascending orbits, c-h) residuals (observed minus modelled) of the slip distribution inversion for the complex dislocation inversion, descending orbit images; mode 2 geometry (c-f), ascending orbit images; mode 6 geometry (g,h). All of the panels are wrapped with adjacent fringe differencing by 2.8 cm along the LOS displacement. For better illustration, a median filter with window size of 5×5 pixel has been applied to all panels. I, j) shear stress on a dip slip receiver fault and strike slip receiver fault, respectively. The receiver dip and strike angle are fixed based on the geometry of the interface, and the rake angle is obtained based on the calculated slip distribution. The positive and negative values of stress are normalized by the maximum positive (red) and negative (blue) values.

10.6 Discussion

In this paper, we presented two very different source models to explain the 2005 earthquake on Qeshm Island. In the following, we discuss some of the advantages and limitations associated with these data and model interpretations. We show that, while simple models are generally favourable in geophysics, likely a complex fault architecture may explain the available geodetic, morphologic and seismic and interaction data.

10.6.1 The dataset

The used data in this study includes 3D location of aftershock data, CMT fault plane solution, body wave modelling, morphological and field observation and InSAR data.

The fault plane parameters obtained from CMT solution is in good agreement with body wave modelling result [Nissen *et al.*, 2007]. We note that these teleseismic methods are not able to precisely identify the depth of the earthquake event. As reported by Nissen *et al.* [2007] fixing the depth at a known value (6 km) or estimating the depth as a free parameter (the optimum value was 9 km) during body wave modelling leads to a similar fit to the observation. This means the depth obtained by body wave modelling is not well constrained.

Considering the result of CMT solution and body wave modelling the range of the estimated depth was between 6 and 12 km. This broad range agrees with the results obtained from both inversions of InSAR data for single fault plane solution and also for the complex multi source solution.

The aftershock data, however, accommodated at the range of 10–20 km. This depth is much deeper than the inferred depth by inversion of InSAR data for single fault plane. To reconcile between these two depths, three hypotheses may be considered;

1) The depth of aftershock data is biased because of an improper velocity model used for aftershock locations. This problem was tested by implementing different velocity models [Gholamzadeh, 2009]. It was found that, although the depth varies upon the different velocity model, the depth undulations never exceed 2-3 km, thus remains deeper than 7km. Moreover, the horizontal location and half ring pattern always remains similar. Therefore we herein are sure that the reported depth of the aftershock is generally valid.

2) The second hypothesis is that the aftershocks are not necessarily occurring at the mainshock fault plane. Aftershocks may be occurring at the fault plane, stressed by the mainshock event rupture [King *et al.*, 1994]. This possibility is assessed by calculating the Coulomb failure stress, induced by mainshock at the receiver fault plane characterized by the parameters obtained via body wave modelling for the largest aftershock [Nissen *et al.*, 2007] and the representative aftershock mechanisms. Using a single fault model, we obtained mostly negative Coulomb stress changes. This means the hypothesis of the aftershock triggered by the mainshock is not supported or that alternative fault model geometry has to be considered.

3) The third hypothesis to be considered is the assumption that aftershocks identify the location, depth and geometry of the mainshock fault plane. If true, this supports a deeper complex dislocation source as presented in this work as an alternative solution.

In addition to the available seismic data, we considered morphology and surface fissures which were reported to be associated to the seismic events [Gholamzadeh, 2009; Nissen *et al.*, 2007; Shahpasandzadeh and Hesami, 2007]. Although, the mainshock might have occurred at the aftershock depth (~13 km) its relatively small magnitude (Mw~6) disfavour apparent surface ruptures. Therefore it is feasible to assume these surface cracks are mostly secondary and resulted by triggering effect of the mainshock at the shallower structures. Surface morphology (Fig. 10.1, 2a) exhibits a folded half ring structure with a margin that appears to be delineated by the aftershock pattern. Therefore, we conjecture that dislocation sources broadly limit the folded surface and the aftershocks at depth >8km.

The interferograms are used to determine the coseismic deformation. Although their temporal baselines are different, the pattern and amplitude of the deformation are similar. This suggests that the effects of the time-dependent deformation occurred either in short time spans or they are included in less than one fringe (2.8 cm). We note, however, these used data sets are unable to address the problem of the contributions from the pre- and post-seismic components of the deformation field.

10.6.2 Inversion

Through geodetic data inversion, we aim to test two different data interpretations; 1) for standard single fault plane solution, 2) for complex multi source solution. The first result was in agreement with those reported by Nissen et al. [2007], body wave modelling and CMT solution. But, as we discussed, that result could not explain the aftershocks and Coulomb stress data.

The complex multi plane fault solution was achieved in two-step inversion procedure: 1) inversion of the geodetic constrained with seismic data aim to estimate uniform slip for the dislocation sources. This constraint was used to approximate the initial geometry and location of the dislocation sources, and 2) a slip distribution inversion was employed to provide additional information on the rupture pattern for the shallow, aseismic region.

The complex multi source model provides only a slightly better fit to the observed InSAR data. It might seem obvious that more dislocation source with more parameters better simulates the observations and we are aware that the herein presented model might not be the unique solution. One should note, that when accomplishing a free inversion all source parameters are free. In the complex model case, both the geometry and location of the dislocation sources are constrained by available data.

The inferred geodetic moment is somewhat larger than the seismic moment for a number of reasons. The most significant reason might be the contribution of post-seismic components. However, other factors, such as the assumption of purely linear elastic half-space rheology, the reference Poisson ratio of 0.25, the propagation of the slip from other dislocation patches and atmospheric artefacts, cannot be ruled out.

To obtain more information about how a rupture progresses in a shallow aseismic zone, we resolved the slip distribution at a depth of 3-9 km. Given the fixed geometry, we were left with a linear optimization problem where the type of slip was the only parameter. For this problem, there was a trade-off between the geometry and slip: selecting an incorrect geometry may affect the slip model. However, the pattern of the slip distribution model was very similar to the pattern obtained from the uniform slip inversion model, suggesting that the inferred base geometry in the uniform slip inversion model is a good approximation.

Coulomb stress modelling allows verifying the strike, dip and rake of the investigated faults. The complex model is in full agreement with these stress models and thus supports the stress interaction concept.

10.6.3 Salt-tectonics systems and Earthquake-salt diapir interaction (two-way)

The location of the earthquake-aftershock sequence studied is also an area of intense local salt-tectonics, which may have played a role.

Evaporite diapirs are major storage systems for hydrocarbon, sulfur and salt [O'Brien, 1965], while also serving as nuclear waste isolators. A salt-tectonic system is generally composed of a layer of rock salt overlying a basement and overlain by sedimentary overburden [Jackson et al., 1994]. Salt typically deforms into a buoyant and viscous fluid with a viscosity ranging between 10^{17} - 10^{19} Pas [Jackson et al., 1994; Van Kenen et al., 1993]. The average Young's Modulus of 24-31 GPa, makes them much softer than common crustal rocks, which have an average Young's Modulus of 50-100 GPa [Hansen et al., 1984]. On one hand, the deformation of salt is controlled by basement faults [Alsop et al., 1996], but on the other hand, salt forms shear zones in the overburden material during rapid strain rates [Jackson et al., 1994]. Moreover, for a rapid stress change the deformation occurs elastically, and thus the assumption of elasticity is appropriate, where the elastic constants are independent of stress [Fossum and Fredrich, 2002].

Salt diapirs are the result of both (a) horizontal compression and (b) gravitational instability [O'Brien, 1965], where the density contrast commonly confines the diapir to the uppermost crust [Jackson et al., 1994]. The average uplift rate of the crest of subsurface salt diapirs is about 2-4 mm/yr [Gera, 1972], this is too slow to be detected by two-pass InSAR method. However, the salt diapirs are affected on a more short-term scale, as this study may suggest. As shown in Figure (10.1), there are about ten

diapirs in the area surrounding Qeshm Island; the diameter of these salt diapirs usually varies between 1 and 15 km [Bruthans *et al.*, 2006].

Based on our observations and models, we have developed some guidelines that may describe the interaction between a tectonic earthquake and a salt diapir. First, we summarize what we learned from this study:

- 1- The study area contains several extruded and embedded salt diapirs.
- 2- The surface morphology indicates a folded crest above the epicentre.
- 3- There is no primary crack or fissure observed at surface as result of the 2005 earthquake mainshock, all are considered to be secondary.
- 4- The 2005 earthquake deformation pattern is fairly concentrated, suggesting that either the deformation source is shallow or the deformation field is controlled by shallower faults or other anisotropies.
- 5- The 2005 mainshock and its aftershocks are located deeper than 8 km, implying that the seismic source is located deeper than 8 km as well.
- 6- Almost 50% of the moment was released aseismically at a depth shallower than 8 km.
- 7- A shallow half ring-like part interacted with a deeper part via shear stress transfer; the normal stress did not play a significant role.

Salt diapirs are often born and grown on the shoulder of tectonic faults [Alsop *et al.*, 1996]. When there is a rapid stress change during an earthquake, these faults can generate shear zones in the soft overburden material [Jackson *et al.*, 1994] and thereby amplify the total deformation field.

Considering this information, the complex inversion model may geologically and dynamically suggest the existence of a salt diapir at shallow aseismic depth, which has a shape that is controlled by deeper tectonic faults. We suggest a conceptual model, where in 2005 this salt diapir affected the deformation field. Figure (10.8a) shows the observed and calculated results, and Figure (10.8b) illustrates our interpretation of how a fault-diapir system interacts via stress transferring. It is also plausible that a rising diapir affects the shear condition of underlying faults. Therefore, we expect that tectonic earthquakes may be more common in regions of intense salt diapir deformation. In particular, the location of the 2005 diapir rise might be the location of a future tectonic earthquake. Indeed, in 2008 an M_w 6.1 earthquake (CMT catalog 200809101100A) occurred nearby, and might represent roughly a similar behaviour.

The response of salt to a rapid stress change is more elastic than the steady state response, which is mostly viscous [Fossum and Fredrich, 2002]. In our study, the slip value at the interface of the inferred salt diapir is about 50% of the total estimated dislocation. The total released geodetic moment is equivalent to an earthquake with a magnitude of $M_w = 6.3$.

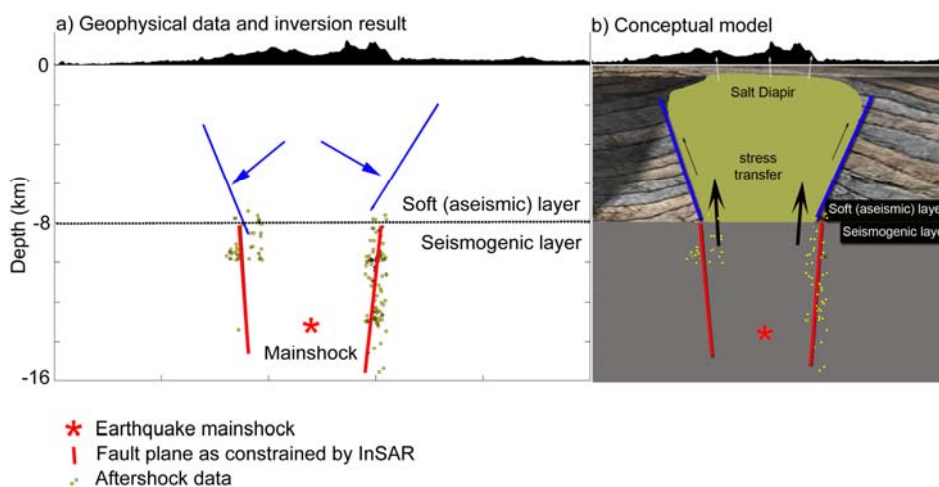


Figure 10.8. This Figure presents a summary of this study. a) The observed seismicity and inferred dislocation model, which is a result of the inversion of the geodetic and seismic data along an east-west profile. b) Our interpretation of the result based on the rheology, morphology and tectonic setting of the area, which suggest the existence of a salt diapir, which may have been reactivated via stress transfer.

Understanding the deformation response of salt diapirs after an earthquake is important for several related disciplines; in particular, diapirs and reservoirs subject to exploitation for oil and gas or nuclear waste deposits may be strongly affected by tectonic earthquakes. Although, we herein emphasize the non-uniqueness of the model and its interpretation, we find its consideration to be of vivid importance, as it is providing an early warning for an earthquake for such regions. Additionally, the interaction between the salt's rapid response and the surrounding material can cause a significant change to the stress in rocks nearby, which may increase the risk of drilling failure in the vicinity of a salt diapir [Fredrich *et al.*, 2003].

10.7 Conclusion

In this paper, we developed a hybrid inversion model for the aftershock and InSAR data obtained for the November 27th, 2005 Qeshm Island earthquake events. The thrust earthquake mainshock had a magnitude of $M_w = 5.9$, and it was followed by a strike slip aftershock with a magnitude of $M_w = 5.5$ and numerous aftershocks at a depth of 8-20 km. The aftershock data were recorded by a local temporary network, and they suggest a deep ring structure at a depth of 8-20 km. This deep seismogenic ring is in contrast to the surface deformation data, which suggest significant deformation at depths shallower than 8 km. we herein explored two data interpretations, one relying on InSAR data alone, and one explaining also seismic and morphologic data as well as Coulomb stress transfers. We propose that the seismogenic zone (>8 km) is overlain by a salt diapir (<8 km) that may have been reactivated. Through modelling, we show that the shallow deformation was induced by the deep earthquake. These two distinct depth regions (0-8 km, 8-16 km) are each simulated as three fault segments that are geometrically constrained by the aftershock and geological data. The model's solution for the mainshock and largest aftershock is in agreement with the Global CMT fault plane solution. A large part of the deformation is found to occur along a ring fracture, resembling the walls of a salt diapir. To understand the details of this deformation, we resolved the slip distribution at the shallow (0-8 km) ring fracture. We find that the change in the sheer stress at the diapir ring fracture is in agreement with the inferred slip pattern, suggesting that the diapir deformation was initiated by a stress change induced by the tectonic earthquake. Furthermore, the salt diapir rise may have unloaded other buried deep basement faults, so new earthquakes are expected to occur in the seismogenic region.

Chapter 11

Summary and outlook

Conventional Interferometric synthetic aperture radar (InSAR) has proven to be an effective tool for measuring crustal deformation. However, occurrence of decorrelation and interference of environmental artifacts may cause no measurement possible or lead to mis-interpretation of the signal. To improve the applicability of the InSAR, time series analysis developed. The current InSAR time series analysis methods usually rely on presumption of the temporal model for deformation behavior which is usually unknown.

I describe in this dissertation a new InSAR time series analysis method (WabInSAR) that over comes most limitation of the earlier approaches. This approach uses verity of wavelet based, Kalman and Wiener filters for identifying a network of stable pixels and reducing environmental artifacts. The key element of WabInSAR is the pattern recognition procedure based on wavelet transform that allows identifying hidden component in time and space domain.

Validation against ground truth data has proven that the WabInSAR approach provides a precise and accurate map of the spatiotemporal crustal deformation field, which allows better understanding the volcanic and tectonic process through inverse modeling. However the inversion methods usually require initially a good approximation of the solution and despite may still trap in local minima.

To overcome this limitations a novel inversion method (RISC-GA/SA) as a combination of the Genetic Algorithm and Simulated Annealing in an iterative manner accompanied with a statistical competency approach is presented in this dissertation. The RISC-GA/SA is applicable to static data inversion and prior knowledge of the approximate solution is not required.

The extension of the RISC approach for modeling the source of the time dependent crustal deformation is demonstrated as a combination with the Kalman Filter. This new dynamic modeling method estimate source parameters as a function of time by minimizing spatial and temporal mean square error.

The applications to verity of the volcanic and tectonic area and comparison with ground truth dada and independent studies have proven the ability of these inversion methods for accurate and efficient modeling the source of crustal deformation field.

Therefore the advancements in this thesis provided significant tools for volcanic and tectonic deformation source monitoring, in particular in remote and hazardous area. These tools also suite to a fast response system where a continuous deformation monitoring and reliable deformation source modeling approaches are required.

11.1 Future Directions

The WabInSAR is using a 2D phase unwrapping approach which is not however exploiting entire spatiotemporal information to retrieve unambiguous phase change map. While the current version of WabInSAR showed merits for precise deformation field mapping, a 3D phase unwrapping operator is still required. This we may achieve by combining artificial intelligence and Kalman Filter into well-known minimum cost flow (MCF) algorithm. MCF is originally developed for 2D phase unwrapping now we are going to extend it in a step-wise manner to 3D problem. We look into the problem of 3D phase unwrapping as a filtering problem. Where, the 2D information is refined by a time consistent approach in statistical manner. There exist several 3D unwrapping approach but none of them are suitable when the deformation rate is high and we are dealing with temporal aliasing problem. We therefore aim to develop an approach which also takes this issue into account.

WabInSAR approach is designed based on multi-master interferometry. It is, however, computationally more intensive than approaches relaying on single master interferometry. As seen,

most of the steps performed in WabInSAR are independent from number of masters considered. It is therefore relevant to apply those filters to a single master interferometry scheme and generate a wavelet based algorithm for single master interferometry (i.e. permanent scatterer InSAR). This approach so-called Wavelet based permanent scatterer InSAR (WaPSI) is now under development and would be published in soon future.

The RISC approach provides an estimation of the source parameters together with their quality. It however does not provide any information about the covariance between unknowns. This covariance is of importance for investigating the correlation between parameters and also systematic error propagation into the optimization result. This might be overcome by combining RISC with Unscented transforms which propagate the full variance-covariance matrix through the nonlinear functions.

The modeling scheme we used here is based on simple analytical models and the aim in our modeling was to retrieve the spatiotemporal amplitude of the deformation. However, the deformation field is obtained by superimposing the effect of several deforming sources which may have different spatial frequency properties. Integrating these frequency properties may help to retrieve more realistic source for the observed deformation field. This might be performed by combining the wavelet multiresolution analysis and optimization algorithms such as RISC.

References

- (2010), Haiti earthquake may have primed nearby faults for failure, *Nature news*.
- Abercrombie, R., A. McGarr, and H. Kanamori, Eds. (2006), *Earthquakes: Radiated Energy and the Physics of Faulting*, edited, AGU, Washington, D.C.
- Aki, K. (1979), Characterization of barriers on an earthquake fault, *J. Geophys. Res.*, *84*, 6140-6148.
- Aki, K., and P. G. Richards (1980), *Quantitative Seismology*, Freeman, San Francisco.
- Akkar, S., and P. Gülkan (2002), A critical examination of near-field accelerograms from the Sea of Marmara region earthquakes, *Bull. Seism. Soc. Am.*, *92*, 428-447.
- Ali, S. T., A. M. Freed, E. Calais, D. M. Manaker, and W. R. McCann (2008), Coulomb stress evolution in Northeastern Caribbean over the past 250 years due to coseismic, postseismic and interseismic deformation, *Geophys. J. Int.*, *174*, 904-918.
- Allenbach, P. (1966), *Geologie und petrographie des Damavand und seiner umgeurg (Zentral-Elburz), Iran*, 114 pp, ETH, Zurich.
- Alsop, G. I., D. Blundell, and I. Davison (1996), *Salt Tectonics*, Special Publication of the Geological Society of London
- Ambraseys, N. N., and C. P. Melville (1982), *A History of Persian Earthquakes*, 219 pp., Cambridge University Press, London.
- Amelung, F., S. H. Yun, T. R. Walter, P. Segall, and S. W. Kim (2007), Stress control of deep rift intrusion at Mauna Loa volcano, Hawaii, *Science*, *316*, 1026-1030
- Amiri-Simkooei, A. (2003), Formulation of L1 Norm Minimization in Gauss-Markov Models, *J. Surv. Eng.*, *129*.
- Amoruso, A., L. Crescentini, A. T. Linde, I. S. Sacks, R. Scarpa, and P. Romano (2007), horizontal crack in a layered structure satisfies deformation for the 2004-2006 uplift of Campi Flegrei, *Geophysical Research Letters*, *34*, L22313.
- Ando, M. (1979), The Hawaii earthquake of November 29, 1975: Low dip angle faulting due to forceful injection of magma, *J. Geophys Res.*, *84*, 7616-7626.
- Aubrey, D. G., and K. O. Emery (1983), Eigenanalysis of recent United States sea levels, *Cont. Shelf Res.*, *2*, 21-33
- Avallone, A., P. Briole, C. Delacourt, A. Zollo, and F. Beauducel (1999), Subsidence at Campi Flegrei (Italy) detected by SAR interferometry, *Geophysical Research Letters*, *26*, 2303-2306.
- Barberi, F., D. P. Hill, F. Innocenti, G. Luongo, and M. Treuil (1984), The 1982- 1984 Bradyseismic crisis at Phlegrean Fields (Italy), *Bull. Volcanol.*, *47*, 173- 411.
- Barbot, S., Y. Fialko, and Y. Bock (2009), Postseismic deformation due to the Mw 6.0 2004 Parkfield earthquake: Stress-driven creep on a fault with spatially variable rate-and-state friction parameters, *J. Geophys. Res.*, *114*, doi:10.1029/2008JB005748.
- Basu, A., and L. N. Frazer (1990), Rapid determination of critical temperature in simulated annealing inversion, *Science*, *249*, 1409-1412.

- Battaglia, M., P. Segall, J. Murray, P. Cervelli, and J. Langbein (2003), The mechanics of unrest at Long Valley caldera, California: 1. Modeling the geometry of the source using GPS, leveling and 2-color EDM data, *J. Volcanol. Geotherm. Res.*, *127*, 195-217.
- Battaglia, M., C. Troise, F. Obrizzo, F. Pingue, and G. De Natale (2006), Evidence for fluid migration as the source of deformation at Campi Flegrei caldera (Italy), *Geophys. Res. Lett.*, *33*, L01307.
- Berardino, P., G. Fornaro, R. Lanari, and E. Sansosti (2002), A new algorithm for surface deformation monitoring based on small baseline differential SAR interferograms, *IEEE Transactions on Geosciences and Remote Sensing*, *40*, 2375-2383.
- Berberian, M. (1995), Master 'blind' thrust faults hidden under the Zagros folds: active basement tectonics and surface morphotectonics, *Tectonophys.*, *241*, 193-224.
- Bertran Ortiz, A., A. Pepe, R. Lanari, P. Lundgren, and P. A. Rosen (2009), Completing the gaps in Kilauea's Father's Day InSAR displacement signature with ScanSAR, paper presented at AGU.
- Bjerhammar, A. (1973), *Theory of errors and generalized matrix inverse*, 127-128 pp., Elsevier publishing company, Amsterdam.
- Bjerhammar, A. (1973), *Theory of Errors and Generalized Matrix Inverses*, 432 pp., Elsevier, NY.
- Bodnar, R. J., C. Cannatelli, B. De Vivo, A. Lima, H. E. Belkin, and A. Milia (2007), Quantitative model for magma degassing and ground deformation (bradyseism) at Campi Flegrei, Italy: Implications for future eruptions, *Geology*, *35*, 791-794.
- Borgia, A. (1994), Dynamic basis of volcanic spreading, *J. Geophys Res.*, *99*, 17,791-717,804.
- Borgia, A., L. Ferrari, and G. Pasquare (1992), Importance of gravitational spreading in the tectonic and volcanic evolution of Mount Etna, *Nature*, *357*, 231 - 235.
- Borgia, A., and B. Van Wyk de Vries (2003), The volcano-tectonic evolution of Concepcion, Nicaragua, *Bull. Volcanol.*, *65*, 248-266.
- Brooks, B. A., J. Foster, D. Sandwell, C. J. Wolfe, P. Okubo, M. Poland, and D. Myer (2008), Magmatically Triggered Slow Slip at Kilauea Volcano, Hawaii, *Science*, *321*, 1177.
- Brown, J., and J. Bethel (1991), Blunder detection in a small geodetic network, *Proc., Am. Congr. Surv. Mapp.*
- Bruthans, J., M. Filippi, M. Gerl, M. Zare, J. Melková, A. Pazdur, and P. Bosák (2006), Holocene marine terraces on two salt diapirs in the Persian Gulf, Iran: age, depositional history and uplift rates, *J. Quaternary Sc.*, *21*, 843-857.
- Bryan, C. J., and C. E. Johnson (1991), Block tectonics of the island of Hawaii from a focal mechanism analysis of basal slip, *Bull Seism. Soc. Am.*, *81*, 491 - 507.
- Bürgmann, R., D. Schmidt, R. M. Nadeau, M. d'Alessio, E. Fielding, D. Manaker, T. V. McEvelly, and M. H. Murray (2000), Earthquake potential along the northern Hayward fault, California, *Science*, *289*, 1178-1182.
- Caccamise II, D. J., M. A. Merrifield, M. Bevis, J. Foster, Y. L. Firing, M. S. Schenewerk, F. W. Taylor, and D. A. Thomas (2005), Sea level rise at Honolulu and Hilo, Hawaii: GPS estimates of differential land motion, *Geophys. Res. Lett.*, *32*, 10.1029/2004GL021380.
- Cannon, E., and R. Bürgmann (2001), rehistoric fault offsets of the Hilina fault system, south flank of Kilauea Volcano, Hawaii, *J. Geophys. Res.*, *106*, 4207-4219.

- Carbone, D., G. Currenti, and C. Del Negro (2008), Multiobjective genetic algorithm inversion of ground deformation and gravity changes spanning the 1981 eruption of Etna volcano, *J. Geophys. Res.*, *113*.
- Cayol, V., J. H. Dieterich, A. T. Okamura, and A. Miklius (2000), High Magma Storage Rates Before the 1983 Eruption of Kilauea, Hawaii, *Science* *288*.
- Cecchi, E., B. Van Wyk de Vries, and J. M. Lavest (2005), Flank spreading and collapse of weak-cored volcanoes, *Bull. Volcanol.*, *67*, 72-91.
- Cervelli, P., and A. Miklius (2003), The shallow magmatic system of Kilauea Volcano, *USGS Professional Paper 1676*, 149–164.
- Cervelli, P., M. Murray, P. Segall, Y. Aoki, and T. Kato (2001a), Estimating source parameters from deformation data, with an application to the March 1997 earthquake swarm off the Izu Peninsula, *Journal of Geophysical Research*, *106*, 11217-11237.
- Cervelli, P., M. H. Murray, P. Segall, Y. Aoki, and T. Kato (2001b), Estimating source parameters from deformation data, with an application to the March 1997 earthquake swarm off the Izu Peninsula, Japan, *J. Geophys. Res.*, *106*, 11,217-211,238.
- Cervelli, P., P. Segall, K. Johnson, M. Lisowski, and A. Miklius (2002), Sudden aseismic fault slip on the South Flank of Kilauea Volcano, Hawaii, *Nature*, *415*, 1014–1017.
- Chen, C. W., and H. A. Zebker (2001), Two-dimensional phase unwrapping with use of statistical models for cost functions in nonlinear optimization, *J. Opt. Soc. Am. A.*, *18*, 338–351.
- Chevrot, S. (2002), Optimal measurement of relative and absolute delay times by simulated annealing, *Geophys. J. Int.*, *151*, 164–171.
- Chou, C. M., and R. Y. Wang (2004), Application of wavelet-based multi-model Kalman filters to real-time flood forecasting, *Hydrological processes*, *18*, 987-1008.
- Costantini, M. (1998), A novel phase unwrapping method based on network programming, *Geoscience and Remote Sensing, IEEE Transactions on*, *36*, 813 - 821.
- Costantini, M., and P. A. Rosen (1999), A generalized phase unwrapping approach for sparse data, paper presented at in Proceedings of the IEEE 1999 International Geoscience and Remote Sensing Symposium (IGARSS), Hamburg.
- Currenti, G., C. Del Negro, and G. Nunnari (2005), Inverse modelling of volcanomagnetic fields using a genetic algorithm technique, *Geophysical Journal International*, *163*, 403–418.
- Dach, R., U. Hugentobler, P. Fridez, and M. Meindl (2007), *Bernese GPS Software Version 5.0*, 640 pp., Astronomical Institute, University of Bern, Bern.
- Darwin, C. (1840), On the Connexion of certain Volcanic Phenomena in South America; and on the Formation of Mountain Chains and Volcanos, as the Effect of the same Power by which Continents are elevated, *Transactions of the Geological Society of London*, *2*, 601-632.
- Daubechies, I. (1992), *Ten Lectures on Wavelets*, 377 pp., SIAM.
- Davidson, J., J. Hassanzadeh, R. Berzin, D. F. Stockli, B. Bashukoo, B. Turrin, and A. Pandamouz (2004), The geology of Damavand volcano, Alborz Mountains, northern Iran *GSA Bulletin*, *116*, 16-29.

- Davis, L. (1987), *Genetic Algorithms and Simulated Annealing*, Research Notes in Artificial Intelligence, London.
- Davis, P. M. (1986), Surface deformation due to inflation of an arbitrarily oriented triaxial ellipsoidal cavity in an elastic half-space, with reference to Kilauea volcano, Hawaii, *J. Geophys. Res.*, *91*, 7429-7438.
- Dawson, J., and P. Tregoning (2007), Uncertainty analysis of earthquake source parameters determined from InSAR: A simulation study, *J. Geophys. Res.*, *112*, doi:10.1029/2007JB005209.
- De Natale, G., S. M. Petrazzuoli, and P. F. (1997), The effect of collapse structures on ground deformations in calderas, *Geophys. Res. Lett.*, *24*, 1555 – 1558.
- Deb, K., S. Agrawal, A. Pratab, and T. Meyarivan (2000), A fast elitist nondominated sorting genetic algorithm for multi-objective optimization: Nsga-ii, paper presented at Proceedings of PPSN-6, Springer, New York.
- Decker, R. W., D. P. Hill, and T. L. Wright (1966), Deformation measurements on Kilauea volcano, Hawaii *Bull. Volcanol.*, *29*, 721-731.
- Delcamp, A., B. van Wyk de Vries, and M. R. James (2008), The influence of edifice slope and substrata on volcano spreading, *J. Vol. Geo. Res.*, *177* 925-943.
- Deming, W. E. (1943), *Data Reduction and Error Analysis for the Physical Sciences*, 328 pp., Wiley, New York.
- Denlinger, R. P. (1997), A dynamic balance between magma supply and eruption rate at Kilauea volcano, Hawaii, *J. Geophys. Res.*, *102*, 18,091–018,100.
- Denlinger, R. P., and P. Okubo (1995), Structure of the mobile south flank of Kilauea, Volcano, Hawaii, *J. Geophys Res.*, *24*,499-424,507.
- Dieterich, J., V. Cayol, and P. Okubo (2000), The use of earthquake rate changes as a stress meter at Kilauea volcano, *Nature*, *408*, 457.
- Dieterich, J. H. (1998), Growth and persistence of Hawaiian volcanic rift zones, *J. Geophys Res.*, *93*, 4258-4270.
- Dieterich, J. H., and R. W. Decker (1975), Finite element modeling of surface deformation associated with volcanism, *J. Geophys. Res.*, *80*, 4094-4102.
- Dixon, T. H., F. Amelung, A. Ferretti, F. Novali, F. Rocca, R. Dokka, G. Sella, S. W. Kim, S. Wdowinski, and D. Whitman (2006), Space geodesy: Subsidence and flooding in New Orleans *Nature*, *441*, 587-588
- Donoho, D. L., and I. M. Johnstone (1994), Ideal spatial adaptation by wavelet shrinkage, *Biometrika*, *81*, 425-455.
- Dvorak, J., F. W. Klein, and D. A. Swanson (1994), Relaxation of the south flank after the 7.2-magnitude Kalapana earthquake, Kilauea Volcano, Hawaii *Bull Seism. Soc. Am.*, *84*, 133-141.
- Dvorak, J., A. Okamura, and J. H. Dieterich (1983), Analysis of surface deformation data, Kilauea Volcano, Hawaii, October 1966 to September 1970, *J. Geophys. Res.*, *88*, 9295-9304.
- Dzurisin, D. (2006), *Volcano Deformation - New Geodetic Monitoring Techniques*, Springer.

- Eggert, S., and T. R. Walter (2008), Volcanic activity before and after large tectonic earthquakes: Observations and statistical significance., *Tectonophysics*, DOI: 10.1016/j.tecto.2008.10.003.
- Eichelberger, J. C., and P. E. Izbekov (2000), Eruption of andesite triggered by dyke injection; contrasting cases at Karymsky Volcano, Kamchatka and Mt Katmai, Alaska, *Philosophical Transactions - Royal Society Mathematical, Physical and Engineering Sciences*, 358.
- Ferretti, A., A. Monti-Guarnieri, C. Prati, and F. Rocca (2007), InSAR Principles: Guidelines for SAR Interferometry Processing and Interpretation, ESA/ESRIN, Frascati.
- Ferretti, A., C. Prati, and F. Rocca (2001a), Permanent scatterers in SAR interferometry, *IEEE transactions on geoscience and remote sensing* 39, 8-20
- Ferretti, A., C. Prati, and F. Rocca (2001b), Permanent scatterers in SAR interferometry, *IEEE transactions on geoscience and remote sensing*, 39, 8-20
- Fossum, A. F., and J. T. Fredrich (2002), Salt Mechanics Primer for Near-Salt and Sub-Salt Deepwater Gulf of Mexico Field Developments, Geoscience and Environment Center Sandia National Laboratories, Albuquerque.
- Foster, J., B. Brooks, T. Cherubini, C. Shacat, S. Businger, and C. L. Werner (2006), Mitigating atmospheric noise for InSAR using a high resolution weather model, *Geophys. Res. Lett.*, 33.
- Fournier, T., J. Freymueller, and P. Cervelli (2009), Tracking magma volume recovery at Okmok volcano using GPS and an unscented Kalman filter, *J. Geophys. Res.*, 114.
- Francis, P. W., and G. L. Wells (1988), Landsat Thematic Mapper observations of debris avalanche deposits in the Central Andes, *Bull. Volcanol.*, 50, 258-278.
- Fredrich, J. T., D. Coblentz, A. F. Fossum, and B. J. Thorne (2003), Stress perturbations adjacent to salt bodies in the deepwater Gulf of Mexico, in *SPE Annual Technical Conference and Exhibition*, edited, Society of Petroleum Engineering, Richardson, Texas, Denver, Colorado, USA.
- Fritsch, F. N., and R. E. Carlson (1980), Monotone Piecewise Cubic Interpolation, *SIAM J. Numerical Analysis*, 17, 238-246.
- Froger, J.-L., O. Merle, and P. Briole (2001), Active spreading and regional extension at Mount Etna imaged by SAR interferometry, *Earth and planet. Sci. Lett.*, 187, 245-258.
- Fuchs, H. (1982), contribution to the adjustment by minimizing the sum of absolute residuals, *Manuscripta Geodetica*, 7, 151-207.
- Fukuda, J. i., T. Higuchi, S. i. Miyazaki, and T. Kato (2004), A new approach to time-dependent inversion of geodetic data using a Monte Carlo mixture Kalman filter, *Geophys. J. Int.*, 159, 17-39.
- Gendron, P., J. Ebel, and D. Manolakis (2000), Rapid joint detection and classification with wavelet bases via Bayes theorem, *Bull. Seism. Soc. Am.*, 90, 764-774.
- Gera, F. (1972), Review of salt tectonics in relation to disposal of radioactive wastes in salt formations, *Bull. Seism. Soc. Am.*, 83, 3551-3574.
- Ghiglia, D. C., and M. D. Pritt (1998), *Two-Dimensional Phase Unwrapping: Theory, Algorithms, and Software* 512 pp., Wiley-Interscience
- Gholamzadeh, A. (2009), Seismicity and seismotectonics in the eastern zone of Zagros, PhD thesis, International Institute of Earthquake Engineering and Seismology, Tehran.

- Goff, J., W. C. Dudley, M. J. deMaintenon, G. Cain, and J. P. Coney (2006), The largest local tsunami in 20th century Hawaii, *Marine Geology*, 226, 65–79.
- Goldberg, D. E. (1989), Genetic Algorithms in Search, Optimization, and Machine Learning, *Addison-Wesley, Reading, Mass.*
- Gorokhovich, Y., and A. Voustianiouk (2006), Accuracy assessment of the processed SRTM-based elevation data by CGIAR using field data from USA and Thailand and its relation to the terrain characteristics, *Remote Sensing of Environment*, 104, 409-415.
- Goswami, J. C., and A. K. Chan (1999), *Fundamentals of Wavelets: Theory, Algorithms, and Applications*, 324 pp., Wiley-Interscience.
- Gottsmann, J., A. G. Camacho, K. F. Tiampo, and J. Fern'andez (2006), Spatiotemporal variations in vertical gravity gradients at the Campi-Flegrei caldera (Italy): a case for source multiplicity during unrest?, *Geophysical Journal International*, 167, 1089–1096.
- Grewal, M. S., and A. P. Andrews (2001), *Kalman Filtering : Theory and Practice Using MATLAB*, 416 pp., Wiley-Interscience.
- Grossmann, A., M. Holschneider, R. Kronland-Martinet, and J. Model (1987), Detection of abrupt changes in sound signals with the help of the wavelet transform, 298-306 pp, Academic Press
- Halldorsson, B., and A. S. Papageorgiou (2005), Calibration of the specific barrier model to earthquakes of different tectonic regions, *Bull. Seism. Soc. Am.*, 95, 1276-1300.
- Hampel, A., and R. Hetzel (2008), Slip reversals on active normal faults related to the inflation and deflation of magma chambers: Numerical modeling with application to the Yellowstone-Teton region *Geophys. Res. Lett.*, 35, L07301, doi:10.1029/2008GL033226.
- Hansen, F. D., K. D. Mellegard, and P. E. Senseny (1984), Elasticity and strength of ten natural rock salt, *First conference on the mechanical behavior of salt*, 71-83.
- Hanssen, R. F. (2002), *Radar interferometry, data interpretation and error analysis*, 328 pp., Kluwer Academic Publishers.
- Haupt, R. L., and S. E. Haupt (2004), *Practical Genetic Algorithms*, John Wiley & Sons.
- Heiskanen, W. A., and H. Moritz (1967), *Physical Geodesy*, 364 pp., W.H.Freeman & Co Ltd
- Hildreth, W., and J. Fierstein (2000), Katmai volcanic cluster and the great eruption 1912, *Geological Society of America Bulletin*, 112, 1594-1620.
- Hofmann-Wellenhof, B., H. Lichtenegger, and J. Collins (2000), *Global Positioning System, Theory and Practice*, 5th Edition, 390 pp., Springer, New York.
- Holland, J. H. (1975), *Adaptation in Natural and Artificial Systems*, Univ. of Mich. Press, Mich.
- Holland, J. H. (1992), Genetic algorithms, *Sci. Am.*, 267, 66–72.
- Holland, P. W., and R. E. Welsch (1977), Robust Regression Using Iteratively Reweighted Least-Squares, *Communications in Statistics: Theory and Methods*, A6, 813-827.
- Holzner, J., and R. Bamler (2002), Burst-Mode and ScanSAR interferometry, *IEEE Trans. Geosc. Rem. Sens.*, 40, 1917-1934.

- Hooper, A., P. Segall, and H. Zebker (2007), Persistent scatterer interferometric synthetic aperture radar for crustal deformation analysis, with application to Volcán Alcedo, Galápagos, *J. Geophys. Res.*, *112*.
- Hooper, A., H. Zebker, P. Segall, and B. Kampes (2004), A new method for measuring deformation on volcanoes and other natural terrains using InSAR persistent scatterers, *Geophys. Res. Lett.*, *31*.
- Hooper, A., and H. A. Zebker (2007), Phase unwrapping in three dimensions with application to InSAR time series, *J. Opt. Soc. Am. A.*, *24*.
- Huber, P. J. (1981), *Robust Statistics*, 320 pp., Wiley.
- Igel, C., N. Hansen, and S. Roth (2007), Covariance Matrix Adaptation for Multi-objective Optimization, *Evolutionary Computation*, *15*, 1-28.
- Jackson, J., J. Haines, and W. Holt (1995), The accommodation of Arabia-Eurasia plate convergence in Iran, *J. Geophys. Res.*, *100*, 15205-15219.
- Jackson, J., and D. McKenzie (1984), Active tectonics of the Alpine-Himalayan Belt between western Turkey and Pakistan, *Geophys. J. R. astr. Soc.*, *77*, 185-264.
- Jackson, J., and D. McKenzie (1988), The relationship between plate motions and seismic moment tensors, and the rates of active deformation in the Mediterranean and Middle East, *Geophys. J.*, *93*, 45-73.
- Jackson, M. P. A., B. C. Vendeville, and D. D. Schultz-Ela (1994), Structural dynamics of salt systems, *Annu. Rev. Earth Planet. Sci.*, *22*, 93-117.
- Jaggard, T. A., and R. H. Finch (1929), Tilt records for thirteen years at the Hawaiian Volcano Observatory, *Bull. Seism. Soc. Am.*, *19*, 38-51.
- Johnson, D. J. (1992), Dynamics of Magma Storage in the Summit Reservoir of Kilauea Volcano, Hawaii, *J. Geophys. Res.*, *97*, 1807-1820.
- Jónsson, S., H. Zebker, P. Segall, and F. Amelung (2002), Fault slip distribution of the Mw 7.1 Hector Mine, California, earthquake, estimated from satellite radar and GPS measurements, *Bull. Seism. Soc. Am.*, *92*, 1377-1389.
- Julier, S. J., and J. K. Uhlmann (1997), A New Extension of the Kalman Filter to Nonlinear Systems. , paper presented at The 11th Int. Symp. on Aerospace/Defence Sensing, Simulation and Controls.
- Julier, S. J., and J. K. Uhlmann (2004), Unscented Filtering and Nonlinear Estimation *Proc. IEEE*, *92*, 401-422.
- Kalman, R. E. (1960), A New Approach to Linear Filtering and Prediction Problems, *ASME-Journal of Basic Engineering*, *82*, 35-45.
- Kampes, B. M. (2005), Displacement parameter estimation using permanent scatterer interferometry, Delft, Netherlands.
- Kato, Y., M. Kawahara, and N. Koizumi (2009), Kalman filter finite element method applied to dynamic ground motion, *Int. J. Numer. Anal. Meth. Geomech.*, *33*, 1135-1151.
- Keilis-Borok, V. I., and T. B. Yanovskaja (1967), Inverse problems of seismology, *Geophys. J. R. astr. Soc.*, *13*, 223-234.

- Kent, P. E. (1970), The salt of the Persian Gulf region, *Transaction of the Leicester Literasy and Philosphical Society*, 64, 56–88.
- King, G. C. P., R. S. Stein, and J. Lin (1994), Static stress changes and the triggering of earthquakes, *Bull. Seism. Soc. Am.*, 84, 935-953.
- King, N. E., J. L. Svarc, E. B. Fogleman, W. K. Gross, K. W. Clark, G. D. Hamilton, C. H. Stiffler, and J. M. Sutton (1995), Continuous GPS observations across the Hayward fault, California, 1991–1994, *J. Geophys. Res.*, 100, 20271–20283.
- Kirkpatrick, S. C., D. Gelatt, and M. P. Vecchi (1983), Optimization by simulated annealing, *Science*, 220, 671–680.
- Klein, F. W. (1982), Patterns of historical eruptions at Hawaiian volcanoes *J. Volcanol. Geotherm. Res.*, 12, 1-35.
- Kohlhase, A. O., K. L. Feigl, and D. Massonnet (2003), Applying differential InSAR to orbital dynamics: a new approach for estimating ERS trajectories, *J. Geodesy*, 77, 493-502.
- Krystek, M., and M. Anton (2007), A weighted total least-squares algorithm for fitting a straight line, *Meas. Sci. Tech.*, 18, 3438-3442.
- Kugler, A. (1973), An interpretation of the Southwest Iran aeromagnetic survey, Oil Service Company of Iran.
- Kumar, P., and E. Foufoula-Georgiou (1997), Wavelet analysis for geophysical applications, *Rev. Geophys.*, 35, 385-412.
- Lanari, R., P. Berardino, S. Borgström, C. Del Gaudio, P. De Martino, G. Fornaro, S. Guarino, G. P. Ricciardi, E. Sansosti, and P. Lundgren (2004), The use of IFSAR and classical geodetic technique for caldera unrest episode: application to Campi Flegrei uplift event of 2000, *Journal of Volcanology and Geothermal Research*, 133, 247-260.
- Lanari, R., F. Casu, M. Manzo, G. Zeni, P. Berardino, M. Manunta, and A. Pepe (2007), An Overview of the Small BAseline Subset Algorithm: A DInSAR Technique for Surface Deformation Analysis, *Pure appl. geophys.*, 164, 637–661.
- Leng, C. H., and H. D. Yeh (2003), Aquifer parameter identification using the extended Kalman filter, *Water Resour. Res.*, 39, 1062.
- Linde, A. T., and P. G. Silver (1989), Elevation changes and the Great 1960 Chilean earthquake: Support for aseismic slip, *Geophys. Res. Lett.*, 16, 1305-1308.
- Lipmann, P. W., and D. R. Mullineaux (1981), The 1980 eruptions of Mount St. Helens, Professional Paper, 844 pp, U.S. Geol. Surv., Washington.
- Lira, M. M. S., H. M. De Oliveira, M. A. Carvalho Jr, and R. M. C. Souza (2003), Compactly Supported Wavelets Derived from Legendre Polynomials: Spherical Harmonic Wavelets, in *Proc. Computational Methods in Circuits and Systems Applications*, 211-215.
- Lundgren, P., S. Usai, E. Sansosti, R. Lanari, M. Tesauro, G. Fornaro, and P. Berardino (2001), Modeling surface deformation observed with synthetic aperture radar intefreometry at Campi Flegrei caldera, *JOURNAL OF GEOPHYSICAL RESEARCH*, 106, 19355-19366.
- Maerten, F., P. Resor, D. Pollard, and L. Maerten (2005), Inverting for slip on three-dimensional fault surfaces using angular dislocations, *Bulletin of the Seismological Society of America*, 95, 1654-1665.

- Mallat, S. G. (1989), A theory for multiresolution signal decomposition: the wavelet representation, *IEEE Transactions on Pattern Analysis and Machine Intelligence*, 11, 674-693.
- Manaker, D. M., E. Calais, A. M. Freed, S. T. Ali, P. Przybylski, G. Mattioli, P. Jansma, C. Pr'épetit, and J. B. de Chabaliér (2008), Interseismic Plate coupling and strain partitioning in the Northeastern Caribbean, *Geophys. J. Int.*, 174, 889-903.
- Manconi, A., R. T. Walter, M. Manzo, G. Zeni, P. Tizzani, E. Sansosti, and R. Lanari (2010), An effective approach to account for the effects of 3-D mechanical heterogeneities at Campi Flegrei caldera, Southern Italy, by using standard source deformation models, *J. Geophys Res.*, 2009JB007099 *in press*.
- Manconi, A., T. R. Walter, and F. Amelung (2007), Effects of mechanical layering on volcano deformation, *geophys. J. Int.* , 170, 952 - 958.
- Marshall, J., and J. Bethel (1996), basic concepts of L1 norm minimization for surveying applications, *J. Surv. Eng.*, 198-179.
- Masson, F., J. Chéry, D. Hatzfeld, J. Martinod, P. Vernant, F. Tavakoli, and M. Ghafory-Ashtiani (2005), Seismic versus aseismic deformation in Iran inferred from earthquakes and geodetic data, *Geophys. J. Int.*, 160, 217-226.
- Massonnet, D., and K. L. Feigl (1998), Radar interferometry and its application to changes in the Earth's surface, *Rev. Geophys.*, 36, 441-500.
- McGuire, J. J., and P. Segall (2003), Imaging of aseismic fault slip transients recorded by dense geodetic networks, *Geophysical Journal International*, 155, 778-788.
- McGuire, W. J. (1996), *Volcano instability: a review of contemporary themes*, 1-24 pp., Geological Society Special Publication
- McTigue, D. F. (1987), Elastic stress and deformation near a finite spherical magma body: resolution of the point source paradox, *J. Geophys. Res.*, 92, 12931-12940.
- Merle, O., and A. Borgia (1996), Scaled experiments of volcano spreading, *J. Geophys Res.*, 101, 13,805-813,817.
- Metropolis, N., M. N. Rosenbluth, A. W. Rosenbluth, A. H. Teller, and E. Teller (1953), Equation of state calculations by fast computing machines, *Journal of Chemical Physics*, 21, 1087-1092.
- Meyer, P. L. (1970), *Introductory Probability and Statistical Applications*, second edition ed., 367 pp., oxford & IBH
- Michalewicz, Z. (1994), *Genetic Algorithms + Data Structures = Evolution Programs*, 2 ed., Springer-Verlag, New York.
- Mikhail, E. M. (1976), *Observations and least squares* 497 pp., IEP, New York.
- Miklius, A., and P. Cervelli (2003), Interaction between Kilauea and Mauna Loa, *nature*, 421.
- Miyazaki, S. i., P. Segall, J. J. McGuire, T. Kato, and Y. Hatanaka (2006), Spatial and temporal evolution of stress and slip rate during the 2000 Tokai slow earthquake, *J. Geophys. Res.*, 111.
- Mogi, K. (1958), Relations between the eruptions of various volcanos and the deformations of the ground surfaces around them, *Bull. Earthq. Res. Inst. (Tokyo)*, 36, 99-134.

- Montgomery-Brown, E. K., P. Segall, and A. Miklius (2009a), Kilauea slow slip events: Identification, source inversions, and relation to seismicity, *J. Geophys. Res.*, *14*.
- Montgomery-Brown, E. K., D. Sinnett, M. Poland, P. Segall, T. Orr, H. Zebker, and A. Miklius (2009b), Geodetic evidence for an echelon dike emplacement and concurrent slow-slip and Kilauea volcano, Hawaii, 17 June 2007, *J. Geophys. Res.*, *in press*.
- Moore, J. G., and D. J. Fornari (1984), Drowned Reefs as Indicators of the Rate of Subsidence of the Island of Hawaii, *J. Geol.*, *92*, 752-759.
- Morgan, J. K., G. F. Moore, and D. A. Clague (2003), Slope failure and volcanic spreading along the submarine south flank of Kilauea volcano, Hawaii, *J. Geophys. Res.*, *108(B9)*, 2415.
- Morris, P. (1977), Basement structure as suggested by aeromagnetic survey in S.W. Iran, Oil Service Company of Iran.
- Natale, G. D., C. Troise, F. Pingue, G. Mastrolorenzo, L. Pappalardo, M. Battaglia, and E. Boschi (2006), The Campi Flegrei caldera: unrest mechanisms and hazards, *Geological Society of London*, *269*, 25-45.
- Newland, D. E. (1997), Practical signal analysis: do wavelets make any difference?, Proceedings of DETC'97, 16 Biennial Conf. on Vibration and Noise, ASME Design Engineering Technical Conferences, September 14-17, 1997, Sacramento, California, 12 pp.
- Nissen, E., M. Ghorashi, J. Jackson, B. Parsons, and M. Talebian (2007), The 2005 Qeshm Island earthquake (Iran)—a link between buried reverse faulting and surface folding in the Zagros Simply Folded Belt?, *Geophys. J. Int.*, *171*, 326–338.
- Nostro, C., R. S. Stein, M. Cocco, M. E. Belardinelli, and W. Marzocchi (1998), Two-way coupling between Vesuvius eruptions and southern Apennine earthquakes, Italy, by elastic stress transfer, *Journal of Geophysical Research*, *103*, 24487-24504.
- O'Brien, G. D. (1965), Survey of diapirs and diapirism, paper presented at Diapirism and diapir, American Association of Petroleum Geologists, New Orleans.
- O'leary, D. P. (1990), robust regression computation using iteratively reweighted least square, *SIAM J. Matrix Anal. Appl.*, *11*, 466-480.
- Okada, Y. (1985), Surface deformation due to shear and tensile faults in a half-space, *Bull. Seism. Soc. Am.*, *75*, 1135-1154.
- Okubo, P. G., H. M. Benz, and B. A. Chouet (1997), Imaging the crustal magma sources beneath Mauna Loa and Kilauea volcanoes, Hawaii, *Geology* *25*, 867–870.
- Owen, S., P. Segall, J. Freymueller, M. A., R. Denlinger, T. Árnadóttir, M. Sako, and R. Bürgmann (1995), Rapid Deformation of the South Flank of Kilauea Volcano, Hawaii, *Science*, *267*, 1328 - 1332.
- Owen, S., P. Segall, M. Lisowski, A. Miklius, R. Denlinger, and M. Sako (2000), Rapid deformation of Kilauea Volcano: Global Positioning System measurements between 1990 and 1996, *J. Geophys. Res.*, *105*, 18,983–918,998.
- Ozawa, S., S. Miyazaki, T. Nishimura, M. Murakami, M. Kaidzu, T. Imakiire, and X. Ji (2004), Creep, dike intrusion, and magma chamber deflation model for the 2000 Miyake eruption and the Izu islands earthquakes, *J. Geophys. Res.*, *109*.
- Parfitt, E. A., and D. C. P. Peacock (2001), Faulting in the South Flank of Kilauea Volcano, Hawai'i, *J. Vol. Geo. Res.*, *106*, 265-284

- Pazos, A., M. J. González, and G. Alguacil (2003), Non-linear filter, using the wavelet transform, applied to seismological records, *Journal of Seismology*, 7, 413-419.
- Peyret, M., Y. Djamour, M. Rizza, J.-F. Ritz, J.-E. Hurtrez, M. A. Gouadarzi, H. Nankali, J. Chéry, K. L. Dortz, and F. Uri (2008), Monitoring of the large slow Kahrod landslide in Alborz mountain range (Iran) by GPS and SAR interferometry *Engineering Geology*, 100, 131-141
- Pollock, D. S. G. (1999), *A Handbook of Time Series Analysis, Signal Processing and Dynamics*, Academic Press, San Diego, Calif.
- Qu, W., X. Jia, S. Pei, and J. Wu Non-stationary Signal Noise Suppression Based on Wavelet Analysis, *Proceed. 2008 Cong. Im. Sig. Proces.*, 4, 303-306.
- Rawlins, G. J. E. (1991), *Foundations of Genetics Algorithms*, Morgan Kaufmann Burlington, Mass.
- Rezai, M., and C. E. Ventura (2002), Analysis of strong and weak ground motions recorded at two sites during Loma Prieta earthquake by wavelet transform, *Can. J. Civ. Eng.*, 29, 157-170.
- Riley, C. M., J. F. Diehla, J. L. Kirschvink, and R. L. Ripperdanc (1999), Paleomagnetic constraints on fault motion in the Hilina Fault System, south flank of Kilauea Volcano, Hawaii, *J. Vol. Geo. Res.*, 94.
- Robinson, E. A., and S. Treitel (1967), Principles of digital Wiener filtering, *Geophys. Prosp.*, 15, 311.
- Rolandone, F., R. Burgmann, D. C. Agnew, I. A. Johanson, D. C. Templeton, M. A. d'Alessio, S. J. Titus, C. DeMets, and B. Tikoff (2008), Aseismic slip and fault-normal strain along the central creeping section of the San Andreas fault, *Geophys. Res. Let.*, 35, L14305.
- Rosen, P. A., S. Hensley, H. A. Zebker, F. H. Webb, and E. J. Fielding (1996), Surface deformation and coherence measurements of Kilauea Volcano, Hawaii, from SIR-C radar interferometry, *J. Geophys. Res.*, 101, 23,109–123,125.
- Rothman, D. H. (1985), Nonlinear inversion statistical mechanics, and residual statics corrections, *Geophysics*, 50, 2784–2796.
- Rowan, L. R., and R. W. Clayton (1993), The three-dimensional structure of Kilauea Volcano, Hawaii, from travel time tomography, *J. Geophys. Res.*, 98, 4355-4375.
- Rundle, J. B., P. B. Rundle, A. Donnellan, P. Li, W. Klein, G. Morein, D. L. Turcotte, and L. Grant (2006), Stress transfer in earthquakes, hazard estimation and ensemble forecasting: Inferences from numerical simulations, *Tectonophysics*, 413, 109-125.
- Saccorotti, G., S. Petrosino, F. Bianco, M. Castellano, D. Galluzzo, M. L. Rocca, E. D. Pezzo, L. Zaccarelli, and P. Cusano (2007), Seismicity associated with the 2004–2006 renewed ground uplift at Campi Flegrei Caldera, Italy *Physics of The Earth and Planetary Interiors*, 165, 14-24.
- Sambridge, M. (1998), Exploring multi-dimensional landscapes without a map, *Inverse Problems*, 14, 427–440.
- Sambridge, M. (1999a), Geophysical inversion with a Neighbourhood algorithm, I, Searching a parameter space, *Geophysical Journal International*, 138, 479–494.
- Sambridge, M. (1999b), Geophysical inversion with a neighbourhood algorithm, II, Appraising the ensemble, *Geophysical Journal International*, 138, 727–746.
- Sambridge, M., and K. Mosegaard (2002), Monte Carlo methods in geophysical inverse problems, *Rev. Geophys.*, 40, 3-1 to 3-29.

- Savage, J. C. (1988), Principal component analysis of geodetically measured deformation in Long Valley caldera, eastern California, 1983-1987, *J. Geophys. Res.*, *93*, 13297-13305.
- Savage, J. C. (1995), Principal component analysis of interseismic deformation in southern California, *J. Geophys. Res.*, *100*, 12691-12702.
- Schaffrin, B., and A. Wieser (2008), On weighted total least-squares adjustment for linear regression, *J. Geodesy*, *82*, 415-421.
- Scharoo, R., and P. N. A. M. Visser (1998), Precise orbit determination and gravity field improvement for the ERS satellites, *J. Geophys. Res.*, *103*, 8113-8127.
- Schmidt, D. A., and R. Bürgmann (2003), Time-dependent land uplift and subsidence in the Santa Clara valley, California, from a large interferometric synthetic aperture radar data set, *J. Geophys. Res.*, *108*.
- Schmidt, D. A., R. Bürgmann, R. M. Nadeau, and M. d'Alessio (2005), Distribution of aseismic slip rate on the Hayward fault inferred from seismic and geodetic data, *J. Geophys. Res.*, *110*.
- Scholtz, C. H. (1998), Earthquakes and friction laws, *Nature*, *391*, 37-42.
- Scholz, C. H. (2002), *The Mechanics of Earthquakes and Faulting*, Cambridge Univ. Press, Cambridge, 2nd. ed. 496 pp.
- Segall, P., R. Bürgmann, and M. Matthews (2000), Time-dependent triggered afterslip following the 1989 Loma Prieta earthquake, *J. Geophys. Res.*, *105*, 5615-5634.
- Segall, P., P. Cervelli, S. Owen, M. Lisowski, and A. Miklius (2001), Constraints on dike propagation from continuous GPS measurements, *J. Geophys. Res.*, *106*, 19,301-319,318.
- Segall, P., and J. Davis (1997), GPS applications for geodynamics and earthquake studies, *Ann. Rev. Earth Planet. Sci.*, *25*, 301-336.
- Segall, P., E. K. Desmarais, D. Shelly, A. Miklius, and P. Cervelli (2006), Earthquakes triggered by silent slip events on Kūlauea volcano, Hawaii, *Nature*, *442*, 71-74.
- Segall, P., and M. Matthews (1997), Time dependent inversion of geodetic data, *J. Geophys. Res.*, *102*, 22,391-322,409.
- Shahpasandzadeh, M., and K. Hesami (2007), Assessment of the surface ruptures of the 2005 Qeshm Island earthquake, *IIEES RESEARCH BULLETIN*.
- Shirzaei, M., and T. R. Walter (2009), Randomly Iterated Search and Statistical Competency (RISC) as powerful inversion tools for deformation source modeling: application to volcano InSAR data, *J. Geophys. Res.*, *114*, B10401, doi:10.1029/2008JB006071.
- Shirzaei, M., and T. R. Walter (2010a), Time-dependent volcano source monitoring using InSAR time series: A combined Genetic Algorithm and Kalman Filter approach, *J. Geophys. Res.*, 2010JB007476.
- Shirzaei, M., and T. R. Walter (2010b), Wavelet based InSAR (WabInSAR): a new advanced time series approach for accurate spatiotemporal surface deformation monitoring, *IEEE Transactions on Geoscience and Remote Sensing*, TGRS-2010-00058.
- Showstack, R. (2010), Haiti quake increased stress along fault, in *EOS*, edited, p. 170.
- Siebert, L. (1992), Threats from debris avalanches, *Nature* *356*, 658 - 659

- Sodoudi, F., X. Yuan, R. Kind, B. Heit, and A. Sadidkhouy (2009), Evidence for a missing crustal root and a thin lithosphere beneath the Central Alborz by receiver function studies, *Geophys. J. Int.*, 177, 733–742.
- Swanson, D. A., W. A. Duffield, and R. S. Fiske (1976a), Displacement of the south flank of Kilauea Volcano: The result of forceful intrusion of magma into the rift zones, Profess. Paper 936, 1-39 pp, U. S. Geol. Surv.
- Swanson, D. A., W. A. Duffield, and R. S. Fiske (1976b), Displacement of the south flank of Kilauea Volcano: the result of forceful intrusion of magma into the rift zones, *U. S. Geol. Surv. Prof. Pap.*, 963, 1 – 37.
- Talbot, C. J., S. Medvedev, M. Alavi, H. Shahrivar, and E. Heidari (2000), Salt extrusion at Kuh-e-Jahani, Iran, from June 1994 to November 1997, *Geological Society, London, Special Publications*, 174, 93-110.
- Talebian, M., and J. Jackson (2004), A reappraisal of earthquake focal mechanisms and active shortening in the Zagros mountains of Iran, *Geophysical Journal International*, 156, 506-526.
- Tatar, M., D. Hatzfeld, and M. Ghafory-Ashtiany (2004), Tectonics of the Central Zagros (Iran) deduced from microearthquake seismicity, *Geophys. J. Int.* , 156, 255–266.
- Tatar, M., D. Hatzfeld, J. Martinod, A. Walpersdorf, M. Ghafori-Ashtiany, and J. Chery (2002), The present-day deformation of the Central Zagros from GPS measurements, *Geophys. Res. Lett.*, 29, 1927.
- Tatarski, V. I. (1961), *Wave propagation in a turbulent medium*, 285 pp., McGraw-Hill New York.
- Thatcher, W. (1982), Seismic triggering and earthquake prediction, *Nature*, 299, 12-13.
- Tizzani, P., P. Berardino, F. Casu, P. Euillades, M. Manzo, G. P. Ricciardi, G. Zeni, and R. Lanari (2007), Surface deformation of Long Valley caldera and Mono Basin, California, investigated with the SBAS-InSAR approach *Remote Sensing of Environment*, 108, 277-289.
- Torrence, C., and G. P. Compo (1998), A Practical Guide to Wavelet Analysis, *AMS*, 79, 61-78.
- Troise, C., G. De Natale, F. Pingue, F. Obrizzo, P. De Martino, U. Tammara, and E. Boschi (2007), Renewed ground uplift at Campi Flegrei caldera (Italy): New insight on magmatic process and forecast, *Geophysical Research Letters*, 34.
- Van Kenen, P. E., C. J. Spiers, A. P. Van Den Berg, and J. Muzyerte (1993), The effective viscosity of rocksalt: implementation of steady-state creep laws in numerical models of salt diapirism, *Tectonophysics*, 225, 457-476
- Van Wyk de Vries, B., and P. Francis (1997), Catastrophic collapse at stratovolcanoes induced by gradual volcano spreading, *Nature*, 387, 387–390.
- Vanicek, P., and E. Krakiwesky (1982), *Geodesy: the concepts*, 697 pp., North-Holand publishing company.
- Vernant, P., F. Nilforoushan, J. Chery, R. Bayer, Y. Djamour, F. Masson, H. Nankali, J. F. Ritz, M. Sedighi, and F. Tavakoli (2004a), Deciphering oblique shortening of central Alborz in Iran using geodetic data, *Earth and planet. Sci. Lett.*, 223, 177-185.
- Vernant, P., F. nilforoushan, D. Hatzfeld, M. Abbassi, C. Vigny, F. Masson, H. nankali, J. Martinod, A. Ashtiani, K. C. Bayer, F. Tavakoli, and J. Chery (2004b), Present-day crustal deformation and plate

- kinematics in the Middle East constrained by GPS measurements in Iran and Northern Oman, *Geophys. J. Int.*, *157*, 381–398.
- Waldhauser, F., and W. L. Ellsworth (2000), A double-difference earthquake location algorithm: method and application to the northern Hayward fault, California, *Bull. Seism. Soc. Am.*, *90*, 1353–1368.
- Walter, T. R. (2007), How a tectonic earthquake may awake silent volcanoes: Stress triggering during the 1996 earthquake–eruption sequence at the Karymsky Volcanic Group, Kamchatka. , *Earth and planet. Sci. Lett.*, *264*, 347–359.
- Walter, T. R., and F. Amelung (2006), Volcano-earthquake interaction at Mauna Loa volcano, Hawaii, *J. Geophys. Res.*, *111*, doi:10.1029/2005JB003861.
- Wan, E. A., and R. Van Der Merwe (2000), The unscented Kalman filter for nonlinear estimation, *AS-SPCC*, 153–158.
- Welch, G., and G. Bishop (2001), An Introduction to the Kalman Filter, edited, p. 81, ACM, Inc, University of North Carolina at Chapel Hill.
- Whitley, D. L. (1994), A genetic algorithm tutorial, *Stat. Comput.*, *4*, 65–85.
- Williams, S., Y. Bock, and P. Fang (1998), Integrated satellite interferometry: Tropospheric noise, GPS estimates and implications for interferometric synthetic aperture radar products, *J. Geophys. Res.*, *103*, 27,051–27,067.
- Wolfe, C. J., B. A. Brooks, J. H. Foster, and P. G. Okubo (2007), Microearthquake streaks and seismicity triggered by slow earthquakes on the mobile south flank of Kilauea Volcano, Hawai'i, *Geophys. Res. Lett.*, *34*, L23306.
- Wooller, L., B. van Wyk de Vries, J. B. Murray, H. Rymer, and S. Meyer (2004), Volcano spreading controlled by dipping substrata, *Geology*, *32*, 573–576.
- Wright, T. L., and F. W. Klein (2006), Deep magma transport at Kilauea volcano, Hawaii, *Lithos*, *87*, 50–79.
- Yang, X.-M., P. M. Davis, P. T. Delaney, and A. T. Okamura (1992), Geodetic analysis of dike intrusion and motion of the magma reservoir beneath the summit of Kilauea Volcano, Hawaii: 1970–1985, *J. Geophys. Res.*, *97*, 3305–3324.
- Yang, X.-m., P. M. Davis, and J. H. Dieterich (1988), Deformation from inflation of a dipping finite prolate spheroid in an elastic half-space as a model for volcanic stressing, *J. Geophys. Res.*, *93*, 4249–4257.
- Yuegang, W., X. Hongtao, and H. Teng (2007), Non-stationary signal denoising based on wavelet transform, *IEEE*, *3*.
- Zebker, H., and J. Villasenor (1992), Decorrelation in interferometric radar echoes, *IEEE Trans. Geosci. Rem. Sensing*, *30*, 950–959.
- Zebker, H. A., P. A. Rosen, and S. Hensley (1997), Atmospheric effects in interferometric synthetic aperture radar surface deformation and topographic maps, *J. Geophys. Res.*, *102*, 7547–7563.
- Zha, X., R. Fu, Z. Dai, and B. Liu (2008), Noise Reduction in Interferograms Using the Wavelet Packet Transform and Wiener Filtering, *Geoscience and Remote Sensing Letters, IEEE*, *5*, 404 - 408.

Zhou, R., F. Tajima, and P. L. Stoffa (1995), Application of genetic algorithm to constrain near-source velocity structure for 1989 Sichuan earthquake, *Bulletin of the Seismological Society of America*, 85, 590-605.

Zimmerman, W. (1969), On the optimum colored noise Kalman filter, *Automatic Control, IEEE Transactions on*, 14, 194- 196.

Zollo, A., N. Maercklin, M. Vassallo, D. D. Iacono, J. Virieux, and P. Gasparini (2008), Seismic reflections reveal a massive melt layer feeding Campi Flegrei caldera, *Geophys. Res. Lett.*, 35, L12306, doi:10.1029/2008GL034242.

Curriculum vitae



Manoochehr Shirzaei Eng.

Born on 21.9.1981, Zahedan, Iran

Section 2.1 Physics of the Earth Natural Hazards,
GFZ Potsdam, Telegrafenberg 14473 Potsdam,
Germany

Tel: +49(0)331-288-1293

Fax: +49(0)331-288-1204

Email: shirzaei@gfz-ptsdam.de

EDUCATION

- | | |
|-----------|---|
| 9/07-1/11 | Ph.D. with reward (Summa cum laude), Potsdam University, Potsdam, Germany . Title of the thesis: "Crustal deformation source monitoring using advanced InSAR time series and time dependent inverse modeling" |
| 2003 | M.S. Geodesy, Tehran University, Tehran, Iran |
| 2001 | B.A. Surveying engineering, Amir-Kabir University of Technology, Tehran, Iran |

PROFESSIONAL EXPERIENCE

- | | |
|--------------|---|
| 6/10-present | Postdoctoral Scholar, German Research Centre for Geosciences (GFZ), Potsdam, Germany |
| 9/07-6/10 | Geophysicist/geodesist, German Research Centre for Geosciences (GFZ), Potsdam, Germany |
| 2004-2007 | Geophysicist/geodesist, International Institute of Earthquake Engineering and seismology, (IIEES), Tehran, Iran |
| 2002-2004 | Geodesist, National Cartographic Centre (NCC), Tehran, Iran |

HONOR AND AWARDS

- | | |
|------------|---|
| 2011 | Reward for best PhD student, German Research Centre for Geosciences (GFZ), Potsdam, Germany |
| 2011 | Rewarded PhD (Summa cum laude), Potsdam University |
| 9/07-6/10 | GEOTECHNOLOGIEN program "Managing volcanic unrest", Fellowship |
| 2003 | Rewarded for top ten master thesis in Tehran University |
| 2003 | Placed first ranked student in M.S. |
| 1999- 2001 | Placed first ranked student in B.A. |
| 1994- 1998 | Placed first ranked student in High school |

TEACHING ACTIVITIES AND UNIVERSITY SERVICES

2003-2004 Lecturer, school of surveying engineering, Hamedan, Iran
2003-2006 Lecturer, Amir-Kabir University of technology, Tehran, Iran

COURSES TAUGHT

Error analysis and adjustment, Global Positioning Systems, Surveying, Geodesy, and Physical geodesy

SUPERVISION OF THE MASTER THESIS

2004-2005 Co-supervisor for M.S. student Leila Karimi at Khaje Nasir Toosi University of Technology, Tehran, Iran

ORGANIZATIONAL INVOLVEMENT

2010-2011 EGU chairman
2002-present Member of EGU
2008-present Member of IAVCEI
2009-present Member of AGU

RESEARCH PROJECTS

6/10-present International plate boundary observatory Chile (IPOC)
9/07-6/10 Exupery: Managing volcanic unrest
2005-2006 GPS network design for geophysical applications, NCC
2003-2004 Blind fault positioning using aeromagnetic data, NCC

INVITED TALKS

2010 CNRS, Laboratoire Magmas et Volcans, Clermont Fround
2010 American Geoscience Union, San Francisco
2009 European Geoscience Union, Vienna
2009 DLR, Germany

PUBLICATIONS

Peer reviewed journals

2011

Shirzaei, M., T. R. Walter, H. R. Nankali, and E. Holohan (2011), Gravity-driven deformation of Damavand volcano detected through InSAR time series, *Geology*, 39, 3, 251–254; doi: 10.1130/G31779.1.

Shirzaei, M., and T. R. Walter (2011), Satellite orbital error reduction using wavelet based robust regression applied to InSAR deformation data, *IEEE Transactions on Geoscience and Remote Sensing*, in press.

Shirzaei, M., and T. R. Walter (2011), Wavelet based InSAR (WabInSAR): a new advanced time series approach for accurate spatiotemporal surface deformation monitoring, *IEEE Transactions on Geoscience and Remote Sensing*, under review.

Shirzaei, M., and T. R. Walter (2011), Wavelet analysis of InSAR time series reveals block-like movement and activity of Hilina fault, Hawaii *Geophys. Res. Lett.*, under review.

Shirzaei, M., and T. R. Walter (2011), Interplay of deformation sources at Hawaii Island investigated through InSAR time series and time-dependent modeling, *J. Geophys Res.*, 2010JB007476, under review.

Shirzaei, M., T. R. Walter, F. Yamini-Fard, and A. Gholamzadeh (2011), Geodetic, seismic and Coulomb stress transfer analysis of the 2005 Qeshm earthquake: competing model interpretation, *Geol. Soc. Am. Bull.*, under review.

Shirzaei, M., and T. R. Walter (2011), The 12 Jan 2010, Haiti earthquake affected by aseismic fault slip, *Naturegeoscience*, under review.

Bathke, H., Shirzaei, M., and T. R. Walter (2011), Inflation and deflation at Llaima volcano (Chile) detected by using InSAR, *Geophys. Res. Lett.*, under review.

2010

Shirzaei, M., and T. R. Walter (2010), Time-dependent volcano source monitoring using InSAR time series: A combined Genetic Algorithm and Kalman Filter approach, *J. Geophys. Res.*, 115, B10421, doi:10.1029/2010JB007476.

2009

Shirzaei, M., and T. R. Walter (2009), Randomly Iterated Search and Statistical Competency (RISC) as powerful inversion tools for deformation source modeling: application to volcano InSAR data, *J. Geophys. Res.*, 114, B10401, doi:10.1029/2008JB006071.

Ruch, J., A. Manconi, G. Zeni, G. Solaro, A. Pepe, M. Shirzaei, T. R. Walter, and R. Lanari (2009), Stress transfer in the Lazufre volcanic area, Central Andes, *Geophys. Res. Lett.*, 36, L22303, doi:22310.21029/22009GL041276.

Other journals

Walter, T. R.; Manzo, M.; Manconi, A.; Solaro, G.; Lanari, R.; Motagh, M.; Woith, H.; Parolai, S.; Shirzaei, M.; Zschau, J.; Baris, S.; Ansal, A. (2010): Satellite Monitoring of Hazards: A focus on Istanbul, Turkey. *Eos, Transactions, American Geophysical Union*, 91, 36, 313-314.

Conference papers

Shirzaei, M. T.R. Walter, (2010), The 12 Jan 2010, Haiti earthquake affected by aseismic fault creep, AGU.

- Shirzaei, M. T.R. Walter, (2010), Untangling temporally and spatially overlapping volcano deformation source signals at Hawaii Island
- Shirzaei, M. T.R. Walter, (2010), Damavand volcano spreading detected by advanced InSAR time series, EGU.
- Shirzaei, M. T.R. Walter, (2010), „Near real time inverse source modeling and stress field assessment: the requirement of a volcano fast response system“, EGU.
- Shirzaei, M. T.R. Walter, (2010), Dynamic influence of volcanic activity at Mauna Loa, Hawaii, on earthquake occurrence in Kaoiki investigated via time dependent source modeling and static stress transfer, EGU.
- Shirzaei, M. T.R. Walter, (2009), Deformation interplay at Hawaii Island, AGU.
- Shirzaei, M. T.R. Walter, (2009), WabInSAR: a new wavelet based InSAR time series technique applied to volcanic and tectonic areas, AGU.
- Shirzaei, M. T.R. Walter, (2008), InSAR time series shows multiple deformation and interaction of gravitational spreading, intrusion and compaction on Hawaii Island, EGU.
- Shirzaei, M. T.R. Walter, (2008), New wavelet based InSAR time series (WAB-InSAR) technique eliminating atmospheric and topographic artifact using wavelet transforms and lead to accurate spatio-temporal deformation field mapping, EGU.
- Shirzaei, M. T.R. Walter, M. Motagh, A. Golamzadeh, F. Yamini-Fard., (2008), Hybrid inversion of InSAR deformation and aftershock data to precise source modeling of the 2005 Qeshm island earthquake (Iran), EGU.
- Shirzaei, M. T.R. Walter, (2008), Wavelet based SBAS approach for InSAR time series: an application to volcanotectonic activities associated with Ol Doinyo Lengai volcano and nearby, IAVCEI.
- Shirzaei, M. T.R. Walter, M. Motagh, A. Golamzadeh, F. Yamini-Fard., (2007), Precise source modeling of the 2005 Qeshm island earthquake (Iran), using a joint inversion of surface deformation and aftershock data, Fringe workshop.
- Shirzaei, M. T.R. Walter, M. Motagh, A. Manconi, R. Lanari (2007), Inversion of InSAR data via Genetic Algorithm and Simulated Annealing methods-first results from the Campi-Flegrei volcanic region, Fringe workshop.
- Shirzaei. M. and Mokhtari. M., (2006), Review on application of GPS in geodynamics and Earthquake prediction, 12th Geophysics conference of Iran.
- Shirzaei. M., Mansouri. B., and Shinozuka. M., (2006), Multiresolution Analysis of Satellite Optical Images for Damage Detection using Wavelet Transform, 4th International Workshop on Remote Sensing for Disaster Response 25-26th September 2006, Cambridge, UK.
- Shirzaei. M. and Ardalani, A., (2005), Gravity tomography for determination of the location and extent of interior structures of the Earth via wavelet transforms, Case study: gravity tomographic map of the oil reservoirs, EUG.
- Shirzaei. M., (2004), Gravity And Magnetic Observation As Pseudo Image, Via Multiscale Edge Analysis For Subsurface Fault Positioning. Case study: Positioning Of Subsurface Faults For Area Of Iran, AGU.
- Shirzaei. M., (2004), Multiresolution And Multiscale Edge Analysis Via Wavelet Transforms, Applied in Inversion of Gravity Field for Oil Exploration. Case study: Oil Exploration in Southern Part of Iran, AGU.
- Shirzaei. M., and Ardalani, A., (2004), Enhancement of Somigliana-Pizzetti reference gravity field for area of Iran, Proceeding of Annual Conference of Geomatics-National Cartographic Center.
- Shirzaei, M.; Ardalani, A., (2004), frequency domain separation of gravity field crustal layers by 2-D wavelet analysis of surface gravity field observations for oil exploration, EGU - 1st General Assembly, Nice, France.

Shirzaei, M.; Ardalan, A., (2004), "Multiscale edge analysis as a tool for oil exploration via gravity Observations". EGU - 1st General Assembly, Nice, France.

Ardalan, A., Shirzaei, M., (2004), Very local gravity field modeling, Case study: Gravity field modeling for Iran, EGU - 1st General Assembly, Nice, France.

Ardalan, A., Shirzaei, M., (2003), A method for precise estimation of volume of oil resource via application of first and second derivation of wavelet transforms, EGS-AGU-EUG Joint Assembly, Nice, France.

Ardalan, A., and Shirzaei, M., (2003), On the robust spectral analysis; Case studies: Mean sea level computation from tide gauge data, EGS-AGU-EUG Joint Assembly, Nice, France.

Shirzaei, M., (2003), Mean Sea Level computation for Persian gulf and Oman sea via Wavelet transforms, Proceeding of Annual Conference of Iranian civil engineers, Amirkabir university of technology-Tehran.

Shirzaei, M., (2003), Cycle slip detection in GPS data via Wavelet transforms, Proceeding of Annual Conference of Iranian civil engineers, Amirkabir university of technology-Tehran,.

DEVELOPED SOFTWARES

RISC-GA-KF	Heuristic confident tool for optimizing variety of dynamic geophysical problems
RISC-SA/GA	Heuristic confident tool for optimizing variety of static geophysical problems
WabInSAR	Wavelet based InSAR time series tool for multi-temporal analysis of radar data
WabRegres	Wavelet based robust regression tool for correcting the effect of orbital error in repeat pas interferometry.

KNOWLEDGE IN SIGNAL ANALYSIS

Familiar with Kalman Filter, Wavelet Transforms, Fourier Transform, Genetic Algorithm, Simulated Annealing

PROGRAMING SKILLS

MATLAB, Maple

SOFTWARE

ENVI, SARscape, DORIS, ROI-PAC, GMTSAR, GMT, BERNESE, GAMIT/GLOBK,

RESEARCH INTEREST

Advanced InSAR time series methods
Inverse problem
Crustal deformation monitoring and modeling

LANGUAGE SKILLS

Persian (native), English, German (under improvement)